Development of an organ-on-chip microfluidic device incorporating an actuatable hydrogel layer to produce barrier tissue mimicries on chips

Nicolas Minier

Par **Nicolas MINIER**

Development of an organ-on-chip microfluidic device incorporating an actuatable hydrogel layer to produce barrier tissue mimicries on chips

Thèse présentée
pour l'obtention du grade
de Docteur de l'UTC

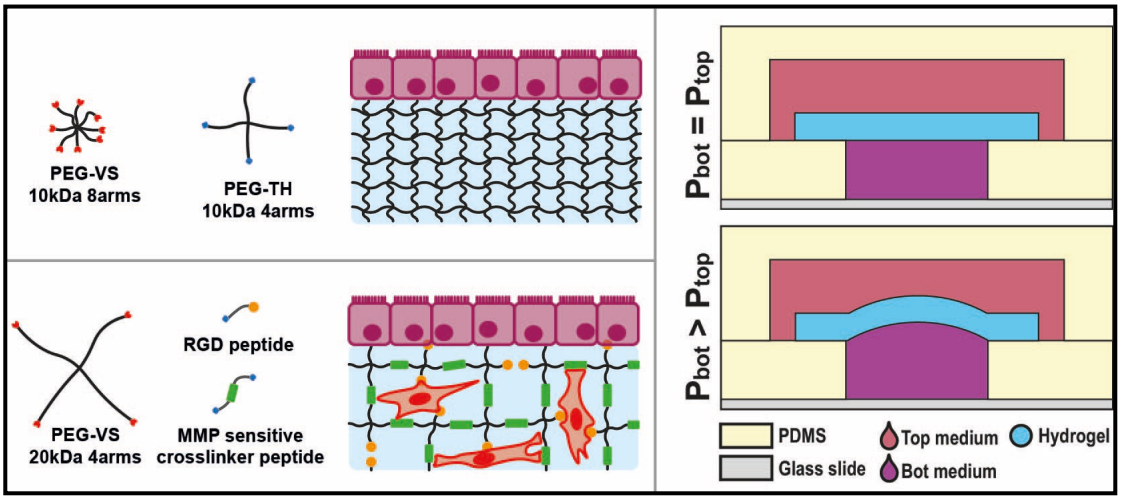

Soutenue le 10 décembre 2021
Spécialité : Bioingénierie : Unité de Recherche Biomécanique et Bioingénierie (UMR-7338)

D2644

École doctorale n°71 : Sciences pour l'Ingénieur

Thèse

Development of an organ-on-chip microfluidic device incorporating an actuatable hydrogel layer to produce barrier tissue mimicries on chips

pour obtenir le grade de docteur délivré par

Université de Technologie de Compiègne

Spécialité : Bioingénierie

présentée et soutenue publiquement par

Nicolas MINIER

Le 10 Décembre 2021

Jury :

M. BOUDOU Thomas	Evaluateur
M. GOBAA Samy	Co-Directeur de thèse
Mme. LE GOFF Anne	Evaluatrice
M. MALAQUIN Laurent	Rapporteur
Mme. SAUVONNET Nathalie	Invitée
Mme. VAYSSADE Muriel	Directrice de thèse
Mme. VILLARD Catherine	Rapportrice

RÉSUMÉ

Alors que l'éthique et la loi poussent la recherche à plus de sécurité, ainsi qu'à une moindre utilisation des animaux, il est devenu crucial de développer des systèmes *in vitro* d'une plus grande pertinence. Depuis la fin du XX^{e} siècle, plusieurs systèmes ont fait leur apparition pour tenter de pallier les difficultés rencontrées, et notamment les « organes-sur-puces » (*organ-on-chip systems*). Ces systemes microfluidiques de culture cellulaire avancés permettant de recreer certaines fonctions tissulaires grâce au contrôle très précis des conditions du microenvironnement cellulaire. Malgré les avancées de la bioingénierie et l'amélioration de nos méthodes de culture *in vitro*, la discipline est jeune et de nombreux progrès restent à faire.

Les travaux présentés ici détaillent le développement d'un organe-sur-puce incluant une membrane d'hydrogel déformable et dégradable, aux propriétés physico-chimiques proches de tissus mous tels que les poumons ou les intestins.Cette puce semble pertinente pour accueillir des tissus barrières, composés de plusieurs types cellulaires, organisés de part et d'autre, ainsi qu'au sein de cette barrière, souvent soumise à des stimuli mécaniques.

Durant ce doctorat, plusieurs objectifs ont été atteints :

- Concevoir et fabriquer un organe-sur-puce incluant un hydrogel biocompatible et déformable, ainsi qu'un système microfluidique permettant le contrôle indépendant du flux et de la déformation de la membrane d'hydrogel.
- Caractériser la déformation subie par l'hydrogel.
- Cultiver dans la puce des cellules intestinales, formant un épithélium structuré en trois dimensions, et caractériser sa perméabilité à des molécules de tailles variées.

Mots clés : HAHL, Organe-sur-puce, microsystèmes, microfluidique, biomatériaux, hydrogel, PEG, intestin, Caco-2/TC7, perméabilité apparente.

SUMMARY

Modern day ethics and laws call for more safety and use of fewer animals in biomedical research. It became crucial to develop novel *in vitro* devices of higher relevance. Since the end of the twentieth century, several systems have been proposed by researchers in attempts to palliate the shortcomings of current systems. Notably, organs-on-chip systems are specifically tailored to recapitulate tissue functions in a manner that remains easily accessible for the experimenter. Despite the significant improvements that were brought during the last century to *in vitro* cell and tissue culture systems, the field of bioengineering is still young and much progress remains to be done.

The work presented here details the development of an organ-on-chip that includes a biocompatible and actuatable hydrogel membrane, with controlled physico-chemical properties. Such chip is relevant when hosting barrier tissues, which are composed of several cell types, disposed on each side of a barrier, as well as within its bulk, and are often submitted to mechanical stimuli.

During this PhD, several objectives have been attained. Notably, we:

- Designed and produced an organ-on-chip including a biocompatible and actuatable hydrogel layer, as well as a microfluidic system allowing the independent control of both flow and actuation.
- Characterized the deformation of the hydrogel layer.
- Cultured intestinal cells within the chip, which formed a three dimensionally structure epithelium, and characterized its apparent permeability to molecules of varying sizes.

Keywords: HAHL, Organ-on-chip, microdevices, microfluidics, biomaterials, hydrogel, PEG, intestine, Caco-2/TC7, apparent permeability.

Les travaux rapportés ici ont été menés au sein des structures suivantes :

Université de technologie de Compiègne, CNRS, Biomécanique et Bioingénierie,
Centre de recherche Royallieu - CS 60 319 - 60 203 Compiègne Cedex

Institut Pasteur, C2RT, Plateforme Technologique Biomatériaux et Microfluidique,
28 rue du Docteur Roux, 75015 Paris

The work presented here was done in the following structures:

Université de technologie de Compiègne, CNRS, Biomechanics and Bioengineering,
Centre de recherche Royallieu - CS 60 319 - 60 203 Compiègne Cedex

Institut Pasteur, C2RT, Biomaterials and Microfluidics core facility,
28 rue du Docteur Roux, 75015 Paris

Scientific production:

Funfak A., Bouzhir L., Gontran E., **Minier N.**, Dupuis-Williams P., Gobaa S. Biophysical Control of Bile Duct Epithelial Morphogenesis in Natural and Synthetic Scaffolds. *Frontiers in Bioengineering and Biotechnology*, December 2019, 7:417.

Article in writing:

Minier N., Gobaa S.
Inclusion of a hydrogel layer in an organ on chip and its hydraulic actuation to submit intestinal epithelial cells to mechanical stimulus.

Scientific communications:

SLAS 2019 “Advanced 3D Human Models and High-Content Analysis Symposium”
October 2019, London (UK). Poster.
Minier N., Gobaa S. *Novel Organ-on-Chip Microfluidic Device Based on Hydraulically Actuated Hydrogel Layers.*

QBio/Cancer initiative joint symposium “The physics of cancer”
October 2021, Paris (FR). Oral presentation.
Minier N., Gobaa S. *Transducing forces using hydrogels on a chip.*

Remerciements

Sur plus d'aspects que je ne l'avais anticipé, cette thèse doctorale aura été placée sous le signe de la découverte, et des premiers pas. Que ce soit d'avoir intégré une toute jeune structure, d'être le premier « thésard » de son directeur de thèse, et bien sûr de par l'innovation qui est au cœur de toute plateforme technologique, ces travaux ont mené à maintes aventures, tant scientifiques qu'humaines. Alors que je couche sur ces pages ce qui constitue presque une rétrospective, je souhaite prendre le temps de remercier celles et ceux qui m'auront accompagné sur cette route, ne serait-ce que le temps d'une rencontre sur le chemin.

En premier lieu, je tiens à remercier Samy GOBAA, pour la confiance dont il m'a fait preuve en me donnant l'opportunité de travailler au projet HAHL. Également pour les occasions, très formatrices, où j'ai pu découvrir les arcanes de la revue par les pairs, et celles où il a pu me reconnaître une compétence et souhaité la mettre au profit de la plateforme. Merci aussi à Muriel VAYSSADE pour sa disponibilité, malgré les kilomètres qui nous séparaient. Ce remerciement, je l'étends à toutes les personnes du laboratoire BMBI que j'ai pu rencontrer, tant elles m'ont marqué par leur bienveillance.

Je tiens à remercier tout particulièrement celles et ceux qui ont accepté de se faire juré·es et d'accorder du temps au jeune chercheur qui se présente devant vous : M. Thomas BOUDOU, Mme Anne LE GOFF, M. Laurent MALAQUIN, Mme Nathalie SAUVONNET, Mme Catherine VILLARD. Je suis honoré par l'intérêt que vous avez manifesté pour mes travaux.

Je ne pourrais pas non plus oublier de remercier mes collègues de la plateforme BMcf, pour tous les temps passés ensemble, et qui rendent la recherche plus humaine. Emmanuel, pour les longues discussions tant scientifiques que philosophico-politiques, ainsi que l'aide apporté par ce vétéran de la maison Pasteur. Anette, pour sa confiance, et pour m'avoir proposé de collaborer avec elle sur son projet. Mélanie et Gizem, ensuite, les deux post-docs de la plateforme et qui immanquablement auront servies de *role models*. Je ne peux non plus oublier Héloïse et Jérôme, qui nous ont rejoints alors que l'équipe s'agrandissait, ainsi qu'Annie et Natacha. À ces personnes ainsi

qu’à celles et ceux qui ont croisé ma route à la plateforme comme utilisateur·ices ou stagiaires (je pense notamment à Charlotte) : Merci !

Je tiens également à remercier ceux qui, par leurs expertises, leurs réflexions, leurs avis, ont grandement fait avancer mon projet, en premier lieu desquels Jean-Yves TINEVEZ.

Enfin, il me faut remercier mes proches et mes ami·es, pasteurien·nes ou non. Chaleureux remerciements à ma famille, Mei, Maxime, Warren, Emeline, Mathieu, Alexis, Guillaume, Yves-Joël, à toutes celles et ceux de la Stapa et du Café des Sciences. Pour tous ces moments à sortir la tête du guidon, à jouer, naviguer, explorer, voyager, ***mersi braz !***

[…] Roll for initiative.

Résumé substantiel

Introduction

Systèmes de culture cellulaire complexes

Aujourd'hui, les biologistes ont à leur disposition un large panel de systèmes de culture cellulaire. Qu'il s'agisse d'outils génériques comme les plaques et flasques de culture (T75, SBS, *etc.*) ou spécifiques comme les chambres de Boyden, la biologie cellulaire du 21^{e} siècle est marquée par cette opulence de moyens à disposition. Cependant, les ponts toujours plus nombreux qui se font entre la biologie cellulaire et d'autres domaines de recherche (physique, sciences des matériaux, mathématiques, *etc.*) nourrissent le développement de nouveaux outils de culture cellulaire avancés, qu'ils soient sur-mesure pour un type d'expérience donnée, ou bien plus complet dans leur capacité à reproduire le microenvironnement natif d'un tissu cultivé. Alors que la culture cellulaire en deux dimensions montre certaines limites pour proprement reproduire *in vitro* la physiologie des tissus, la fin du 20^{e} siècle a proposé de nouveaux outils de culture cellulaire en trois dimensions. Notamment, deux grandes modalités font aujourd'hui l'objet de nombreuses recherches et avancées.

D'une part, la production d'organoïdes se base sur l'encapsulation de cellules dans une matrice aux propriétés physico-chimiques plus ou moins contrôlées selon qu'elle soit naturelle (Matrigel, Collagène, Fibrine, *etc.*) ou synthétique (ex : polyéthylène glycol). Au sein de cette matrice, les cellules vont pouvoir s'autoorganiser, et reproduire la morphologie ainsi que la physiologie du tissu natif. Les cellules souches intestinales Lgr5+ recréant, au sein de Matrigel, un organoïde complexe organisé en structures semblables à des cryptes et villi intestinaux en sont l'illustration parfaite[1].

D'autre part, les *organs-on-chips* capitalisent sur les avancées de la microfluidique et de ce qu'elle permet (manipulation de petits volumes, imagerie, *lab-on-chip*, *etc.*) afin de concevoir et créer un microenvironnement sur mesure, tant dans ses propriétés physiques que chimiques, ou dans sa topographie par exemple. Il existe aujourd'hui de très nombreux *organs-on-chips*, qui peuvent être dédiés à la reconstruction d'un tissu ou organe spécifique (peau[2], vaisseaux sanguins[3], barrière hémato-

encéphalique[4], *etc.*), ou de soumission à un stimulus et/ou à une infection par exemple[5-7].

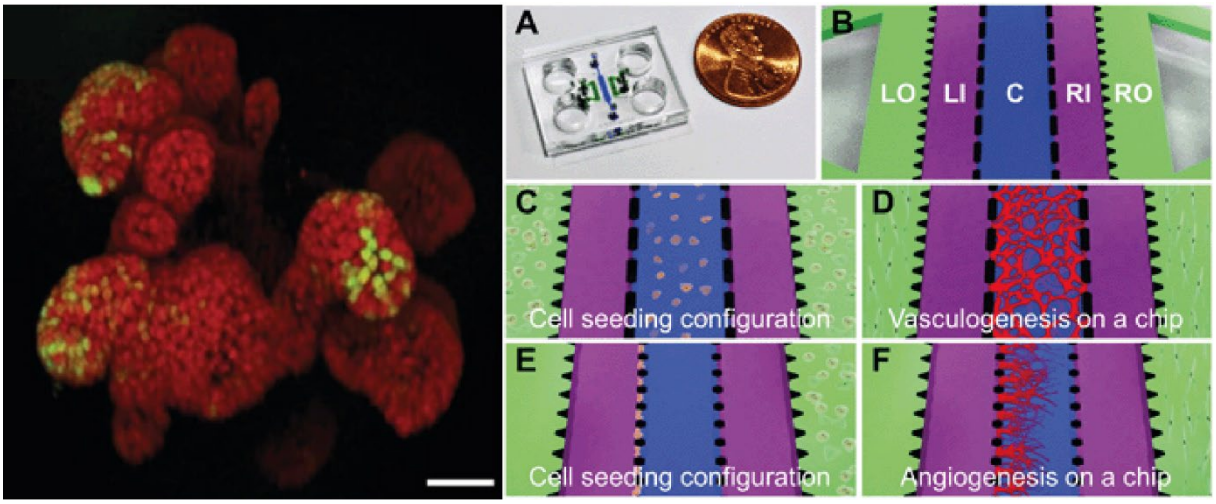

Figure R1 : Organoïdes et organs-on-chips sont deux modalités de culture cellulaire cherchant à reproduire avec fidélité la physiologie native d'un tissu.
(Gauche) *placée dans un hydrogel adéquat, une cellule souche unique peut produire un organoïde complexe structurée d'une manière proche des cryptes et villi intestinaux. Echelle = µm. Adapté de Sato* et al.*, 2009[1].* ***(Droite)*** *Organ-on-chip destiné à observer la formation de capillaires sanguins grâce à l'invasion d'un hydrogel par des cellules. Adapté de Kim* et al.*, 2013[8].*

L'un des nombreux avantages des *organs-on-chips* réside dans leur capacité à offrir un système qui puisse être suivi en microscopie, et de révéler à l'observation ce qui est difficilement accessible *in situ*, au sein d'un organisme vivant. À ce titre, les tissus barrières attirent l'attention des équipes de recherche, ainsi que le suivi de leur infection par des agents pathogènes. Aujourd'hui, de nombreuses puces servent à accueillir des tissus barrières, intestinaux[6, 7, 9] et pulmonaires[5, 10] notamment.

Le projet Hydraulically Actuated Hydrogel Layer (HAHL)

En 2010, Huh et collègues proposent une puce microfluidique permettant de cultiver ensemble, de part et d'autre d'une membrane de PDMS perforée, des cellules épithéliales pulmonaires ainsi que des cellules endothéliales[5]. Par un système de

canaux latéraux mis en sous-pression, il est possible d'étirer la membrane sur laquelle sont cultivées les cellules, reproduisant l'étirement du tissu sous l'effet de la respiration. Cette puce sert aujourd'hui par exemple à évaluer l'impact des flux et étirements sur la physio- et pathologie des tissus barrières, pulmonaire ou intestinal par exemple. Malgré les avantages que propose cette puce, on note que la membrane perforée de PDMS présente quelques limites. D'une part, les propriétés mécaniques du PDMS restent éloignées de celle des tissus mous (Module de Young ~MPa *vs.* ~kPa). D'autre part, la membrane perforée ne permet pas d'accueillir des cellules (stromales, immunitaires, *etc.*) en son sein, et ne demande pas aux cellules de mettre en place les mêmes mécanismes d'extravasation qu'*in vivo*.

Le projet HAHL ambitionne de développer une puce microfluidique qui puisse accueillir un tissu barrière, stroma compris, aux propriétés mécaniques proches des tissus mous. Pour cela, le projet se propose de passer par une membrane d'hydrogel mécaniquement couplée à la puce, en remplacement de la membrane de PDMS perforée. Plusieurs obstacles doivent être levés : identifier des recettes d'hydrogel aux propriétés mécaniques pertinentes, assurer leur inclusion dans la puce microfluidique, maîtriser et caractériser la déformation de la membrane, permettre d'une part la culture de cellules sur et au sein de l'hydrogel, mais également son emploi dans des expériences types d'évaluation de la fonctionnalité du tissu, ainsi que l'accès en microscopie de la puce et/ou de l'échantillon fixé.

La puce HAHL

Principe et conception de la puce

Deux versions de la puce ont été développées. Bien que différentes dans leurs dimensions et orientations, elles partagent des points communs. Pour coupler mécaniquement la membrane d'hydrogel au PDMS de la puce, celui-ci est traité en surface avec des vapeurs de (3-Mercaptopropyl)trimethoxysilane afin d'exposer à sa surface des groupements thiols, qui peuvent être intégrés dans un réseau d'hydrogel par addition de type « thiol-Michael ». Ensuite, le principe derrière la déformation de la membrane d'hydrogel est inchangé. Pour y parvenir, la pression dans chacun des

canaux microfluidiques de part et d'autre de la membrane d'hydrogel est maîtrisée. Lorsqu'un différentiel de pression est appliqué (typiquement, un des canaux est mis sous pression tandis que l'autre reste à pression ambiante), la membrane se déforme à la manière d'un ballon de baudruche, en s'étirant selon l'axe transversal au canal microfluidique (voir Figure R2 ci-dessous).

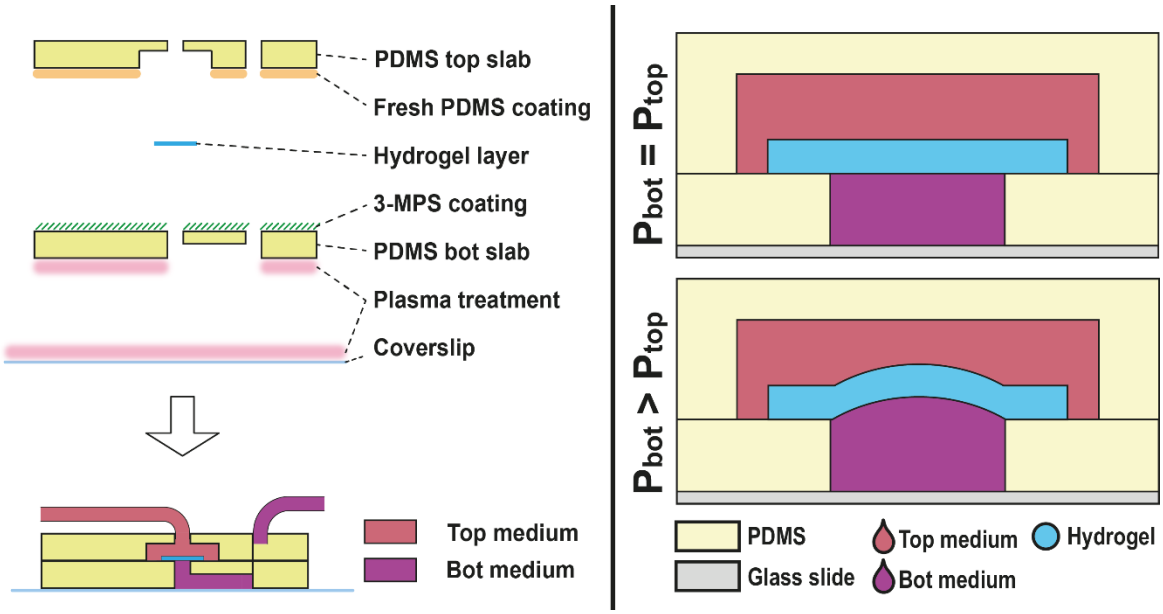

Figure R2 : Conception et principe de la puce HAHLv2.

Gauche : *Assemblage de la puce HAHLv2. Chronologiquement, les étapes se déroulent de bas en haut.* ***Droite :*** *Principe de différentiel de pression gouvernant la déformation de la membrane d'hydrogel.*

Selon les besoins en termes de résolution spatiale et de propriétés optiques, les différentes pièces de PDMS ont été coulées dans des moules conçus par photolithographie (épaisseur contrôlée de résine photosensible exposée sélectivement au travers d'un masque haute résolution), creusés dans une pièce de laiton, ou imprimé en 3D (résine SLA).

Composition des hydrogels

Les hydrogels retenus partagent la caractéristique de mettre en place un réseau de molécules formé par addition de type « thiol-Michael ». Plus précisément, les molécules impliquées sont porteuses soit de groupes vinyle-sulfone (VS), soit de

groupe thiol (TH). En présence d'une base, et à pH et température permissives, vinyle-sulfones et thiols réagissent pour former une liaison covalente carbone-soufre stable dans le temps. Les molécules choisies pour porter les fonctions VS sont toutes des polyéthylène glycols (PEG), de poids moléculaires et nombres de bras différents. Les molécules porteuses de fonctions TH peuvent être selon les cas des PEGs, ou des peptides d'intérêt, porteurs de deux cystéines (et donc de deux fonctions TH) ainsi que d'une séquence sensible aux MMPs.

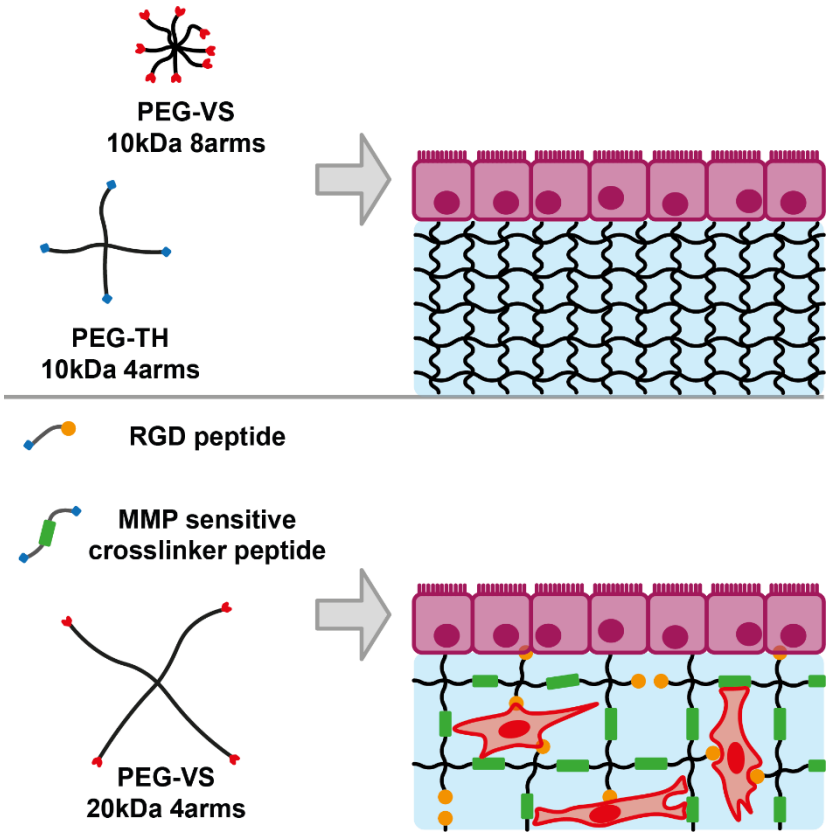

Figure R3 : Principe de la composition des hydrogels.

Haut : *Des hydrogels PEG10-10 permettent d'obtenir un hydrogel densément maillé, plus facilement manipulable, mais qui ne se prêtent pas à l'encapsulation de cellules.* ***Bas :*** *Des hydrogels formés de PEGVS à haut poids moléculaire et/ou faible nombre de bras, couplés à des peptides porteurs de fonctions TH et sensibles aux* matrix metalloproteinases, *produisent des hydrogels moins rigides et capables d'accueillir des cellules en son sein.*

Pour illustration, dans les applications n'impliquant pas d'encapsulation de cellules au sein de l'hydrogel, la principale recette utilisée correspond à un mélange de PEGVS10k8a (PEG à 8 bras fonctionnalisés VS, d'un poids moléculaire de 10 kDa) et PEGTH10k4a, dans des proportions telles que les fonctions VS et TH sont présentes

en proportions stœchiométriques, avec une concentration finale en PEG de 5% (w/v). Dans les applications incluant une encapsulation de cellules, une recette reprise plus loin correspond au mélange de PEGVS40k4a et de 16R (hexadécapeptide acétylé portant une arginine en position 12, le différenciant des autres peptides utilisés durant ces travaux).

Dispositif microfluidique

Plusieurs dispositifs ont été testés. Les deux premiers s'appuient sur la relation $P = Q.R$ entre pression (P), flux (Q), et résistance (R), pour contrôler la pression dans les canaux microfluidiques. Le premier contrôle le flux grâce à un pousse-seringue, et augmente celui-ci jusqu'à déformation de l'hydrogel. Le second applique une pression en amont de la puce, et contrôle le flux grâce à des résistances (tubes fins) en aval de celle-ci. Le dernier dispositif retenu place des pousse-seringues en amont de la puce, contrôlant le flux. En aval, un des réservoirs est mis sous pression, permettant l'actuation de la membrane d'hydrogel sans impacter la perfusion. Ainsi, flux et pression sont contrôlés indépendamment.

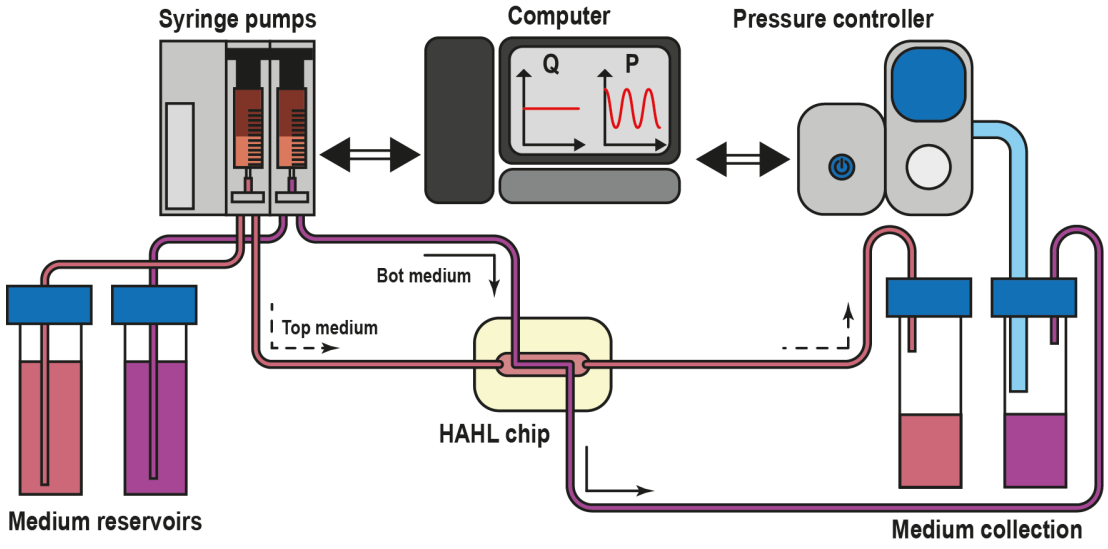

Figure R4 : Dispositif microfluidique HAHL.

Principaux résultats

Caractérisation des hydrogels

Les propriétés physiques des hydrogels ont été explorées. D'une part, le gain de masse/de volume des hydrogels au moment de leur hydratation. D'autre part en rhéologie, en mesurant les modules complexe, de conservation, et de perte. Au-delà de l'emploi de PEGTH ou de peptides, l'impact de plusieurs paramètres ont été explorés : balance stœchiométrique, inclusion de RGD (endecapeptide PEGylé portant une séquence RGD permettant l'adhésion cellulaire), concentration en PEG/peptide.

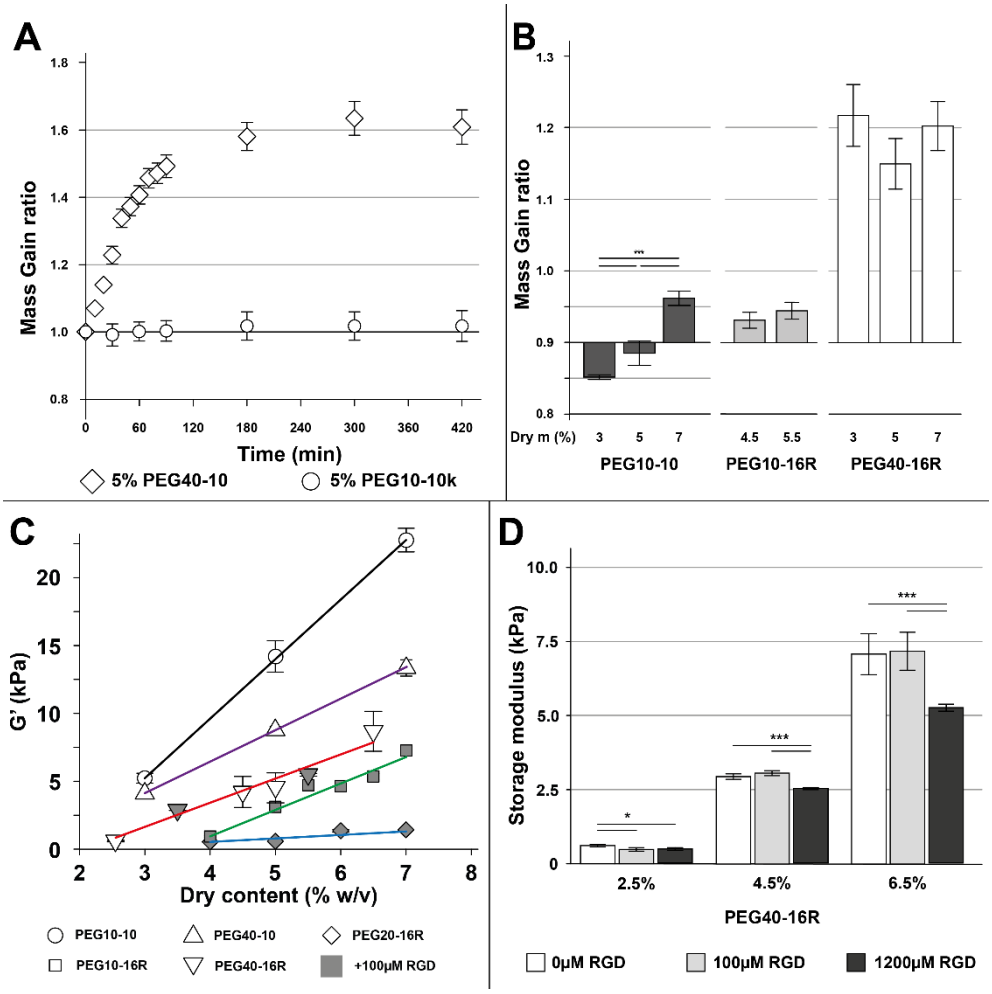

Figure R5 : Caractérisation physique de divers hydrogels.

*(**A**) Evolution du ratio de masse au cours de l'hydratation. (**B**) Ratio de masse final de divers hydrogels. (**C**) Module de conservation de divers hydrogels en fonction de leur fraction solide. (**D**) Impact de l'addition de RGD sur le module de conservation des hydrogels.*

Caractérisation de la déformation de l'hydrogel

Pour comprendre et cartographier la déformation de la membrane d'hydrogel, nous avons incorporé des billes fluorescentes dans des hydrogels (5% w/v PEG10-10). Leur position était ensuite suivie alors qu'un différentiel de pression était mis en place de part et d'autre de la membrane. Plusieurs approches ont été utilisées. La première consiste en le suivi de paires de billes. La seconde consiste en l'analyse du déplacement de larges populations de billes observées avec un objectif à faible grossissement. La dernière, nécessitant de localiser en 3D l'ensemble des billes, explore les déformations locales de l'hydrogel, en dissociant les deux surfaces de la membrane. Cette cartographie permet de construire un maillage précis des surfaces, de mesurer les surfaces et leur évolution.

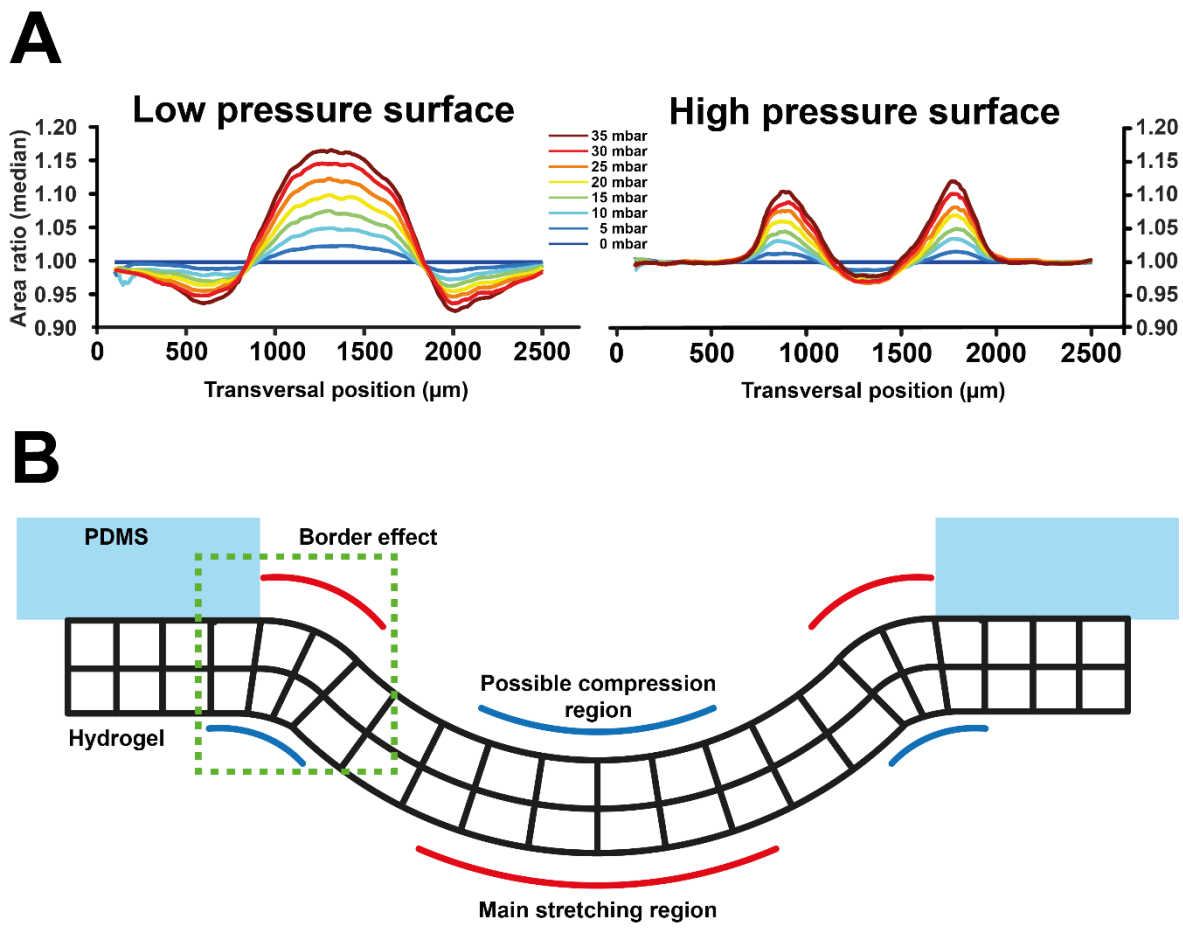

Figure R6 : Déformation de la membrane d'hydrogel.

(A) *déformation tangentielle à la surface de la membrane d'hydrogel, en fonction du différentiel de pression entre les deux surfaces.* ***(B)*** *Résumé compréhensif de la déformation, basé sur les données collectées.*

Les premières mesures, bien que permettant de quantifier l'étirement, ont révélé la nécessité de cartographier plus précisément la déformation de la membrane, puisque les valeurs obtenues variaient grandement selon la position observée. Seule une approche s'intéressant aux deux surfaces indépendamment a permis de décrire la déformation de manière satisfaisante. En détail, il apparaît que le ratio épaisseur/largeur de la membrane, associé à la courbure prise par celle-ci, amène à l'apparition d'une zone de compression au centre de la surface exposée à la plus forte pression (voir Figure R6). De plus, des zones de compression apparaissent également sur les berges du canal, du côté de la pression la plus faible.

Production et caractérisation d'épithéliums intestinaux

Comme première preuve de la pertinence de la puce microfluidique développée, nous nous sommes attachés à cultiver des épithéliums intestinaux, en cultivant des cellules Caco-2/TC7. L'impact des molécules inclues dans l'hydrogel ou recouvrant celui-ci sur l'adhésion des cellules a été évalué, ainsi que l'impact des conditions de flux et d'actuation sur l'apparition de structures tridimensionnelles.

Dans un premier temps, différentes conditions de flux (30, 100, ou 200 $\mu L.h^{-1}$) et d'actuation (cycles sinusoïdaux de pression de 1 à 31 mbar, à une fréquence de 0.1 Hz, ou absence d'actuation) ont été testées et la formation ou non de structures tridimensionnelles a été observée en microscopie (Bright Field). Sur les épithéliums formés sous les conditions de flux et d'actuation jugées les plus prometteuses (en l'occurrence, flux constant de 100 $\mu L.h^{-1}$), illustré en Figure R7 A, la fonctionnalité de l'épithélium a été évaluée, après six jours de culture sur la puce. D'une part, en évaluant la perméabilité apparente de l'épithélium face à de petites molécules (ici, Dextran de 4 kDa) et la comparant à celle de la membrane d'hydrogel seule. D'autre part, en immunofluorescence, afin de confirmer l'expression et localisation de l'actine et E-cadhérine.

Ces expériences ont permis de confirmer que le tissu agit comme barrière à l'encontre de molécules, même de petites tailles (Figure R7 B), ainsi que la facilité d'usage de la puce HAHL pour explorer de telles questions. De même, la puce HAHL s'est révélée

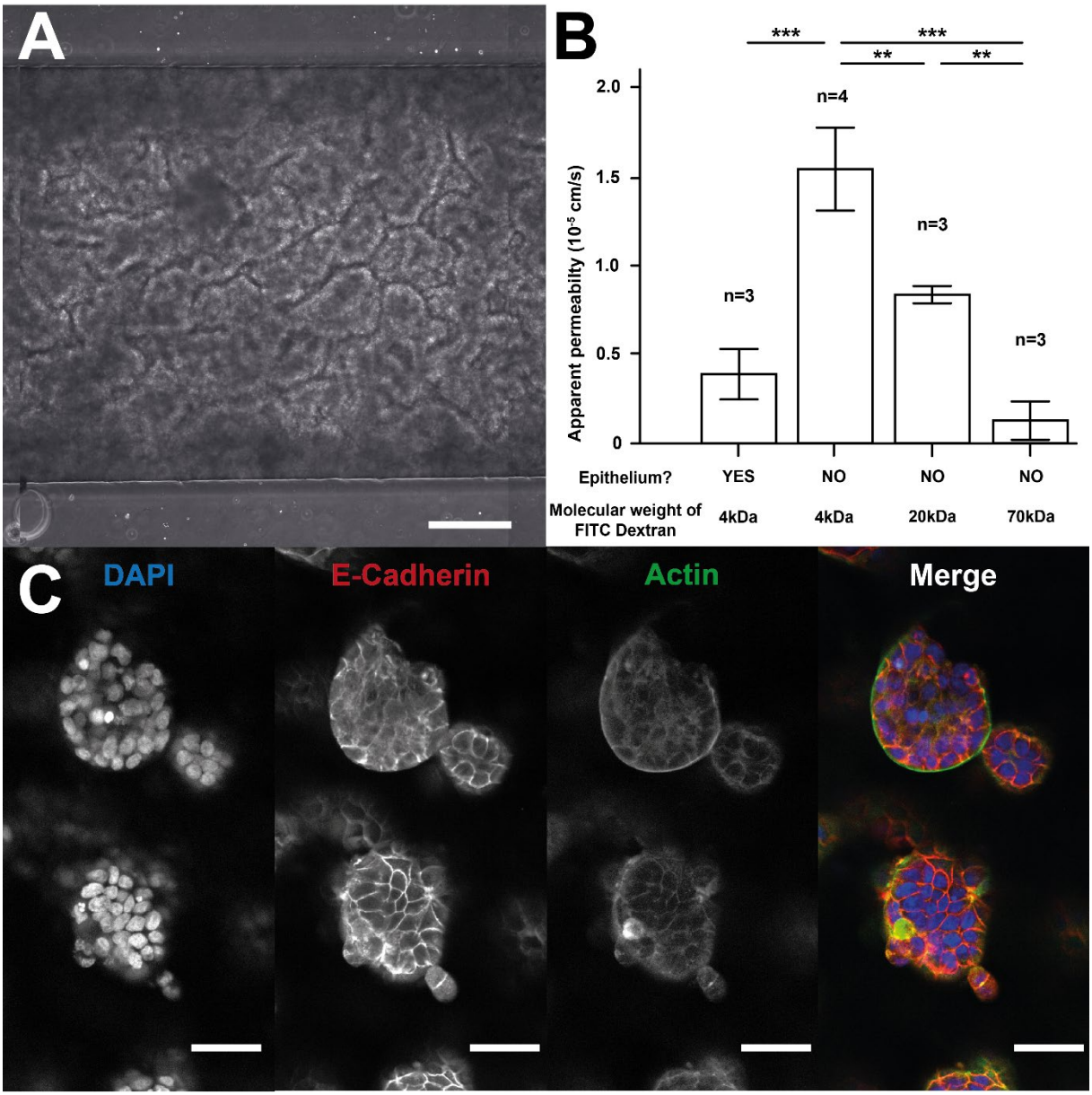

Figure R7 : Production d'un épithélium intestinal sur puce.

(A) *Epithélium imagé après six jours de culture sur puce, laissant voir une organisation tridimensionnelle. Echelle = 200 µm.* ***(B)*** *Perméabilité apparente de la membrane d'hydrogel à des molécules de différentes tailles, en présence ou non d'un épithélium intestinal après 6 jours de culture sur puce.* ***(C)*** *Image en immunofluorescence révélant l'expression apicale d'actine* ***(vert)****, et basolatérale d'E-Cadhérine* ***(rouge)****.* ***Bleu :*** *DAPI. Echelle = 50 µm.*

particulièrement aisée à fixer, perméabiliser et *stain* en amont de l'imagerie en immunofluorescence. Imager l'échantillon passe nécessairement par son extraction de la puce. De plus, l'épaisseur de l'hydrogel force à imager l'échantillon renversé, épithélium vers le bas. Afin qu'il ne s'affaisse pas sous son propre poids durant la

session d'imagerie, il a été nécessaire de développer un protocole d'encastrement de l'échantillon dans un hydrogel PEG10-10 permettant de figer sa structure sans l'altérer. Le résultat est reporté en Figure R7 C, montrant l'expression d'actine et d'E-Cadhérine, ainsi que leur localisation (apicale et basolatérale, respectivement), confirmant la bonne polarisation de l'épithélium.

Encapsulation cellulaire

Un des avantages du système HAHL, et de la membrane d'hydrogel, et de permettre d'envisager l'encapsulation de cellules stromales, offrant un compartiment cellulaire supplémentaire. Afin de préparer ces travaux, j'ai pu profiter d'une collaboration avec une collègue (Anette FUNFAK), intéressée par la production de kystes de cholangiocytes, que j'ai pu aider à identifier des conditions physiques et chimiques permettant leur formation et leur croissance. La nature des hydrogels PEG40-16R nous a permis d'établir une « matrice » de conditions physico-chimiques, avec des modules de conservation allant de 0,5 à 7,2 kPa, et une concentration en ligand RGD allant de 0 à 1200 µM **(Figure R8A)**. Cela nous a permis évaluer indépendamment l'impact de ces deux paramètres sur la fréquence d'apparition de kystes, ainsi que leur diamètre, en fonction de ces paramètres.

Concernant l'apparition de kystes à partir de cellules uniques, nous avons trouvé que les hydrogels de 0,5 à 3,0 kPa permettent leur formation dans des proportions comparables à l'encapsulation dans du Matrigel **(Figure R8B)**. Seule la condition 4,5% PEG40-16R + 1200 µM RGD a produit une fréquence de formation inférieure au Matrigel ($p < 0.05$). En revanche, les hydrogels avec un module de conservation >5 kPa ont produit beaucoup moins de kystes. Concernant le diamètre atteint au dixième jour par les kystes, celui-ci est d'autant plus élevé que l'hydrogel a un module de conservation faible **(Figure R8C)**. De plus, l'impact favorable de l'ajout de ligand RGD est d'autant plus marqué que l'hydrogel a un module de conservation faible, induisant une multiplication par 3,9 du diamètre dans la condition 2,5%, et de 1,7 dans la condition 6,5%.

Dans l'ensemble, ces résultats suggèrent un impact majeur de l'élasticité sur la capacité des cholangiocytes à former des kystes, ainsi qu'une action combinée de l'élasticité et de la concentration en ligand RGD pour croitre en taille.

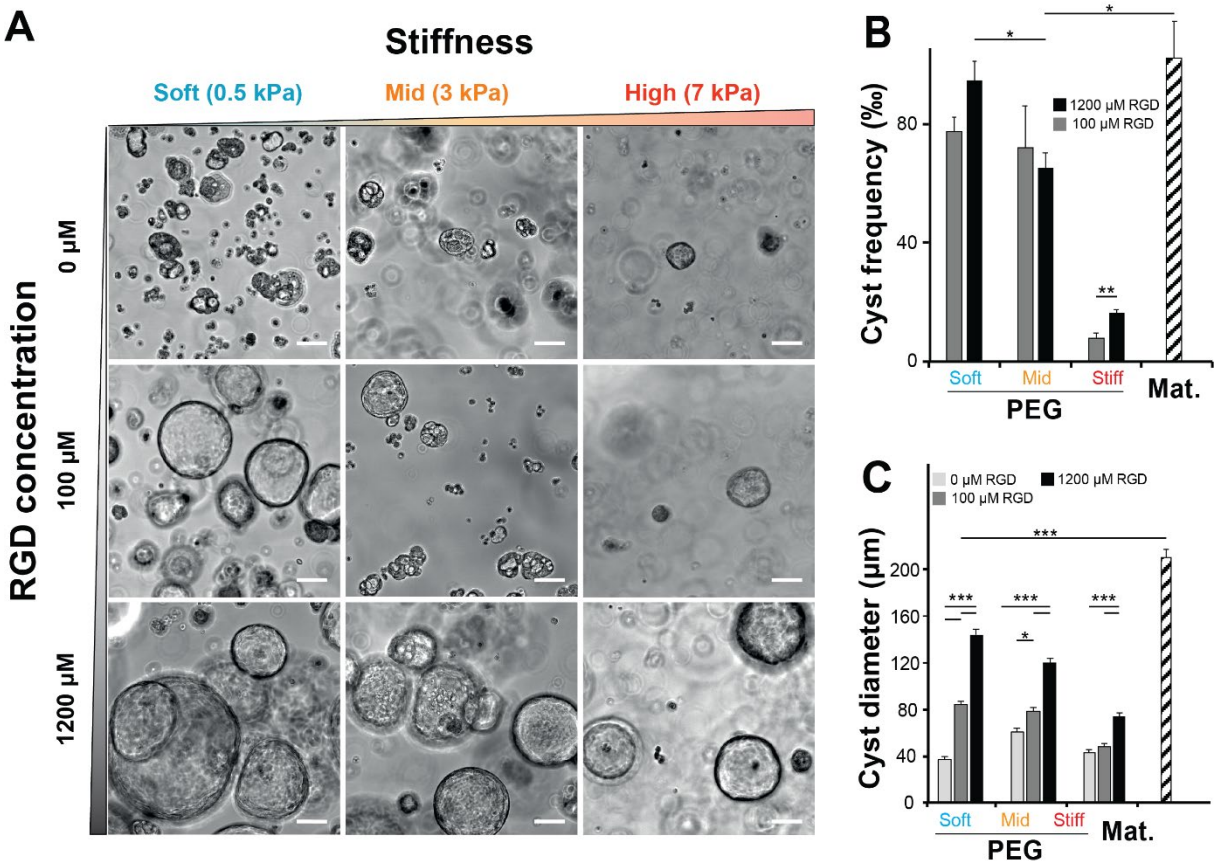

Figure R8 : Encapsulation de cholangiocytes dans des hydrogels PEG-peptides.

(A) *Les hydrogels PEG40-16R permettent de moduler indépendamment les propriétés physiques et chimiques du substrat de culture 3D.* ***(B)*** *Impact de la composition du substrat sur la fréquence de formation de sphéroïdes 10 jours après encapsulation de cellules.* ***(C)*** *Impact de la composition du substrat sur le diamètre des sphéroïdes de cholangiocytes formés après 10 jours de culture.*

Cette encapsulation n'a pas empêché l'accès à l'échantillon en immunofluorescence à condition d'adapter les temps d'incubation (jusqu'à 4 jours pour le *staining* primaire) pour prendre en compte la faible perméabilité de l'hydrogel à des molécules de grande tailles. Nous notons donc l'aspect prometteur des hydrogels PEG40-16R, du fait de (a) leur biocompatibilité, (b) la facilité à moduler leurs propriétés physico-chimiques, et (c) l'accès préservé pour des expériences biologiques impliquant de larges molécules.

Conclusion

La conception d'organes-sur-puces se trouve sujette à un équilibre entre la complexité du système d'une part, cherchant à offrir des conditions similaires au microenvironnement du tissu *in vivo* sur plusieurs tableaux (nature et concentration des molécules présentes, propriétés mécaniques du substrat, *etc.*), et d'autre part la pertinence des apports de la puce microfluidique comparée à des systèmes plus simples. Dans ce projet, nous faisons le pari d'apporter conjointement sur une même puce plusieurs paramètres qui ont, individuellement, fait la preuve de leur pertinence pour permettre le développement de tissus *in vitro*. Notamment, la puce HAHL propose de réunir en une puce (a) trois compartiments cellulaires (typiquement épithélial, stromal, endothélial), (b) le contrôle les propriétés mécaniques du substrat de culture cellulaire, (c) le contrôle partiel de la composition de l'hydrogel et des molécules présentées aux cellules cultivées, et (d) la possibilité de stimuler mécaniquement le tissu cultivé.

Durant ce projet, nous avons tout d'abord proposé un *design* de puce microfluidique permettant d'accueillir une membrane d'hydrogel faisant barrière entre deux compartiments perfusables. Nous avons également développé un système microfluidique permettant d'agir indépendamment sur les flux et le différentiel de pression. La déformation de la membrane produite par ce différentiel de pression a pu être explorée, et nous avons aujourd'hui une compréhension fine des mécanismes à l'œuvre ainsi que des forces de compression ou d'étirement auxquelles sont soumises les différentes régions de la membrane. Parallèlement, un travail exploratoire sur les propriétés physiques et chimiques de nombreuses recettes d'hydrogel a été mené, afin d'identifier les recettes pertinentes pour une inclusion dans la puce HAHL.

Dans un second temps, nous nous sommes attachés à produire une première démonstration de la possibilité de cultiver des cellules sur la puce HAHL, d'observer les tissus reproduits, et de réaliser un certain nombre d'essais biologiques sur ce tissu. Cela a pris la forme de la cultures de cellules épithéliales intestinales Caco-2/TC7. Cela nous a permis d'étudier les conditions favorisant l'apparition de structures tridimensionnelles, et d'évaluer la polarisation ainsi que la fonction barrière du tissu produit.

Enfin, des travaux exploratoires ont été menés pour préparer la montée en complexité du système. Tous ces résultats nourrissent l'espoir de voir le système HAHL utilisé à court terme pour reproduire les physio- et pathologie de tissus barrières.

TABLE OF CONTENT

LIST OF ABBREVIATIONS

3-MPS	(3-Mercaptopropyl)trimethoxysilane
Caco-2	Immortalized cell line of human colorectal adenocarcinoma cells
CBC	Crypt Base Columnar (stem cells)
CHO	Chinese Hamster Ovary
DMEM	Dulbecco's modified Eagle's medium
DMSO	Dimethyl sulfoxide
DPBS	Dulbecco's phosphate buffered saline
DTT	DL-Dithiotreitol
ECM	Extracellular Matrix
EGF	Epithelial Growth Factor
ENS	Enterous Nervous System
FBS	Fetal Bovine Serum
FGF	Fibroblast Growth Factor
Fn9-10	Recombinant fibronectin fragment containing the 9^{th} and 10^{th} repeats of Type III modules of fibronectin
FnPEG	Linear hetero-bifunctional PEG, grafted on one end with a fibronectin fragment containing the 9^{th} and 10^{th} repeats of Type III modules of fibronectin
GALT	Gut Associated Lymphoid Tissue
GI	gastro intestinal
hIPSC	human induced Pluripotent Stem Cell
Hh	Hedgehog
HTS	High Throughput Screening

IEC	Intestinal Epithelial Cell
ISC	Intestinal Stem Cell
LVER	Linear viscoelasticity region
MDCK	Mardin-Darby Canine Kidney
MMP	Matrix Metalloproteinase
MuSC	Muscle Stem Cell
MyoD	Myosin D
NGF	Nerve Growth Factor
NMR	Nuclear Magnetic Resonance
NRC	Normal Rat Cholangiocytes
ooc	Organ-on-chip
PCR	Polymerase Chain Reaction
PDMS	Polydimethylsiloxane
PEG	Poly(ethylene glycol)
PEP	Peptides (16A, 16 or 16W)
PGMEA	Propylene glycol monomethyl ether acetate
PMMA	Polymethyl methacrylate
RGD	Endecapeptide containing an RGD sequence allowing for integrin binding
RH	Relative humidity
RT	Room temperature
SBS	Society for Biomolecular Screening, which proposed a standard for microwell plates
SEM	Scanning Electron Microscopy
T75	75 cm² cell culture flask

TEA	Triethanolamine
TEER	Transepithelial Electrical Resistance
µCCA	micro Cell Culture Analog

How to read abbreviated forms of PEG molecules

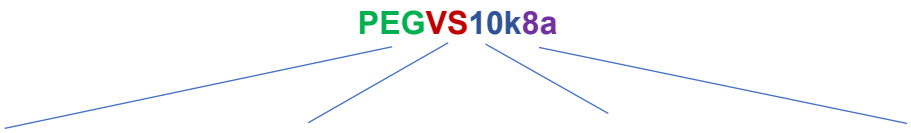

PEG	VS	10k	8a
Polyethylene glycol	Vinyl sulfone functionalization	10 kDa average molecular weight	8 arms

How to read abbreviated forms of PEG hydrogels

For the sake of readability, and as only one PEG of a given molecular weight was used, we can simplify the name of PEG-PEG and PEG-PEP hydrogel as follow:

		TH-bearing molecule			
		PEGTH10k4a	**16A**	**16W**	**16R**
VS bearing molecule	**PEGVS10k8a**	“PEG10-10”	“PEG10-16A”	“PEG10-16W”	“PEG10-16R”
	PEGVS20k4a	“PEG20-10”	“PEG20-16A”	“PEG20-16W”	“PEG20-16R”
	PEGVS40k8a	“PEG40-10”	“PEG40-16A”	“PEG40-16W”	“PEG40-16R”

LIST OF FIGURES

GENERAL INTRODUCTION

Throughout the last two centuries, scientific advances in the field of biology have been closely related to technical advances in other fields, such as chemistry, physics, and informatics. Notably, the post-war era has brought many breakthroughs in these three fields. Initially thought as inert materials suitable for use in medical devices such as contact lenses[11], poly(2-hydroxyethyl methacrylate) (PHEMA) later transitioned to be used as cell culture substrate in cancer research, after the pioneering work of the team of Bissell[12]. Advances in microfabrication were followed by the birth of many microfluidic tools dedicated to exploring the physio- and pathology of living tissues[13], while our capacity to monitor tissues now allows us to monitor single cells among a larger population. Describing how advances and breakthrough in several scientific field have fed biology and cell culture is the topic of the first part of the state of the art I present in this document.

This heritage leaves us biologists with access to a large panel of cell culture tools, from generic flasks to specific instruments such as Boyden chambers or tailored microfluidic devices. Yet, bridges between biology and fields such as material sciences are ever-increasing in number, and one could anticipate that most remains to be done. Since the demonstration, in 2006, that the physical properties of the substrate can serve as cues for stem cell differentiation just as much as chemical cues were already described to be[14], faithful reproduction of the cellular microenvironment has been the focus of many research teams. Notably, two modalities have emerged, each having advantages and shortcomings.

On one hand, organoids rely on the capacity of cells and cell aggregates encapsulated in a biocompatible matrix to self-organize. Said matrices can be either natural (Matrigel, Collagen, Fibrin, *etc.*) or synthetic (PHEMA, polyethylene glycol, *etc.*), and can have physical and chemical properties more or less controlled by the experimenters[15]. Within the bulk of the matrix, cells can reproduce the morphology and physiology of native tissues. A perfect example of such potency of the cells to auto-organize is the

production of intestinal organoids displaying complex structures resembling the crypts and villi observed *in vivo*, within a polyethylene glycol (PEG) hydrogel[16] or in Matrigel[1].

On the other hand, organs-on-chips capitalize on advances in microfluidics to design to build custom-made microenvironments, in which cells can thrive while remaining easily accessible for observation and experimentation. As of today, many organs-on-chips have been designed, tailored for recapitulation of a specific tissue (skin[2], blood-vessels[3], blood-brain berrier[4], *etc.*), or designed to submit tissues to mechanical stimuli and/or infection[5-7]. The second part of the state of the art will document the last advances and trends in the production of *in vitro* models, including organoids and organs-on-chips.

In this context, the Biomaterials and Microfluidics core facility (BMcf) of the Institut Pasteur (Paris), as well as the Biomechanics and Bioengineering (BMBI) lab of the Université de Technologies de Compiègne (UTC), are working to develop new tools for cell culture. Through their participation to a research campus notably interested in infectious disease, BMcf has a keen interest for barrier tissues, and proposing adequate and advanced microdevices to collaborating research teams. A good example of that is the use of the chip proposed in 2010 by Huh and colleagues. This chip consists of two channels (one on top of the other) separated by a perforated PDMS membrane, and flanked by two other channels[5]. Applying vacuum to the side channels deforms the walls between them and the central channels, resulting in the stretch of the perforated PDMS membrane, and of the epithelium and endothelium that can be cultured on and under it. This chip has already been of great help to address questions relative to the impact of flow and strain on gut physiology and pathology[6].

However, this chip (and other ones similar in design) suffers from some shortcomings. Notably, the mechanical properties of PDMS differ greatly from that of soft tissues (Young's modulus ~MPa *vs.* ~kPa). In addition, the PDMS membrane does not allow for cell encapsulation, while stromal cells are known for their role in tissue homeostasis[17]. Here, the chip is not able to consider higher complexity than 2 resident-cell compartments.

A novel chip that would not present such shortcomings should capitalize on soft materials to replace the perforated PDMS wall, which present a first challenge of

ensuring the mechanical coupling of a thin piece of soft material with the PDMS. The way of producing actuation must also be rethought. On that end, BMcf has proposed the idea of using pressure differentials to deform a hydrogel wall placed in between two perfusable channels. The resulting chip, named HAHL (Hydraulically Actuated Hydrogel Layer), aims to propose a microfluidic device able to host a barrier tissue (including epithelium, endothelium, and stroma), with mechanical and chemical properties controlled by the experimenter. If successful, the HAHL chip should palliate some of the shortcomings or other microfluidic chips commonly used and who rely on perforated PDMS membrane to separate the luminal and vascular compartments[5].

The goal of my PhD project was to develop the HAHL chip, and demonstrate its possible use to host barrier tissues on chip. To do so, several challenges had to be addressed. Following the state-of-the-art section, a detailed Material and Method presents the reader with all the relevant pieces of information needed to understand how the experiments were performed and their motivation. This section, as well as the third one (Results & Discussion) will broach the progresses that were done in thematic chapters:

- Characterization of hydrogel recipes with relevant mechanical properties.
- Design and assembly of the HAHL chips, including how the hydrogel layer is mechanically coupled to a PDMS chip.
- Pursuit of independent control over flow and strain in the HAHL chip, and description of the microfluidic setups allowing it.
- Precise characterization of the deformation of the hydrogel layer.
- Use of the HAHL chip to culture an intestinal epithelial wall, and functional characterization of the epithelium.
- Exploratory work on the use of PEG hydrogels for cell encapsulation.

Each result chapter includes a discussion, putting the presented work in perspective of the recent literature. In a last section, the main findings are summarized and put in context, in a general conclusion section.

SECTION I
STATE OF THE ART

MAMALIAN CELL CULTURE: 100+ YEARS OF REFINMENT

Today, biologists have access to a large panel of cell culture systems. Either very generic (T75, SBS plates, *etc.*) or very application specific (Boyden chamber, *etc.*), this wealth of systems is the base for the large majority of cell biology work. The ever-increasing number of bridges that are currently being built between biology and several other fields or research and engineering such as physics, material and computational sciences, among many others, is progressively feeding the development of more advanced cell culture systems.

Since advances and breakthrough in cell biology and cell culture techniques have been fed by progress in other fields of science, this introductory chapter aims at placing the challenges of today in their historical context. This first chapter will thus cover the major developments that occurred since the birth of cell biology in a chronological fashion, and segmented in a way that will help the reader get a grasp of how advances in various fields fed one another and led to the current tools and practices. Simply put: where do we stand, and how did we get there?

Early developments

Genesis of cell biology

During the early nineteenth century, the cell theory is slowly taking shape, paving the way for experimental biology. Nearly two centuries after Robert Hooke's described what he called *"cells"* in cork[18] and the numerous descriptions of microscopic life by Antoni van Leeuwenhoek, scientists sketched the first draft of what is now commonly called after Theodor Schwann's *"cell theory"* (*Theorie des Zellen*). Largely inspired by exchanges with contemporary scientists, among which Matthias Jakob Schleiden, Schwann proposes in his book *Mikroskopische Untersuchungen ueber die Uebereinstimmung in der Struktur und dem Wachstum der Thiere und Pflanzen* (1839; *Microscopical Researches on the Similarity in the Structure and the Growth of Animals and Plants*, 1847)[19] two central conclusions that are still at the core of our understanding of cell biology:

(1) "All organized bodies are composed of essentially similar parts, namely, of cells."
(2) "We must ascribe to all cells an independent vitality."

Though he also suggested at the time the formation of cells happening *"by a sort of crystallization from out of a concentrated fluid"*, Theodor Schwann was among the biologists who largely contributed to disprove the spontaneous generation theory later on[20].

In the late 19th century, several renowned scientists rebutted the theory that life commonly arises spontaneously when the proper conditions are met. The life-permitting media these scientists used varied largely. For Theodor Schwann and Charles C. de la Tour, who studied fermentation, brewing beer foams were used[20], while Theodor von Dusch and Heinrich G. F. Schröder used a large variety of organic materials. Louis Pasteur however, following the experiments of John Needham and Lazzaro Spallanzani, mostly used meat broths. That is unlike one of his opponents of the time, Felix-Archimède Pouchet, convinced of the validity of the spontaneous generation theory, and who sometimes used hay broth as a life-permitting medium. If he did, he would probably have found himself in the awkward position of seeing heat-resistant spores (notably *Bacillus subtilis*) taking over the medium. That was the case for John Tyndall, who continued Pasteur's experiments, and notably used *"strong infusions of beef, mutton, turnip, and cucumber"*, but encountered difficulties whenever his recipe included hay[21].

The mid-19th century was also the moment for Robert Remak, together with Rudolf Virchow and Albert Kölliker, to conclude to the idea that living cells come from the scission of pre-existing cells, fixed in the now famous aphorism of Virchow proposed in 1855: *omnis cellula e cellula*[22, 23]. Together with the two first axioms of Schwann, they form the pillars of the cell theory, as we know it.

After it appeared impossible to have cells spawn from life-permitting solutions alone, and that cells were recognized as both part of an organism and independent living entities, scientists took on the new challenge of isolating and culturing them, in the hope to both understand the mechanics of living things, and understand their diseases. This step marked the emergence of biology as a field of its own as it progressively detached itself from medicine.

Cultivating mammalian cells, the first steps

Prior to using any culture media, plasma was often used, together with cells obtained from animal which plasma was easily obtained and stored, such as chicks and frogs. In the late nineteenth century, Wilhelm Roux demonstrated that living cells (in this case, obtained from the neural plate of chick embryos) could be kept alive for several days in a saline buffer of appropriate concentration [24]. Attempts to extend that period of time were made by using homogenic plasmas.

Montrose Burrows and Alexis Carrel are credited for the establishment of the first cell culture protocols. In 1911, they published together an article in which they explained their use of the word "*culture*", distinct from the sole survival of cells, summed up the findings they had shared in the previous months with several scientific societies, and described their technique to produce cell cultures in vitro[25]. Initially adapted from Ross G. Harrison's protocol[26], itself being a modified hanging drop setup[27] already described at the time, it was improved as a plate culture protocol, allowing to grow larger quantities of tissues. While Harrison used lymph that was left to clot (due to its fibrin content) to procure a substrate mimicking the native extracellular matrix (ECM), Burrows and Carrel relied on the animal's plasma to form such clot. Fresh plasma was then used as culture medium. These alterations allowed them to cultivate *"almost all the adult and embryonic tissues of dog, cat, chicken, rat, and guinea pigs"*. While the culture would last from five to about twenty days, they managed to prolong it by secondary and tertiary cultures. Later, they also demonstrated the possibility to cultivate a large variety of malignant tissues.

Still in 1911, they substantially improved their culture methods. Tissue fragments were placed on a plasma-moistened silk veil, which provides support and allows for easier manipulation. Plasma as medium is modified with Ringer's solution (a salt solution containing Na, Cl, lactate, K, Ca that allowed Sydney Ringer to keep frog hearts beating after dissection[28, 29]) and serum mixed in various concentrations. Some fragments are cultivated for a whole month, and the two authors foresee *"a great many improvements"* to follow[30].

Quickly after, Carrel pursued the goal of producing immortal cell lines. Indeed, he observed that medium renewal allowed him to extend the lifespan of cultured cells, leading him to the hypothesis that *"senility and death of the cultures, instead of being necessary, resulted merely from preventable occurrences; such as accumulation of*

catabolic substances and exhaustion of the medium."[31] Envisioning that living bodies could fall short of what artificial nutrition could allow, he had the intuition that culture cells could easily outlive the host organism: *"It is even conceivable that the length of the life of a tissue outside of the organism could exceed greatly its normal duration in the body […]"*[31]*.* It seemed to him, that his intuition was proven correct right away: the protocol he describes in his paper (including a change of media every few days, alternating between homogenic serum and plasma) started a cell culture that would eventually be maintained alive for 34 years. With the apparition of trypsinization protocols to ease cell passages[32], the cells obtained from a chicken embryo died in 1946, 2 years after Alexis Carrel's own death.

Another great improvement to the culture medium that allowed for such longevity was the use of what Carrel called *"tissue juices"* and notably embryonic extracts[33, 34]. Nevertheless, the heavy protocols, the high variability between replicates, and the many contaminations were such that cell culture did not meet much success until after the Second World War[24]. In addition, Carrel being the only one managing to keep cells living for so long (some later suspected for instance that his embryonic extracts were not exempt of fresh cells[35]) explains why, despite the seemingly major outbreak, the first half of the 20th century did not yield as much as one would expect. Nonetheless, the period saw many experimenters trying to break down media, identify their content and the use of each constituent.

Paving the way for synthetic media

In the biographical memoirs of Warren H. Lewis (written by George W. Corner) a piece of History *"not at once appreciated"* is described. There is related an experiment done by the woman he will later marry, Margeret Reed: In 1908, she placed a bit of bone marrow from a guinea pig into a tube of nutrient agar, which was used by her colleague Rhoda Erdmann to cultivate amoebae. After a few days, she noticed that the cells now formed *"a membrane-like growth on the surface of the agar, and that some of their nuclei exhibited mitotic figures"*[36]*.* Two years prior to Carrel's and Burrows established protocol, Reed was probably the first to observe mammalian cell proliferation *in vitro*, despite it being fortuitous, and without sharing the observation with the community. Though the first trials of the couple to reproduce such cultures were

inconclusive, they were encouraged by the success of Carrel and Burrows to pursue, and eventually succeeded.

Contrarily to Carrel, who was a surgeon and mostly preoccupied by finding the medium most proper for cultivating large explants, Reed and Lewis were interested in the biology of cells and were seeking an optically clear medium. This focus led them to investigate the minimal compositions that would allow cells to proliferate. In doing so, they modified Locke's solution (a modified Ringer's solution that contains glucose in addition, and more NaCl than Ringer's solution) to include amino acids, bouillon, and glucose[37, 38], and identified the importance of glucose for cell survival[39]. Later on, Alexis Carrel and Lilian E. Baker would eventually get involved in identifying key components of their medium. In 1926, they concluded to the presence of active substances in the protein fraction of embryonic extracts[40], described the effects of partially hydrolyzed proteins on cell growth[41], and the growth-promoting activity of amino acids[42]. Despites these efforts, and those of other teams such as Johannes P. M. Vogelaar and Eleanor Erlichmann who extended the cultivation time of human fibroblasts by relying on insulin and thyroxine[43], the new media developed all included some natural products (usually serum or plasma, but also bouillon or tissue extracts)[43-45].

Development after the second half of the 20th century

The first half of the 20th century has birthed many advances in physics and chemistry. Notably, Max Planck, Albert Einstein, Niels Bohr, Erwin Schrödinger, and many others participated to enhance our understanding of chemistry at the atomic scale. Such theoretical advances, as well as the many techniques developed to observe and/or isolate (NMR, chromatography, R-ray crystallography, electron microscopy, electrophoresis, *etc.*) participated to a large blooming of advances in understanding the chemical composition and structuration of life. In additions, many projects were boosted by war efforts, such as the plasma fractionation project, led by Edwin J. Cohn, and aiming at isolating the serum albumin fraction of blood plasma[46].

By 1951, Frederick Sanger had fully characterized the amino acid sequence of insulin[47]. In 1953, Francis H. Crick and James D. Watson conclude to the double-helix configuration of DNA[48], a conclusion drawn after much emulation with colleagues, and

knowledge of the advances made by two other groups, and which are published in the same edition. Namely, that of Maurice H. F. Wilkins[49] and that of Rosalind E. Franklin (including the now famous “Photo 51”)[50].

The post war era was also a fruitful moment for chemistry, and protocols to synthesize or purify many biomolecules were established at the time, often leading to the founding of companies. For instance, the mid-twentieth century sees the birth of Sigma, created in 1946 and which manufactured adenosine triphosphate, or Aldrich, founded in 1951 and dedicated to produce 1-methyl-3-nitro-1-nitrosoguanidine. Many others will follow and participate to both scientific advances and treatments of yet incurable diseases.

Cell lines

A few decades after the first cell cultures, and the claims of Carrel about seemingly immortal cell cultures, many tried to either identify immortal cells or voluntarily immortalize them. Around the middle of the 20th century, several notable cell exhibiting seemingly immortal traits were described. Some were discovered fortuitously, such as the famous HeLa, described in 1952 by George O. Gey, cell biologist at Johns Hopkins Hospital[51]. The cells were obtained (in consent conditions that would not fit today’s standards nor did meet that of the time) from the cervical carcinoma of a patient named Henrietta Lacks, and proved themselves suitable for *in vitro* culture. In fact, they are thought to be the first immortal cell strain cultured, as they did not seem to hit a limit in how many times they could divide. In 2010, HeLa cells were estimated to have been used in more than 60 000 research papers[52].

The discovery of a seemingly immortal cell line bore the promise of palliating a major drawback of fresh cells, and opened the path to more reproducible experimentation. Indeed, immortal cells would mean no need for fresh cells obtained from biopsies and human donors. With cells being easier to access without patients, biologists and medical doctors were one step closer to branching off. In addition, biopsy sourced cells showed a variability often complained about. With immortal cell lines, one could hope to conduct more reproducible experiments. This discovery marked a major milestone in the development of cellular assays.

The need for specific immortal cell lines pushed biologists to try and artificially immortalize cells. Indeed, it had been noticed that cancerous cells could be cultured

for extended periods of time[53, 54]. Starting 1938, Wilton R. Earle and Carl Voegtlin investigated the effect of methylcholanthrene on fibroblast, hoping to describe the transition from normal fibroblasts to sarcomas[55, 56]. In their experiments and in later ones[57], Earle noticed that not all fibroblasts exposed to the carcinogenic molecule would exhibit the same behavior. His experiments led him to describe several strains of cells that could give rise to sarcomas when injected into mice. From one of these strains (strain L), he sourced a single cell (clone 929) to use in later experiments[58]. Eventually, his strain was still alive for experiments ten years later[59], and survived to this day, making it the oldest established cell line, known under the name “NCTC clone 929”.

During these trials to produce immortalized cell lines, scientists often encountered a problem regarding genetic stability of the cells, and especially aneuploidy. Cells would regularly end up with several sets of chromosomes, which made them unfit many biological studies. To further investigate these effects, Joe H. Tjio and Theodore T. Pluck decided to work on the cells of Chinese hamsters and American opossums, which only have 11 pairs of chromosomes, with a wider range of sizes than that of humans. In 1958, they describe the Chinese Hamster Ovary (CHO) cell line, still in use today[60]. At the same time, Stewart H. Madin and Norman B. Darby (Jr) would start the Mardin-Darby Canine Kidney (MDCK) cell line, which was later shown to prove useful as a model for viral infection of mammalian cells[61]. Though hyperploid (chromosome number varying from 77 to 90), it is considered a useful model for kidney tubule epithelial cells since 1970[62].

In a 1961 article, Leonard Hayflick and Paul S. Moorhead reported their observation as they were attempting to culture cells over long periods of time[63]. Notably, they noticed how a primary cell culture would typically undergo three distinct phases. In phase I, the primary culture spreads until it reaches confluence for the first time. Then, phase II is characterized by a *“luxuriant growth necessitating many sbcultivations”*. Finally, the culture enters a third phase (phase III) of decay. Eventually, all cells are lost. Hayflick and Moorhead noted that each cell type behaved as if they had a limited *“passage potential”, i.e.* would enter phase III after a set number of passages. Moreover, in their experiments, Wistar Institute-1 cells were passaged until death, and excess cells were frozen at various time points. The cells were eventually shown to have a passage potential of 51 passages. Strikingly, cells frozen at passage 9 and

revived would undergo 41 more passages before dying, and cells frozen at passage 41 would undergo 9[63]. This observation led to what is now known as the Haylfick limit. This biological limit fueled the search for ways to immortalize cell lines, in the hope of avoiding variability between experimental replicates.

Media and enzymes

Following the establishment of aforementioned cell lines, Harry Eagle used two of them (namely Earle's L cells, and HeLa cells) with the goal to assess the minimum amount of small molecules that are required for proper cultivation of cells[64, 65]. Following Albert Fischer's method of serum dialysis[66, 67], Eagle identified thirteen amino acids and eight vitamins that he considered necessary for cell culture[68]. This served as the basis of the minimal essential medium (MEM) he developed four years later[69]. On his side, Thomas McCoy, relying on the same dialysis procedure, identified components necessary for the culture of Jensen sarcoma, and developed the "5A medium"[70]. Later on, both Eagle's MEM and McCoy's 5A medium would be modified to best suit desired application, such as Dulbecco's modified MEM (DMEM) in 1959[71], or Roswell Park Memorial Institute (RPMI) media "RPMI 1640" in 1966[72, 73], which is based on McCoy's 5A medium.

On the other hand, some experimenters sought to build a serum-free medium from scratch. In 1946, Philip R. White was the first to claim to have achieved long term (here, two months) culturing of animal cells (fibroblasts obtained from a chick embryo) [74]. However, other labs have found themselves unable to reproduce these results, and White's medium was put in question. Notably, F. Jacoby and S. J. Darke reported in 1948 their inability to reproduce it, while noting that addition of 10 to 20% of serum to a medium similar to that of White (containing only glucose, inorganic salts, amino acids, iron, vitamins, and glutathione), allowed for culturing of macrophages for up to two months. Jacoby and Darke noted the *"very satisfactory"* use of White's solution *"as a supplementary medium"*[75]. Relying on Earle's L cells, three major attempts at improving White's solution were successful (CMRL1066[76], NCTC109[77], and MB 752/1[78] media), but eventually required at the very least 40 constituents (MB 752/1 medium), and up to 68 (NCTC109), making them difficult to produce, and hardly suitable for experiments.

It is only in the 1970s that serum-free media took a new start, after the identification of selenite as a necessary component of serum-free media for human cell culture[79], and of transferrin and albumin as good serum substitute[80]. In 1976, Izumi Hayashi and Gordon H. Sato capitulated on a decade of work from their peers, investigating hormones (insulin, NGF, EGF, FGF, *etc.*), and described a serum substitute recipe containing transferrin in addition to four hormones (triiodothyronine, thyrotropin-releasing hormone, parathyroid hormone, somatomedin A)[81]. In their experiments, they showed that the proposed recipe allows for proliferation of GH_3, a rat pituitary cell line, while omission of any of the five ingredients lead to drastic decrease of GH_3 proliferation.

We can already note from these experiments two different ways to address the question of the biological complexity and how to break it down. A first approach consists in subtracting elements from a biological material (here, culture medium) to decrease its complexity until reaching the point where it fails to serve its purpose (supporting cell life and growth, for instance). This framework is that of Eagle and Fischer, who relied on dialysis. While it provides a clear roadmap to obtain results, it still presents the shortcomings of biologically sourced material, *i.e.* lot-to-lot variability, and a qualitative and quantitative composition that is not always fully described. The second consists in the identification of the role of single constituents of the material, and the fabrication of a fully synthetic medium. This is the approach attempted by White, and which later led to the description of serum-free media. These two methodological approaches remain today largely in competition in bioengineering to provide answers and tools when facing the complex composition of biological materials.

Triggering cell adhesion

With the exception of circulating cells, most animal cells require a physical substrate on which to adhere. That problematic was quickly understood, and many potential substrates were tested, such as agar or tissue explants from other individuals[82]. While Harrison, Carrel, and other pioneers of the times relied on clotted lymph or plasma to allow cell attachment[25, 26, 30], the use of immortal cell lines, such as Earle's L cells and HeLa cells, allowed to culture cells directly on glass flasks and dishes[68, 70, 71, 83].

While this strategy proved feasible for some cells, others (and notably primary cells) would not so easily attach to glass. While Theodor Huzella was already working on collagen as a culture substrate since a two decades[84], R. L. Ehrmann and George O. Gey reported in 1956 a protocol to produce transparent gel of reconstituted rat-tail collagen[85]. This advance allowed them to produce a sheet of biocompatible substrate, instead of individual fibers on or around which the cells could grow. 29 cell strains or tissues were tested (24 human, 2 rat, 3 frog). They noted (a) that all tissues except frog skin showed slight to greatly improved growth on collagen, (b) that the most successful collagen-to-collagen subcultures were obtained with strains which could grow vigorously on glass despite retractions, and (c) that none of the cell strains tested caused any visible lysis of the collagen substrate, placing collagen at an advantage over the traditional plasma clot.

Due to the heaviness of the procedure, and despite the clear improvements reported by Ehrmann and Gey for various cell lines and tissues, another technology took the lead: plastic wares. Indeed, after the Second World War, the plastic industry grew rapidly, and dishes, flasks, and well plates were commercially available at affordable price and in great quantity during the 1960s. Most of them were made in polystyrene, made hydrophilic by exposing their surface to oxygen ions (by mean of corona discharge[86], or gas plasma[87, 88] for instance). The many hydrophilic functions exposed by oxidized polystyrenes allows proteins such as fibronectin found in the medium to coat the plastic dish, and provide a surface to which cells can attach[89].

The composition of the ECM was progressively unveiled from the 40s onward, starting with collagen[90]. Later, adhesion molecules were discovered one after another, in the 70s and 80s[91]. In 1987, a review article gathered under the name integrin a family of adhesion receptors that were not always initially identified as such[92]. Indeed, we had yet to understand how adhesion not only hold tissues together, but also generates signals that are integrated by the cell and take part in many cellular processes such as survival, proliferation, or migration, in addition to its involvement in pathological phenomena (for example, fibronectin was initially labelled Large External Transformation-Sensitive protein by Hynes, having witnessed its loss by virus-transformed cells[93]). Being the first that was identified, collagen was also the first component of the ECM for which we accumulated proofs of its involvement in complex processes, such as the differentiation of several cell types[94-97]. Once again, the

complexity of ECM composition fueled the need for its breakdown to better understand the role of each of its constituent.

Towards condition screening

Through the 30s and 40s, a dogma progressively crumbled. Indeed, prior to being able to explore in detail the genetic and molecular diversity across cell types, it was thought that cell-virus interaction would mostly (if not only) occur between specific cell-virus couples. For instance, poliomyelitis virus mainly causing damages to neurons, not many attempts were made to infect non-nervous tissues. Despite an infructuous attempt made by Albert B. Sabin and Peter K. Olitsky in 1936[98], investigators were contemplating an extraneural site of multiplication for the virus, notably in the intestinal tract. In 1949, John F. Enders and colleagues published two papers reporting cultivation of a poliomyelitis virus strain in various embryonic and mature human tissues, and notably foreskin[99-101].

In his Nobel Prize lecture (1954), Enders admitted that his group profited from indulging in what one could call *"fishing in troubled waters"*[102]. Indeed, it appeared to him and his colleagues that virus-cell couples could have no obvious logic to them, and that finding a good host for virus replication required testing many cell lines.

In 1954, Renato Dulbecco and Marguerite Vogt adapted a plaque assay (then used by their colleague Salvatore Luria) that allowed fine quantification of viral titer, compared to previous methods[103]. In addition, plaque assays present the great advantage of allowing to assess the yield of a viral production, and to isolate viral strains. Indeed, in proper dilution conditions, each plaque can be assumed to originate from a single viral particle. Thus, plaque assays allow for the selection and isolation of a pure viral strain according to the conditions to which it was exposed (drug resistance, host specificity, *etc.*).

In 1955, the Doctor Gyula Takátsy reported in *Acta Microbiologica* the tools he has been using for several years, since Hungary faced an influenza surge in 1951. Pushed by necessity and urgency, he had to find ways to augment the throughput of his experiments. He achieved it by developing microwell plates. Despite previous devices describing mini wells placed together were described, such as that of Jonas Salk who drilled a series of wells in a plastic plate[104], Takátsy completed his system with several

homemade tools to dispense precise volumes in series, centrifuge the plates, and is often regarded as the father of microwell plates. Though initially mostly used to identify influenza strains, the system had the advantages of allowing both, to screen the susceptibility of different bacterial strains facing newly synthesized substances, and to perform virology experiments on mammalian cell biology[105].

Progressively, multiwall plates would be recognized as a must-have in all biology laboratories. Indeed, such setup presents several advantages, such as handling of smaller volumes, meaning that the volumes used before could be split to serve in several experimental conditions, and that expenses could be spared on costly reagents, Also, the handling of small plates eased the running of experiments, compared to larger utensils. The production of polymeric microwell plates met the development of immunoassays such as described by Catt and Tregear in 1967, relying on adsorption of antibodies on polymeric surfaces to perform radioimmunoassays[106]. Not long later, Enzyme-linked immunosorbent assay (ELISA) was described[107], which proposed yet new ways to selectively assess the presence of single molecules within the complex biological samples. Over the course of the 70s and 80s, pipetting robots, plate readers, and fully automated test instruments were proposed by various companies (Micromedics, Hamilton, Boehringer-Mannheim, Abbott, *etc.*), accelerating the race to decipher biological complexity and perform quantitative assays.

Modern era

Technological bloom

The last two decades of the twentieth century saw the blooming of several fields of biology, fed by the aforementioned advances. Some will be briefly broached in this last chapter, while other will be covered in more details in the following, as they constitute crucial context for the experiments presented in this manuscript.

Directly linked to the advances in computational sciences and statistical analysis tools, assay platforms such as microwell plates took a turn towards increasing their productivity, allowing what is now coined High Throughput Screening (HTS). This method aims to serialize the testing of many compounds, typically with the intent of

identifying drug candidates, either for a biochemical activity or for its impact on cell activity[108].

Since the description in 1986 of the Polymerase Chain Reaction (PCR)[109], the life of cells and tissues has been increasingly accessible to the genetic expression level. Today, transcriptomic occupy a large place in readouts of cell biology experiments, and whole genome sequencing has become more accessible and affordable, to the point of being considered a tool in nosocomial outbreak situations[110, 111] while two decades prior, the sequencing of the first complete genome (*Haemofilus influenza* Rd) necessitated a large collective effort[112].

Following the earlier discovery of specific restriction endonucleases[113], the development of molecular cloning[114] paved the way to the construction of plasmids of interest to transfect bacteria, even though biologists had to wait until the description of electroporation in 1989 to allow the transformation of a large variety of genera[115]. Genetic alteration of mammalian cells was first described in 1982, when Palmiter an colleagues microinjected rat DNA fragments in mice[116] and, thought more tedious than bacterial transformation at the time, we benefit today from new tools such as CRISPR-Cas9 which make genome edition accessible to most biology lab to produce genetically modified animals and cell lines tailored for their needs[117, 118].

Ultimately, the inherent complexity of biological materials, and the increasing ways at our disposal to address cell behavior (phenotypically, genetically, functionally, *etc.*) led to the development of a new paradigm: system biology. This approach postulate that biology can be tackled as an informational science[119], with genes and their expression at the core, involved in a crosstalk with the cellular environment. It aims at gathering comprehensive information on numerous levels of observation (from DNA to cells and ecologies), and building models to generate predictive hypothesis on the biological system.

The limits of in vivo *experimentation*

As our investigation techniques grew more and more precise, we faced more often the limits of our models and how results could be translated to human biology and health, especially for toxicity assays[120]. For organs of major interest to the question, such as the liver, we have known for long that significant differences exists between

humans and rodents[121], even though they constitute the vast majority of our animal models. Differences are also observed notably in aging process[122], dose-response profiles, cutaneous and intestinal absorption profiles[123-125], or hepatic and intestinal metabolism[126], for instance.

For these reasons, alternative methods were sought for, in the hope to overcome the shortcomings of relying on non-human organisms to address human biology questions. To do so requires upgrading our *in vitro* cultures systems to a point where it can faithfully reproduce to translate to human biology (or at least reliably enough).

A changing ethical and regulatory landscape

In addition to the scientific interest of novel in vitro culture systems, legal and ethical evolutions have shaped the needs and restrictions around tests, and notably toxicological assays. These evolutions are often considered to have been initiated in 1959 with the publication *"The Principles of Humane Experimental Technique"* by Russell and Burch[127] which proposes the 3R rules of (1) Replacing animal tests by other methods, (2) Reducing as much as possible the number of animals needed to obtain relevant data, and (3) Refining protocols to minimize potential pain, suffering or distress.

In Europe, these principles have been translated into law by numerous European regulations. Notably, the EU Comestics Directive 76/768/CEE (introduced in 1976, revised several times since) prohibits the animal testing for cosmetic products since 2004, and for their ingredients since 2009. The regulation, however, does not alleviate the need for the industrials to prove the non-toxicity of their products, forcing them to seek alternatives. Effective since 2007, the REACH (Registration, Evaluation, Authorization, and Restriction of Chemicals) n°1907/2006 tightened the regulation around human health protection, and imposed industrials to test or re-test about 30 000 chemicals for proper registration, as a condition for production or import of said chemicals. This regulation also incited companies to rely on non-animal testing solutions

CURRENT TRENDS IN THE PRODUCTION ON IN VITRO MODELS

Petri dishes and other SBS format plastic wares became standard cell culture vessels in both academia and industry. As seen above, these culture systems remain imperfect, and investigators often rely on “immortalized” or cancerous cell lines to allow a better and long-lasting growth of mammalian cells. However, our advances in exploring the complexity of living systems provides us with many approaches to investigate the importance and role of each characteristic (be it physical or chemical) of the microenvironment.

In this chapter, we will detail several features of said microenvironment, and the crucial impact they have on cell growth, differentiation, and viability. Notably, we will focus on the physical properties of the substrate, including stiffness and topography. Later, we will describe new tools born from the need to improve or replace previous culture dishes. Namely, organoids and organs-on-chips.

Importance of physical microenvironment

Both the ECM and the cells themselves participate to give a tissue its elastic properties, which have long been known to vary, depending on the tissues they are parts of. And yet, while investigating the impact of the microenvironment on stem cell fate, soluble chemical cues (such as growth factors) were focusing most of our attention, and mechanical cues were often discarded. We will review here a few experiments that proved us wrong, and highlighted the critical role of substrate physical properties.

Early hints

As early as 1990 it was known that mechanical stress such as hemodynamic flow, or gravity, could induce the opening of specific ion channels[128, 129], or modulate cell growth[130] for instance. However, while downstream elements sur as c-fos

expression and ion channels were identified, the processes and molecules able to convert mechanical sensing into chemical signaling (that is, mechanotransduction) were yet to be identified.

In addition to mechanical stimulations, von der Mark and colleagues observed that chondrocytes losing their typical polygonal phenotype and transition to a flattened, amoeboid-like shape after several passages in monolayer, were also losing their type II collagen expression and instead produced type I collagen[131].

Topographical cues and shape-function relation

Aside from mechanical stress, the sole topography of the local microenvironment, and the shape it constrains the cell to adopt was found to be alone sufficient to induce proliferation, or death. To get to this conclusion, Chen et al. designed beads, and microprinted surfaces, of varying geometries, coated with fibrinogen to allow cell-ECM adhesion[132]. They first showed that, when the fibrinogen-coated bead was 10 µm large or smaller, the cells started to engulf the bead, and presented a round shape close to that of unattached suspended cells, with a similar apoptosis rate. That is contrarily to cells attached to bigger beads, which survived in over 90% of cases when said beads were above 25 µm of diameter. In a second time the experiment was perform on flat surfaces, with printed “islands” coated with fibrinogen, with consistent results. The smallest islands gave rounded cells with higher mortality rates than large islands allowing cells to spread. Lastly, to confirm that the key apoptosis-inducing factor was the round shape and not the small surface of contact, they designed archipelagos constituted of smaller islands. In said archipelagos, its total dimension (including the space in between islands) corresponded to islands that allowed cell survival and growth in the previous setup, while the fibrinogen-coated area was not higher than that which lead to apoptosis in the single island setup. Chen et al. showed that this setup led to cell survival and growth, confirming that survival was induced by cell spreading instead of adhesion alone[132].

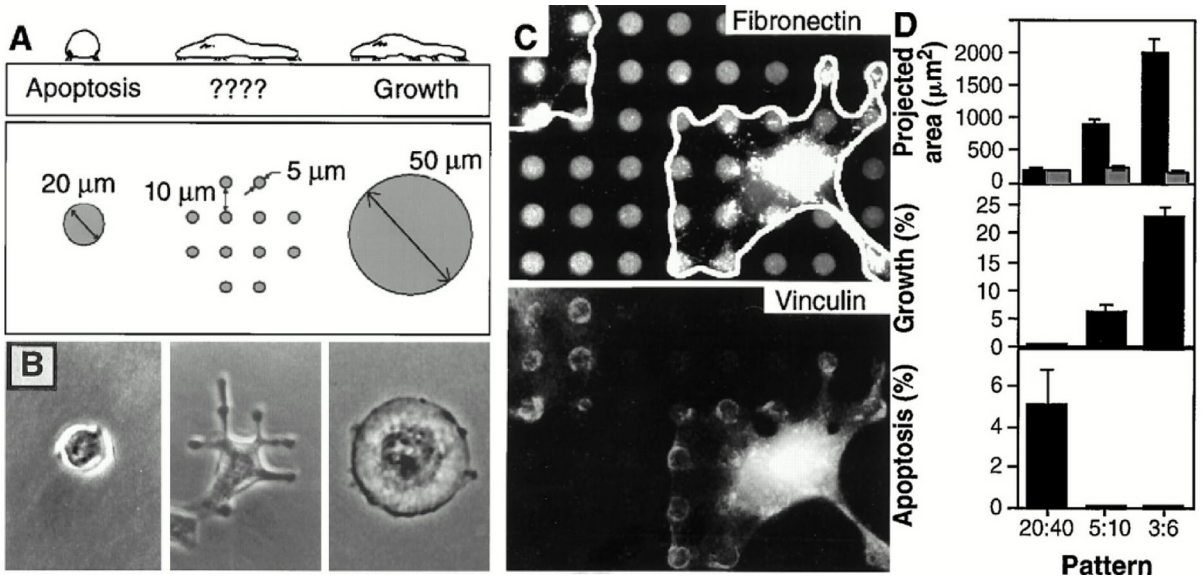

Figure 1: Cell-ECM contact area versus cell spreading as a regulator of cell fate.

*(**A**) Diagram of substrates used to vary cell shape independently of the cell-ECM contact area. (**B**) Phase-contrast micrographs of cells spread on single 20- or 50-µm-diameter circles or multiple 5-µm circles patterned as shown in (A). (**C**) Immunofluorescence micrographs of cells on a micropatterned substrate stained for FN (top) and vinculin (bottom). (**D**) Plots of projected cell area (black bars) and total ECM contact area (gray bars) per cell (top), growth index (middle), and apoptotic index (bottom) when cells were cultured on single 20-µm circles or on multiple circles 5 or 3 µm in diameter separated by 40, 10, and 6 µm, respectively. From Chen* et al.*, 1997.*

Aside from survival, other cellular processes are known to be associated to special arrangement of the cytoskeleton. For instance, during cell migration, the greatest traction is produced in a focal adhesion point localized close to the base of the main forward-extending lamellipodia[133]. Thus, Parker *et al.* investigated if constraining the shape of a cell could force the orientation of its migration, and showed that on square coated islands, cells will focus their cytoskeleton on the corners of the square. Moreover, lamellipodia, filopodia and microspikes originated from these corner, unless actomyosin-based tension inhibitor was used[134].

Seeing how little is understood about the topography impact on cell behaviour, Unadkat and colleagues proposed an algorithm-based topographical library generation in the hope to efficiently screen nonbiased random features[135].

Matrix elasticity directs stem cell lineage specification (Engler* et al.*, 2006)

In 2006, Engler *et al.* were the first to document an unequivocal effect of matrix stiffness on stem cell differentiation[14]. To that end, they relied on mesenchymal stem cells (MSCs), which are known for being the precursors of several and clearly different lineages: neurocytes, chondrocytes, adipocytes, osteoblasts[136, 137]. In their experiment, they plated MSCs onto polyacrylamide gels of varying stiffness, ranging from 0.1 to 34 kPa. Gels bellow 1 kPa served as mimics of brain stiffness, while 11 kPa and 34 kPa gels served as mimics of muscle and bone ECM stiffness, respectively. When plated for 1 to 3 weeks on a specific gel, MSCs already started to express genes specific to the corresponding lineage. When this period lasted for at least 3 weeks, the cells kept a strong commitment to their matrix-defined lineage, even if the experimenters changed the substrate gel. The level of expression of specific genes (β3 tubulin for neurogenic lineage, for instance) showed no statistically significant changes, and expression of genes specific to other commitments remained "essentially undetectable". However, when myoblast induction media was added after only 1 week of culture on 0.1 to 1 kPa gels, the level of expression of β3 tubulin was reduced by half, and that of MyoD (which was previously negligible) was increased by several folds. Thus, cells of mixed lineage could be obtained, by superposing physical cues and chemical cues specific of different commitments.

Our understanding of such unexploited mechanisms allowed to achieve what previously appeared hardly feasible *in vitro*. For instance, previous attempts to culture muscle stem cells (MuSCs) on rigid dishes led to massive cell death, and experiments were performed on the surviving ones. Indeed, the stiffness of plastics commonly used in culture systems is around 3 GPa, while living tissues rarely go above a few tens of kPa. Thus, culturing cells on such dishes now seems utterly inappropriate. To palliate this, Gilberts *et al.* cultured MuSCs on soft PEG hydrogel, with an elastic modulus of 12 kPa, close to that of muscle ECM. The hydrogel, covered with laminin for adhesiveness, allowed stem cell proliferation to outnumber cell death, and MuSCs could finally be successfully cultured *in vitro.* When cultured on pliant gels, MuSCs could then be successfully grafted in a few mice, even after several divisions. On the contrary, MuSCs cultured on rigid substrate never showed engraftment or contribution in myofiber renewal[138]. Thus, it should be easier in the future to perform experiment on larger populations, and in more relevant culture conditions.

Mechanotransduction

In 1993, Wang (et al.) designed a magnetic twisting device to investigate the cell response to mechanical stress applied to specific membrane proteins only. Their results showed that such stress applied specifically to integrins β_1 induced a stiffening response from the cell, in a force-dependant fashion[139]. Such effect required the participation of intact and connected elements of the cytoskeleton, such as microtubules, and micro- and intermediate filaments. These findings supported the model of tensegrity, where the cytoskeleton is modelled as if composed of rigid rods interconnected through pre-tensed strings, and which has been especially detailed by Donald E. Ingber[140].

A major feat of such paradigm is that computational tensegrity models were able to reproduce the spreading behaviour of cells in substrate of different stiffness. In addition, such results predicted that spreading could be obtain by rearranging the cytoskeleton, without involving production of new cytoskeletal constituents. This was consistent with the finding of Mooney (et al.) who demonstrated that cell (here, hepatocytes) spreading on coated matrices did not directly depend on net polymerization of either microfilaments or microtubules[141]. Moreover, this pre-tensed model explains the fast transmission of the signal through the entire cell, and around via focal and adherens adhesions.

A clear example of the crucial role of mechanotransduction occurs during embryonic development. Indeed, the control of specific morphological features in embryo (disc shape, remodelling and notochord formation, etc.) requires precise regulation of cell proliferation, or the different cellular sheets might fold itself and lose shape. A demonstration of that was brought by Wang et Riechmann in 2007. In their experiments, they showed that the somatic epithelium of Drosophila eggs would collapsed in null mutant for sqh gene (required for regulatory light chain of non-muscle myosin II - RMLC). In Drosophila this epithelium consists in a sheet of cells covering the growing germline cyst. After demonstrating that the growth of the germline cyst is what drives the deformation of the epithelium, this indicates that myosin is needed to

maintain the integrity of the epithelium. Moreover, they demonstrated that myosin activity resulted in local cell proliferation[142].

When placed on low stiffness poly(ethylene glycol) (PEG), smooth muscle cells will exhibit a decrease in their proliferation rate[143], so do hepatic stellate cells and cardiomyocytes when their contractility is impaired by Rho Kinase (ROCK) inhibition[144, 145]. The cellular role of ROCK being the contraction of myosin, it appears that cytoskeletal tension is a major actor of cell proliferation. Indeed, in vivo stretching models showed that resulting RhoA signalling was a powerful inducer of smooth muscle cell proliferation[146], while inhibition of ROCK signalling pathway blocked this stretch-induced proliferation[147]. Moreover, aside from proliferation itself, mechanical stress can induce specific differentiation, as shown by Altman et al., on mesenchymal progenitor cells[148].

Taken together, these results indicates that cytoskeletal tension plays a role in both tissue integrity and in regulating cellular and tissue processes such as cell proliferation[149].

Emergence of novel bioengineering tools

The recognition of topographical, physical, and mechanical cues as biological information that cells and tissue will integrate in their behavior fueled the need for adequate tools, able to provide such cues *in vitro*. Two fields have brought significant advances on the matter: microfabrication, which led to the development of microdevices able to embark complex designs, and the use of natural or synthetic matrices, which allowed the encapsulation of cell in three dimensions.

Microfabrication and microfluidic chips

In 1979, Terry and colleagues designed a miniaturized analytical tool: a silicon-made gas chromatographic analyzer[150].The 5-cm-diameter silicon wafer on which it was fabricated hosted a 1.5 m long spiral capillary capable of separating hydrocarbon mixtures in less than 10 s. This achievement triggered a race for miniaturization, and in the following ten years, miniature micropumps, microvalves, and chemical sensors

were proposed in numbers[151]. In 1990, the term miniaturized total chemical analysis system (μTAS) was proposed to designate a new generation of tools embarking pretreatment, separation and detection[152].

Microscale physics present several advantages, including the rapidity of heat transfers. This was capitulated on to miniaturize biochemical reactors, such miniaturized PCR amplification systems, which are now reaching a point where the time-limiting factor is the length of the sequence and the rate of DNA polymerization[153]. The reduction consumed volumes also worked as an incentive for biochemical assays to develop miniaturized platforms[154].

Quickly enough, biologists grew interested in microfabrication, after identification of materials and protocols suitable for use in cell culture. Today, PDMS has emerged as a predominant material to be used in microfluidic chips. Indeed, prior to mixing with a reticulating agent, PDMS is liquid and allows for casting on molds of micrometric precision. After reticulation, PDMS is optically transparent, flexible, and permeable to gas while impermeable to aqueous solutions. Over time, microfabricated devices are increasingly used in cell culture, and biologists have developed a wide range of applications to suit their needs, from droplet encasing of cells to perform high throughput condition screening and sequencing[155] to measurement of mechanical forces[156], and migration assays in confined environments[157].

Natural 3D culture substrates

Addressing the composition of the ECM has been a tedious work. To provide themselves with sufficient quantities of source materials, Kleinman *et al.* relied on ECM-producing tumors, such as the EHS tumor, named after J. Engelbrecht-Holm (who discovered it) and R. Swarm (who cultured them). Initially considered a poorly differentiated chondrosarcoma[158], it was later identified to emanate from the parietal endoderm[159]. After purification and sterilization, they noticed that the resulting solution could be stored in a freezer, and that it would form a strong and clear gel when warmed up to 37 °C. When tested as a cell growth substrate, it showed remarkable performances, but also promoted cell differentiation. Indeed, in their first experiments, Kleinman et al. showed that melanocytes pigmented rapidly, and that endothelial cells

would spontaneously form tube-like structures that were able to uptake low density lipoproteins (LDLs)[160, 161].

This preparation was later named Matrigel, but is also known as Cultrex, EHS extract, or reconstituted basement membrane. Its potential is now well documented[162], and even though it is subject to variability between lots, it remains an essential tool in many biology labs[163]. We know today that Matrigel presents cells with an elastic modulus around 0.4 kPa[164], and chemically mostly composed of laminin (~60%), followed by collagen IV (~30%), entactin (~8%), and perlecan (~2-3%)[165].

A field that greatly benefited from Matrigel is that of cell encapsulation. Indeed, when cultured on 2D flat surfaces, cells can lose their original shape and state of differentiation[131]. However, when encapsulated in agarose gel, dedifferentiated chondrocyte could regain their collagen phenotype[166]. Matrigel, by the complexity of its composition, was helpful to culture cells in 3D, sometimes allowing completely different behaviours. For instance, malignant and non-malignant breast tumour cell lines do not differ much in behaviour and appearance when culture on 2D plastic substrate but, when cultured in 3D Matrigel, the two become clearly distinguishable[12]. Moreover, 3D cultures of such breast tumour cells led to the discovery of a cross-regulation between β_1 integrin and EGF signalling pathways, that do not exist in 2D cultures[167, 168].

However, it is to be noted that Matrigel presents certain limitations. Notably, it presents inconsistencies in biochemical properties from one batch to another, including the detection of growth factors and bioactive peptides, hindering the ability to draw conclusions on stem cell response to Matrigel[169, 170]. Today, more than 14,000 peptides and 2,000 proteins have been reported in Matrigel, including some growth factors, transcription factors, and cytokines[165]. Moreover, the mechanical properties of Matrigel can greatly vary between lots, and exhibit a large variability within a gelled bulk[164].

To palliate the imperfections of Matrigel, two strategies exist in parallel. The first one being to rely on purified components from Matrigel, such as collagen or fibrin, which can produce water-swollen polymer network by themselves[171]. Collagen presents the advantage of forming gelling networks even at low concentrations, allowing to produce a wide range of stiffness by increasing collagen concentration, or by addition of

crosslinking compounds[172, 173]. Plus, collagen gels can be oriented, for instance by slowly gelling large collagen fibers under flow condition[174].

Synthetic hydrogels

The second strategy to palliate the imperfection of biologically sourced substrates is to rely on entirely synthetic hydrogels. Natural matrices are forming networks of large molecules with high water content, allowing soluble elements (nutrients, metabolic wastes, *etc.*) to diffuse. Recapitulating such a porous structure can be achieved with large crosslinked polymers other than the constituents of the ECM[175]. Ideally, it should also provide chemical cues, and notably adhesion-ligands. Though many polymers have been proposed and used, such as poly(acrylic acid) (PAA), polyacrylamide (PAAm), poly(vinyl alcohol) (PVA), or polypeptides, today, poly(ethylene glycol) PEG has gained a vast popularity. This success is due notably to its biocompatibility and non-immunogenicity[176]. In addition, PEG polymers are easily tunable in their properties: they can be produced in a wide range of molecular weights, branching, and end-functionalization. This last point allows to select the mechanism that will lead to crosslinking of the hydrogel, and can eventually be used to integrate molecules of interest in the networks, such as growth factors or cell adhesion-triggering molecules[177]. Two commonly used functionalization are acrylate groups (forming PEG-diacrylate, PEGDA), which can crosslink through UV-initiated free radical polymerization in the presence of a photoinitiator, and click-chemistry, in which two differently functionalized PEG polymers engage in spontaneous reaction. While the first method allows the experimenter to control when (and possibly where) to initiate crosslinking, it presents the disadvantage of requiring UV light exposure, and presence of a photoinitiator which can have a certain cytotoxicity, which click chemistry can avoid. The example of thiol-Michael addition of thiol-functionalized PEG (PEG-TH) polymers with a vinyl sulfone-functionalized PEG (PEGVS) in the presence of a base is provided in Figure 2 below. Numerous other reactive group couples exists, each exhibiting different features, which can be of interest (conditions of reversibility, speed, simplicity, batch reproducibility, *etc.*)[178, 179].

Michael type additions are nucleophilic additions of a carbanion (or another nucleophile group) to an α,β-unsaturated carbonyl compound, resulting in the formation of a carbon-carbon bond. By extension, the term is also used in biomaterial

sciences to describe other reactions leading to the formation of a covalent bond through a nucleophilic attack involving a carbanion, such as thiol-alkene reactions. Some authors favor the name of thiol-Michael addition for such reactions[179]. This “click” reaction is highly interesting for biomaterial applications: no byproducts, biocompatible molecules, thermodynamically “spring loaded” reaction. Depending on the reactive group of the Michael acceptor (maleimide, vinyl sulfone, acrylate, methacrylate, *etc.*), the sensibility to hydrolysis can be adjusted, to create gels that will quickly be degraded, or remain stable for the time of their use. Figure 2 below shows the steps of the Michael-type addition of two molecules, one exhibiting a thiol group while the other exhibits a vinyl sulfone group, in the presence of a base. In this example, the basic conditions leads to the deprotonation of the thiol by the base **(1)**. This nucleophile Sulfur will react with the electrophilic alkene end of the vinyl sulfone. This new covalent bond leads to the displacement of the double bond, and formation of a carbanion **(2)**. Proton transfer from the protonated base **(3)** to the carbanion ends the click reaction in a stable configuration **(4)**.

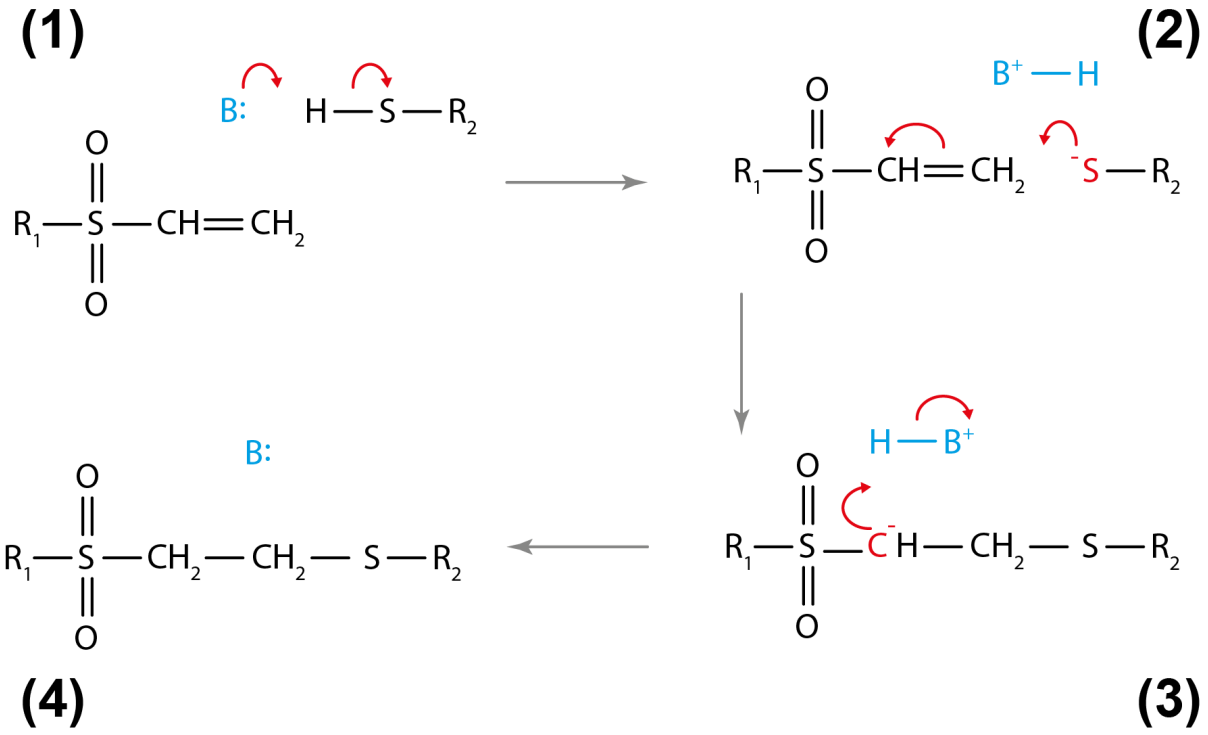

Figure 2: Thiol-Michael addition reaction involving a vinyl-sulfone group.

(1) Deprotonation of the thiol by the base. (2) Addition reaction between the Sulfur and Carbon atoms, leading to the formation of a carbanion. (3) Proton abstraction from the base by the carbanion. (4) Final and stable configuration.

The physical properties of the hydrogels will be Impacted by the mesh size ξ, which is the average distance between adjacent crosslinks, and by the average molecular weight between crosslinks M_c. In detail, increased molecular weight will increase mesh size, which will decrease hydrogel stiffness (at constant polymer concentration and arm number), while increasing the volumetric swelling ratio Q (ratio between volume of swollen hydrogel relative to volume of polymer). On the contrary, increased arm number (at constant MW and polymer concentration) will decrease mesh size and increase hydrogel stiffness. As polymer concentration increases, mesh size will decrease, thus increasing hydrogel stiffness[180-182]. Other ways to impact mesh size include addition of chain terminator, or stoichiometric imbalance to leave free ends in the network[183]. Overall, thiol-michael addition network of PEG hydrogels offers a versatile basis for tailored application[184-186].

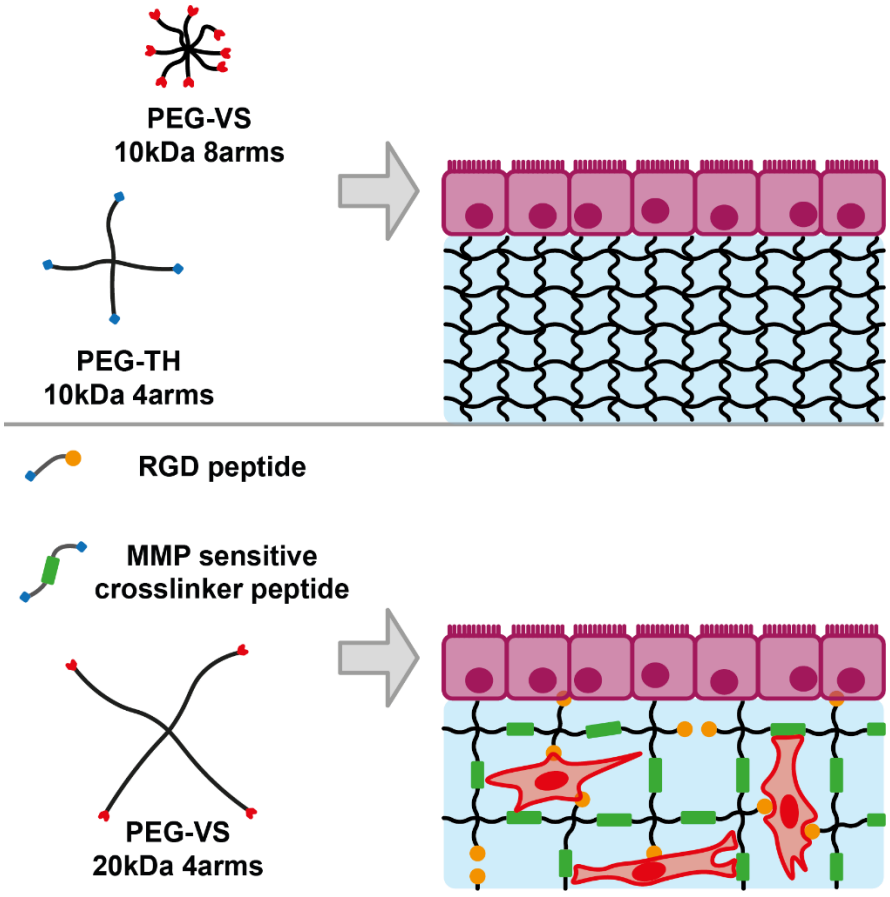

Figure 3: PEG-PEG and PEG-PEP hydrogel networks.

Top: *PEG-only hydrogels allow the experimenters to present cells with a substrate of known and tunable physical properties.* ***Bot:*** *PEG-peptide hydrogels allow for further tuning of the network, which can for instance be rendered sensitive to enzymatic degradation, allowing for cell migration.*

Interestingly, thiol-Michael addition networks require two different polymers, functionalized with different reactive groups. This is particularly suited to combine PEGVS with cysteine-bearing (thus thiol-bearing) peptides. This property has been capitalized on by several teams to build bioactive networks, notably by using as crosslinkers matrix metalloprotease (MMP) sensitive peptides, which cells can degrade and in which they can migrate [183, 187-189].

Today, synthetic hydrogels have conquered a large range of applications, including stem cell fate guidance[190-192], controlled drug release[193-195], or substrate attachment screening[196] for instance.

Betting on self-organization: Organoids

The use of natural and synthetic matrices as 3D culture substrate brought the hope of recapitulating the architecture of tissues, which was hardly feasible starting from a 2D culture substrate. In addition, the large use of cancerous or transformed cell lines hindered the relevance of biological assays performed. Thus, several teams attempted during the 20th and early 21st centuries to cultivate fresh cells and stem cells in the novel substrates. The first long-term culture of non-transformed cells is thought to have been achieved by Rheinwald and Green in 1975, by placing human epidermal keratinocytes cells in coculture with mouse 3T3 fibroblastic cells[197]. In their experiment, plating efficiency from fresh epidermal cells was below than 1%, and their survival depended on the experimenter controlling the proliferation of 3T3 cells, so that it would not enter overgrow the human cells. This allowed them to culture epidermal cells forming a stratified and apically keratinized epithelium, for the 20-50 divisions that basal could undergo.

Birth of organoid culture

In 2006, Nahmias *et al.* managed the long-term culture (>2 months) of hepatocytes, by presenting them to endothelial vascular structures formed in Matrigel, and provided that they were in coculture with either fibroblast-contaminated human dermal microvascular endothelial cells or a combination of human umbilical vein

endothelial cells and normal human dermal fibroblasts[198]. Later, in 2008, the team of Yoshiki Sasai managed to recapitulate, in embryonic stem cell aggregate in suspension, the early spatiotemporal events of corticogenesis, displaying a remarkable self-organized structuration in ventricular, early and late cortical-plate and Cajal-Retzius cell zones[199].

Despite these advances, the experiment that is often coined today the production of the first organoid is the demonstration of Sato and colleagues in 2009[1], in the sense that stem cells could maintain their multiplication potential *in vitro* for an extended period of time (>8 months), producing and maintaining a near-physiological epithelium in a setup that did not rely on coculture. Here, the team of Hans Clevers built upon their recent identification of of *Lgr5*+ small intestine and colon stem cells and demonstration of their multipotency[200] to isolate them and culture them either alone or together with their crypt, using Matrigel as a matrice, and supplementing it with various growth factors identified as key for stem cell niche maintenance: WNT, Noggin, R-spondin, and EGF.

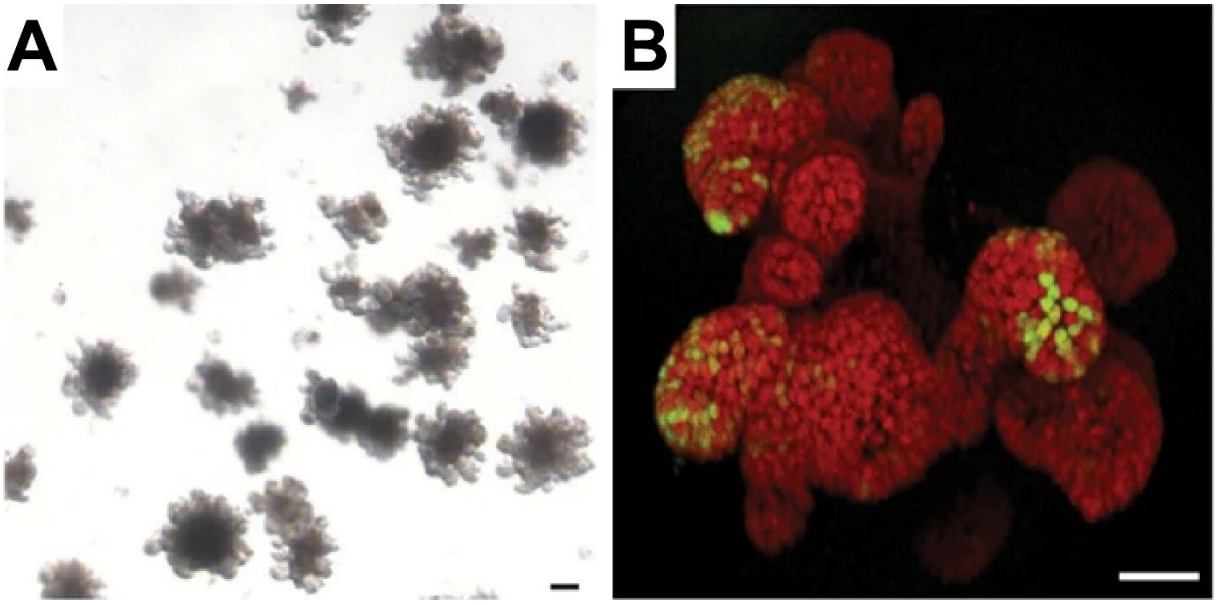

Figure 4: First intestinal organoid.

(A) *Single isolated crypts efficiently form large crypt organoids within 14 days.* ***(B)*** *Three-dimensional reconstructed confocal image after 3 weeks in culture. Lgr5-GFP⁺ stem cells (green) are localized at the tip of crypt-like domains. Counterstain, ToPro-3 (red). Scale bar, 50 µm. Adapted from Sato* et al., *2009[1].*

Today, organoids have been established for a large variety of organs, including gut[1, 201, 202], stomach[203-205], kidney[206, 207], liver[208-210], mammary glands[211, 212], lung[213, 214], and brain[215-217], among many others[218].

Uses of organoids

A straightforward use of organoid is linked to their establishment: identifying the factors that elicit their formation. More generally, organoids can serve to investigate tissue development and homeostasis, and identify the chemical (factors, nutrients, *etc.*) and physical (stiffness, stimulation) cues that play crucial roles in tissue homeostasis or cell differentiation[219]. For example, human prostate organoids have permit the identification of multipotent progenitor cells[220], and unveiled the Interleukin 6 (IL-6) in regeneration of airway ciliated cells from basal stem cells[221]. When derived from pluripotent stem cells, organoids can also assist in modeling embryonic development[207, 222, 223].

In addition, organoids have been used to model diseases, for instance through selective mutations recapitulating pathological condition, such as HPS1 deletion in lung organoids to induce intractable pulmonary fibrosis[224], or podocalyxin KO models to trigger organizational defects in kidney organoids[225].

In the last 5 years, organoids have had the opportunity to prove their potency. First, during the Zika virus (ZIKV) outbreak of 2015-16 that started in Brazil and was linked to increased cases of microcephaly among newborns, organoids played an important role documenting developmental defects *in vitro*[226], including impairment in neurosphere growth[227], and deciphering pathways of action[228]. Later, during the COVID19 pandemics, organoids were quickly put to work, and notably proposed very early (May 2020) that capillaries and kidney could suffer damages, as organoid models were directly infected by Severe acute respiratory syndrome coronavirus 2 (SARS-CoV-2)[229].

Organoids also present a certain interest for screening of molecules, be it for drug discovery purpose[230, 231], or for personalized medicine. Indeed, cancer patients have long been in demand for personalized medicine, since no two cancers tumors have the

exact same pattern of genetic defects. In addition, cancers often exhibit a large cellular heterogeneity which hinders the efficacy of anticancer treatments, since subpopulations resistant to said treatment can take over after elimination of susceptible cancerous cells[232]. Ten years ago, cancer genomics was welcomed as a powerful tool to grasp tumor heterogeneity and propose personalized treatment[233]. Today, organoids join the toolbox of personalized medicine, as they can serve as screening platform to assess numerous drugs on patient-derived cancer organoids, simultaneously modeling the response of the patient to multiple therapeutic strategies, and accelerating the time to identify the best treatment to propose[234-236].

Overall, 3D cell culture, and especially organoids, have clearly demonstrated that they have advantages over flat culture, on which we can capitalize: better survival, better differentiation profile, possibility to produce complex architecture, more relevant cell shape and mechano-responses[237]. Some are already asking if it is time to start transitioning to 3D cell culture? [238]

Challenges, limitations

However, organoids present some limitations, and many challenges are still ahead before they can replace 2D cell culture everywhere. First of all, organoids inevitably suffer from being a still young technology. The microenvironment of tissues and niches are not always completely understood, and ensuing protocols are not perfectly established. Moreover, protocols are not yet standardized. As a result, experimental results and conclusions might vary from group to group[218].

Another shortcoming of organoids is their overall difficult accessibility for both large molecules and physical tools. Especially, their lumen is not accessible for foreign bodies, including bacteria. For that reason, infection assays often rely on microinjection, which can be traumatic for the integrity of the cell layers[239, 240]. To palliate the inaccessibility of the lumen, inside-out models have been developed to easily present pathogens to the apical cells of the host[241].

The inaccessibility of the luminal compartment also prevents its renewal, its perfusion, or exposure to air in a setup similar to Air-Liquid Interfaces (ALI). While organoids and 3D cell culture claims to count expression profile among its advantages, the inability to

provide the tissue with cues that are known to play a role in cell maturation[242, 243] is a serious drawback.

While the field is still young, and many challenges remains, human organoids come with great promises for both fundamental biology and clinical applications, thanks to an active community leading technology development[244]. Notably, many pushing for engineering approach centered around the control of the stem cells and their self-organization in order to provide organoid suiting the needs of the experimenters[245, 246].

Tailored micro-environment: Organs-on-chip

The choice of an *in vitro* platform on which to perform assays largely depends on the question addressed by the experimenter. Regardless of the prowess of 3D culture and organoids, there are questions which can simply not be addressed. Organs-on-chips take into consideration needs relative to an assay (topography, ease of imaging, submission to various chemical and/or physical cues) and propose an engineering approach to address them. Typically, they will attempt to establish a minimally functional unit, recapitulating one or several functions of a tissue or organ, and present it in a manner accessible for experimentation.

Birth of organs-on-chips

During the first decade of the 21st century, many microscale culture analogs (μCCAs) were proposed, relying on microfabrication to embark toxicity assays[247], sensors[248, 249], or drug screening assays[250] on a microscale platform, together with cultured cells. The first organ on chip was born when the microfabrication tools were instead used to provide a microenvironment for the cells: in 2010, the team of Dongeun Huh and colleagues presents a microfluidic device dedicated to the reconstitution of some of the lung's function[5].

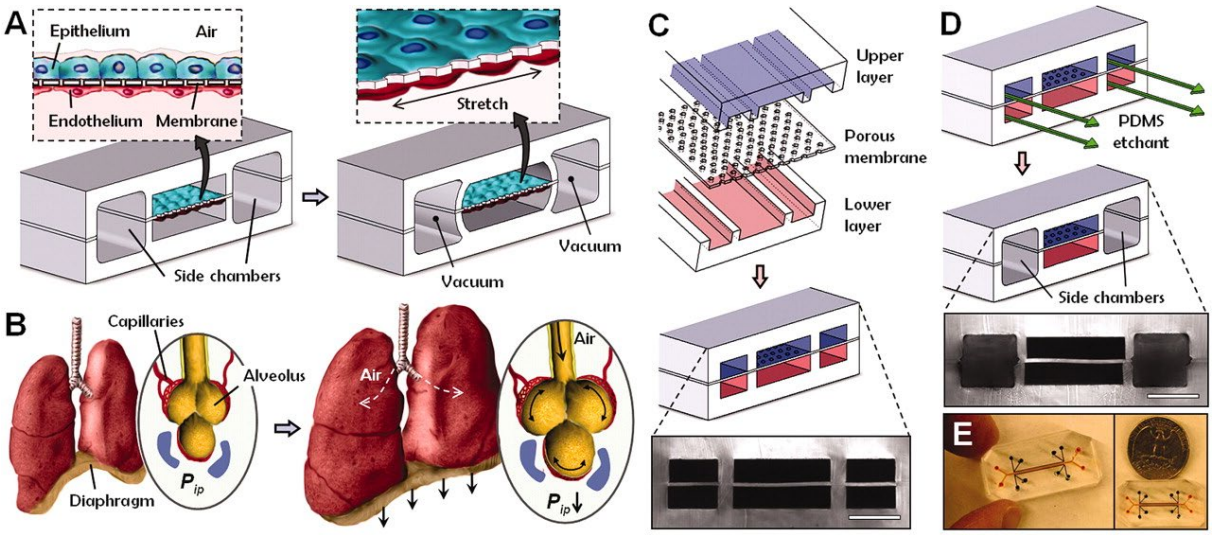

Figure 5: Design of the first lung-on-chip microdevice.

*(**A**) The lung-on-chip mimics an alveolar-capillary barrier on a thin, porous, flexible PDMS membrane coated with ECM. The device recreates physiological breathing movements by applying vacuum to the side chambers and causing mechanical stretching of the PDMS. (**B**) Physical stretching of the alveolar-capillary interface during breathing movements. (**C**) Assembly of the 3-layeres PDMS chip. Scale bar, 200 µm. (**D**) Etching of the PDMS membrane in the side channels produces two large side chambers. Scale bar, 200 µm. (**E**) Images of an actual lung-on-a-chip microfluidic device viewed from above. Reproduced from Huh* et al.*, 2010[5].*

Briefly, the microfluidic chip comprises 2 superposed channels, separated by a porous PDMS layer. On each side is a large side channels to which vacuum can be applied, to deform the lateral walls of the central channels, leading to the stretching of the porous layer (see Figure 5). The microdevice was used to emulate the lung epithelial barrier, by allowing two cell layers to form a dual layer barrier on each side of the porous membrane. The PDMS membrane can be coated with fibronectin or collagen to allow cell adhesion, while flows are introduced in the two channels (airflow on the epithelial side, medium flow on the endothelial side), and vacuum cycles in the side channels produce cyclic stretch of the membrane. Overall, the device places several cell types next to one another, and submit them to chemical (coating molecules) and physical (shear stress and stretch) cues.

In their first paper, Huh *et al.* demonstrate the feasibility to use the microdevice for imaging, infection and translocation assays, transepithelial resistance (TER) measurement, among other assays, clearly demonstrating the potential of such tailored platform. Later, the same chip design was used to mimic a gut barrier, once

again composed of an epithelial and an endothelial layer[7]. Only minor adjustments in dimensions were made.

Uses of organs-on-chips

Rather than organ specific, organ-on-chip designs target a functional unit. Thus, it is often easier to compare function than approach the diversity of chip by organ, since a same chip can serve for several organs or tissues. For instance, organs-on-chips have been particularly useful to investigate the physiology and pathology of barrier tissues, placing two cell types in close contact, such as lung[5], gut[7, 9, 251], or Blood-Brain-Barrier (BBB)[252, 253] for instance.

A large variety of very specific needs are being addressed with organs-on-chips: simple perfusion assays unveiling the role of flow in drug trasnport[254] electrical stimulation of pluripotent stem cells derived cardiomyocytes[255], substrate invasion for angiogenesis assay[8, 256], among others. Today, several companies propose “ready-to-use” organ-on-chip platforms dedicated to specific assays, including Mimetas, Emulate Bio, *etc.*

Several teams have contemplated the possibility to connect several organs-on-chips together, in what is often called “body-on-chip” or “multi-organ-on-a-chip” (MOC). Aside from the prowess a complete body-on-chip would be, associations between tissues that are not in close contact *in vivo* can meet a serious need. It is the case for heart-liver dual systems. Indeed, cardiotoxicity is one of the major failure reason in phase 1 of drug testing[257]. Cardiotoxicity of liver metabolites is easier to access in organs-on-chips than in traditional culture systems[258, 259]. Four organ systems have also been described[260].

Lastly, microsensors can be embarked on the chip to monitor in real time a parameter of interest, such as O2 concentration and pH[261], enzymatic activity[262], barrier properties[263], or transport of fluorescent xenobiotics[264].

Challenges, limitations

Organs-on-chips have much to offer both fundamental biology and preclinical research. The position of each biological and engineering component being under the control of the experimenter, organs-on-chip are often uncontested in term of imaging

and data accessibility. However, they can fall short of other culture systems on several points. For instance, design and use of organs-on-chips by a group requires specialized microfabrication capacities, and often involves microfluidic systems which can be prone to contamination or bubble apparition which can injure or destroy tissues.

Stability of adhesion coating over time can also hinder the advantage of continuous flow renewal on long term survival that OoCs could have on organoids. To overcome the organoid-OoC dilemma, some have proposed to combine the approaches by seeding OoCs with mature organoids, or to imprint microsystems within a natural matrix bulk for instance[265, 266].

DESIGNING A BARRIER TISSUE-ON-A-CHIP

Barrier tissues, such as the skin, gut, blood-brain-barrier, or lung for example, present specificities of interest. They are at the interface between two compartments and must answer needs that are not easy to satisfy. On one hand, they must allow the passage of molecules and/or cells of interest (absorption of nutrient, of dioxygen, passage of immune cells, *etc.*). However, they must play a barrier role and prevent unwanted molecules and cells (typically pathogens) to pass their wall. This implies a high cohesiveness of the tissue, while allowing for very selective transfers and passages. In the case of the lung and GI tract, surface of exchange plays a crucial role in the ability of the organ to maximize the absorption of oxygen and nutrients, and both the respiratory and digestive systems have evolved to produce complex 3D architecture that is hardly reproducible on 2D culture setups. In addition, both systems are experiencing dynamic motion that plays important roles in both optimizing absorption (by renewing the volumes in close contact with the tissue) and in cell function and/or differentiation[267, 268].

Taken together, these constraints make organs-on-chips especially good candidates to improve our ability to produce barrier tissue mimicries. We will review in this chapter the specificities of barrier tissues, and advances made to recapitulate their functions and architectures. Doing so, we will put a particular focus on the small intestine.

Biology of barrier tissues

Topographical organization and cellular diversity

The small intestine wall is composed of 4 layered tissues[269]. In contact with the lumen, the mucosa is composed of a monolayered epithelium anchored on a thin connective tissue, the lamina propria, accompanied by a small layer of smooth muscle cells. Briefly, the intestinal epithelium is composed of several cell types specialized in absorption, mucus production, or maintaining the stem cell niche at the bottom of the crypts. The monolayer is highly cohesive, with strong cell-cell contact to maintain the integrity of the barrier, helped notably by the presence of tight junctions[270]. Just below, the *lamina propria* hosts blood and lymph vessels, as well as the Gut-Associated Lymphoid Tissues (GALT), composed of isolated or aggregated lymphoid follicles (Peyer's patches). Lastly, the *muscularis mucosa* is responsible for slow movements of the villi, brewing of the bolus to help put it in contact of all the surface of the epithelium.

Below the mucosa, the submucosa is a connective tissue penetrated by blood and lymphatic vessels. It is also the residence of the submucosal plexus of neurons, which is part of the enteric nervous system (ENS) playing a role in food propulsion, nutrient handling, blood circulation, and immunological defenses[271, 272]. Further away from the lumen is the muscularis, composed of two layers of smooth muscle cells, and which plays two roles: imposing peristaltic motion to the gut, helping mechanical breakdown of bolus and its progression through GI tract, and mechanically helping the formation villi during organogenesis[268], which noticeably occurs prior to establishment of intestinal crypts[273]. Last, the serosa is a serous membrane placing the GI tract in suspension in the abdomen, and composed of connective tissue in addition of an epithelium which lubricates the GI tract to prevent friction with surrounding tissue in the abdominal cavity.

Though the serosa, muscularis, and submucosa display a roughly regular organization through the length of the small intestine, the mucosa exhibits a much more complex architecture, which varies along its length. In the first few millimeters of its

duodenal portion (the 25-30 first centimeters of the small intestine), secretory duodenal glands protect the epithelium from gastric acids, producing epithelial growth factors and lysozyme[274]. Second in order, the jejunum has a structure highly specialized towards absorption of nutrients: it presents circular folds which multiplies several times the surface of absorption. On circular folds, villi form protrusion increasing even more the surface area. The last and longest portion of the small intestine, the ileum, is the main place of absorption of bile salts which are sent back to the liver *via* the portal vein. With a lower pH, most of the bacterial populations are located here. This is also where most of the GALT are located, which concentrate 70% of the body's immunocytes[275].

The intestinal epithelium is renewed from crypts, which constitute a stem cell niche. The base of the crypt is occupied by *Lgr5*+ Crypt Base Columnar (CBC) stem cells placed in between Paneth cells which maintain the crypt niche[276, 277]. Directly above (usually 4 cell spaces from the base) reside Intestinal Stem Cells (ISCs), which periodically produce CBCs. In the track leading out of the crypt are found the transit-amplify progeny cells, produced by CBCs. As these progeny cells divide, migrate, and commit to their differentiation, they can produce Paneth cells, goblet cells, enteroendocrine or (for about 80%) enterocytes[278] (see Figure 6) which are the main site of absorption of nutrients.

Enterocytes present on their apical surface a brush-border, composed of hundreds of microvilli 1-3 µm in length[279]. Overall, the absorption capacity of the small intestine is largely linked to the capacity of circular folds, villi, and microvilli to multiply their exchange surface, allowing a 3 m long and 2.5 cm wide cylinder to expose around 30 m² of surface[280].

Above GALTs, some epithelial cells present a peculiar phenotype. Contrarily to their neighbors, microfold cells, or "M cells", do not express glycoprotein 2 (*Gp2*), and are thus less protected from the content of the lumen than the rest of the intestinal epithelial wall[281]. In addition to reduced glycocalyx, M cells exhibit an irregular brush border and reduced microvilli. In the specific case of M cells, this participate to a specific role played by this cell. Indeed, the cells are highly specialized in phagocytosis and transcytosis of macromolecules, and pathogen or commensal bacteria from the lumen to the subjacent Peyer's patch. The role of M cell is described as that of antigen

presentation to the immune system[282], notably to lymphocytes and mononuclear phagocytes, residing in the intraepithelial pocket beneath the M cell.

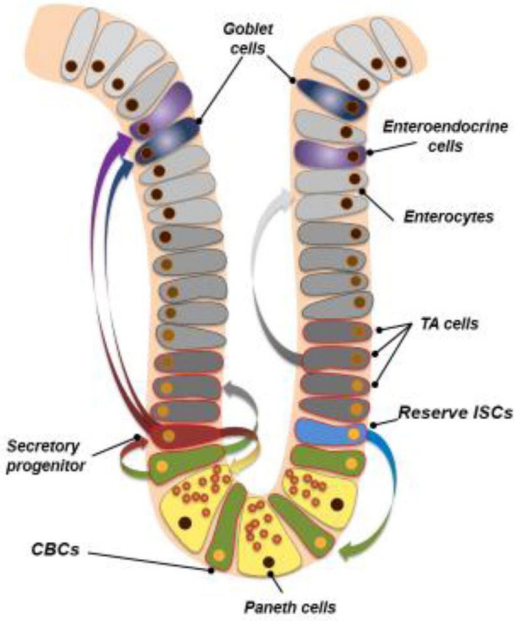

Figure 6: Cellular diversity and their distribution in the intestinal crypt.

Visual summary of the distribution and fate of intestinal stem cell in the various cells composing the intestinal epithelium. Reproduced from Yousefi et al.*, 2017[278].*

Below the epithelium, the stroma (lamina propria) hosts a dense population of so called "stromal cells", including myofibroblasts, fibroblasts, pericytes, and smooth muscle cells among others[283]. These cells take part in a cross-talk with the epithelial cells since early stages of development, where epithelium-derived hedgehog (Hh) growth factors are thought to participate in the mesenchymal differentiation of surrounding cells[284]. In return, they contribute to the supportive microenvironment of the crypt stem cell niche[285, 286]. Aside from their role in matrix remodeling, wound healing and fibrosis, stromal cells are now described to play an active role in immune response, through sensing of inflammatory signals and recruitment of lymphocytes and macrophages *via* the production of chemokines[287], to the point that they are often coined "non hematopoietic immune cells"[288].

Physiology and dynamics

The intestinal epithelium displays the highest self-renewal rate among mammalian tissues. ISCs divide roughly every 24 h, and the life span of intestinal epithelial cells (IECs) is short (3 to 6 days)[269]. Proliferation is under the control of Wnt pathway[289], which regulates several genes expressed in the crypt. Sources of Wnt antagonists have been located in the stroma[290], suggesting a modulating role of the mesenchyme on ISCs proliferation. Interestingly, Paneth cells, located next to ISCs are major Wnt expressors[291].

Further away from the crypt, stromal cells engage in a crosstalk with EICs. Past the transit-amplifying cells, epithelial cells express Hh proteins as they differentiate, leading to a gradient of concentration which increases as cells move away from the crypt. This Hh promotes stromal Bmp expression, which antagonize Wnt signaling, inhibiting ISCs proliferation and promoting epithelial differentiation[284, 292].

In addition to human cells, the gut also hosts large microbial populations, up to 10^7 for the ileum alone[293], which colonize us after birth and follows us for the rest of our lives. This “supplementary organ” is mostly composed of commensal cells, which play many roles in healthy gut physiology, including assisting in the metabolism of otherwise indigestible polysaccharides, producing essentials vitamins, protecting against opportunistic pathogens, and are required for the development of both the intestinal epithelium and immune system[294]. Also, their implication in homeostasis could span beyond the digestive tract as microbiota has been shown to regulate bone mass in mice[295].

Overall, the healthy gut is the scene of many cross talk and regulatory events, between stromal cells, the stem cell niche, the epithelium, and the microbiota.

In addition to molecular crosstalks and other chemical interactions, the small intestine is also home to mechanical work, which is essential to propel the bolus forward, ensure digestion and discharge of the intestine. Motility in the small intestine is set in place by three essentials components: the enteric nervous system (ENS) which can be triggered by pressure, the Interstitial Cells of Cajal (ICCs) which makes the connection between neurons and smooth muscle cells, and the muscularis layers that serves as effector and produce the contraction[296]. Interestingly, ICCs present a

spontaneous rhythmic activity, which is not sufficient to reach the excitatory threshold of the smooth muscle cells, and contraction is achieved only if the wave is concomitant with an impulse from the ENS. Thus, ICCs dictate the rhythm of contractile waves[297].

Pathology

Normal passage of molecules through the epithelial wall can occur in two fashions: paracellular or transcellular. The paracellular way is limited, compared to the transcellular. Only small molecules (<200 Da), typically polar or highly hydrosoluble, can cross the tight junctions of the epithelium. Other molecules, including xenobiotics, uses the transcellular path, relying on transporters to cross through the epithelium[298]. Typically, Solute Carrier (SLC) family of transporters allows the absorption of molecules, while ATP Binding Cassette (ABC) transporters will excrete molecules. Even though local expression of these families of transporters varies along the GI tract, most of the SLC and ABC transporters are expressed at least somewhere in the tract[299].

In pathological setups, this barrier function can be altered. Such is the case following *Shigella flexneri* infection for instance[300]. Typically, enteroinvasive pathogens such a *S. flexneiri* are described to sometimes exploit M cells transcytosis capabilities to invade the mucosa[301]. Infection by enteroinvasive pathogens leads to local destruction of the epithelium, often leading in return to disentry, which can be a major threat especially to young children without access to safe tap water, and killing 40,000 pediatric patients each year[302].

Non-infectious pathological setups include inflammatory bowel disease (IBD), which notably includes ulcerative colitis (CU) and Crohn's disease (CD). Caused by a dysfunctional host immune response to commensal microbiota and dietary factors[303], IBD lead to chronic inflammation of the intestinal wall. IBD are associated with complex interactions between the microbiota, the epithelial and the immune cells, and much work remains to be done to fully uncover their biological mechanisms[304, 305].

Gut barrier-on-chip models

Choice of cells

Once isolated and when cultured on 2D susbtrate, primary enterocytes adhere poorly, and lose their polarity[306], and they are generally not cultured *in vivo*. Other cell lines are often preferred to primary enterocytes, such as Caco-2 cells. Isolated by Fogh and colleagues[307] from a human adenocarcinoma, Caco-2 cells is the most used model for intestinal epithelial cell. After reaching confluence, Caco-2 cells differentiate to resemble small intestine enterocyte, despite their colonic origin, and express a large variety of enzymes, ionic channels, transporters, *etc.*[308].

Despite these facts, Caco-2 cells suffer from a few shortcomings: no cellular diversity, non-expression of mucin, TEER higher than physiological.[309]. Also obtained from a human adenocarcinoma, HT29 cells consist in a variety of sub-clones, which can differentiate into mucin-producing goblet cells[310]. Caco-2/HT29 coculture can produce a cellular mix of higher relevance[311].

Differentiation of Caco-2 cells into expressing M-cell phenotype has been shown feasible by coculture of Caco-2 cells with either freshly isolated lymphocytes from Peyer's patches[312], or with Raji B lymphocytes[313], with interesting results. Following coculture, Caco-2 cells expressed disorganized brush border and displaed an intraepithelial pocket filled with lymphoid cells. Later, *in vitro* experiment would demonstrate the improved transepithelial passage of macromolecules[314-316].

Even though *in vitro* gut models benefit from well established lines such as Caco-2/TC7 cells, the situation is different for most of the cells types composition the complex GI tract, limiting the ease to produce complex gut-on-chip systems, and highlighting the interest of hybrid systems[266].

Existing gut-on-chip setups

Since 2012, a series of gut-on-chip models have been proposed. All address specific needs, depending on the physiological or pathological events we want to explore. Investigating the barrier function, and absorption profiles of nutrients and

drugs do not necessitate complex setups. They are usually done with immortalized cell lines such as Caco-2 cells, in microdevices comprising 2 channels separated by a porous membrane allowing the support of an epithelial monolayer while permitting the passage of molecules if the epithelium is not impermeable[317, 318].

The chip developed in 2010 by Dongeun Huh[5] has known many variations, and is widely used today to investigate the impact of physical cues such as flow and stretch on both physiological and pathological events, such as maturation of the epithelium[319] or its infection by pathogens[6] for instance.

To palliate the difference in stiffness between the PDMS typically used in microfluidic setups and the native properties of soft tissues, several teams have developed hydrogel-embarking gut-chips. This has been done either as porous membrane and hydrogel bilayer over static Transwell[320], or by capillary guidance of hydrogel in a microfluidic chip to form a wall of the channel in which epithelial cells are seeded[9]. Interestingly, hydrogels allow the encapsulation of a stromal compartment that previous microdevices lacked. This property can prove useful to add resident cells such as fibroblasts[320] or macropahes[9].

Aside from seeking to bring more microenvironmental cues together on a chip, improved designs sometimes seek to embark sensors, to propose relevant analysis directly on the chip. For instance, to follow the absorption of molecules over time *via* embarked optical sensors[264, 321]. When no such sensors are embarked, the experimenters have to rely on additional analysis. As an example, loss of barrier function can be addressed with fluorescent molecule such as Lucifer Yellow[322].

CONCLUSION AND OBJECTIVES

We saw in this first section how historically the field of bioengineering built itself on the advances of various other scientific fields. We saw how organoid and organ-on-chip strategies emerged to face the growing need for advanced cell culture systems, while answering ethical concerns.

Both strategies have advantages and shortcomings. Notably, while organoids can boast to be linked to better survival and better differentiation profile[237], they typically remain difficult to access for the experimenter. They can be deep within a bulk and hard to image in immunofluorescence. Their complex shape can also hinder the possibilities to extract morphological data from bright field images. Importantly, organoids typically organize themselves around a lumen, which is closed and will accumulate debris until leading to death of the organoid. To palliate that, organoid scientists are now increasingly borrowing the microfabrication tools of organs-on-chip to design the microenvironment of the cultured cells to better suit the needs of the experiment (observation needs, increased reproducibility, *etc.*)[218, 246, 266]

Organs-on-chip, on the contrary, are specifically designed for the control of the microenvironment. Since they are the product of the experimenter's will, they are usually well suited for observation. However, as they often aim at the simplest required complexity to emulate in order to faithfully mimic the microenvironment, they can often fall short of producing and maintaining fully differentiation cells. Nonetheless, they remain easy to access for the experimenter and occupy a growing place in both fundamental biology labs and preclinical research[323-325].

We have also reviewed a certain number of organs-on-chip aiming at recapitulating the complex gut barrier, and observed the variety of setups that exist to emulate a specific function of interest for the experiment. From this review, one realization is striking: while flow, stretch, and substrate stiffness are today all recognized as cues having the potency to alter cell behavior and fate[14, 326-328], no single platform had tackle the challenge of submitting a barrier tissue mimicry with the three.

Thus, the goal of this thesis project was to design and fabricate an organ-on-chip microfluidic device which would faithfully recreate the microenvironment of a barrier tissue, while allow the experimenter to have control over the flow, stretch and stiffness conditions. Such a chip, dishing porous membranes for a hydrogel layer, can be anticipated to allow for the encapsulation of a third cellular compartment, which could also be of high interest, as stromal cells are known for their role in tissue homeostasis[17, 287, 288].

We will cover through this manuscript (1) the selection of hydrogel recipes suitable for cell culture and inclusion in a microfluidic chip, (2) the conception and fabrication of the microfluidic device that will include a hydrogel layer, (3) the setup of a hydraulic system that allows for the independent control of flow and actuation of the hydrogel layer, (4) the characterization of the deformation of the hydrogel layer, (5) the screening of conditions leading to intestinal epithelial structuration, and (6) the functional characterization of an intestinal epithelium produced on the chip.

SECTION II

MATERIALS AND METHODS

1 – HYDROGELS

a) Components

For the experiments done during this thesis, we constituted a bank of molecules that would be used in different hydrogel recipes. They are presented below (**in bold,** how they are named later in the manuscript). Globally, all the gel components were stored as powder aliquots under inert gas (Argon).

PEGVS10k8a – Star shaped poly(ethylene glycol) (PEG) macromolecule with eight arms and a molecular weight (MW) of 10 kDa. The PEG arms are built around a tripentaerythritol core and are all terminally functionalized with a vinyl-sulfone group. This compound was sourced from XIAMEN SINOPEG BIOTECH (China).

PEGVS20k4a – Star shaped PEG macromolecule with four arms and a MW of 20 kDa. The PEG arms are built around a pentaerythritol core and are all terminally functionalized with a vinyl-sulfone group. This compound was sourced from XIAMEN SINOPEG BIOTECH (China).

PEGVS40k8a – Star shaped PEG macromolecule with eight arms and a MW of 10 kDa. The PEG arms are built around a tripentaerythritol core and are all terminally functionalized with a vinyl-sulfone group. This compound was sourced from NOF (Japan).

PEGTH10k4a – Star shaped PEG macromolecule with four arms and a MW of 10 kDa. The PEG arms are built around a pentaerythritol core and are all terminally functionalized with a thiol group. This compound was sourced from XIAMEN SINOPEG BIOTECH (China).

16A – Acetylated hexadecapeptide (Ac-GCRDGPQGIAGQDRCG-H2) containing a MMP cleavage site. This compound was sourced from Bachem AG (Switzerland).

16W – Acetylated hexadecapeptide (Ac-GCRDVPMSMWGGDRCG-NH2) containing an efficient MMP cleavage site. This compound was sourced from Bachem AG (Switzerland).

16R – Acetylated hexadecapeptide (Ac-GCRDVPMSMRGGDRCG-NH2) containing an extremely efficient MMP cleavage site. This compound was sourced from Bachem AG (Switzerland).

RGD – Acetylated endecapeptide (Ac-GCGYGRGDSPG-NH2) containing a RGD sequence allowing for integrin binding (Pepmic Co., China).

PEG linker – Hetero-bifunctional PEG with a MW of 3.4 kDa ("Sunbright MA-034TS*", NOF, USA) functionalized on one end with a maleimide group, and with a succinimidyl ester on the other end.

Fn9-10 – Recombinant fibronectin fragment containing the 9th and 10th repeats of Type III modules of fibronectin[329, 330]. This compound was sourced from the PF3PR technological platform (Institut Pasteur, Paris). Cloned sequence:

NQEQVSPLGLDSPTGIDFSDITANSFTVHWIAPRATITGYRIRHHPEHFSGRPREDR
VPHSRNSITLTNLTPGTEYVVSIVALNGREESPPLIGQQSTVSDVPRDLEVVAATPTS
LLISWDAPAVTVRYYRITYGETGGNSPVQEFTVPGSKSTATISGLKPGVDYTITVYAV
TGRGDSPASSKPISINYRT

FnPEG – PEGylated Fn9-10 fragment obtained by reacting Fn9-10 and PEG linker together.

b) Quality controls

All PEGs and peptides were received as powders. When constituting stock solutions, a filtration test was performed to detect defective lots where compounds started to aggregate. Briefly, if the corresponding 12% (w/v) solution could not be filtered on a 0.22 µm sieve, the lot was rejected.

Thiol containing macromolecules (PEGTH10k4a, 16R, 16W and RGD) were systematically tested for thiol activity after resuspension and filtration in order to detect potential disulfide bonding. For that, we used an Ellman's assay (Sigma-Aldrich, Germany) according to manufacturer's instructions to assess the quantity of free thiols available for Michael type addition. Briefly, Ellman's reagent (or DTNB) is a compound that reacts with free sulfhydryl groups to yield a mixed disulfide and 2-nitro-5-

thiobenzoic acid (TNB). TNB being a species with high molecular extinction in the visible range (412 nm), its concentration can easily be assessed relying on a standard curve prepared in parallel of the experiment. Here, optical density of solutions containing known concentration of thiol-containing molecules (PEG, peptide) in solution with DNTB was read on a plate reader (Infinite 200 PRO, Tecan Life Sciences, Switzerland) and compared to a Cysteine standard (L-Cysteine hydrochloride, Sigma-Aldrich, Germany).

The Ellman assay was also used to investigate RGD - PEGVS binding kinetics in order to detect untethered peptides (either forming disulfide bonds or failing to graft onto PEG macromers). To do so, we relied on an “Ellman test” to follow in time the concentration of free thiol groups. In detail, the Ellman test was performed on several conditions. First, on a 200 µM solution of RGD. Then, on solutions containing both 200 µM of RGD and 200 µM of VS functions, brought by a 216 µM solution of PEGVS40k8a with 0.925 functionalization rate. The dynamic of RGD-PEGVS binding was assessed by an performing an Ellman test immediately after mixing, as well as 15, 30, and 60 min after mixing. In addition, hydrogel samples of 100 µL (PEG40-16R at 7% w/v concentration with 200 µM RGD) were prepared with or without a 30 min waiting time after RGD addition, and the Ellman test was performed after swelling in contact with 100 µL of distilled for two hours in an incubator preventing evaporation. Measures were compared to a standard dilution of N-Acetyl cysteine prepared in parallel, ranging from 10 µM to 1.5 mM. All conditions were performed in triplicates.

c) Hydrogel preparation

Standard hydrogel preparation entailed the use of PEGVS and PEGTH with 1:1 stoichiometric ration between available VS and TH groups. This resulted in cell inert PEG hydrogel (no MMP sequence, no integrin anchors) with tractable mechanical properties. When cell encapsulation was considered, we replaced thiol-functionalized PEGs with peptide sequences containing two thiols function (brought by cysteines) and an MMP sensitive sequence. Furthermore, the introduction of an RGD peptide or of a functionalized fibronectin fragment was used to ensure proper integrin-mediated cell adhesion.

Initially, stock solutions were constituted as follows: vinyl-sulfone functionalized PEGs where solubilized at 12% (w/v) triethanolamine (TEA) buffer (0.3 M, pH 7.5). Thiol containing molecules (PEGTH and the different peptides) where solubilized at 12% (w/v) in distilled H2O. RGD was further diluted to create a 10 mM solution in distilled water. All stocks went through a 0.22 µm filter to ensure sterility. In cases where cells were to be included in the hydrogel, TEA was replaced with HEPES buffer (Dominique Dutscher, France), adjusted to the same 0.3 M concentration and pH 7.5.

PEG-only hydrogels were prepared by mixing stock solution of PEGVS and PEGTH in a TEA solution (0.3 M, pH 7.5). RGD was added if cell adhesion was planned. Relative volumes of the different stock solutions where adjusted to ensure that:

1. Thiol and vinyl-sulfone functions are stoichiometrically balanced.
2. The final concentration of PEG reaches the targeted concentration.

Practically, to produce 100 µL of a 5% PEG10-10 gel, we mixed 14.43 µL of PEGVS10k8a with 57.33 µL of TEA buffer. Optionally 1 µL of the RGD peptide was introduced into the mix. The resulting solution was left to react for 20 min at room temperature (RT). Finally, 27.23 µL PEGTH10k4a was added. After a quick vortexing, the resulting hydrogel mix was incubated 45 min at 37 °C, 80% relative humidity (RH) to obtain full gelation.

MMP sensitive PEG hydrogels were obtained by mixing stock solution of PEGVS and PEP in a TEA solution (0.3 M, pH 7.5). RGD was added if cell adhesion was planned. Relative volumes of the different stock solutions where adjusted to ensure that:

1. Thiol and vinyl-sulfone functions are stoichiometrically balanced.
2. The final concentration of PEG+PEP molecules reaches the targeted concentration.

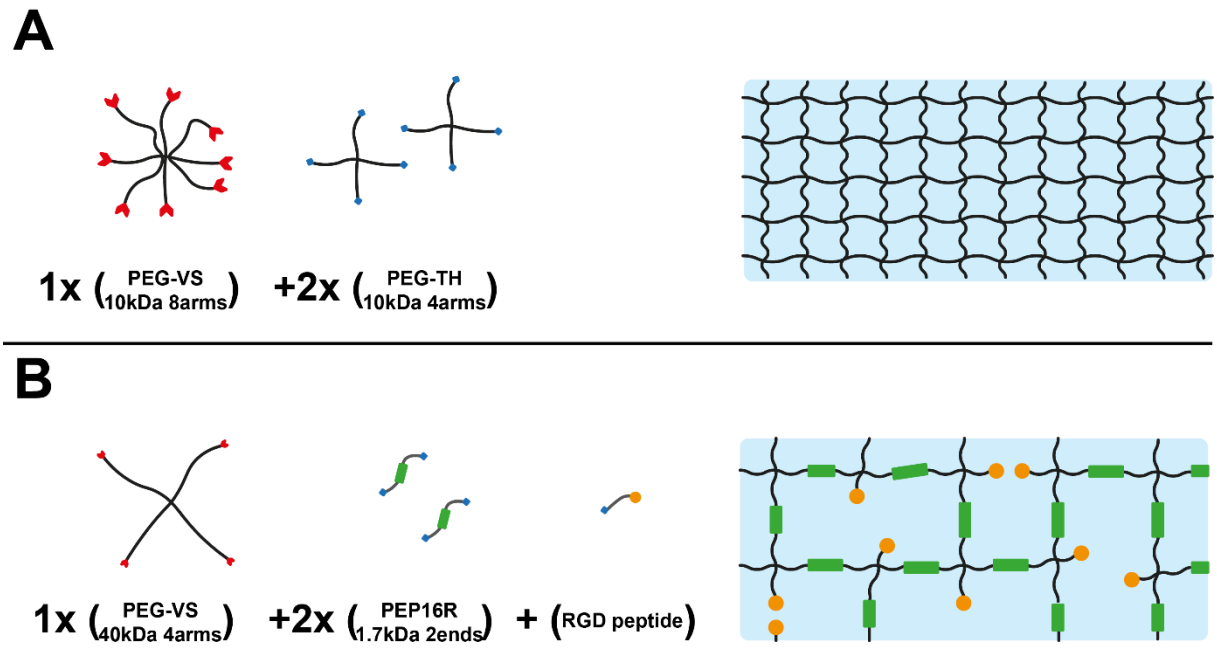

Figure 7: Hydrogel recipes.

Relying on different molecules allows to create hydrogel of tunable properties. ***(A)*** *PEG-PEG hydrogel using low molecular weight PEGs with high number of arms leads to dense networks.* ***(B)*** *High molecular weight PEGs, proteinase sensitive peptides, and dead-ends leads to sparse and degradable networks, able to host cells.*

Practically, to produce 100 µL of a 5% PEG40-16R gel, we mixed 35.39 µL of PEGVS10k8a with 57.33 µL of TEA buffer. Optionally 1 µL of the RGD peptide was introduced into the mix. The resulting solution was left to react for 20 min at RT. Finally, 6.28 µL 16R was added. After a quick vortexing, the resulting hydrogel mix was incubated 45 min at 37 °C, 80% RH to obtain full gelation.

Example recipes showcasing the volumes for various hydrogel recipes are displayed in Figure 9 below.

		A	B	C	
GEL PROTOCOL					
BUFFER		58,33	58,33	57,33	µL
PEG-VS	**12% (w/v)**	14,43	12,07	14,43	µL
GG11	**10 mM**	0,00	0,00	1,00	µL
PEG-TH	**12% (w/v)**	27,23	29,60	27,23	µL
TOTAL		100	100	100	µL

FINAL CONCENTRATIONS					
VS		12,324	10,304	12,324	mM
TH		12,324	13,395	12,324	mM
DIFF.		0,000	3,091	0,000	mM
TH/VS ratio		1,00	1,30	1,00	

		D	E	F	
GEL PROTOCOL					
BUFFER		75,00	50,00	49,00	µL
PEG-VS	**12% (w/v)**	20,54	41,08	41,08	µL
GG11	**10 mM**	0,00	0,00	1,00	µL
PEP-TH	**12% (w/v)**	4,46	8,92	8,92	µL
TOTAL		100	100	100	µL

FINAL CONCENTRATIONS					
VS		4,485	8,971	8,971	mM
TH		4,485	8,971	8,971	mM
DIFF.		0,000	0,000	0,000	mM
TH/VS ratio		1,00	1,00	1,00	

Figure 8: Examples of hydrogel recipes.

*Hydrogels **A, B, and C** are composed of a mix of PEGVS10k8a and PEGTH10k4a, with a final 5% (w/v) dry content. Gel **A** corresponds to a hydrogel with equimolar VS and TH concentration, and no added RGD peptide. Gel **B** corresponds to the stoichiometric imbalance leading to 1.3:1 TH/VS ratio. Gel **C** corresponds to the addition of 100 µM RGD to a stoichiometrically balanced gel. Hydrogels **D, E, and F** are composed of PEGVS40k4a and 16R, in equimolar proportions of TH and VS groups. Gels **D and E** correspond to 3% and 6% dry content gels, respectively. Gel **F** is similar to gel **E**, with addition of 100 µM RGD.*

d) Measuring hydrogel swelling

We approached hydrogel swelling by measuring the mass gain after reaching equilibrium in water. Our idea was to find gel formulas that minimize swelling in order to ease Hydrogel/PDMS coupling. A secondary objective was to anticipate swollen gel volumes in order to obtain swollen gel with a diameter matching the plate geometry of the rheometer. In the literature two methods are described: (1) the swelling ratio Q corresponding to the ratio of $Volume_{swollen\ gel}$ / $Volume_{polymer}$ and (2) the swelling ratio Q' corresponding to the ratio of $Volume_{swollen\ gel}$ / $Volume_{crosslinked}$ [331]. We found our mass-based method easier to access while providing a good approximation of the volumetric swelling of the hydrogel. The mass gain ratio (M_g) we assessed corresponds to:

$$\frac{Mass_{swollen}}{Mass_{crosslinked}}$$

Based on this method (which assumes) isotropic swelling, we know the initial volume (V_i) required to be placed in between two siliconized glass slides separated by spacers of known height (H) to create a cylinder that, after swelling, will match the diameter (D) of the geometry of the rheometer can be computed as follow:

$$V_i = \frac{D^2 \times H \times \pi}{4 \times {M_g}^{2/3}}.$$

If need be, approaching the volumetric swelling Q' can be achieved with mass measurement data as both PEG and water density are known and provided that all the PEG introduced in the system end up totally bound to the network (no free PEG fraction).

e) Rheology

Relying on the previous equation, cylindrical hydrogel samples were prepared by casting small droplets of hydrogel mix in between two glass slides siliconized with Sigmacote (“SL2”, Sigma-Aldrich, Germany) and separated by spacers 1.105 mm in height. The glass slides were then secured together using paper clips and everything was placed in an incubator (37 °C, max humidity) for 45 min. Once cross-linked, the hydrogels were placed overnight in 1X DPBS to reach its final volume and mass. For example, 7% PEG10-10 hydrogel with a mass gain ratio measured at 1.12 will require a ~12.9 µL droplet to form a ~3.86 mm diameter cylinder that, after swelling, will reach a final diameter of ~4.00 mm.

Rheology was performed on a rotational rheometer (Kinexus Ultra+, NETZSCH-Gerätebau GmbH, Germany). In detail, a parallel plate geometry of 4 mm diameter (PP04) was used to apply shear deformation to a hydrogel cylinder (4 mm diameter, ~1.1 mm height). Prior to measurements, each cylinder was submitted to an initial compression strain of 10% to prevent slippage. First, an amplitude sweep was performed with an oscillatory shear strain ranging from 0.1 to 10% at a fixed frequency of 1Hz to determine the Linear ViscoElasticity Region (LVER). Then, a frequency sweep was performed at a constant shear strain of 1% (which was included in the LVER of all the tested hydrogels) and with a frequency ranging from 0.1Hz to 10Hz. The values presented in this paper correspond to values measured at 1Hz. For each gel recipe, we measured the complex, storage, and loss moduli (G*, G’, and G” respectively) at least 3 times. These values where measured across different PEG composition, concentration, stoichiometric ratios and presence of integrin-binding components.

f) Impact of gel functionalization on stiffness

To assess the impact on the physical properties of changes in the hydrogel recipe, and be certain to properly dissociate the impacts of physical and chemical cues, we explored the rheology and swelling behavior of several gels as their recipes, and

notably their integrin ligand content, changed. Briefly, we investigated the impact of: **(a)** stoichiometric imbalance, **(b)** RGD concentration.

2 – HAHL CHIP PRODUCTION

a) Microfabrication and photolithography

Photolithography was used for molds requiring micrometric precision and/or perfectly smooth surfaces. Briefly, photolithography masks were designed on CleWin 5.2 (WieWeb software, Netherlands), and printed at a resolution of 50 800dpi on plastic sheets by Selba S.A. (Switzerland). The upper stage of the second version of the chip (HAHLv2, described in detail later) only required millimetric precision, but perfect surface. It was designed on Illustrator (Adobe, USA), and laser-cut out of an opaque PMMA sheet using a Speedy 300 laser cutter (Trotec Laser, Germany). All masks served to selectively expose SU8 photosensitive resin (Chimie Tech Services, France) spin coated as a layer of controlled height on a silicon wafer (“WAK4PP”, Neyco, France) and placed under a MJB4 mask aligner (Süss Microtec SE, Germany).

Other chip molds were produced by micromilling (brass) or 3D printing (resin). Brass molds were carved out of brass bulks using a Mini-Mill/GX CNC milling machine (Minitech Machinery, USA). Resin molds were 3D printed using a stereolithography printer (“SLA Form 3”, Formlabs, USA). All molds were designed on Fusion 360 (Autodesk, USA).

b) PDMS

Polydimethylsiloxane (PDMS) has emerged as one of the most used material for bioengineering applications. It combines many advantages, including transparency, accessibility for microscopy imaging, and non-toxicity. Its Silicon content makes it amenable to surface chemistry based on silanization, and thus allows for advanced

functionalization. It is supple and easy to manipulate. While impermeable to liquids, it allows for gas exchanges. Lastly, it presents itself in a liquid state until mixed with a curing agent and left to rest. Thus, it can be poured over a mold and take the shape of very precise geometries, down to the nanoscopic scale.

PDMS mix and baking

The microdevices described here rely on a 10/1 (PDMS/curing agent) mixture of polydimethylsiloxane (Sylgard 184 Kit, Dow, USA), mixed in an ARE-250 mixer (THINKY, Japan). For each stage of the chip, different methods were used to shape them, which are described later (*cf.* pages 97, 101). In all cases, the mixture is degassed in a vacuum chamber until no visible bubbles remain, and then baked in an oven for at least 3h at 60 °C.

PDMS-glass bonding

In the instances where PDMS had to be covalently bound to glass, it was done by oxygen plasma treatment. Briefly, a glass coverslip and the PDMS slab were thoroughly cleaned, and exposed to oxygen plasma in a CUTE vacuum plasma system (Femtoscience, Rep. of Korea). The surfaces were exposed for 40s to an oxygen plasma created in 67 Pa (0.5 Torr), 20 SCCM O2 and 60 W at 50 kHz. Immediately after exposure, the surfaces were gently pressed against each other, to avoid bubbles. Then, they were placed in an oven for at least 1 h at 80 °C.

Covalent PDMS-hydrogel bonding

HAHL chip production was based on the strong binding of PEG hydrogels onto PDMS surfaces. This was achieved by first functionalizing the PDMS surface in order to provide correct handles (Thiol groups) for Michael Type addition as shown in the Figure 10 below.

Surface modification was performed in a vacuum chamber that was placed on a hot plate at 80 °C, under a chemical hood. In the chamber, still at atmospheric pressure, a few drops of (3-Mercaptopropyl)trimethoxysilane (3-MPS) (Sigma-Aldrich, Germany) were deposited in a Becher and left for around 30 min. In parallel, the molded PDMS

slabs were thoroughly cleaned and exposed to an oxygen plasma following the procedure described above. Immediately after exposure, the PDMS slabs were transferred in the vacuum chamber, with the surface that needs to be treated right above the 3-MPS containing Becher. The whole setup is then placed under vacuum, on the 80 °C hotplate, for 30 ± 5 min. Please note that longer exposure can lead to the loss of optical transparency of the PDMS slab.

The treated PDMS slabs could either be used right away, or stored at 4 °C for several weeks. In the latter case, the many thiol functions could engage in unwanted di-sulfur bounds which could prevent efficient hydrogel bonding. This could be reversed by reducing the disulfide bonds by treating PDMS slabs with a 10 mM solution of DL-Dithiotreitol (DTT) (Sigma-Aldrich, Germany) for 20 min.

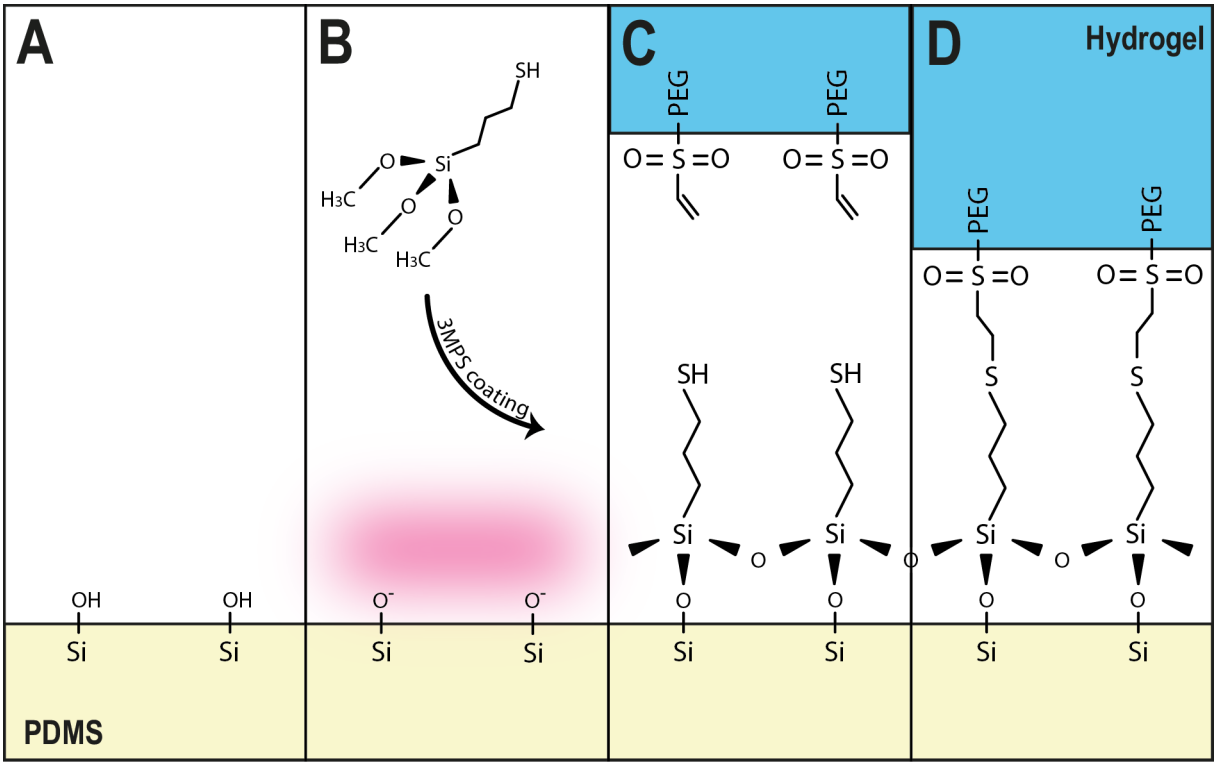

Figure 9: Hydrogel to PDMS bonding.

*(**A**) Inert PDMS surface. (**B**) Plasma treatment of PDMS activates its surface and allow for 3MPS surface treatment. (**C**) 3MPS coated PDMS can engage in thiol-Michael addition reaction, leading to formation of covalent bounds between PDMS and a hydrogel layer (**D**).*

c) HAHL v1 (secured in holder)

One method used to secure the different stages of the chip together consisted in a specifically designed and manufactured holder, allowing to press all stages together relying on a screwable tightening ring such as described in the figure 11 below.

In this configuration (version 1, or HAHLv1), the whole chip is composed of (a) a **tightening ring**, (b) a **PDMS upper layer** which is imprinted with the upper channels, (c) a **hydrogel layer**, (d) a **PDMS ring** of controlled thickness, (e) a 24 mm diameter **glass coverslip**, and (f) a **holder** (see Figure 11).

Holder

The chip holders were designed in the CAD software Fusion 360 (Autodesk, USA). The actual production of the holders in a medical grade NiCr alloy was outsourced. Briefly, they consist in 42 mm diameter cylinders (36 mm inner diameter), which can host the 34 mm diameter PDMS chip, and hold it firmly in place when the tightening ring is screwed in.

At the bottom, the 1 mm thick floor gets thinner towards the center, until it opens on a 18 mm diameter opening, to allow a microscope to come as close as possible.

PDMS chip v1

In this configuration, the lower PDMS ring is made by pouring fresh PDMS/curing agent mix in a plastic dish, in quantity leading to a 2 mm thick PDMS layer. After baking, rings were obtained by cutting the slab with 18 mm and 34 mm diameter punchers.

On the other hand, the upper slab was casted on a mold obtained by soft lithography with a high-resolution mask (*cf.* above). Briefly, two stages compose the imprints in the PDMS upper slab. The first corresponds to an 18 mm diameter wide, and 250 µm deep pool. A small 1 mm thick ring is also present on this first stage, with an outer diameter of 34 mm. The second corresponds to 1 mm wide, 10 mm long channels, placed in the center of the pool, with 2 mm diameter large circular chambers on each end. These

chambers allow the experimenter to easily punch inlets and outlets to connect the upper channels to tubing and the rest of the microfluidic setup.

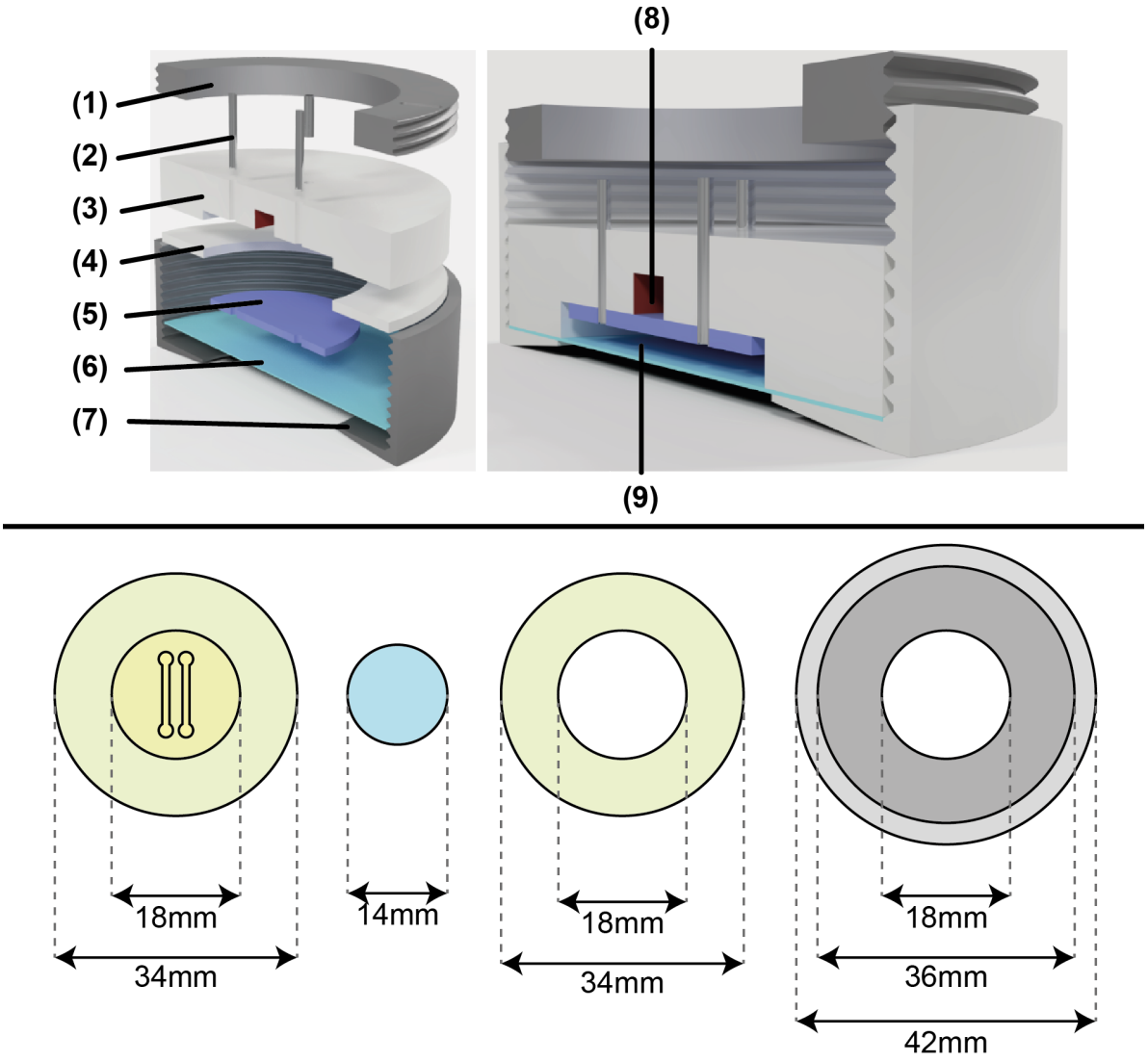

Figure 10: HAHL v1 system.

Top: *Section view of an unmounted (left) and mounted (right) HAHLv1 device.* ***(1)*** *Tightening ring.* ***(2)*** *Fluidic connectors.* ***(3)*** *PDMS upper layer.* ***(4)*** *PDMS ring.* ***(5)*** *Hydrogel layer.* ***(6)*** *Coverslip.* ***(7)*** *Chip holder.* ***(8)*** *Upper channel.* ***(9)*** *Lower chamber.* ***Bottom:*** *Top view of the chip elements, with dimensions.*

Photolithography for PDMS upper stage

Spin coating of SU8-2100 resin at 1000 rpm (with a first acceleration period of 100 $rpm.s^{-1}$ up to 500 rpm, a 5" waiting phase, and final acceleration at 300 $rpm.s^{-1}$) allowed us to produce 253 ± 8 µm thick layers in the resin mold. This was done a first

time for the 18 mm wide pool. A soft bake (6'20" at 65 °C, 39'20" at 50 °C) made the resin hard enough to be put under the mask aligner, and UV exposure at 379 mJ.cm^{-2} for 28" allowed the resin to crosslink where exposed through the mask. Then, the spin coating and soft bake are done once again with the mask corresponding to the channels. This was followed by a post-exposure bake (5' 00" at 65 °C, 13' 45" at 95 °C), and removal of non-crosslinked resin by immersion for 16' 20" in an agitated bath of propylene glycol monomethyl ether acetate (PGMEA). Molds were then rinsed with isopropanol, dried, and underwent a 30' hard bake to get rid of the cracks in the resin.

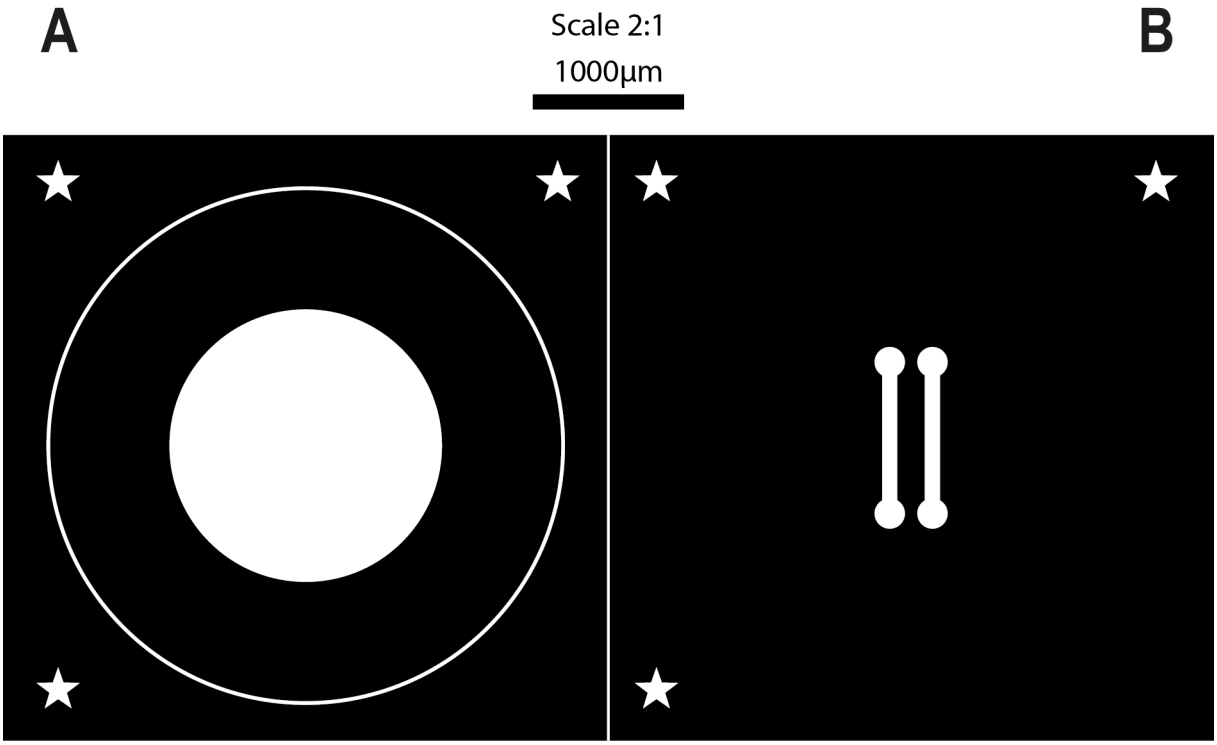

Figure 11: Photolithography masks for the upper stage.

(A) *The first layer comprises an 18 mm diameter pool, and a 34 mm circle to help the experimenter align their puncher.* ***(B)*** *The second layer comprises two 1 mm wide and 10 mm long channels, each with a 2 mm pool at each end. Both masks contain marks (here stars) to ensure proper alignment of the masks.*

After unmolding the PDMS upper layer, their bottom surfaces are 3-MPS treated as described above, to allow covalent bonding to the hydrogel layer. Then, they are either used right away, or stored at 4 °C until later use.

Hydrogel

Hydrogel discs were obtained by casting fresh hydrogel mix in a ~200 µm deep circular pool (14 mm diameter) carved in a Teflon block, which is then covered by a Sigmacote-treated glass slide (“SL2”, Sigma-Aldrich). The ensemble is put in an incubator at 37 °C.

After 45 min incubation time, the glass slide was removed, and the hydrogel discs were carefully detached with Brucelle tweezers, removed from the Teflon pool, and deposited on the bottom surface of the PDMS upper layer. A drop of DPBS is deposited on top of it to avoid desiccation. After a few minutes, the PDMS-hydrogel ensemble can be included in the whole setup, and channels can be filled without risk for the PDMS-hydrogel bond.

Chip assembly

Provided that the upper stages of the PDMS are produced and stored in numbers beforehand, the chip can be assembled in a few hours. Typically, 2 hours prior to including the chip in a microfluidic system, 3MPS is pre-heated in a vacuum chamber to start the PDMS-hydrogel binding protocol described earlier. Then, gel mixes are prepared, and casted in the Teflon pools. Ten minutes later (that is, 35 min prior to the end of gel incubation time), the upper stages of the chips are placed in vacuum chambers and exposed to 3MPS vapors for 30 min. Past that time, the chips are left to cool down 5 min in the bio safety cabinet, and sterilized by 5 min exposure to 36W UV light (Nailstar Professional, UK). Finally, the hydrogel discs are taken from their molds as described above, and placed on the chip.

Once the hydrogel is bound to the PDMS upper stage, the whole chip can be assembled. For easier handling, the upper stage is place upside-down on the tightening ring, and the PDMS ring above it. The pool is loaded with medium of DPBS (depending on the experiment to come), and sealed with the glass coverslip. Precision wipes (Kimtech-Clark, USA) are used to absorb excess liquid. Finally, the chip holder is placed over the whole chip and screwed upside-down until tight.

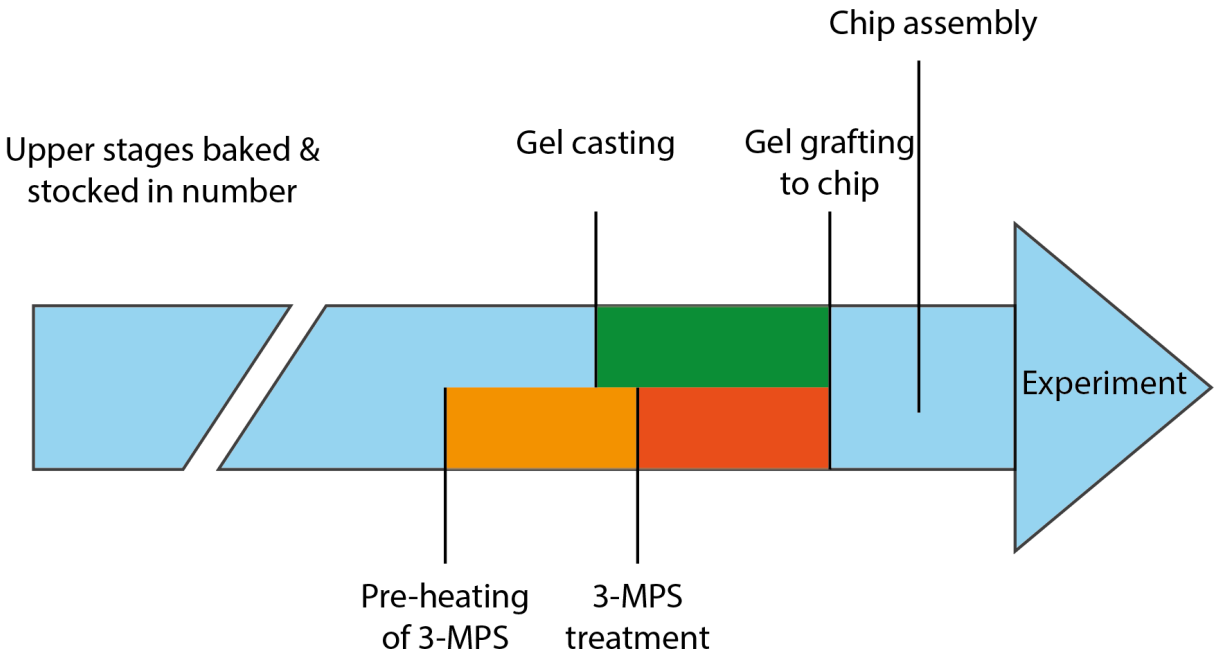

Figure 12: Assembly of the HAHLv1 chip.

d) HAHL v2 (self-contained design)

Later down the development cycle, a second design of the chip was identified in order to address to different shortcomings of V1. V2 did not rely on manually tightening the chip's stages together but sealing them with PDMS. In this configuration (HAHLv2), the chip is composed of (a) a glass coverslip, (b) a PDMS lower stage, (c) a hydrogel layer, and (d) a PDMS upper stage (see Figure 14).

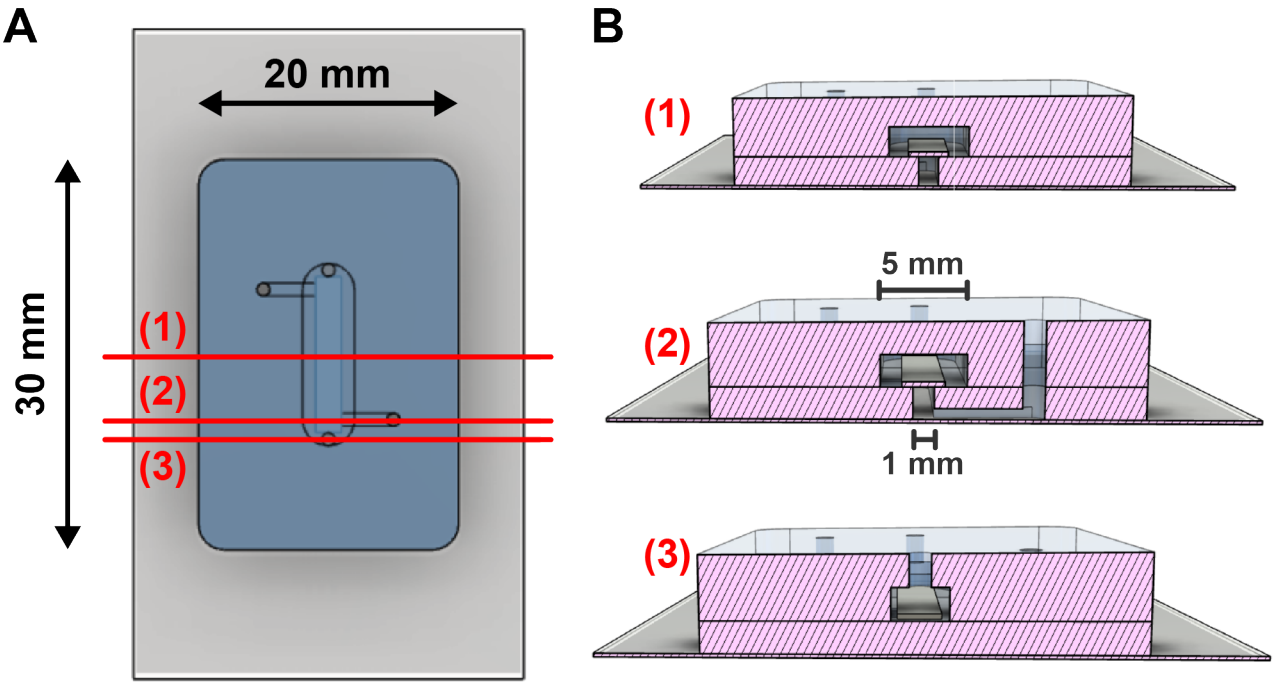

Figure 13: HAHLv2 design.

(A) Top view of the chip. (B) Cross section views of HAHLv2 chip.

PDMS parts

In this configuration, the lower PDMS stage was casted in a brass mold produced as described above. Briefly, it consists in a 1.5 mm deep, 20 mm wide, and 30 mm long pool, in the middle of which is the imprint of the lower channel. On two opposite corners of the pool, round extensions are placed to allow excess PDMS to overflow. The central channel is 1 mm wide, 10 mm long, and 1.5 mm high. On each end of it, an access channel spreads 5 mm to the side, and is 0.5 mm high (see Figure 15).

To properly level the lower stage, fresh PDMS is poured in the mold in slight excess, and a Sigmacote (“SL2”, Sigma-Aldrich) treated slab of PDMS is gently pressed over the mold. A small weight is added on top to maintain it in position. After curing of the PDMS, the lower stage is easily retrieved from the sandwich.

In a second time, 1.5 mm diameter inlets and outlets are punched at the end of the access channels, and the lower stage is bound to a glass coverslip relying on the plasma-treatment protocol previously described.

Lastly, the surface of the lower stage is 3-MPS treated (as per already described protocol) to allow for later binding to the hydrogel layer.

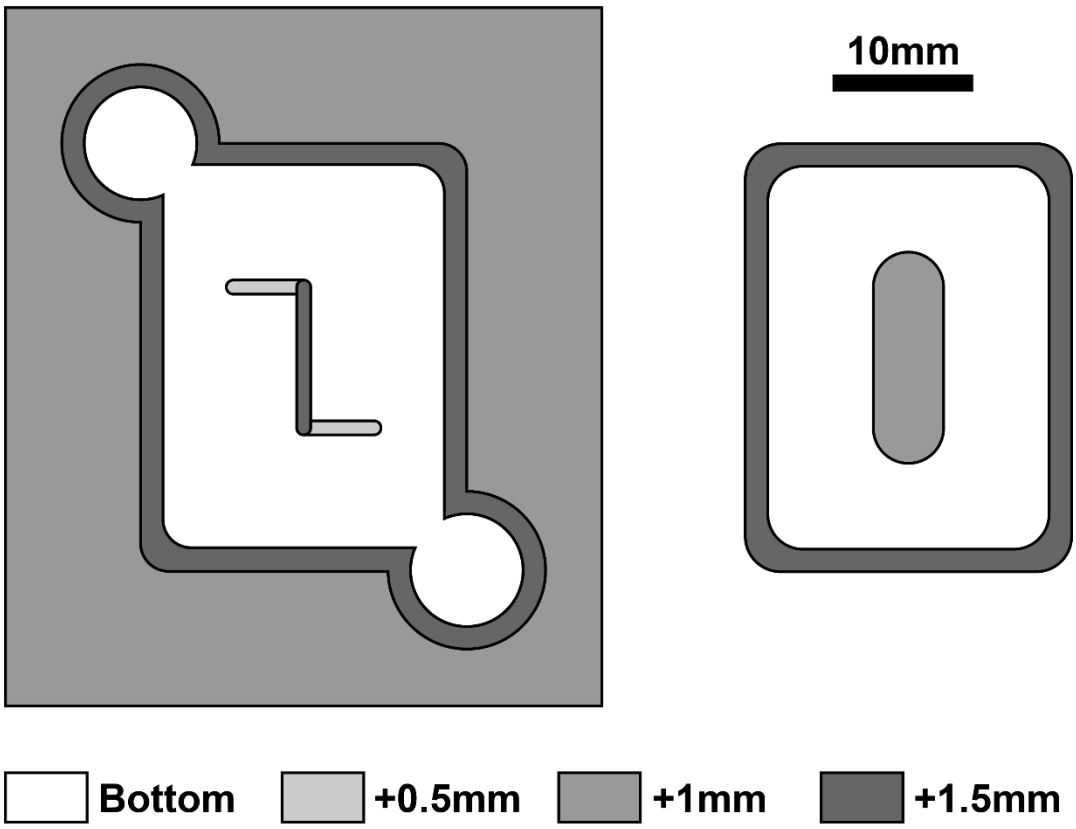

Figure 14: Mold for upper and lower stages of HAHLv2.

In the second version of the HAHL chip, the upper stage is much simpler, and 3D printed in resin as described above. It consists in one large hippodrome-shaped channel, measuring 1.5 mm in height, 5 mm in width, and 14 mm in length (see Figure 15). Evacuating excess fresh PDMS with a spatula proved sufficient to ensure a leveled top surface that does not affect imaging. Inlet and outlet are punched at each end of the channel.

Photolithography for the hydrogel mold

In the second version of the HAHL chip, the hydrogel layer has the shape of a hippodrome, 1 mm larger than the central channel. Briefly, it can be viewed as a 3 mm large, 10 mm long channel, with round ends (1.5 mm radius circles, centered on the central channel's end). The mold for casting the hydrogel layer was obtained by photolithography, with a mask in PMMA selectively cut with a laser-cutter.

Spin coating of SU8-2100 resin at 1700 rpm (with a first acceleration period of 100 $rpm.s^{-1}$ up to 500 rpm, a 5" waiting phase, and final acceleration at 300 $rpm.s^{-1}$) allowed us to produce 196 ± 8 µm thick molds for hydrogel casting. A soft bake (6'20" at 65 °C, 39'20" at 50 °C) made the resin hard enough to be put under the mask aligner, and UV exposure at 379 $mJ.cm^{-2}$ for 28" allowed the resin to crosslink where exposed through the mask. This was followed by a post-exposure bake (5' 00" at 65 °C, 13' 45" at 95 °C), and removal of non-crosslinked resin by immersion for 16' 20" in an agitated bath of propylene glycol monomethyl ether acetate (PGMEA). Molds were then rinsed with isopropanol, dried, and underwent a 30' hard bake to get rid of the cracks in the resin.

Hydrogel layer

The hydrogel layer is formed in sandwich between a flat slab of PDMS, and another imprinted with the design of the hippodrome produced by pouring fresh PDMS over a photolithography mold obtained as described above. Both PDMS slabs being treated with Sigmacote ("SL2", Sigma-Aldrich, Germany).

An inlet and an outlet were punched at each end of the hippodrome imprinted PDMS slab. To form the hydrogel layer, the two slabs and put on one another, and fresh hydrogel mix is poured in the inlet until overflowing on the other end. The sandwich is put to incubate for 45 min at 37 °C. Once fully gelled, the two slabs are separated (the hydrogel layer spontaneously stays in the hippodrome), and a thin dentistry spatula is used to detach the gel from the inlet/outlet and from the borders.

The hydrogel in its pool can then be transferred on top of the lower stage, gently pressed, and the PDMS slab can be removed after 20-30 seconds. A drop of DPBS is deposited over the hydrogel layer to avoid drought, for 5 to 10 minutes, until the hydrogel is considered definitively bound to the lower stage of the chip.

Assembly

Provided that the upper stages of the PDMS are produced and stored in numbers beforehand, the chip can be assembled in a few hours. Typically, 2 hours prior to including the chip in a microfluidic system, 3MPS is pre-heated in a vacuum

chamber to start the PDMS-hydrogel binding protocol described earlier. Then, gel mixes are prepared, and casted in their PDMS molds. Ten minutes later (that is, 35 min prior to the end of gel incubation time), the upper stages of the chips are placed in vacuum chambers and exposed to 3MPS vapors for 30 min. Past that time, the chips are left to cool down 5 min in the bio safety cabinet. Finally, the hydrogel discs are taken from their molds as described above, and placed on the chip.

Once the hydrogel is bound to the PDMS lower stage, the whole chip can be assembled. To bind the lower and upper PDMS stages, a very thin layer of fresh PDMS is spread over the lower surface of the upper stage, using a thin spatula. Then, the two stages are joint together, and put in the incubator for at least 1h. Past that time, the chip can be connected to a microfluidic setup and loaded with medium/DPBS.

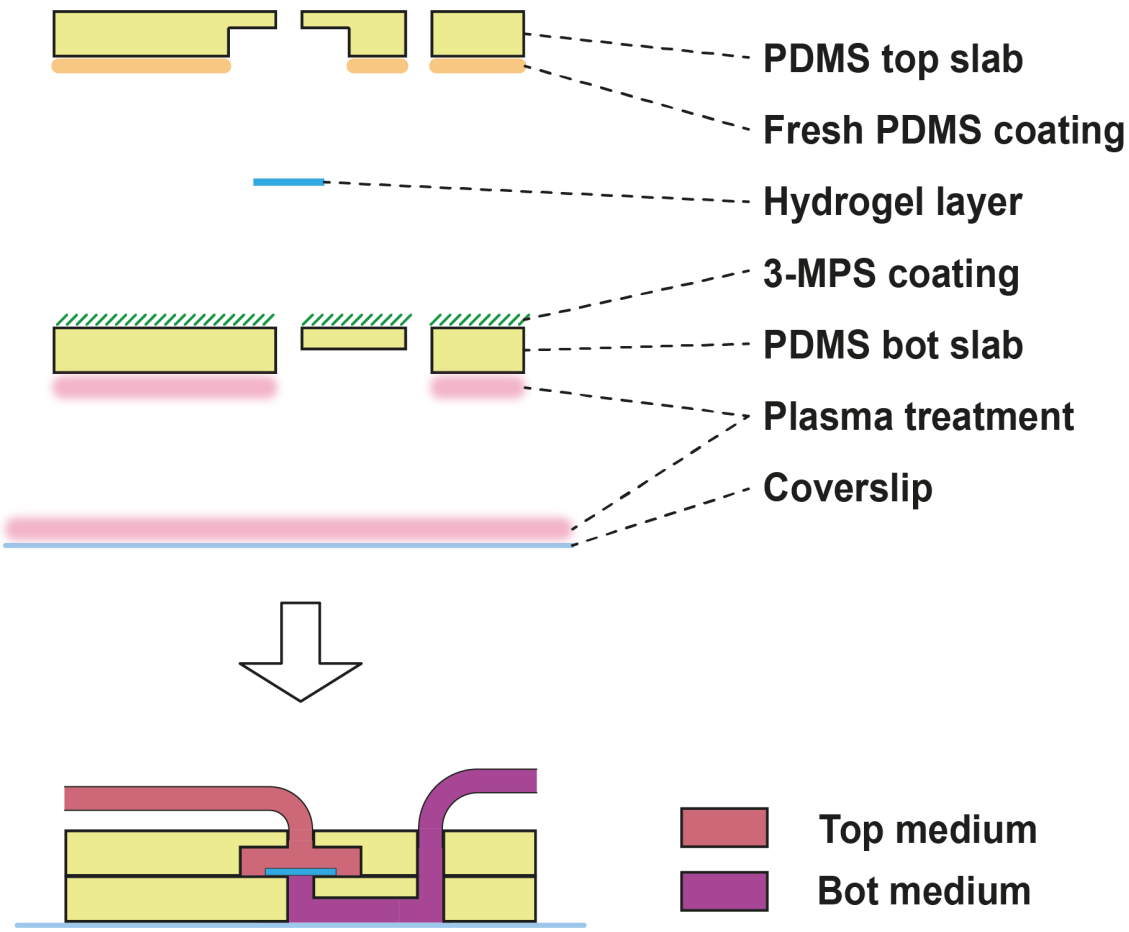

Figure 15: HAHL v2 system assembly.

Assembly of the HAHLv2 chip requires, in order: (a) plasma bonding of the bottom slab of PDMS on a coverslip, (b) 3MPS treatment of the bottom slab, (c) grafting of the hydrogel layer, and (d) addition of the top slab of PDMS with a thin layer of fresh PDMS as joint.

3 – FLOW AND PRESSURE CONTROL

The actuation principle behind the HAHL chip is as follow. Instead of relying on side vacuum chambers to produce deformation of the channel's walls, we rely on a differential of pressure between the two channels to deform the hydrogel layer that separates them. When this pressure differential is null (pressures are equal), the hydrogel layers remains in its resting state. When one channel experiences higher pressure conditions than the other, the hydrogel layer will be deformed, as shown in Figure 16 below.

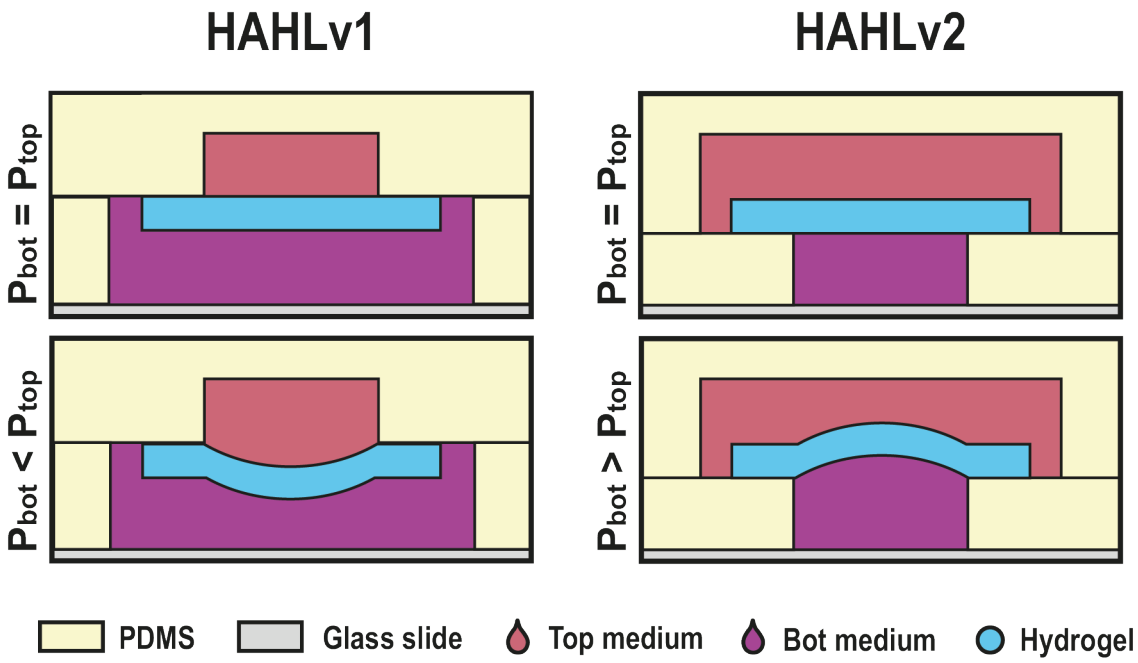

Figure 16: HAHL chip actuation principle.

Pressure differential between the channels leads to deformation of the hydrogel layer separating them.

a) Use of microfluidic resistance

In any microfluidic system, pressure (P), resistance (R), and flow (Q) relate to each other according to the following equation:

$$Q = \frac{P}{R}$$

In a flow-driven microfluidic system (that is, when the experimenter controls syringe pumps, and inject a liquid in the microfluidic channels), the pressure in one point of the circuit will depend on the microfluidic resistance brought by all the elements downstream of that point. The implication is that, if the resistance brought by the microfluidic chip itself (or the part of it of interest) is non-negligible compared to the resistance downstream of the chip, the pressure conditions might not be comparable everywhere within the device. A common way to palliate the problem consists in the addition of a resistance element, downstream of the chip, with a resistance such that all upstream elements amount for a negligible resistance in comparison, so that the pressure in all points upstream of it is sensibly the same. Obtaining a specific pressure of interest, at a flow of interest, can be done by carefully choosing the resistance added downstream of the chip.

In the case of a cylindrical channel, assuming its length (L) being much greater than its diameter (D), the resistance exerted by a tubing on a fluid of known dynamic viscosity (μ) can be approximated with the following formula:

$$R = \frac{128\mu L}{\pi D^4}$$

In the case of a rectangular channel of known length (L), width (w), and height (h), with $w > h$ and assuming $L \gg w$, the resistance exerted by a tubing on a fluid of known dynamic viscosity (μ) can be approximated with the following formula:

$$R = \frac{1}{1 - 0.63\frac{h}{w}} \times \left(\frac{12\mu L}{h^3 w}\right)$$

b) Microfluidic hardware

In total, three different microfluidic setups were used, as we improved the system. In its first version, the perfusion was performed with a Nemesys syringe pump (CETONI, Germany) controlled by a dedicated software (“Elements”, CETONI, Germany), and relied on the base resistance of the chip to impact the pressure differential between each side of the hydrogel layer (Figure 17A).

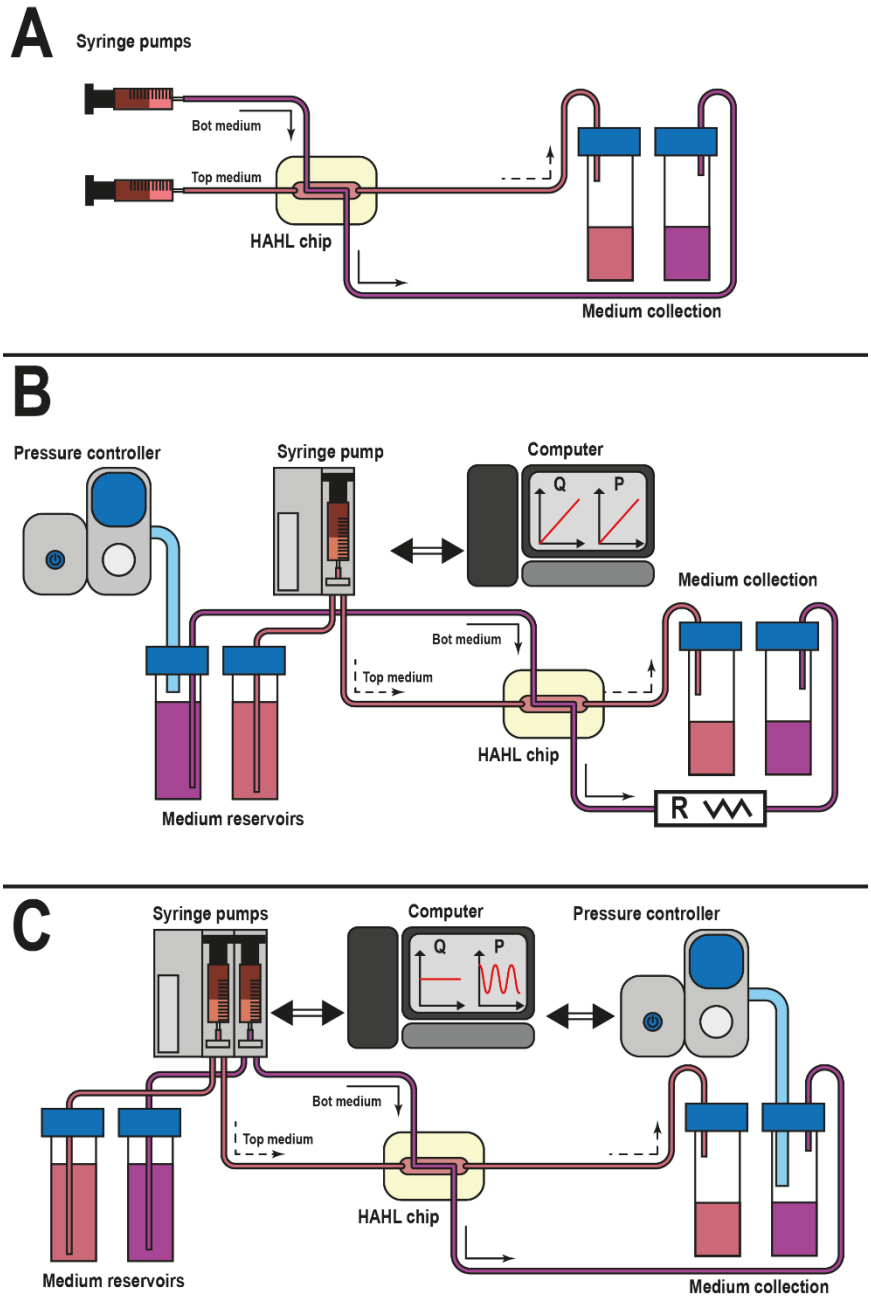

Figure 17: HAHL microfluidic setups.

Schematic resume of the three microfluidic tested to produce actuation of a hydrogel layer on a chip. ***(A)*** *Without downstream resistance.* ***(B)*** *Control of the flow in the high-pressure channel through a pressure controller. The flow is adjusted to relevant levels by addition of a downstream microfluidic resistance.* ***(C)*** *Independent control of flow and pressure. In this setup, syringe-pumps are placed upstream of the chip and delivers a controlled flow to both channels. The media are collected downstream in reservoirs. One of them is put under pressure, controlled by a Flow EZ module, leading to actuation of the hydrogel layer independently of the flows.*

Addition of downstream microfluidic resistances was not compatible with a flow-driven setup, as it led to many hydrogel layer ruptures. We adapted by developing a second microfluidic setup, in which the flow in one of the channels is driven by a pressure controller (“LINEUP Flow EZ module”, Fluigent, France) and associated software (“MAT”, Fluigent, France). In that setup, relevant flows were attained by adding thin fused silica tubing (Trajan Scientific and Medical, Australia) downstream of the chip for added resistance. Here, flow is directly linked to pressure and cannot be controlled independently.

Finally, we pursued independent control over flow and pressure, and developed a third setup in which the chip is linked to both a syringe-pump controller and a pressure controller, on each end of the tubing. In detail, a syringe-pump is placed upstream of the chip and delivers a controlled flow. The medium is collected downstream in a reservoir that is put under pressure, controlled by a Flow EZ module. This system allowed for the precise control of the hydrogel deformation under pressure while maintaining a physiological flow rate.

4 – MAPPING HYDROGEL DEFORMATION

As PEG hydrogels are optically clear, mapping their deformation cannot be achieved without placing within (or on) it markers which positions can be tracked. In our experiments, we relied on microscopic fluorescent beads (Fluoro-Max R200, Thermo Fischer Scientific, USA) at a final concentration of 1 drop diluted in 2 mL of buffer, that we included in the fresh mix to visualize stretching of the hydrogel layer. Moreover, it is much harder under a microscope to follow the vertical displacement of beads compared to their lateral displacement. Prior to investigating the deformation in 3D, we tried to approximate it relying only images obtained in 2D. The protocols for each approach are detailed below.

All images were acquired using an Axio Observer Z1 inverted microscope (Carl Zeiss, Germany), mounted with 5x (EC Plan Neofluar 5x/0.16 Ph1 M27), 10x (Fluar 10x/0.5 M27) objectives.

a) Following bead couples

Prior to fine mapping of the hydrogel deformation, conditions could still be compared by tracking beads placed roughly in the same part of the hydrogel. Since the median region of the hydrogel, along the long axis of the channel, was expected to remain locally quasi-horizontal, we decided to track bead couples in this region. This was done at 10x magnification, as the pressure differential increased, and for various downstream resistance conditions.

b) Automatizing the process

As manually tracking specific beads through their 3D displacement under a microscope is tedious and time consuming, we tried to automatize the procedure. To achieve that, we observed the channel at 5x magnification, so that most beads could remain in-focus even during the deformation of the hydrogel layer. Doing so, hundreds of beads could be followed at the same time, relying on ImageJ's TrackMate plugin (NIH, USA).

Briefly, shots were taken with the channel's main axis along the horizontal (X) axis of the image. Using TrackMate plugin, beads were followed through the deformation of the hydrogel going from 0 mbar to 35 mbar of pressure differential between the sides of the hydrogel. Their displacement along the vertical (Y) axis can be plotted as a function of their original Y position.

c) Fine mapping of the deformation

A more detailed approach was also tested, relying on the help of the BioImaging Analysis hub of the Institut Pasteur. This attempt explores the local deformations of the hydrogel. Notably, the lateral verges of the hydrogel were not expected to behave in the same fashion as the center of the channel. Moreover, difference could also be expected between the high pressure and the low pressure side of the channel.

To track bead displacement in 3D, Z-stacks were acquired for several pressure differentials (0, 5, 10, 15, 20, 25, 30, 35 mbar) covering the entirety of the hydrogel's height (163 stacks at 5x magnification, with 2 µm voxel height). Relying on TrackMate's plugin on ImageJ, single beads can be tracked over the deformation of the hydrogel layer. All analysis performed afterward rely on scripts written for MATLAB (MathWorks, USA).

To simplify the 3D analysis, we focused on the tangential strain at the surface of the hydrogel. Briefly, an alpha-shape of the layer was extracted, and Delaunay triangulation yielded a mesh of its surfaces. Considering the first position (0 mbar) to be the reference, we were able to explore changes in the area of the triangles composing the mesh. Sibson interpolation of these measures was used to report, on the initial coordinates of a point on the surface of the hydrogel layer, the tangential strain it will undergo as the pressure differential increases.

5 – CELL CULTURE

a) Cell culture

Caco-2/TC7

Caco-2/TC7 cells were obtained from ATCC (USA). The cells were expanded and maintained in 75 cm² flasks in GlutaMAX DMEM (Gibco), supplemented with 10% FBS (Gibco) and 1X penicillin/streptomycin (Sigma-Aldrich). The flasks were kept in an incubator (37 °C, 5% CO2, 80% RH) with medium changes every two days. Before cells reached confluence, which was approximately every five days, cells were detached relying on DPBS rinsing followed by exposure to 2 mL of 0.05% trypsin solution (Sigma-Aldrich), and 10% of the cells collected in suspension were passed into a new flask.

Cholangiocytes

Normal rat cholangiocytes (NRC) were obtained from N. LaRusseo's laboratory[332]. The cells were expanded and maintained on collagen coated T72 flasks with DMEM F12 medium supplemented with 5% FBS (Life Technologies), 1X penicillin/streptomycin (Sigma-Aldrich). Growth factors were added as described by de Groen and colleagues[333]. Briefly, the growth factor mix includes Insulin (Life Technologies), Dexamethasone (Sigma-Aldrich), 3,3,5-Triiodo-L-Thyronine sodium salt (Sigma-Aldrich), and bovine pituitary extract (BPE). The flasks were kept in an incubator (37 °C, 5% CO2, 80% RH) with medium changes every two days. Before cells reached confluence, cells were detached relying on DPBS rinsing followed by exposure to 1 mL of 0.05% trypsin solution (Sigma-Aldrich), and cells collected in suspension were passed into a new flask.

b) Cell banking in liquid Nitrogen

To rely on a source of cells from the same passage, they were banked in liquid Nitrogen. To do so, cells were suspended in their medium at a concentration of approx. 10^6 cells/mL. 1 mL of the cell solution was mixed with 4.4 mL of FBS, and 0.6 mL of dimethyl sulfoxide (DMSO). This suspension was put in a vial, in a slow-cooling container ("Mr. Frosty", Sigma-Aldrich, Germany) and stored at -80 °C overnight. Then, the vials were transferred to a liquid Nitrogen tank.

Prior to their use in an experiment, cells were retrieved by rapid thawing in a 37 °C hot water bath, and immediately seeded in a T75 flask with 10 mL medium. After a few hours, medium was replaced with fresh one.

c) Hydrogel cell adhesion assay

Most of the experiments presented here rely on a common Matrigel (Corning, USA) coating diluted to 150 µg/mL. However, we also tested a variety of adhesion-triggering molecules, in coating or included in the gel. Briefly, we tested FnPEG included in the hydrogel mix or coated in the channel after chip assembly, and Matrigel

mixed or not with collagen type I (“CellMatrix type 1-P”, Fujifilm WAKO, Japan) in three different concentrations.

For this experiment, ten 200 µL discs of 5% w/v PEG10-10 hydrogel were made between two Sigmacote treated glass slides. Three of them contained FnPEG at 0.1, 0.2, or 0.5 mg.mL^{-1} concentration. After gelling, small drops (20 µL) of the same hydrogel recipe (without FnPEG) were deposited at the bottom of a 24 well plate, and the hydrogel discs deposited on top. This ensure that the hydrogels would stick to the bottom of the well, and not float when medium is added. Then, the seven discs that did not include FnPEG in their bulk were coated by being immersed in solutions containing either FnPEG (0.1, 0.2, 0.5, or 1.0 mg.mL^{-1}) or a Matrigel/Collagen mix (50/100, 100/50, or 150/0 µg.mL^{-1}). After 1h in solution, the discs were rinsed several times with PBS, and submerged in culture medium (DMEM, +10%FBS, +1X Penicillin/Streptomycin). All were seeded with the same concentration of cells, near confluence.

Two hours after seeding time, the medium was changed, trying not to create too much turbulences, and bright field images were taken at 10x magnification, in three different positions of each disc. The procedure was repeated 24h after seeding. Then, a mask was drawn on Photoshop (Adobe) to compute the portion of the imaged hydrogel covered by adherent cells.

6 – BIOLOGY ON HAHL CHIPS

a) HAHL chip biocompatibility assessment

To assess the biocompatibility of our initial protocol, we performed a Live/Dead assay. Briefly, four HAHLv1 chips (high-pressure channel on top) were prepared as previously described. The hydrogel recipe used corresponds to a 5% (w/v) PEG10-10 network, in stoichiometric ratio, with the addition of 100 µM RGD peptide. After assembly, the upper channel was fill with 150 µg/mL Matrigel solution to help cell adhesion, and left to rest overnight. After that, the chips were rinsed in DPBS 3 times.

Caco-2/TC7 cells were seeded in the upper channel of the chips, at a near-confluence density of 0.5 10^6 cell/cm². After 2h of sedimentation, the medium was gently changed, and the cells were left to rest overnight. 24h after seeding, we performed the Live/Dead assay as per manufacturer's instructions ("LIVE/DEAD viability/cytotoxicity kit", Thermo Fischer Scientific, USA). Live and dead cells were then counted using Icy's spot detector (http://icy.bioimageanalysis.org).

b) Producing a structured Caco-2 epithelium on HAHL chip

HAHL chip preparation

HAHL chips (v1) were prepared as previously described. The hydrogel recipe used corresponds to a 5% (w/v) PEG10-10 network, in stoichiometric ratio, with the addition of 100 µM RGD peptide. After assembly, the upper channel was fill with 150 µg/mL Matrigel solution to help cell adhesion, and left to rest overnight. After that, the chips were rinsed in DPBS 3 times.

On-chip cell culture

Caco-2/TC7 cells were seeded in the upper channel of the chips, at a near-confluence density of 0.5 10^6 cell/cm². The seeding moment is noted as Day0, Hour0. After seeding, cells are let to rest 6h to sediment and attach to the hydrogel. Past that time, the chip was connected to the microfluidic setup, and the cells could be submitted to various stretch and flow conditions.

Notably, we explored several flow and stretch conditions. Three included a continuous flow without strain. Two other consisted of a constant flow, with the addition of pressure variations, either relying on a "pressure-controlled" setup or one with independent control of flow and pressure. Other conditions were tried, without enough replicates to be reported here.

The "continuous" conditions consisted in a setup driven by syringe pumps, without any resistance downstream of the microfluidic chip. Starting H6, the chip was submitted to a constant flow of either 30, 100, or 200 µL.h^{-1}.

The “decoupled” condition consisted in a setup in which a 100 µL.h^{-1} flow is controlled by a syringe pump upstream of the chip, while a pressure controller imposes a sinusoidal cycle pressure, at 0.1Hz frequency, ranging from 1 mbar to 31 mbar.

All conditions were maintained for at least 6 days, with microscopy images taken at least at D1, D4, and D6. At D6, chips could undergo various further experiments.

c) HAHL chip barrier function assays: Apparent permeability

Apparent permeability

Depending on the setup (*e.g.* static or dynamic), several equations have been designed to quantify and compare the barrier functions of various tissues. In the case of dynamic flow on both sides of a permeable barrier, it is possible to get rid of the time component, and relate only to the flows in donor channel (Q_d) initially loaded with a known molecule and in the receiver channel (Q_r) initially void of said molecule, as well as to the surface of exchange (S) and the concentrations of the molecule of interest downstream of the barrier in both the donor and receiver channels (C_d and C_r respectively). The apparent permeability (P_{app}) of the wall separating the two perfused channels can be expressed as[334]:

$$P_{app} = -\frac{Q_r Q_d}{S(Q_r + Q_d)} * ln\left[1 - \frac{C_r(Q_r + Q_d)}{Q_r C_r + Q_d C_d}\right]$$

Practically, thirteen chips (HAHLv1) were prepared for this experiment. All included the same hydrogel recipe: a 5% (w/v) PEG10-10 network, in stoichiometric ratio, with the addition of 100 µM RGD peptide. Three of them hosted Caco-2/TC7 cells following the protocol described above, and spent 6 days maturing under a continuous 100 µL.h^{-1} flow. Prior to the experiment, two 10 min PBS washes were done to rinse the chip from anything that could alter the readout.

For the assay, the chips were perfused with PBS solutions containing 1 $mg.mL^{-1}$ of Fluorescein isothiocyanate-Carboxymethyl-Dextran (“FITC Dextran”, Sigma-Aldrich) in their upper channel, while the lower channel was perfused with PBS alone. Three chips were perfused with 70 kDa FITC Dextran, three with 20 kDa FITC Dextran, and seven, among which the three chips hosting a Caco-2/TC7 epithelium, were perfused with 4 kDa FITC Dextran.

After 1h of perfusion, the collected PBS was discarded, as we did not consider that the system had reached equilibrium yet. After at least three more hours, PBS was collected from Eppendorfs downstream of both upper and lower channels, and fluorescence read for 490nm excitation using a spectrophotometer (“NanoDrop 2000”, Thermo Fischer Scientific, USA). The readout was compared to a standard established in parallel of the experiment.

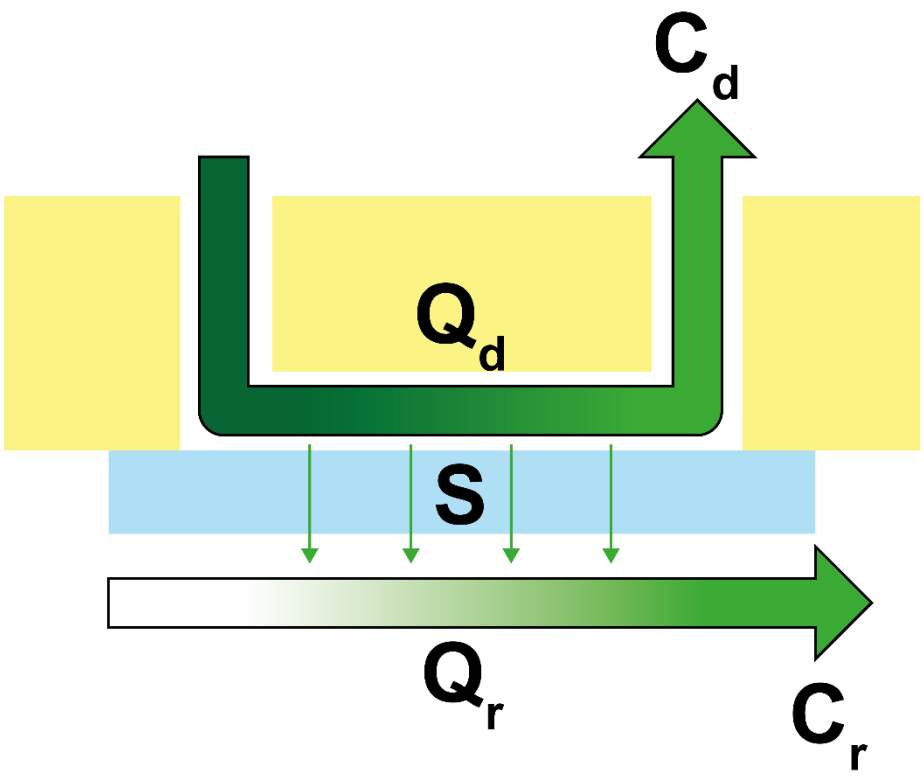

Figure 18: Principle of apparent permeability assay.

*Knowing the flows in donor channel (**Qd**), receiver channel (**Qr**), and the surface of exchange (**S**), one can deduce the apparent permeability of the barrier covering the surface from the repartition of concentration of a molecule of interest between the donor (**Cd**) and receiver channels (**Cr**).*

7 – IMAGING HAHL CHIP

a) Bright field imaging

Bright field images were acquired using an Axio Observer Z1 inverted microscope (Carl Zeiss, Germany), mounted with 5x (EC Plan Neofluar 5x/0.16 Ph1 M27), 10x (Fluar 10x/0.5 M27), 20x (EC Plan Neofluar 20x/0.5 Ph2 M27), and 63x (LD Plan-Neofluar 63x/0.75 Korr M27) objectives (Carl Zeiss, Germany).

b) Immunofluorescence of epithelial tissue

Immunostaining protocol

At D6, HAHLv1 chips were retrieved from the microfluidic setup, and washed with PBS twice for 10 min. Then, the tissue was fixed with 4% paraformaldehyde (Thermo Fischer Scientific, USA) for 20 min, and washed thrice in PBS for 10 min. Following fixation, the samples were permeabilized with 0.5% Triton X-100 in PBS for 20 min, and washed thrice with PBS for 10 min. Prior to staining, the samples spent at least 2h at 4 °C in a blocking solution, composed of 2% w/v Bovine Serum Albumin (BSA, Sigma-Aldrich, Germany) and 0.2% Triton X-100, in PBS.

Immunolabeling was done relying on the same working solution, composed of 0.5% w/v BSA and 0.2% Triton X-100, in PBS for both primary and secondary antibodies. Primary antibody was incubated overnight at 4 °C (5 µg/mL anti-ECadherin goat antibodies AF748, R&D systems, USA). Secondary antibody (donkey anti-goat A-21432, Invitrogen, 10 µg/mL), phalloidin (10 µg/mL) and DAPI were incubated 2h at 4 °C.

Sample preparation

First attempts at imaging epitheliums upright proved difficult, due to the added thickness brought by the hydrogel layer, limiting the exploration of the tissue placed above. Epithelium placed upside down without embedding in hydrogel was impossible

to image, since the structures would progressively be crushed under the weight of the hydrogel layer, leading to a visible shift across channels when building the composite image. To solve the issue, we developed an embedding protocol to help maintain the structure's shape. Since in 5% PEG10-10 does not swell, it allowed to stabilize the structures over time, without noticeable alteration of morphology.

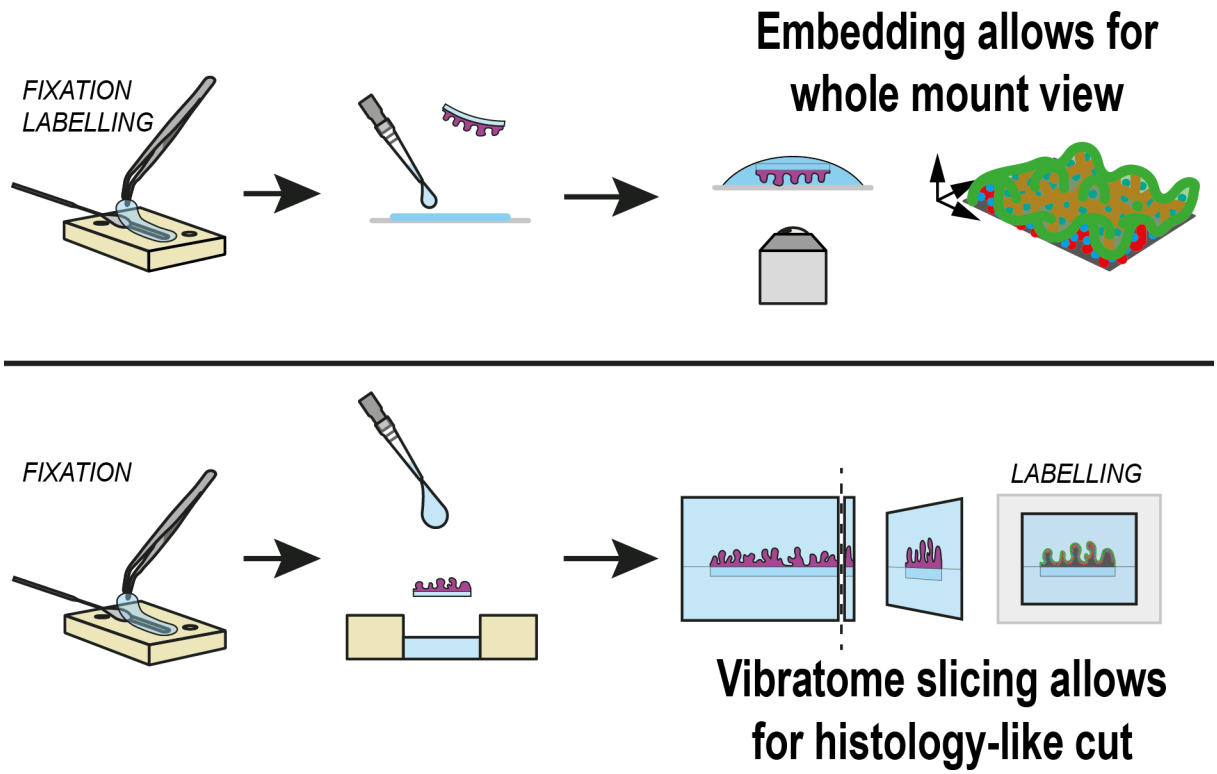

Figure 19: Embedding allows for whole mount and slice views.

Top: *Depositing the hydrogel layer with cells facing downward on a fresh hydrogel droplet allows to embed it, and to preserve its morphology for long sessions of confocal imaging.* ***Bot:*** *Embedding the sample in between two hydrogel layers preserves its morphology and allows for vibratome slicing of the sample.*

Briefly, 100 µL of 5% w/v PEG10-10 hydrogel mix was prepared. As soon as the mix was done, the hydrogel layer was gently detached from the chip using a thin spatula and Brucelle tweezers and deposited upside-down over a thin drop of hydrogel mix placed on a glass cover slip, as depicted in Figure 19. Since this specific hydrogel recipe has a Mass gain ratio close to 1, it gels without gaining in mass or volume. Thus, the structures can be preserved for later observation.

A protocol was also in development to allow to mount cuts for microscopy imaging, in a fashion similar to that described by Altay and colleagues[335]. Briefly, 400 µL of 5%

w/v PEG10-10 were placed in a 16 mm diameter PDMS pool to form a roughly 2 mm thick disc after gelling. Later, the sample was gently detached from the chip using a thin spatula and Brucelle tweezers and deposited the hydrogel disc, still in its mold, as depicted in Figure 19. Then, 400 µL of fresh hydrogel mix were poured over to embed the sample within the hydrogel. The resulting disc was then sectioned using a vibratome (Leica VT 1200S, Leica Biosystems). Various parameters (amplitude, velocity, frequency) were promptly screened, to select the set of values reported in Figure 20.

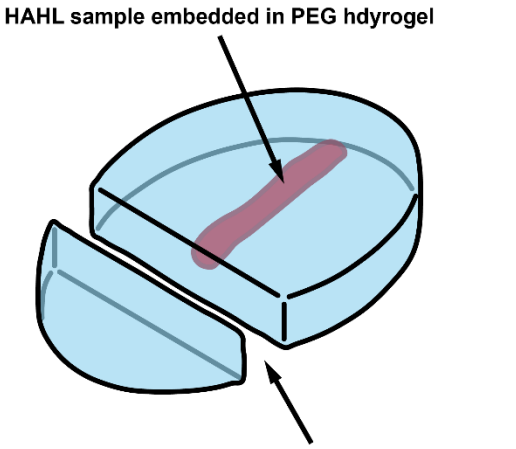

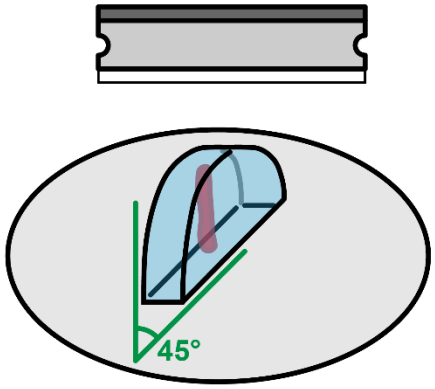

Dry% / thickness	5%	10%
200 µm	easy	easy
150 µm	easy	easy
100 µm	very hard	easy
50 µm	very hard	hard

Optimal parameters	
Amplitude	0.9-1.0 mm
Velocity	1 mm.s^{-1}
Frequency	81 Hz
Thickness	150 µm

Figure 20: Optimal parameters for vibratome slicing protocol.

Top left: *to maintain in place the sample during vibratome slicing, the disc is cut clean to provide a smooth surface that can be glued to the stage.* ***Top right:*** *to ease the slicing, the sampled is fixed at an angle of roughly 45° from the axis of progression of the blade.* ***Bottom left:*** *reported difficulty to obtain cuts of a given thickness from 5 or 10% PEG10-10 hydrogels.* ***Bottom right:*** *Optimal parameters retained to produce cuts from 5% PEG10-10 hydrogels.*

Practically, the disc sample is cut clean to provide a smooth surface that can be glued to the vibratome stage, at a 45° angle relative to the direction of progression of the blade. Said blade is set to vibrate at 81 Hz frequency, with a 0.9-1 mm amplitude, and progressing at 1 mm per second. These parameters allowed us to easily produce cuts down to 150 µm of 5% PEG10-10 hydrogel. This thickness can go down to 100 µm in 10% hydrogel. Lower thickness were either hard to cut, or hard to retrieve without damaging them.

Microscopy imaging

Images were taken on an inverted confocal microscope (TCS SP8 MP, Leica Microsystems, Germany) mounted with a white light laser and relying on dedicated software (LASX). Two types of images were taken: cross section at approximately mid height of the structures, and Z-stacks of the whole height of the sample. Images were taken with either a dry 10x objective ("HC PL APO CS2 10x 0.4 DRY", Leica) or a 20x immersion objective ("HC PL APO CS2 20x 0.75 IMM", Leica)

c) Scanning Electron Microscopy

Prior to explore the feasibility of observing samples from our chip under scanning electron microscopy (SEM), we first assessed the behavior of our PEG hydrogels in ethanol baths. Indeed, critical point SEM requires such baths, and we wanted to know if our samples would end up deformed.

Submitting PEG hydrogels to ethanol baths

Eight hydrogel samples were produced by casting 70 µL of hydrogel mix in between two Sigmacote-treated glass slides, separated by 1 mm spacers. All of them were 5% (w/v) PEG10-10 in stoichiometric ratio. After gelling, 4 were put in ultra-pure water, as would have been a biological sample, and 4 in ethanol. After being let to swell overnight, their diameter were measured with microphotographs. The 4 discs who swelled in ultra-pure water then underwent successive 20 min baths with ethanol in increasing concentration (25%, 50%, 75%, and 100%), while their diameter were

measured after each bath. This way, we could detect any gain or loss in size if it were to be affected by the baths.

SEM protocol

Previously fixed sampled of Caco-2/TC7 epithelium cultured in HAHLv1 chips under constant 30 µL.h^{-1} flow for 6 days were used as trials to assess to possibility to visualize samples in SEM. First, they were fixed on a coverslip using fresh 5% w/v PEG10-10, with the epithelium facing up. Samples spent one night in 2.5% Glutaraldehyde (Sigma-Aldrich, Germany) in PHEM buffer 1X (prepared by the institute's Ultrastructural BioImaging unit), then rinsed 3x10 min in PHEM buffer 1X. Post-fixation was done using 1%OsO4 in ultrapure water for 1h at ambient temperature.

Dehydration of the sample was obtained by successive baths in increasing concentrations of ethanol, as described above. Critical point desiccation was done in CO2 using a CPD300 (Leica, Germany). The dry sample was metallized in an ionized argon beam coater ("Model 681", Gatan, USA) used in the 2-8kV range, leading to the deposition of approx. 15nm of Gold/Palladium. Finally, the metallized sample was observed using the secondary electron detector of a JSM 6700F scanning electron microscope (JEOL, Japan) (1.6 10^{-6} Pa, 10 µA emission, 5kV acceleration tension).

8 – 3D CELL CULTURE

a) Formation of NRC cysts

Encapsulation

We encapsulated NRCs within the bulk of several PEG40-16R and PEG40-16A hydrogels, with dry content ranging from 2.5 to 6.5%, and varying concentrations of RGD (0 µM, 100 µM, 120 µM). Hydrogels were prepared as described above, with HEPES replacing TEA as a solvent. NRCs were seeded at a concentration of 1.5 x 10^{6}cells/mL. Before gelation of the hydrogels, 50 µL discs were formed in between

mirror-polished PTFE blocks separated by 1 mm spacers, then placed to incubate (37 °C, 100% RH, 30 min). Upon crosslinking, gel disks were demolded and transferred to a 12 well plate (Corning) loaded with the adequate cell culture medium.

The same cells were also encapsulated in Matrigel, in two steps. First, NRCs were mixed in 7 $mg.mL^{-1}$ growth factor reduced Matrigel (Corning) at 6 x 10^5 cells/mL. Then, the solution was diluted to 3.5 $mg.mL^{-1}$ Matrigel (3 × 10^5 cells/mL) with NRC complete medium which was cooled on ice beforehand. 300 µL of Cell/Matrigel solution was deposited in each wells of an 8-well micro-slide which had previously been coated with 50 µL of 3.5 $mg.mL^{-1}$ Matrigel. The micro-slide was incubated for 15 min (37 °C, 5%CO2) before addition of medium.

Cell viability in PEG hydrogels

PEG hydrogels and Matrigel were washed with PBS and then incubated for 30 min at 37 °C, 5% CO2 with 4µM Ethidium homodimer-1 and 2µM Calcein, AM (ThermoFisher scientific) in growth medium. After a second washing step, the gels were imaged as described below. In average 12 images were acquired per condition. Fluorescence intensity was measured after background correction and normalized for the variations in cyst surface using ImageJ, an image analysis software available on the NCBI website (https://imagej.nih.gov/ij/).

b) Cyst characterization

Immunostaining of encapsulated structures

Immunostaining was performed after 10 days of culture, without disrupting Matrigel or PEG hydrogels. PEG hydrogels were washed twice in PBS and fixed with 4% PFA overnight at 4 °C. Cysts were permeabilized with 0.5% Triton X-100 in PBS for 1–2 h at 4 °C and then blocked with 2% BSA, 0.1% Tween-20 in PBS for 3 h. The primary polyclonal anti-E-cadherin antibody (Thermo Fisher Scientific PA5-32178, 1: 400) was diluted in blocking solution and incubated for 2–4 days at 4 °C. Unbound primary antibodies were washed by incubating the gels in blocking buffer 3 times (10 min each). The secondary antibody Goat anti-Rabbit IgG (H+L), Alexa Fluor Plus 647

(Thermo Fisher Scientific A32733, 1:400) was diluted in blocking solution and incubated for 2–4 days at 4 °C. Nuclei and f-actin filaments were stained by adding 10 µM Hoechst and 16.5nM Phalloidin 488 (Thermo Fisher Scientific) in PBS containing 1% BSA. Gels were incubated for 2 days at 4 °C. Stained gels were then washed intensively in PBS. Matrigel hydrogels were washed with PBS and fixed with 4% paraformaldehyde and 5% sucrose in PBS. Cyst were permeabilized with 0.5% Triton X-100 in PBS for 30 min and then blocked with 0.1% BSA and 1% goat serum for 30 min at RT. The primary polyclonal anti-E-cadherin antibody (Thermo Fisher Scientific PA5-32178, 1:400) and 16.5nM Phalloidin 488 (Thermo Fisher Scientific) were diluted in blocking solution and incubated overnight at 4 °C.

Confocal imaging was performed on an SP8 inverted microscope (Leica Microsystems, Germany) equipped with HC FLUOTAR L 25×/0.95W 0.17 VISIR objective and a white laser system. Confocal imaging of cyst polarization in Matrigel was acquired with a confocal microscope Nikon Eclipse TE-2000-E equipped with an X20/0.45 Plan Fluor ELWD Ph1 DM objective (∞/0–2WD 7.4).

Rhodamine transport assay

Activity of the multidrug resistance protein 1 (MDR1) transporter was assessed relying on fluorescent rhodamine (“Rh123”, Sigma-Aldrich). In detail, both PEG and Matrigel were placed in a 50 µM rhodamine solution for 1h, followed by three washes in serum-free medium, and subsequent incubation for 2h in fresh complete medium. In a second experiment, inhibition of MDR1 transporter was assessed by exposure to 50 µM verapamil (Sigma-Aldrich) for 30 min, prior to exposure to rhodamine. The experiment then pursued as described above. In both experiments, we counted cysts for which rhodamine was located in the luminal space of around epithelium.

c) Impact of hydrogel recipe on cyst formation

We quantified and followed over time (D1, 2, 4, 7, 10) the formation and growth of NRC cysts in both Matrigel and PEG hydrogel of varying composition (2.5-6.5% dry content, 0-1200 µM RGD). For each condition, Z-stacks were taken from non-

overlapping regions within a hydrogel. Size and number of cysts were analyzed using Matlab image processing toolbox. Cyst formation frequency was determined by relating the cyst number per z-stack to the corresponding initial cell number per z-stack.

9 – STATISTICAL ANALYSIS

The data are presented in the figures as mean ± standard deviation. The error bars represent the standard deviations of at least three replicates. Statistical comparisons were performed using two sample Student's t-test, one-way ANOVA test, or two-way ANOVA tests according to conditions and as described later in the results. Prior to these parametric tests, normal distribution and homogeneity of variances were checked relying on Shapiro-Wilk and Bartlett tests, respectively. The data were processed with R software (R-4.1.1, R Project) and plotted with Adobe CS Illustrator (Adobe, USA).

Graphical representation of the p-values <0.001, < 0.01, and < 0.05 were noted ***, **, and * respectively.

SECTION III
RESULTS & DISCUSSION

1 – HYDROGELS

Developing an organ-on-chip including a hydrogel layer posed several challenges. Ideally, the selected hydrogel should not change in dimensions after being integrated in the chip, be able to form covalent bonds with the chip, have mechanical properties close to that of living tissues, and allow for cell encapsulation. That required use to investigate many recipes and gain in-depth understanding of the properties of our hydrogels. In this section, I will describe the pipeline we used to characterize mechanically and biochemically the synthetic PEG hydrogels we developed for 3D cell culture and inclusion in the HAHL chip.

a) Quality controls

Ellman's assay is a widely used test to determine the concentration of free thiols in a solution. It is based on the reduction of the disulfide bond of 5,5′-Disulfanediylbis(2-nitrobenzoic acid) (DTNB, also known as Ellman's reagent), releasing 2-nitro-5-thiobenzoate (TNB^-) in equimolar proportions with the thiol groups with which DTNB reacted. In neutral or alkaline pH, TNB^{2-} dianion yields colorimetric signal at 412 nm, which can be measured with a spectrophotometer. This method was used both to quantify the amount of free thiols in the 16W and 16R that we received, and to assess the kinetics of RGD to PEGVS, as reported below.

Free thiols in MMP sensitive peptides

As peptides bearing multiple thiol functions can have the tendency to engage in disulfide bonds, it was important to us to assess the extent of it, in order to adjust the volumes of each molecule when preparing the hydrogels. L-Cysteine hydrochloride used in solution as a cysteine standard yielded a correlation coefficient $R^2 = 0.9997$. This allowed us to assess the amount of free thiols in 12% (w/v) solutions of 16W and 16R, theoretically comprising 138.1 and 137.5 mM of thiol functions respectively, and according to their molecular weights. Optical density of 16W solution corresponded to 130.5 mM free thiols (94.5% of the theoretical amount), while 16R solution yielded

122.4 mM (89.1%) (See Figure 21). Note that the peptide solutions were diluted 200x to fall within the standard curve range.

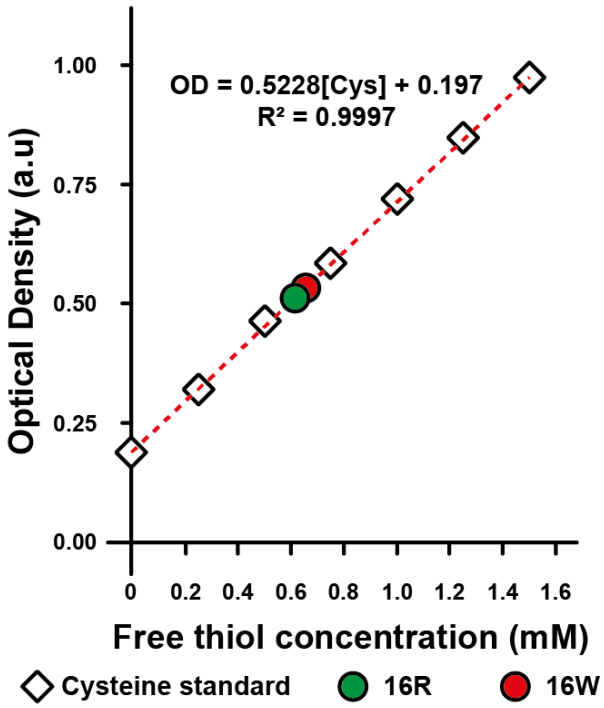

Figure 21: Quality control on 16R and 16W peptides.

Standard curve showing optical density of solution containing cysteine in increasing concentrations, compared to 12% (w/v) solutions of thiolated peptides.

Thiolated peptide to PEGVS binding kinetics

Standard curve established with cysteine yielded a 0.9996 R^2. This correlation coefficient remains above 0.97 even for concentrations lower than 200 µM, allowing us to work at these low concentrations (Figure 22B). Ellman's test performed on a 200 µM RGD stock solution yielded a colorimetric signal (412 nm) corresponding to 183 µM of free thiol groups according to the standard curve. This might indicate that roughly 8-9% of the peptides engaged in disulfide bonds, highlighting the need for short manipulation times when preparing hydrogels. Ellman's tests performed after putting RGD and vinyl-sulfone groups (brought by PEGVS) in equimolar proportions reveal a quick binding dynamic. The first test was done as soon as possible, which was roughly 3 minutes after mixing. At that time point, 43.4% of the thiol groups remained available. For the 15, 30, and 60 minutes time points, this portion was reduced to 4%, 5%, and 4.3% respectively (Figure 22C).

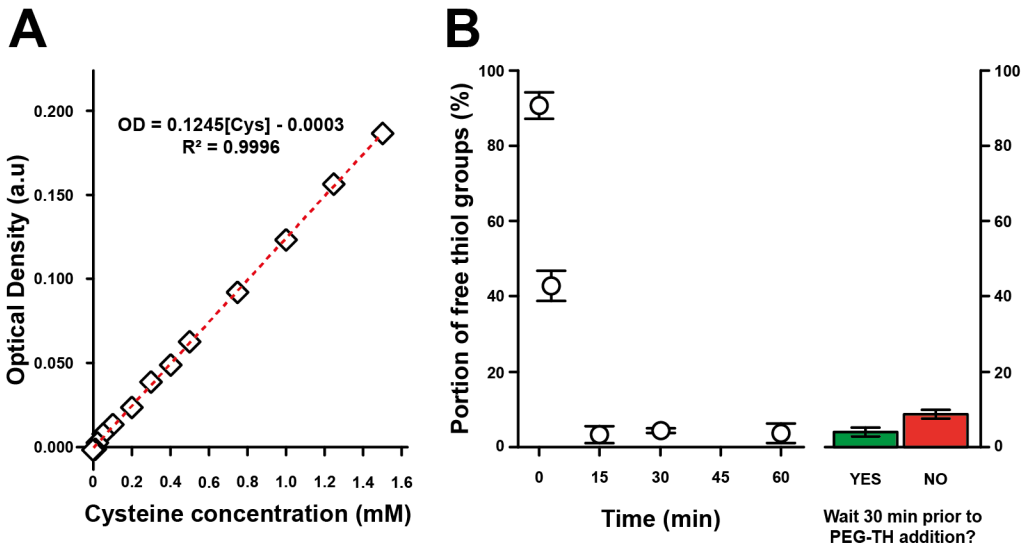

Figure 22: Quality controls on thiol bearing molecules.

*(**A**) Standard curve showing optical density of solution containing cysteine in increasing concentrations, allowing for the quantifications in B. **(B)** Left: kinetics of thiolated peptide binding to PEGVS. Right: waiting 30 min prior to addition of PEG-TH decreases the amount of unbound thiolated peptides.*

Ellman's tests performed on hydrogel discs' surrounding water after 2 hours hydration yielded the equivalent of 10.5 µM of free thiols in the case where 16R was added after a 30 min incubation period, and 19.8 µM in the case where 16R was added right after RGD. Assuming that all 16R engaged in the hydrogel network, and that none was retrieved in the surrounding water, that would indicate that roughly 5.2% and 9.9% of RGD failed to engage in the network, respectively.

b) PEG Hydrogel production

After performing the quality controls described above, and according to both the measured functionalization rates, free thiol concentrations, and molecular weight (measured either by us or by the provider), we could properly prepare hydrogels as follow. Examples are given here for 100 µL. In cases where RGD was added to mix, we waited at least 20 min prior to adding the crosslinking molecule (either PEG-TH or peptide), according to the thiolated peptide to PEGVS binding kinetics described above.

c) Swelling behaviors

Swelling over time

For the sake of practicality, the swelling ratio of the different gel recipes were measured as mass (M_g) gain as a proxy for volume change. This assumes isotropic swelling as well as a volumetric density of final hydrogel close to 1. In practice, these assumptions did not pose any problem. These measurements were made at regular intervals for the first 4h of swelling in H2O. 5% PEG40-16R hydrogel was shown to stabilize at around 1.61 ± 0.05 mass gain ratio after a quick increase to 1.41 ± 0.03 in the first hour. On the other hand, 5% PEG10-10 was shown to stabilize at 1.02 ± 0.05 mass gain ratio, with no significant difference between the post-gelling and swollen masses ($p \approx 0.47$) (Figure 23A).

Impact of concentration

Several gel recipes were tested at various dry mass content. In the case of PEG10-10, mass gain ratio was found to increase significantly ($p < 0.001$) with dry content. In detail, mass gain ratio was found to be 0.91 ± 0.01, 0.97 ± 0.03, and 1.12 ± 0.02 for 3%, 5%, and 7% dry content respectively (Figure 23B)

Interestingly, other gel recipes containing peptides showed much milder effects. No significant differences were found between 4.5% and 5.5% of PEG10-16R. No significant differences were found across 3%, 5% and 7% PEG40-16R hydrogels either (Figure 23C).

Impact of stoichiometric balance

Altering the VS:TH stoichiometric ratio was found to significantly alter the swelling behavior of 5% PEGVS10k8a-PEGTH10k4a hydrogels. In detail, the M_g ratio was increased for any non-stoichiometrically balanced gel, up to 1.13 ± 0.06 mass gain ratio for the 1:0.7 condition (-30% thiol content relative to vinyl-sulfone content). When compared to balanced gels, significant differences were found for gels with 1:1.1, 1:1.3 and 1:0.7 ratios ($p < 0.05$, $p < 0.01$ and $p < 0.001$ respectively) (Figure 17D).

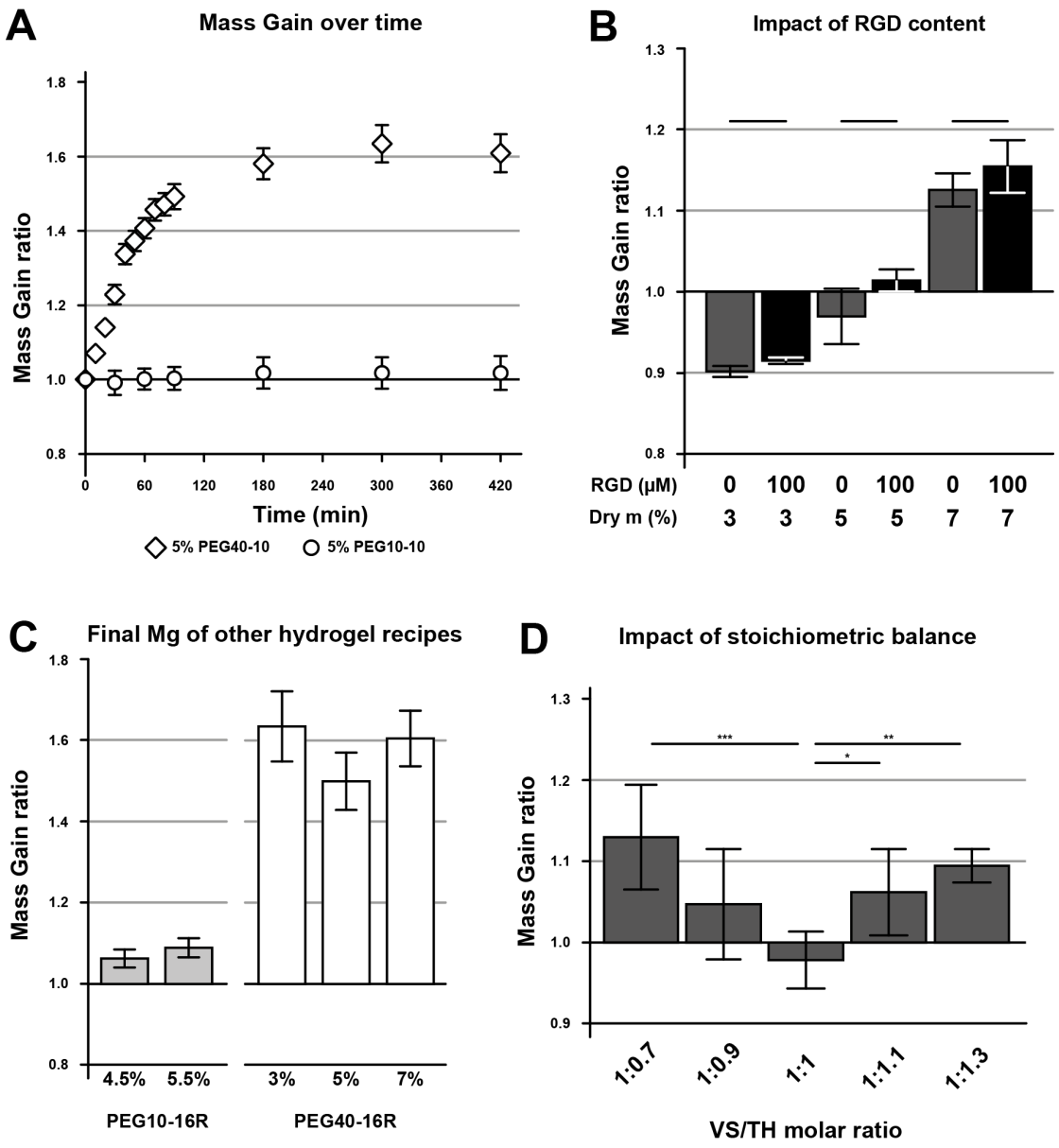

Figure 23: Mass gain ratio for various hydrogel recipes.

*(**A**) Mass gain dynamics. Here, mass gain ratio tends to stabilize after at least three hours of hydration. (**B**) Impact of RGD content on mass gain ratio on 5% PEG10-10 hydrogels. (**C**) Final mass gain ratio of other hydrogel recipes. (**D**) Impact of stoichiometric balance on mass gain ratio of 5% PEG10-10 hydrogels.*

Impact of adding a chain terminator RGD

Across 3%, 5%, and 7% PEGVS10k8a-PEGTH10k4a hydrogels, the addition of 100μM RGD was not found to significantly alter mass gain ratios ($p<0.99$, 0.17, and 0.75 respectively).

d) Rheology

General visco-elastic behavior of PEG hydrogels

All tested hydrogels exhibited a complex modulus largely dominated by storage modulus. In detail, 3% PEG10-10, 5% PEG10-16R, 5% PEG20-16R, and 5% PEG40-16R yielded phase angles of 2.50 ± 3.19, 0.03 ± 0.03, 0.46 ± 0.38, and 0.08 ± 0.04 degrees, respectively.

Impact of PEG macromeres / crosslinking peptide on storage modulus

A diversity of hydrogel recipes allowed us to cover a large variety of stiffness, ranging from around 500Pa to over 22 kPa. For PEG10-10, PEG40-10, and PEG10-16R, dry content 2% and lower never formed a cohesive bulk that would be able to hold itself enough to be investigated under the rheometer. For PEG40-10 and PEG10-16R, that limit was around 4% of dry content.

In detail, 3 to 7% PEG10-10 hydrogels produced storage modulus (G') ranging from 5.3 to 22.7 kPa, while PEG40-10 hydrogels produced storage moduli ranging from 4.2 to 13.4 kPa over the same PEG concentration range. On the other hand, PEG40-16R with concentrations ranging from 2.5 to 6.5% resulted in G' comprised between 0.6 and 7.1 kPa. Lastly, for concentrations between 4 and 7%, PEG10-16R produced G' ranging from 0.9 to 7.3 kPa, while the lowest values were found for PEG20-16R with storage modulus between 0.5 and 1.5 kPa (Figure 24B).

Impact of gel functionalization on storage modulus

Inclusion of 100 µM of the endecapeptide was globally found not to significantly impact the storage modulus of tested hydrogels, with the single exception of 2.5% PEG40-16R ($p \approx 0.014$). However, inclusion of 1200 µM of RGD was found to significantly decrease storage modulus of the PEG40-16R hydrogels that served for this experiment (see Figure 24C).

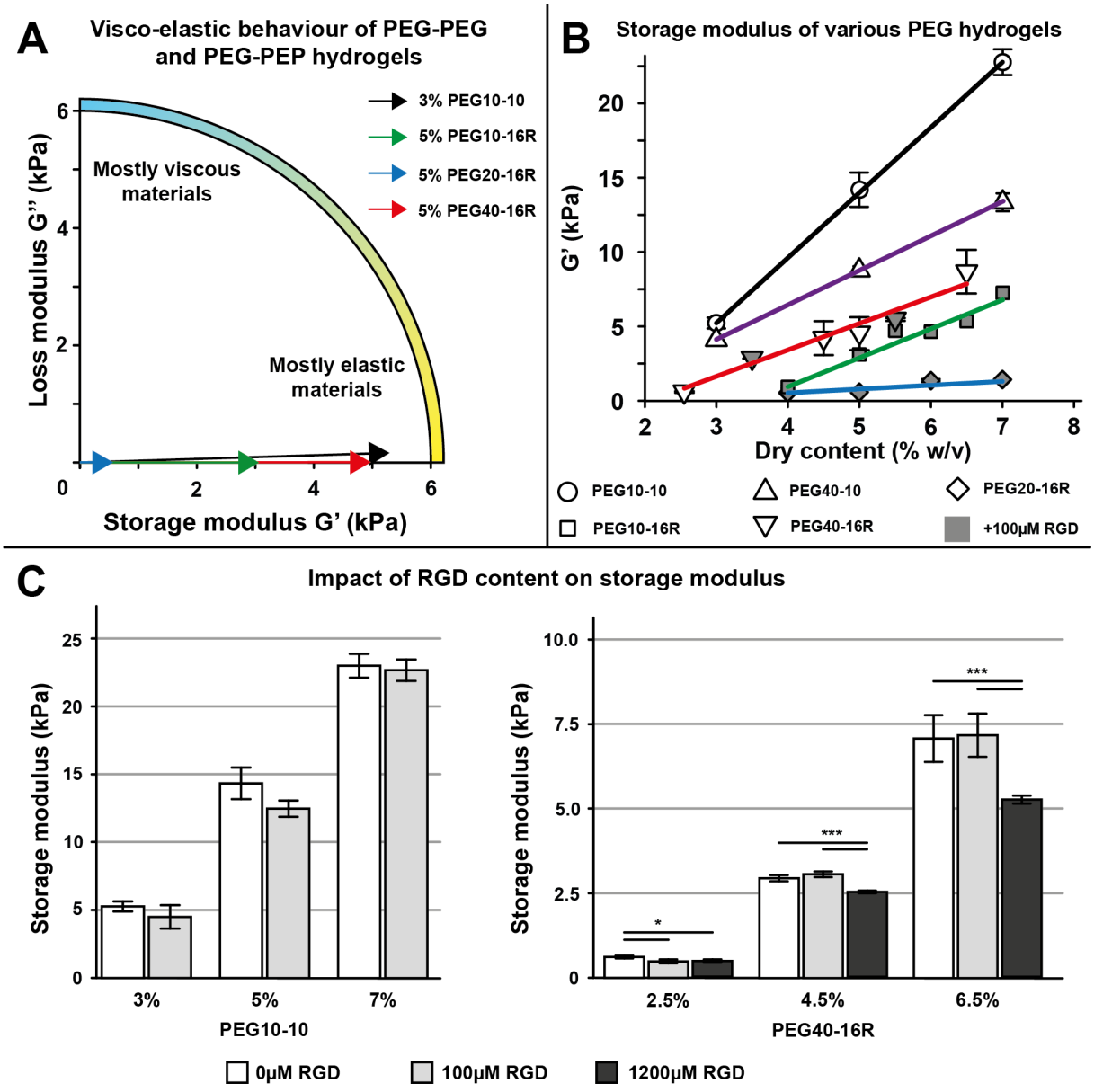

Figure 24: Mechanical properties of PEG hydrogels.

(A) Viscoelastic behavior of PEG-PEG and PEG-PEP hydrogels. (B) Impact of dry mass content on the storage modulus of various hydrogel recipes. (C) Impact of RGD content on storage modulus of two hydrogel recipes.

e) Discussion

PEG hydrogels cross-linked through thiol-vinylsulfone click reaction are among the simplest hydrogels to use and study, since they are easily formed, and will retain their physical properties for extended periods of time. Most of the hydrogels described here are of that sort. One of their main advantages is their ease of tuning. Notably,

relying on thiol-Michael addition network as described here allows for easy inclusion of other thiol-bearing molecules such as peptides[169, 183, 188, 189]. PEGylated molecules can also be included. Since PEG molecules are themselves inert, culturing cells in or on such hydrogel requires to either coat its surface, or directly include adhesion-triggering molecules in its network.

By modifying the arm length and number of the PEG molecules, one can alter the physical properties of the resulting gel, notably its stiffness and swelling ratio, as described above[181]. The roughly 1 mass gain ratio of 5% PEG10-10 makes them highly interesting, since they can be loaded into chips without the experimenter worrying about gain in volume. However, it is rather stiff (approx. 14.3kPa) and does not include MMP sensitive peptides. Thus, we only relied on them when no encapsulation was required. In other circumstances, we used cysteine-bearing (thus thiol-bearing) MMP sensitive peptides as crosslinkers, which have been shown to allow cell invasion of the gel[183].

Compared to natural matrices such as Matrigel which has a shear storage modulus below 1 kPa[164], most of the hydrogels reported here present higher stiffness, with the notable exception of PEG20-16R. This makes it an obvious candidate for further encapsulation work.

2 – HAHL CHIPS

a) Chip assembly

Both versions of the chip proved easy to assemble. At the inlets, the friction between PDMS (punched at 1.5 mm) and 1.6 mm diameter Tygon tubing was sufficient to prevent leakage without need for supplementary measures. However, the sealing of the first version of the chip was highly dependent of the horizontality of the PDMS stages. If not perfectly flat, the tightening failed to apply pressure in a uniform manner, leading to leakage that could appear right away or later on during the experiment.

The ease of manipulation of the various hydrogel depended on their physical properties. Notably, 5% PEG10-10 hydrogel was easily retrieved from its mold and deposited on the PDMS chip, though the operation requires some dexterity. The second version of the chip, with a transfer of the hydrogel to the chip using a supple PDMS mold, allowed us to avoid manipulation of the hydrogel with tweezers, and to easily graft softer hydrogels, such as 6% PEG20-16R (1.4 ± 0.1 kPa storage modulus).

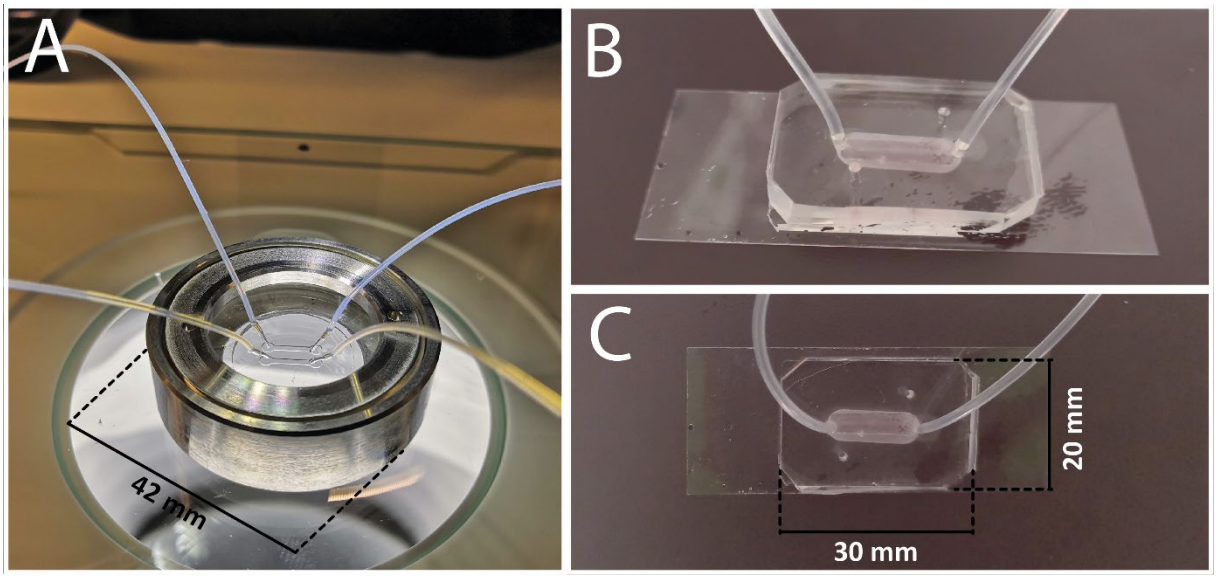

Figure 25: Microphotographs of HAHL chips.
(A) *HAHLv1 chip mounted without hydrogel.* ***(B, C)*** *HAHLv2 chip mounted with hydrogel and seeded with Caco-2/TC7 cells.*

b) Microfluidic setup

Correcting pressure drop along the length of the channel

In the microfluidic setup as it existed at the beginning of the work presented here, the chip was controlled by a syringe pump only. As the chip itself exerted a fluidic resistance greater than that of downstream tubing, it presented a major shortcoming. Indeed, the flow required to obtain large deformation of the hydrogel layer was physiologically not relevant (too great by more than two orders of magnitude). In addition, the pressure differential was lower in the distal part of the channel, compared to the proximal end of it. This led to differences in strain (accessed by measure the

distance between fluorescent beads encapsulated within the hydrogel) along the length of the channel (Figure 27A).

To correct this effect, we sought to add microfluidic resistances downstream of the chip, exerting a resistance at least 2 orders of magnitude greater than that of the chip (computed to be approx. 7 x10^9 Pa.s.m^{-3}, see Table 20). That way, we expected to keep the pressure drop along the length of the channel below 1%. That strategy bore its fruits, as can be seen in Figure 27B. In a pressure driven setup, the addition of an important resistance downstream of the chip seems to maintain constant the pressure differential along the length of the channel.

Choosing a relevant downstream resistance

In order to generate flow rates that are compatible with cell culture while maintain pressure levels that can actuate the hydrogel layer, fluidic resistances were added to the circuit. In detail, microfluidic tubing of various dimensions were added downstream of the HAHLv1 chip. As the flow-controlled setup led to rupture of the hydrogel layer when a resistance was placed downstream, we used the second setup (pressure-controlled) to assess the effect of various resistances (see Table 20 below) on both flow and strain.

Diameter (µm)	Length (mm)	Resistance (Pa.s.m^{-3})
75	50	5.7 10^{13}
50	86	5.0 10^{14}
75	500	5.7 10^{14}
50	172	1.0 10^{15}
20	5	1.1 10^{15}
NB: base resistance of the chip ≈ 7 10^9 Pa.s.m^{-3} 1 m of Tygon tubing (508 µm Ø) ≈ 5 10^{11} Pa.s.m^{-3}		

Table 26: Downstream resistances tested.

Tubing of various diameter and length allows to exert resistance on the microfluidic setup placed upstream, leading to increased pressure at constant flow.

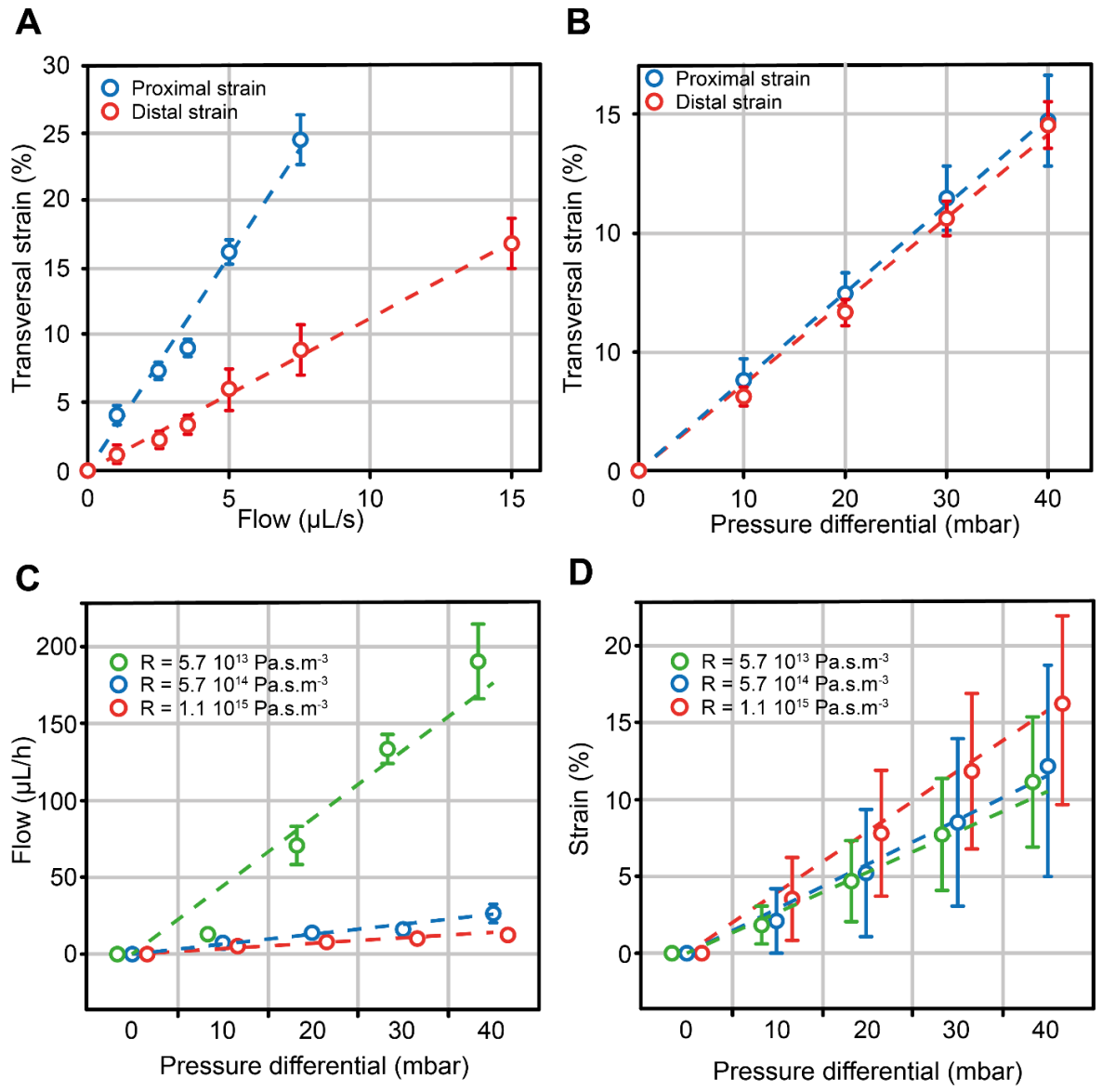

Figure 27: Impact of downstream resistances on transversal strain.

__(A)__ Proximal (blue) and distal (red) transversal strain according to perfused flow, in a flow driven setup without downstream resistance. Proximal strain for 15 µL.s^{-1} flow is not plotted, as the assumption that gel surface was quasi-horizontal no longer held. __(B)__ Proximal (blue) and distal (red) transversal strain according to pressure differential, in a pressure driven setup with clamped tubing downstream of the chip. __(C)__ Impact of pressure differential on flow, for different downstream resistances. __(D)__ Impact of pressure differential on transversal strain, for different downstream resistances.

In the pressure-controlled setup, addition of significant downstream resistances allowed to reduce flow, from over 2 x10^4 µL.h^{-1} without any resistance to around 30 µL.h^{-1} for 5.7 x10^{14} Pa.s.m^{-3} resistance, for instance, at 30-mbar pressure differential (Figure 27C). Modulating the resistance allows to select a flow window of interest. While downstream resistances had a large impact on flow, the impact on transversal

strain was limited, but also difficult to assess precisely, leading to large standard deviations seen in Figure 27D. This difficulty is part of the reason that motivated more precise approaches to understand hydrogel deformation.

Max pressure before rupture

During this trial period, we explored the rupture point of the hydrogel layer. Below are presented the data gathered from 48 chips, which faced increasing pressure differential (ΔP). We retained here only those who had a downstream resistance above 10^{15} Pa.s.m^{-3}, which corresponds to a hundred fold more than the resistance of the chip itself. Thus, the pressure differential experienced by the hydrogel layer can be considered to be that delivered to the chip by the pressure controller. All of the 48 chips could support a 40-mbar ΔP without breaking, while only 14 withstood a 50-mbar ΔP. Going further, only 11 were still intact at 60 mbar, and one at 70 mbar. No chip withstood an 80-mbar pressure differential. This relates well to firsthand experience: later, in practice, virtually all chips withstood a 40-mbar pressure differential, while most would break over 60 mbar. After dissection, the rupture in the hydrogel layers was almost always found near the inlet, within the 2 mm wide pool upstream of the channel.

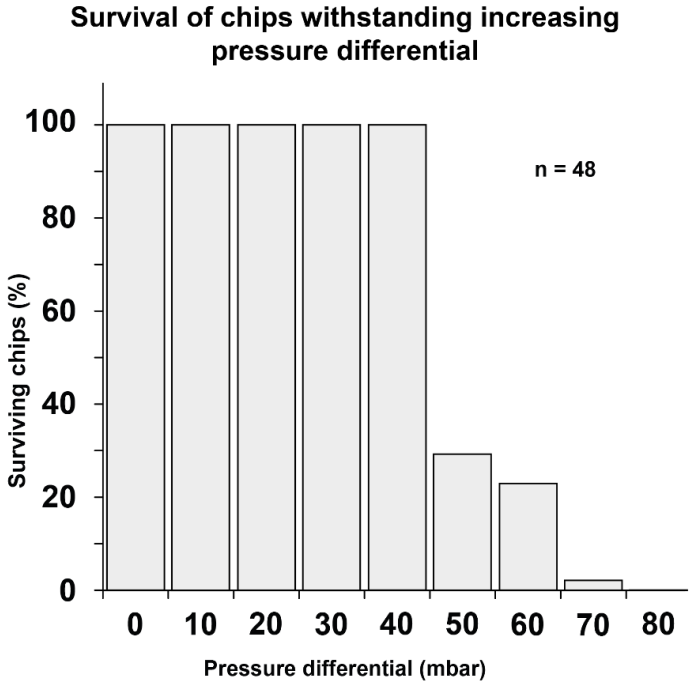

Figure 28: Pressure differential withstood by the hydrogel layer chips.

All chips assembled resisted to 40-mbar pressure differential without breaking. Starting 50 mbar, many hydrogel experience rupture. No hydrogel was observed intact at 80-mbar pressure differential.

c) Discussion

Various ways of achieving stretch of an *in vitro* tissue mimicry have been described. The use of channels dedicated to applying vacuum is widespread[5, 336-339], with PDMS membrane separating channels. In our case, the use of a soft material like hydrogel constituted a challenge for chip assembly, as it could not be included in a tight "sandwich" as is often the case in multilayered PDMS chip. Moreover, considering it would be difficult to attach the borders of a hydrogel layer to walls within the chip (difficult to maintain planarity, to avoid small gaps, *etc.*), we decided not to pursue an approach relying on vacuum side channels. Instead, we decided to directly alter the pressure within a potentially cellularized channel. Indeed, the pressure differential leads to deformation of the membrane, in a fashion comparable to that of an inflated balloon. The material properties of the hydrogel layer allowed us to visibly deform it while applying pressures in the tens of mbar (thousands of Pa).

We note that the rupture point of the hydrogel layer was 10-20 mbar away from the pressure that would elicit relevant levels of stretch. Quite luckily for us, the result was rather consistent, and we rarely lost chips for that reason. However, it could be opportune to investigate if other modes of inclusion of the hydrogel layer could improve its anchoring to the PDMS chip.

The first version of the HAHL chip was easy to assemble. Aside from giving the hydrogel a few minutes to graft itself on the PDMS, the chip is ready to use as soon as screwed in place. Moreover, aside from the upper PDMS slab and hydrogel, all other pieces could be sterilized and reused. However, it presented several shortcomings: (1) as it is preferable to culture Caco-2/TC7 cells in the upper channel to avoid gravity impacting the formation of downward structures, it would have been preferable to increase pressure in the bottom channel, (2) the chip would easily leak in the case where pressure was added to the bottom channel. This led to the design and fabrication of HAHLv2 chip (high-pressure channel below, plasma-bonded to a coverslip).

Achieving relevant levels of flow is crucial, as the shear stress induced by it is integrated by cells in the behaviors, from opening of ion channels[128] to proliferation and differentiation[327, 340, 341]. Several strategies exist to bring flow in microfluidic chip,

including syringe-pump, pressure controllers, peristaltic pumps, gravity induced flow, among others[342]. The final microfluidic setup described here, including upstream syringe pump and downstream pressure controller, allows us to avoid the introduction of fluidic resistances, which had to be so thin to serve our purpose that they could be clogged with small dead cell aggregates.

3 - MAPPING HYDROGEL DEFORMATION

a) Quantifying pairwise relative displacement

In order to get an idea on the pressure driven strain on the chip-mounted hydrogel, we embedded florescent beads in the mass of the hydrogel and followed their displacement while applying pressure. Following bead couples proved to be an easy method to quantify strain (Figure 29). However, depending on the initial positions of the beads, both in depth and across the width of the channel, measure of strain could greatly vary, and lead to large standard deviations across replicates (see Figure 28D).

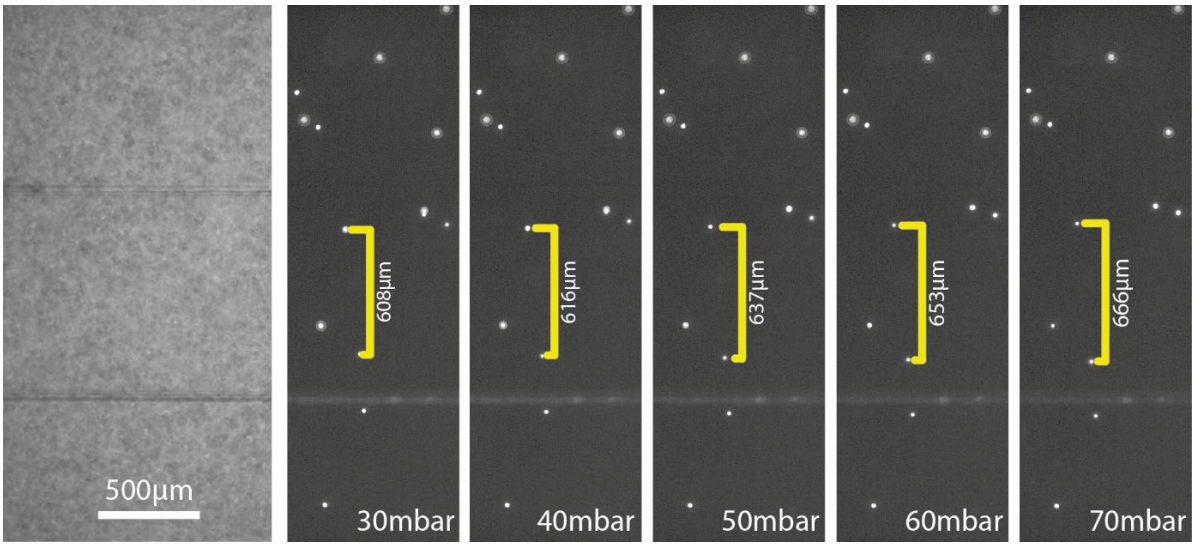

Figure 29: Following bead couples.

To prevent errors coming from the experimenter's choice of beads, we plotted the displacement of large populations of beads. We attempted to extract the shape of the

graph displaying lateral displacement according to initial placement along the width of the channel. The result is shown in Figure 30 below.

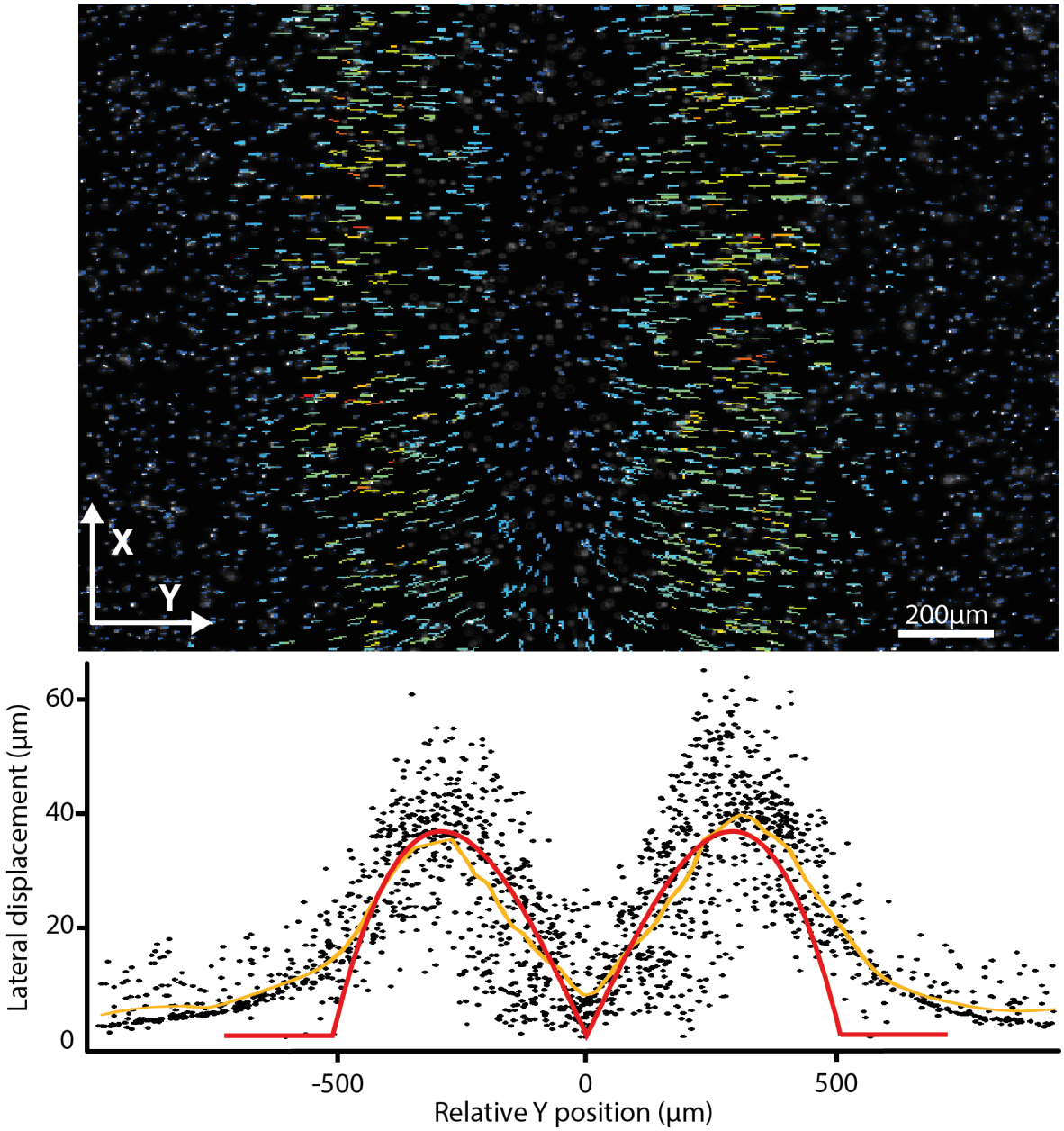

Figure 30: Attempt at automatically extracting stretch level.

Top: *Bead displacement projected on XY plane. Color map indicates displacement of the bead as the pressure differential increases from 0 mbar to 35 mbar (Blue = 0 µm displacement; Red = 65 µm displacement).* ***Bottom:*** *Bead displacement along Y axis as a function of the bead's initial position along the same axis. Yellow = local average. Red = theoretical displacement observed if the hydrogel layer is assumed to by a 2D sheet with no thickness, and the deformation uniform along its width.*

This graph was compared to a theoretical model obtained by plotting the Y displacement of points of a circular arc, according to their initial position along the width of the arc (considering uniform deformation to transition from a straight line to the arc). When comparing the theoretical displacement line (in red in Figure 30) and the data gathered, we observe an overall match between the two shapes. However, there also are several a few neat differences. First, on the lateral limits of the channel, there is a smooth transition towards immobility outside the channel, probably driven by the fact that only the close vicinity of the PDMS layer remains immobile. Secondly, we note a vast range of displacement at a given point. For instance, at +250 µm initial position, some beads will drift by only 10 µm, while other by more than 60 µm. These results highlighted the need for an in-depth understanding of the hydrogel layer deformation.

b) Fine mapping of the tangential strain

Data filtration

In total, more than six thousand beads were detected in the Z-stacks. This corresponds to a mean distance to the 12 nearest beads of 84.7 ± 27.2 µm (see Figure 31). To avoid spurious links between frames (*i.e.* pressure conditions), we selected a maximum linking distance of 50 µm. Also, since beads are not expected to move in the X axis (along the channel's main axis), we penalized links that implied a shift in X (Figure 31A).

In a second step, tracks were filtered to discard the suspicious ones and clean the data set. First, we only kept the tracks that follow a bead over all the 8 frames. That first filtering step left us with 5264 tracks. Another filter was added to discard all tracks that had a sum displacement in X larger than 10 µm. This second filter removed 448 tracks, leaving us with 4816 relevant tracks (Figure 31B).

Extracting surfaces

Projection in the YZ plane of the retained beads' location results in the profile shown in Figure 31C. Extracting the surfaces from the many bead locations was done relying on an alpha-shape (in red, in Figure 31C). Briefly, this method aims to

approximate the shape of an unorganized set of data points. To do so, it draws the outer limits of the object as segments connecting two data points in between which a circle of radius α cannot enter.

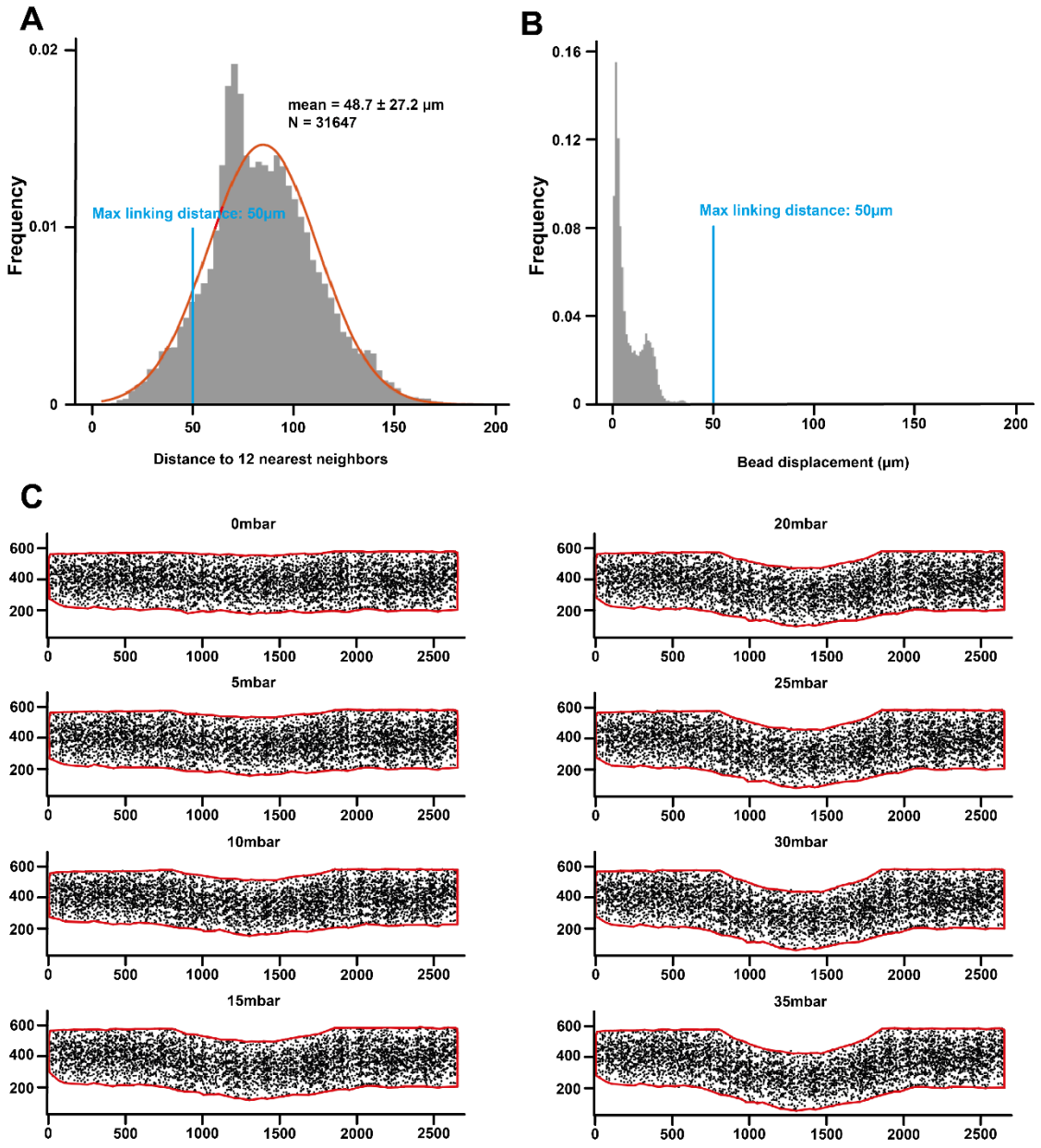

Figure 31: Preparing data for strain analysis.

*(**A**) Distances between a bead and its 12 nearest neighbors. (**B**) Bead displacement through frames. (**C**) Alpha-shape of the hydrogel, projected on XZ plan, at different pressure differential conditions.*

The strong covalent bound between the PDMS and the thiol-Michael network is clearly visible in the corners of the high-pressure channel. As the alpha-shape considered the hydrogel layer as a whole object, we extracted the surfaces in accordance with the

bead's position in the first frame (without pressure differential). Here, with the coordinates of Figure 31C, 948 beads had initial Z position >500 µm and constituted the **high-pressure surface**, while 789 beads had initial Z position <300 µm, and constituted the **low-pressure surface**.

Mapping local strain

The beads retained to form the high- and low-pressure surfaces (in this case upper and lower surfaces, as the pressure was set to be higher in the upper channel) were used to build a Delaunay triangulation of each surface. This yielded 621 triangles on the high-pressure surface, and 512 triangles on the low-pressure side, all of which could then be tracked through the pressure changes. The area ratio (A_r) was computed as the area of a given surface at a certain frame divided by its area in the first frame, when the pressure differential was null.

To map local tangential strain onto the 2D surface of the hydrogel, we used a scattered interpolation scheme (Sibson interpolator) to generate a high-density image of measurements, assuming the position of each measured area ratio to be located at the center of the triangles. The result can be seen in Figure 32. We note a strong stretch for on the left and right borders of the image, which were not considered to be relevant and seemed to be caused by a border effect that is clearly visible in the tridimensional mesh plot (Figure 32 A).

Figure 32 reveals two very different profiles, when comparing the high- and low-pressure surfaces. Please note that the strain experienced at 35 mbar of pressure differential is displayed in Figure 32 B at the coordinates of origin (*i.e.* of the first frame, with a null pressure differential).

Considering the large differences in strain profiles between high-pressure and low-pressure sides, we see that the first simplifications that assumed the hydrogel layer to behave comparably to a 2D sheet were wrong. Moreover, this explains the difference observed in Figure 30 between the simplified model's expectations and the gathered data. An updated understanding of the hydrogel layer's behavior can be seen in Figure 34. Here, we see that a hydrogel with a large thickness/width ratio will produce a zone of compression in the middle of the high-pressure side.

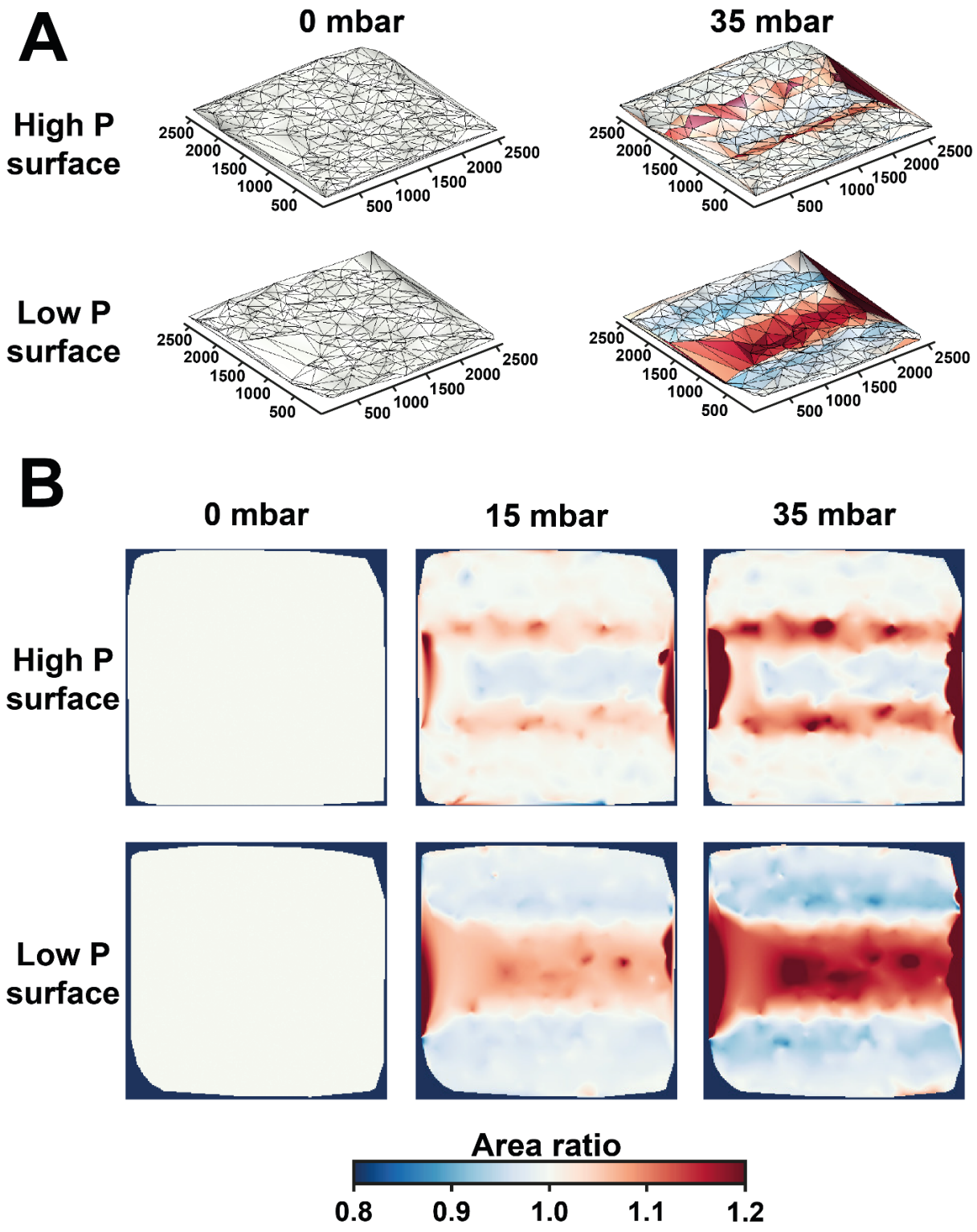

Figure 32: Local strain maps.

Top: *3D mesh plot obtained from alpha-shape of the hydrogel layer. Colors correspond to the area ratio changing through increase of pressure differential.* ***Bottom:*** *interpolation map of the local strain.*

Tangential strain profiles

Considering that the tangential strain is independent from the X position of the beads (casting aside the border effects seen in Figure 32), we projected the 2D interpolation on its Y axis (transversal to the channel). This yielded a strain profile as a function of Y coordinate. Plotting the local median value (which allows us to neglect the border effects) results in the Figure 33 below.

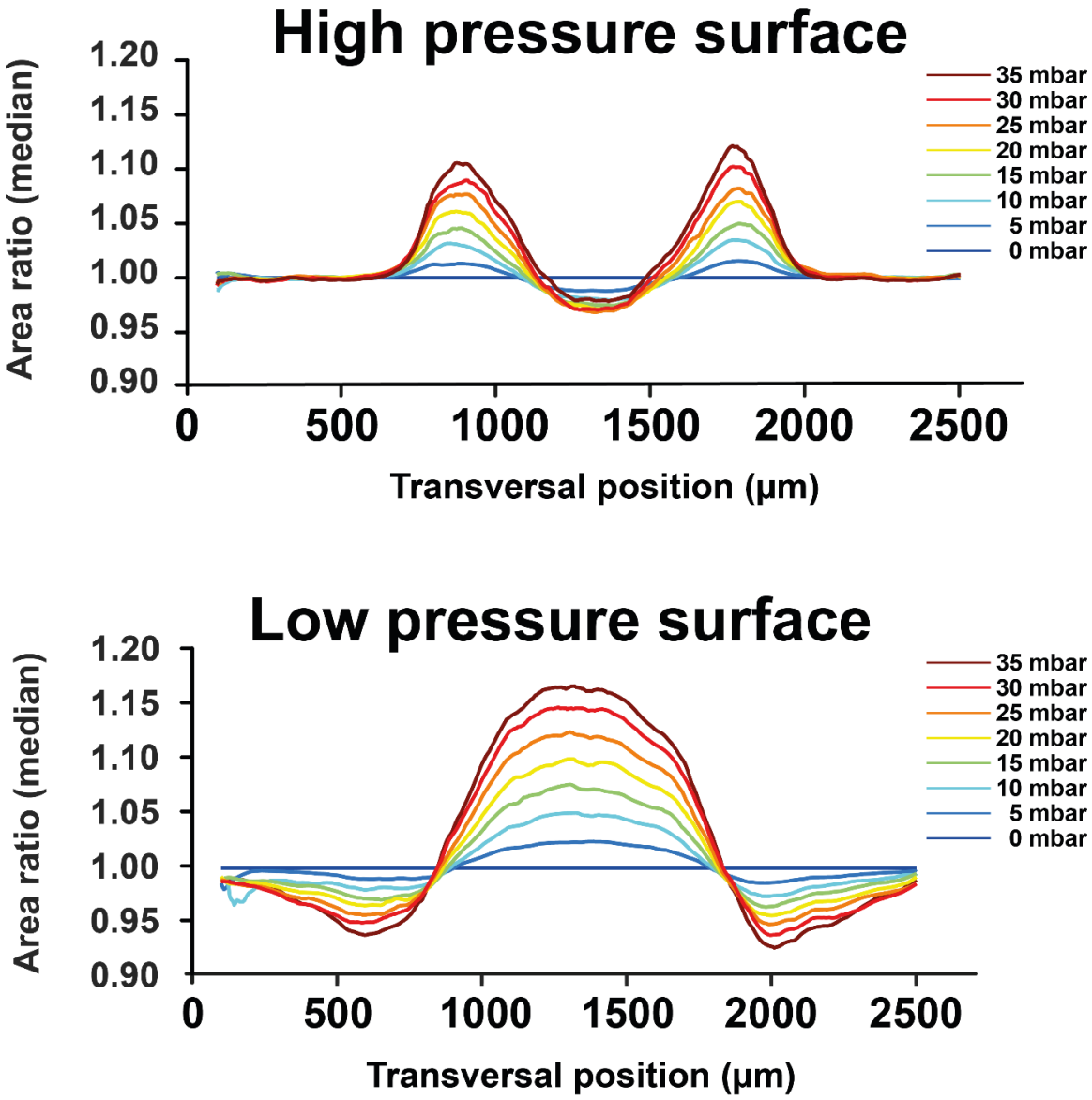

Figure 33: Tangential strain profiles.

Tangential strain profiles clearly show two strain regions on each size of the channel on the surface of the high-pressure surface ***(top)****, flanking a small compression region in the axis of the channel. On the low-pressure surface* ***(bottom)****, one main strain region is flanked by two small compression regions on each side of the channel.*

Strain along the X axis cannot be plotted since we filtered out all tracks that underwent an X movement over 10 µm. However, considering that such a harsh rule (pixel resolution being 2.6*2.6 µm) only filtered out less than 10% of the tracks, we can assume that strain in X direction is marginal.

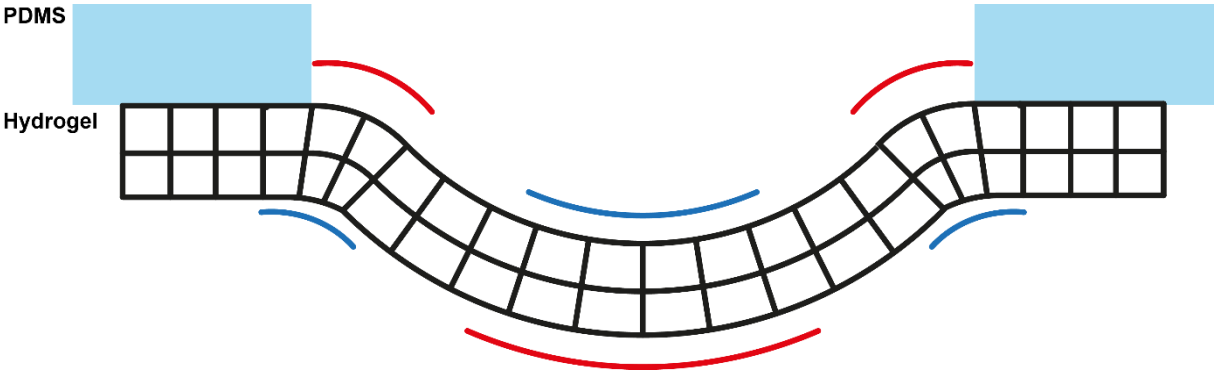

Figure 34: Model of hydrogel layer deformation in the HAHLv1 chip.
*When the thickness to width ratio of the hydrogel layer is non negligible, the curved shape of the deformed layer leads to a compression zone **(blue)** in the middle of the channel. In addition, small compression zones appear on each side of the channel, on the low-pressure side. Strain **(red)** mostly occur in the central region of the channel, on the low-pressure side.*

c) Discussion

Tailored for observation under a microscope, most organs-on-chip devices producing stretch on chip try to keep the deformation in the focal plane. This is generally true for stretch obtained relying on vacuum channels placed on the sides or below the cellularized channel[5, 336, 337], or via electromagnetic stretch for instance[343]. In such cases, the tracking of landmarks such as pores in the membrane allows us to map the displacement of each point and extract a stretch map[5].

However, a few exceptions exist, and some microdevices propose actuation going out of the focal plane. In 2021, Zamprogno *et al.* proposed an array of stretchable alveoli made in a collagen-elastin gel on which pulmonary epithelial cells are cultured[10]. In their scenario, stretch was computed by observing the displacement of a single point, at the center of the alveola, and assuming the deformation occurs following a circular

shape. Knowing alveoli spans about 260 µm, and that they produced gel layers roughly 5 to 13 µm thick, the assumption might not be unreasonable, even though it probably leaves a few blind spots in the analysis.

In our case, it appeared clear that a hydrogel layer measuring in thickness 20% of the channel's width is too important to assume it insignificant. This asked from us to develop a dedicated imaging analysis pipeline, which is presented above. Though time consuming to setup, it efficiently unveiled local deformations, and provided us with in-depth understanding of the constraints at play.

It would have been interesting here to pursue until rupture of the hydrogel, since as the strain increases, so does the width of the hydrogel layer, until a point where both high-pressure and low-pressure sides are both stretched. However, it seems inevitable (to our understanding) to avoid the side compression (on low-pressure side) and stretch (on high pressure side) zones as the pressure differential increases. Transition from a horizontal hydrogel covalently bound to the PDMS to the free part of the layer implies a turn that we do not expect to happen without these local stretch/compression zones occurring.

4 – GUT-ON-(HAHL)-CHIP

a) Viability of the setup

We performed the first viability assay on the HAHLv1 chip, seeding enterocyte cells on the top surface of the hydrogel layer, in the high-pressure channel. We relied on 5% (w/v) PEG10-10 hydrogels, including 100 µM RGD. After assembly of the chip, the hydrogel was coated with a solution containing 150 µg/mL of Matrigel. Cell survival to culture in HAHL chips was briefly assessed in the first version of the chip. HAHL chips revealed themselves suitable for culture of Caco-2/TC7 cells. LIVE/DEAD assays 24h after seeding revealed that 99.9 ± 0.3% of cells were alive, as seen in Figure 35 below.

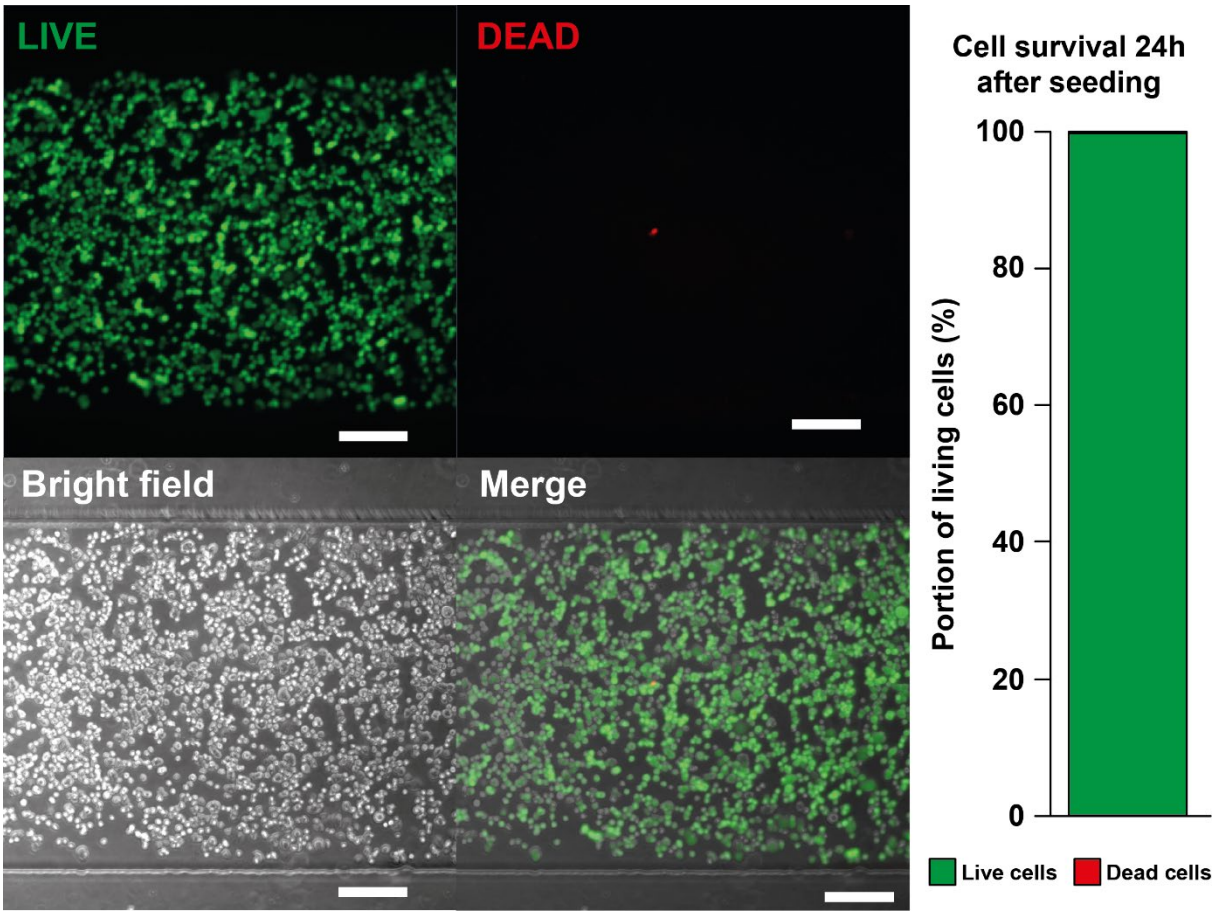

Figure 35: Cell survival on HAHL chip.

24h after seeding, very few cells died on HAHL chips. Scale bars represent 200 µm.

b) Modulating coating and incorporation of adhesion triggering molecules to improve cell culture conditions

As we observed peeling of the epithelium layer in 200 µL.h^{-1} flow, and since PEG hydrogel provides ease of tuning, it was interesting to investigate the possibility of modulating the adhesion triggering content of the hydrogel layer, either by incorporating molecules of interest within the bulk of the hydrogel or by coating its surface. Hydrogel discs (5% (w/v) PEG10-10) were prepared as previously described, without inclusion of RGD. Each disc was stuck at the bottom of a well. Four conditions received no coating: the control condition, and 3 conditions including varying concentrations of FnPEG in the bulk (100, 200, and 500 µg.mL^{-1}). Other conditions were coated with either FnPEG (100, 200, 500, or 1000 µg.mL^{-1}) or a Matrigel/Collagen mix (50/100, 100/50, or 150/0 µg.mL^{-1}).

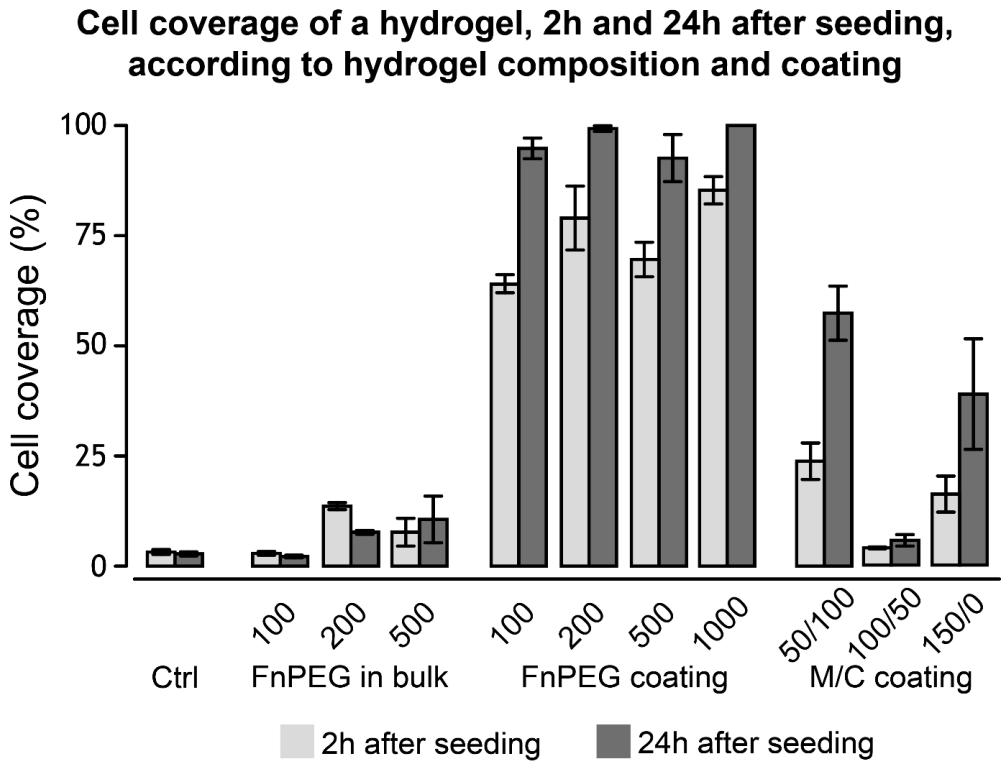

Figure 36: Cell coverage of a hydrogel.

Cell coverage of hydrogel discs (5% PEG10-10), 2h (light gray) and 24h (dark gray) after seeding depending on adhesion-triggering strategy. Concentrations are expressed in µg/mL. ***M/C:*** *Matrigel/Collagen.*

In our experiment, success of Caco-2/TC7 seeding onto hydrogels proved to greatly differ depending on the cell-adhesion strategy, as can be seen in Figure 36. Overall, the most successful conditions were those relying on FnPEG coating, with more than 60% of the surface keeping cells attached after a gentle medium change 2 h after seeding. In conditions where FnPEG is included in the bulk, such an efficacy is not visible. This is probably due to the fact that FnPEG in solution in the channel can accumulate in the hydrogel and saturate the binding sites, whereas in the case where FnPEG in included in the bulk of the hydrogel, its concentration is fixed by the amount that is included in the recipe.

Strikingly, the diluted Matrigel coating strategy did not prove to be as efficient as FnPEG coating, while it never posed problems on HAHL chips 24 h after seeding. As expected, non-coated hydrogels failed to host living cells. This might be because we didn’t incorporate any RGD in the bulk of the discs here. Another control, including RGD, would have been interesting.

c) Impact of flow rate and hydrogel deformation

Relying on the hydrogel recipe described above, we varied the flow and strain conditions over a week of culture on-chip to assess their impact on the formation of tridimensional structures. Caco-2/TC7 were seeded at near confluency in the top channel of HAHL chips in their first version (hydrogel layer attached to the upper part of the chip, receiving the highest pressure), and the chips were connected to the microfluidic setup 6h later. Four chips underwent constant 30 $\mu L.h^{-1}$ flow without actuation, three chips 100 $\mu L.h^{-1}$ flow, and four chips 200 $\mu L.h^{-1}$ flow. Three chips underwent constant flow (30 $\mu L.h^{-1}$ or 100 $\mu L.h^{-1}$) in addition to cyclic strain provided by a pressure controller imposing a sinusoidal pressure cycle, at 0.1 Hz frequency, ranging from 1 mbar to 31 mbar. All conditions were maintained for at least 6 days, with microscopy images taken at least at D1, D4, and D6. At D6, chips could undergo various further experiments.

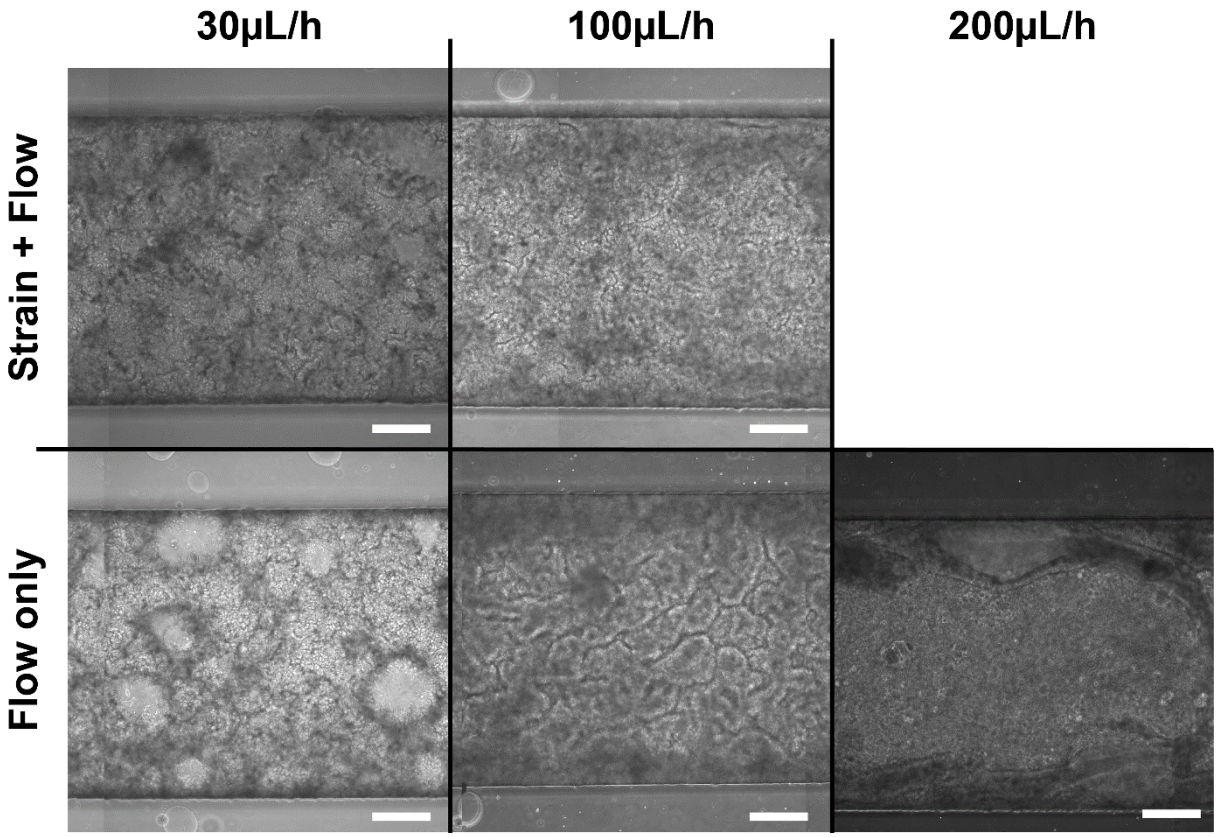

Figure 37: Impact of culture conditions on epithelium.

Top: *constant flow, with 0-35 mbar cyclic strain (0.1Hz).* ***Bottom:*** *constant flow only. All images taken 7 days after seeding. Scale bar = 200 µm.*

All experiments led to confluent monolayers after 24 h of culture. Overall, setups involving both flow and actuation led to little formation of 3D structures visible in bright field, as can be seen in Figure 37. This remains true for both 30 µL.h^{-1} (0.013 dyne.cm^{-2}) and 100 µL.h^{-1} (0.042 dyne.cm^{-2}). The condition that seems to produce to most visible structures corresponds to constant 100 µL.h^{-1} flow. Weaker flow (30 µL.h^{-1}) led to death and detachment of many cells after 1 week. On the other hand, 200 µL.h^{-1} (0.083 dyne.cm^{-2}) often led to what we interpret as peeling of the monolayer, suggesting weak attachment to the hydrogel. Though Matrigel or Matrigel/Collagen mixes can be used in similar chips[6], it is possible that the hydrogel layer does not provide the ideal conditions for such coating strategy, or that 0.083 dyne.cm^{-2} shear stress would have been too great for non-covalent attachment regardless of the nature of the Matrigel coated substrate.

Overall, these results suggest that either mechanical stimulation is of little interest in the matter of eliciting the formation of tridimensional structures from Caco-2/TC7, or that the setup in question did not provide the adequate stimulation. Others have demonstrated improvements in the maturation of Caco-2 cells with addition of cyclic strain[7], notably increased amino peptidase activity and apparent permeability, but without investigating its impact on 3D structuration. Knowing that HAHLv1 chips actually produce several zones undergoing either strain of compression at the surface of the upper channel, we cannot definitely conclude on the matter. This led us to develop a second version of the chip, with a high-pressure channel at the bottom, and placing the Caco-2/TC7 on the surface of the hydrogel layer that is largely submitted to strain.

d) Apparent permeability

P_{app} of the HAHL chip

Permeability assays were performed as described earlier, on naked PEG10-10 hydrogels, with fluorescent dextrans of various sizes (4, 20, and 70 kDa). In addition, the apparent permeability of mature Caco-2/TC7 epithelium were assessed with 4 kDa dextran. Said epithelium correspond to Caco-2/TC7 cells cultured for 6 days in HAHLv1 chips and submitted to constant 100 µL.h^{-1} flow, without actuation.

The permeability assay showed, for naked hydrogel, a clear and expected decrease of the P_{app} of the hydrogel layer to FITC Dextran as their molecular weight increased. While the P_{app} of the hydrogel layer to 70 kDa dextran was found to be 1.33 ± 1.05 $x10^{-6}$ cm/s, it was found to be 8.35 ± 0.40 $x10^{-6}$ cm/s for 20 kDa dextran, and 1.54 ± 0.23 $x10^{-5}$ cm/s for 4 kDa dextran (Figure 38).

When a Caco-2/TC7 epithelium was present over the hydrogel, we observed an important decrease in apparent permeability, which dropped to 3.87 ± 1.41 $x10^{-6}$ cm/s for 4 kDa dextran. Normal distribution and homogeneity of variances were checked relying on Shapiro-Wilk and Bartlett tests, respectively, and one-way ANOVA test found significant difference between every group.

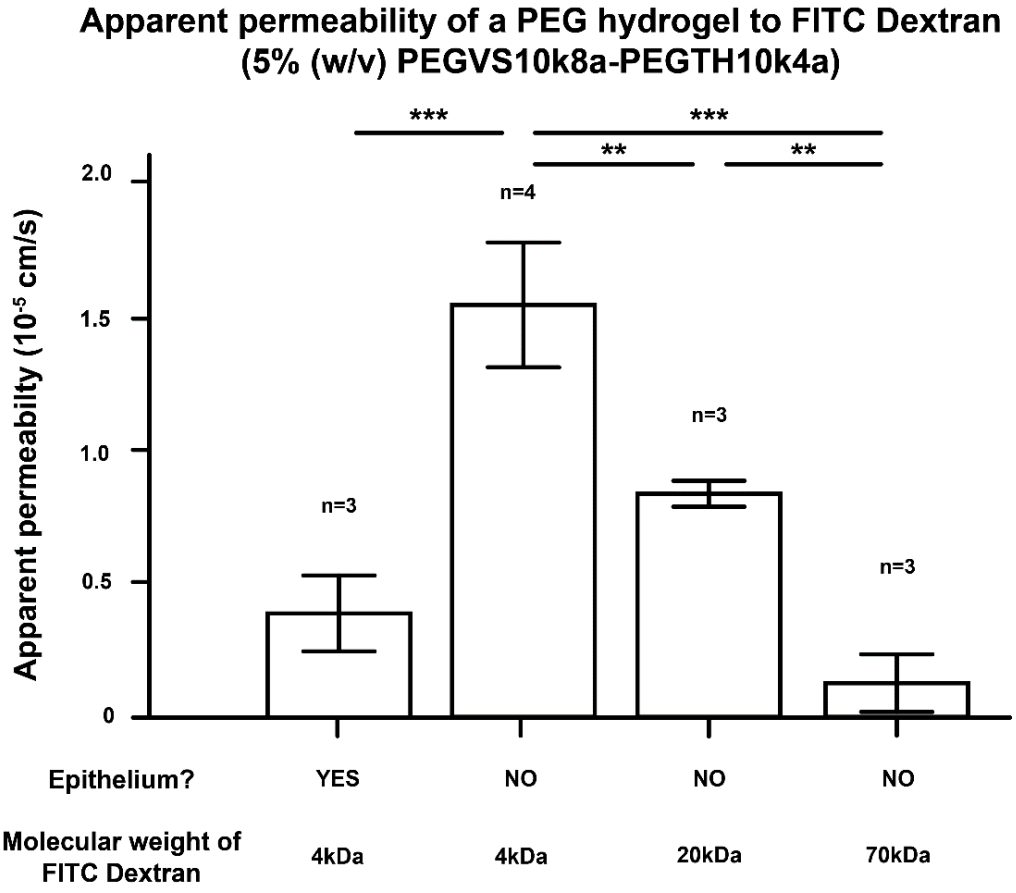

Figure 38: Apparent permeability of HAHL chip.

From left to right: *apparent permeability of the 5% PEG10-10 hydrogel layer to 70 kDa, 20 kDa, and 4 kDa dextran molecules. The last condition corresponds to an apparent permeability assay performed on a Caco-2/TC7 epithelium after 6 days of culture with constant 100 µL.h^{-1} flow.*

It appears clearly that the epithelium acts as a barrier, blocking the passage of most of the 4 kDa dextran molecules. Here, the lower channel collected about 1.6% of the fluorescent molecules, while 98.4% remained in the upper channel. In previous experiments, Kim (*et al.*, 2012)[7] and Shin (*et al.*, 2018)[344] reported values inferior to 10^{-6} for 20 kDa FITC dextran. Aside from comparing apparent permeability to molecules of different sizes, it probably is also difficult to compare the two systems. Indeed, the chip used by both teams comprise a PDMS layer separating the two channels. This layer is perforated by holes 10 µm in diameter. Overall, only 7-8% of the surface below the epithelial layer allows molecules to pass to the other channel.

e) *Epithelium polarization*

The epithelium cultured in the most promising conditions (cultured for 6 days in HAHLv1 chips, and submitted to constant 100 µL.h^{-1} flow, without actuation) were chosen to assess the polarization of the epithelium, and ease of imaging of the HAHL setup. Notably, we were interested in the expression and localization of actin and E-Cadherin. The epithelium was fixed, permeabilized, and stained while still being in the chip, as described earlier. This was easily done, by flushing the channel and filling it with the working solutions described earlier. Later, the hydrogel would be separated from the PDMS chip by gently sliding a razor blade in between the two.

First attempts at imaging epitheliums upright proved difficult, due to the added thickness brought by the hydrogel layer, limiting the exploration of the tissue placed above. Epithelium placed upside down was impossible to image, since the structures would progressively collapse under the weight of the hydrogel layer, leading to a visible shift across channels when building the composite image. Embedding the tissue upside down in 5% PEG10-10 solved both issues, allowing to stabilize the structures over time.

For epithelium observed 6 days after seeding, and cultured under constant 100 µL.h^{-1} flow, immunofluorescence clearly revealed the 3D organization of the tissue (Figure 39A). Imaging through a villus-like structure revealed clear polarization of the hydrogel layer, with actin being expressed apically, and E-Cadherin basolateraly (see Figure

39B). Orthogonal views allow us to have a rough estimate the height of the structures (Figure 39C).

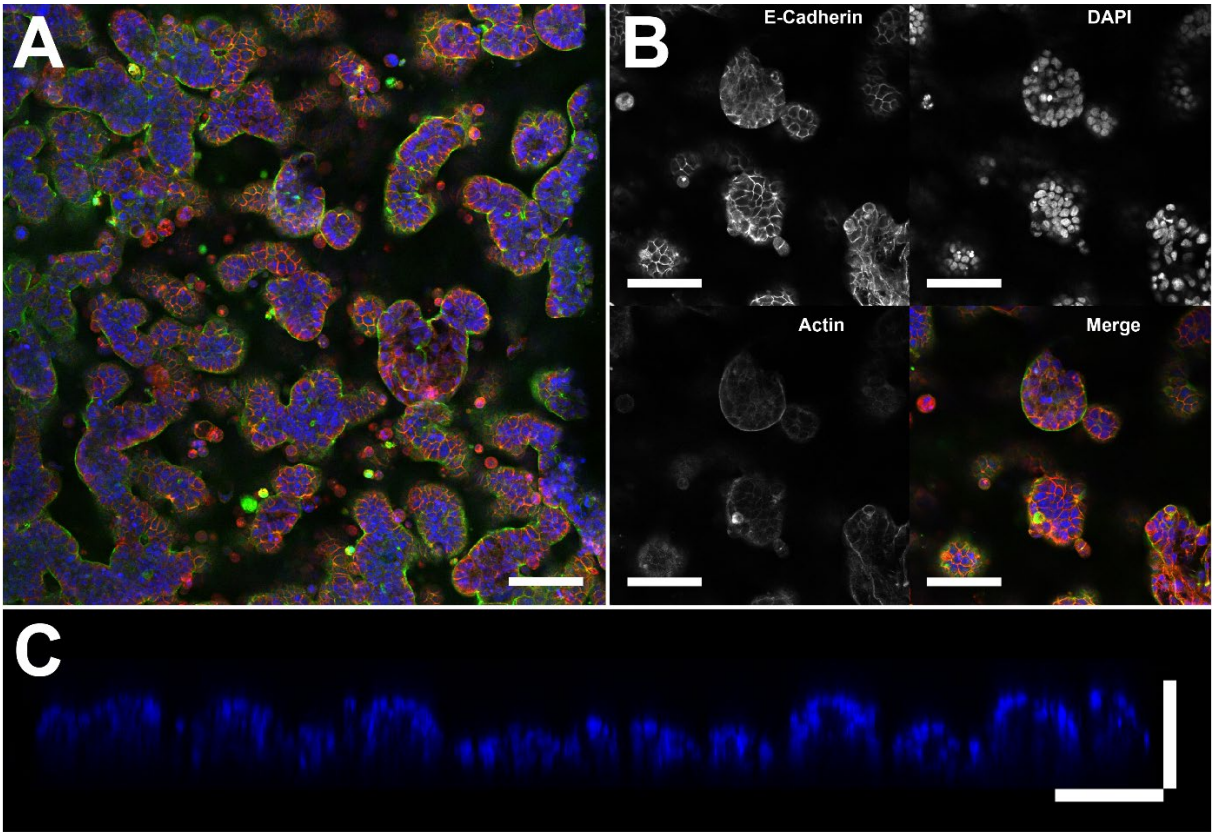

Figure 39: Immunofluorescence image of Caco-2/TC7 epithelium on HAHL chip.
(A) *Composite image showing the whole width of the epithelium.* ***(B)*** *Close-up view and decomposition of the signals, showing basolateral expression of E-Cadh, and apical expression of actin.* ***(C)*** *Orthogonal view of the DAPI staining, showing roughly 100 µm high structuration of the epithelium. Displayed epithelium was cultured for 6 days under constant 100 µL.h^{-1} flow.*

Overall, we note the ease of staining of the sample and the possibility to access the epithelium in immunofluorescence. However, the thickness of the hydrogel layer prevented us from imaging the sample in an upright position. That led to the development of the embedding protocol for upside-down imaging, and for vibratome slicing for slice imaging.

f) Scanning Electron Microscopy

Sample preparation for SEM

Prior to critical-point SEM, samples had to undergo replacement of water with ethanol as a solvent. Not knowing what impact the procedure would have on the sample, we first assessed the impact of successive ethanol baths (with increasing concentration, from 25% to 99.5% ethanol) on 5% PEG10-10 hydrogel discs. The results are reported in Figure 40.

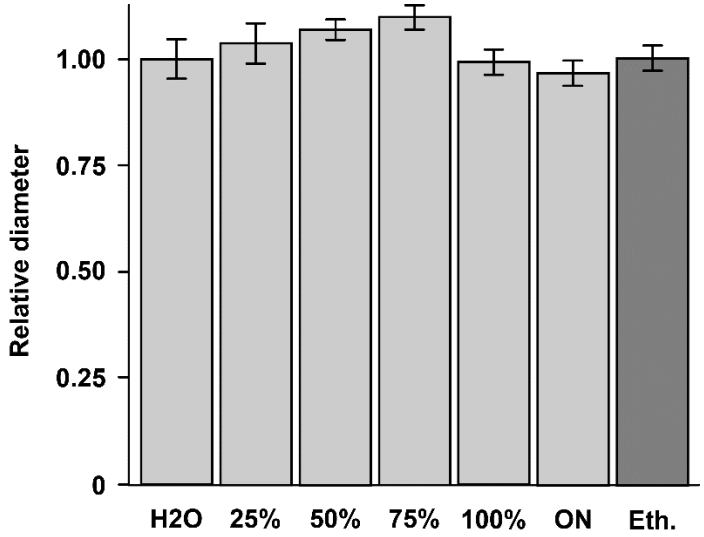

Figure 40: Impact of ethanol baths on hydrogel.

H2O: *after swelling in ultrapure water.* ***25% to 100%:*** *after 20 min bath in ethanol solution.* ***ON:*** *After being left overnight in ethanol.* ***Eth:*** *Independently prepared sample let to swell in ethanol.*

Notably, we observed that swelling in H2O or 99.5% ethanol produced similar relative diameters (1.00 ± 0.05 *vs.* 1.00 ± 0.03). However, we noticed that, throughout the successive ethanol baths, the diameter of the hydrogel discs would increase, up to 1.10 ± 0.03 for 75% ethanol bath. Strikingly, this relative diameter drops to 0.99 ± 0.03 for 99.5% ethanol, and reaches 0.97 ± 0.03 after spending the night in ethanol.

SEM observation

Critical point SEM was performed on samples retrieved from representative HAHL chips. The best way to present the sample was found to stick it to a coverslip with a drop of 5% PEG10-10. Upon inspection, very few defects or cracks were

observed, only found in the hydrogel supporting the sample (yellow arrows in Figure 41 Left). The sample remained largely unaltered by the procedure. That is an improvement compared to other samples obtained from PDMS-only chips. As the PDMS layer and the sample did not shrink together, the sample tend to break apart (not shown). On the contrary, HAHL chips and the protocol described here allow to keep the whole sample intact. Close-up observations allowed to confirm the aspect of cells, and notably the presence of cells expressing microvillosities (see Figure 41 Right). Note that the sample presented here corresponds to a Caco-2/TC7 epithelium cultured for 6 days under constant 30 µL.h^{-1} flow.

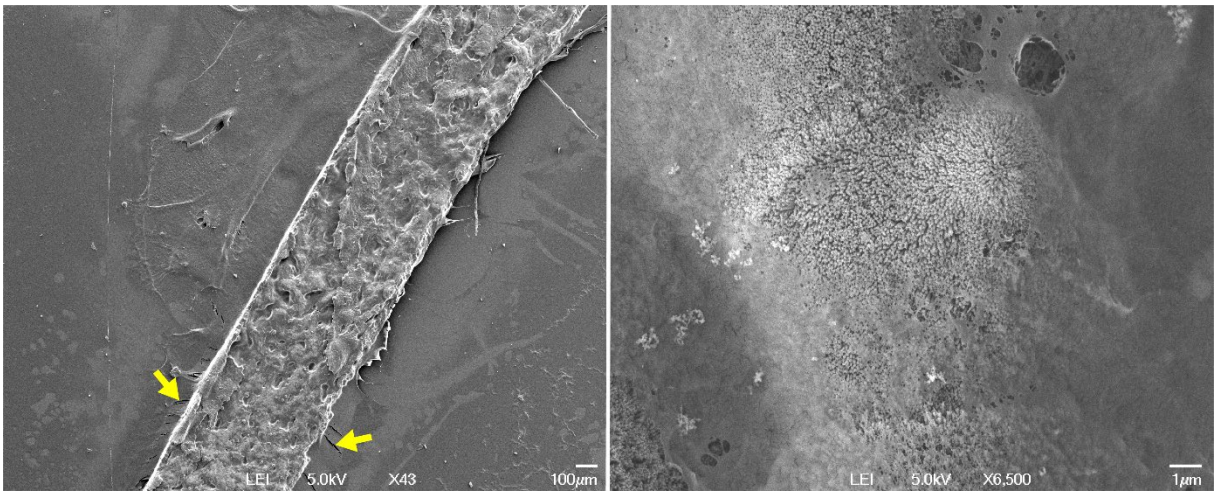

Figure 41: SEM observations of an intestinal epithelium.

Left: *x43 observation of the whole width of an intestine-on-chip, showing that no fragmentation of the sample occurred.* ***Right:*** *x6500 observation of Caco-2/TC7 cell exposing microvillosities.*

g) Discussion

HAHL chip are biocompatible and can elicit cell adhesion

Enjoyed for their ease of tuning, PEG-based remain largely biologically inert (confirmed here by the excellent survival of Caco-2/TC7 in the chip). Thus, their use as culture substrate requires to dedicate time to identify candidates for coating and/or grafting to elicit cell adhesion. During our experiments, we started by coating our chip with Matrigel, which showed good results. Epithelial cells were adherent, spread, multiplied, and could be maintained for more than 10 days without problem. Later during the project, we thought to capitalize on our hydrogels and explore the possibility

to incorporate a Fibronectin fragment to trigger cell adhesion. Results show the clear superiority of FnPEG over Matrigel and collagen coating to resist a wash 2 h after seeding.

Condition screening to produce structured Caco-2/TC7 epithelium

In 2012, Kim and colleagues documented that, compared to static Transwell condition, both 0.02 dyne.cm^{-2} flow-induced shear stress and shear stress in addition to cyclic stretch (10%, 0.15 Hz) conditions improved cell height in culture. On other biological markers too such as specific aminopeptidase activity, flow+strain condition was shown to elicit an improved state of function.

We thought to produce ourselves a matrix of condition, and notably try to witness the impact of actuation on the epithelium. Strikingly, our results do not correlate the finding. In our experiments, the only condition that elicited formation of a structured epithelium corresponds to the 100 µL.h^{-1} (0.042 dyne.cm^{-2}) condition. Addition of actuation only worsen the aspect of the epithelium. However, it is difficult to conclude in terms of responsibilities, as we were shown later that the actuation of the hydrogel layer did not actually impose stretch on much of the surface of the high-pressure channel. The HAHLv2 chip should be able to propose an adequate setup to test the hypothesis.

Difficult comparison of Papp to other systems

Permeability assays are widely used when working on barrier tissues. First, they give useful information regarding the integrity of the barrier (intestinal, vascular, pulmonary, *etc.*). In addition, they can be used as a first approach to approximate absorption of molecules, notably drugs. Permeability assays can be performed in various setups. Typically, epithelial or endothelial cells are seeded and culture on a permeable (typically porous) membrane separating two compartments. After formation of a confluent monolayer of cells, molecules of known size (typically, fluorescent-tagged polymers) are injected in one of the compartments and its concentration is followed in both compartments over time.

This method is notably use to quantify the effect of a disruption of the barrier, be it by chronic diseases of the gastro intestinal tract, or by an enteroinvasive pathogen[6, 300,

[301], for instance. Contrarily to trans-epithelial electric resistance (TEER), apparent permeability assays are easier to include on a chip, especially in setup of large height. Indeed, the quality of TEER measurement depends on the distance between the electrodes, making it particularly suited for flat monolayers of cells, even though efforts have been to propose TEER in organ-on-chip devices[345].

It appears clear that the epithelium acts as a barrier, blocking the passage of most of the 4 kDa dextran molecules. Here, the “vascular” channel collected about 1.6% of the fluorescent molecules, while 98.4% remained in the “luminal” channel. In previous experiments, Kim (*et al.*, 2012)[7] and Shin (*et al.*, 2018)[344] reported values inferior to 10^{-6} for 20 kDa FITC dextran. Aside from comparing apparent permeability to molecules of different sizes, it probably is also difficult to compare the two systems. Indeed, the chip used by both teams comprise a PDMS layer separating the two channels. This layer is perforated by holes 10 µm in diameter. Overall, only 7-8% of the surface below the epithelial layer allows molecules to pass to the other channel.

It would be interesting to pursue barrier disruption assays on both HAHL chips and Emulate’s colon chip. As the membranes separating the two compartments in the two chips have very different properties, one could be found to be more suited than the other for this kind of experiment.

Possible improvements to the cell model

Caco-2 cells are immortalized epithelial cells sourced from a human colorectal carcinoma. Despite their colon origin, they spontaneously differentiate into a heterogeneous mixture of intestinal epithelial cells with morphological and functional resemblances with small intestine enterocytes. Today, they are widely used as model of the small intestine barrier[346]. Notably, Caco-2 express tight junctions, microvilli, and various enzymes and transporters typically found in enterocytes. However, we note several differences between native small intestine enterocytes. Among other things, Caco-2 cells have stronger tight junctions and do not express the entire variety of metabolic proteins and transporters the native enterocytes do[347, 348]. Notably, they do not express mucins, making Caco-2 epitheliums incapable of producing mucus. To improve reproducibility between experiments, clones of Caco-2 cells have been established and described. Despite above-mentioned shortcomings, Caco-2 cells

remain easy to use, and are considered a gold standard in research, and pharmaceutical development.

Still, improvements can be made, by coculturing Caco-2/TC7 cells with HT29 cells for instance, for added sub-clonal diversity and presence of goblet cells, and with Raji B lymphocytes, which are known to promote upon Caco-2 cells differentiation in M-like cells, specialized in transcytosis and poorly expressing a brush border. Another approach to improve cell diversity and function would be to seed gut organoids[265], though more tedious. This was not sought for yet, at this stage of development, but could come soon.

HAHL samples are accessible in SEM

Scanning Electron Microscopy (SEM) is often used to investigate barrier tissue biology on chip. It allows to easily read the surface and shape of a 3D structured tissue, to visualize cell types such as secreting cells or cells possessing microvilli, or to spot host-pathogen sites of interaction[6].

Critical point SEM involves the use of ethanol as a solvent. Typically, the initial solution in which the samples are preserved is replaced by progressive baths of ethanol in increasing concentration. However, not all biological structures withstand this step, and we wanted to verify if the highly hydrophilic hydrogel layer on which our tissues are cultured could undergo such protocol without altering the sample.

5 – CELL ENCAPSULATION IN PEG HYDROGELS

A key advantage of the HAHL chip system is that, unlike other OoC systems, it offers the possibility to culture a 3rd cell type within the bulk of the hydrogel. In order to prepare for this development, we had to explore 3D cell culture with PEG hydrogels compatible with their inclusion on HAHL chip. To do so, I first tried to master 3D cell encapsulation in PEG synthetic hydrogel by contributing to a project aimed at exploring the impact of physical and chemical conditions on cholangiocytes. My contribution was

focused on the design of hydrogel recipes and on their mechanical characterization. This "side project" led to a publication in *Frontiers in Bioengineering and Biotechnology*[349].

a) Modulating hydrogels properties to alter cysts formation and growth

We investigated the impact of modulating the hydrogel properties on cell survival, but also cyst formation frequency and size, and compared it to a Matrigel gold standard. In detail, we varied composition (PEG40-16R or PEG40-16A), stiffness, and integrin RGD ligand density.

16A and 16R peptides were selected for their different sensitivity to MMP degradation, as previously reported[183, 189]. Briefly, 16R is labelled "very sensitive" to MMP degradation, while 16A is simply labelled "sensitive". An almost 17-fold difference exists between their relative turnover numbers k_{cat} to MMP-1[189].

PEG hydrogels allow for cyst survival and growth

First, we quickly confirmed that NRCs can survive and proliferate in PEG hydrogels as it does in Matrigel drops. Over a culture period of 10 days, cultured NRCs self-organized into hollow spheres termed cysts composed of a very thin layer of epithelial cells marking the boundary between an inner lumen and the extracellular milieu. When assessing cell viability, we found that encapsulated NRC showed globally a good viability in PEG and in Matrigel. At day 10, a modest decrease in viability was observed in PEG (see Figure 42A et B), most probably due to the death of the cells that could not form cysts. In addition, we found that cell survival was independent of the proteolytic degradation of the substrate (Figure 42C). Across PEG hydrogels including 0 to 1200 µM of RGD, cell survival was not significantly different between 4.5% PEG40-16A and -16R hydrogels. However, formation of cysts from single cells or small aggregates was found to be highly dependent of the susceptibility of the crosslinking peptide to enzymatic degradability (Figure 42D). Indeed, in 2.5 and 4.5% hydrogels with addition of 100 µM RGD, cyst formation frequency was significantly

higher ($p < 0.001$ and $p < 0.05$, respectively) in PEG40-16R than in PEG40-16A, with a >2-fold increase. In 6.5% hydrogel, both composition resulted in frequencies lower than 10‰.

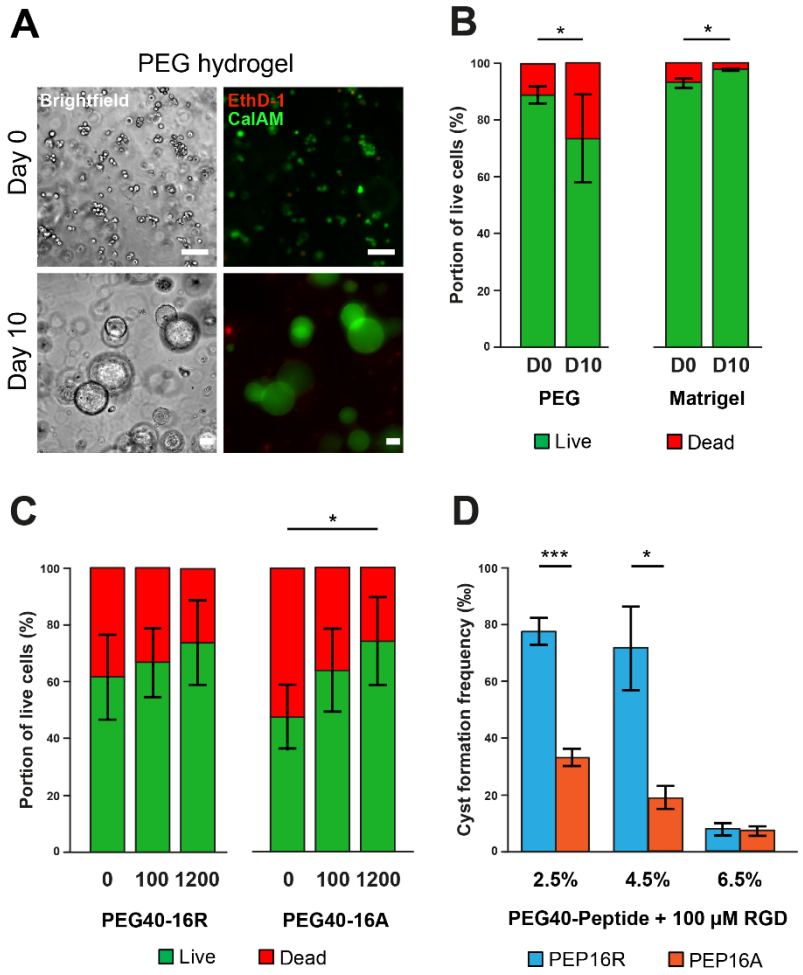

Figure 42: Cell survival in PEG40-16R and -16A hydrogels.

*(**A**) LIVE/DEAD assays performed on 4.5% PEG40-16R hydrogels, after seeding and after 10 days of culture, and (**B**) Subsequent analysis. (**C**) Impact of RGD content (in µm) and MMP sensitivity of peptide crosslinker on cell survival 10 days after seeding. (**D**) Impact of MMP-sensitivity and dry content on cyst formation frequency. Scale bars = 100 µm.*

Impact of RGD content and stiffness

Overall, the growth kinetics in both PEG40-16R and Matrigel allowed for the formation of cysts with sizes ranging from 40 to 800 µm. At this stage, we did not observe obvious differences between cysts cultured in either synthetic or natural scaffolds. Altering independently RGD ligand density and stiffness of the substrate

allowed us to build a “matrix” of conditions across which several measures can be made on cholangiocyte cysts, notably the frequency at which a single cell (or small aggregate of cells) will give rise to a cyst, and cyst diameter (Figure 43A).

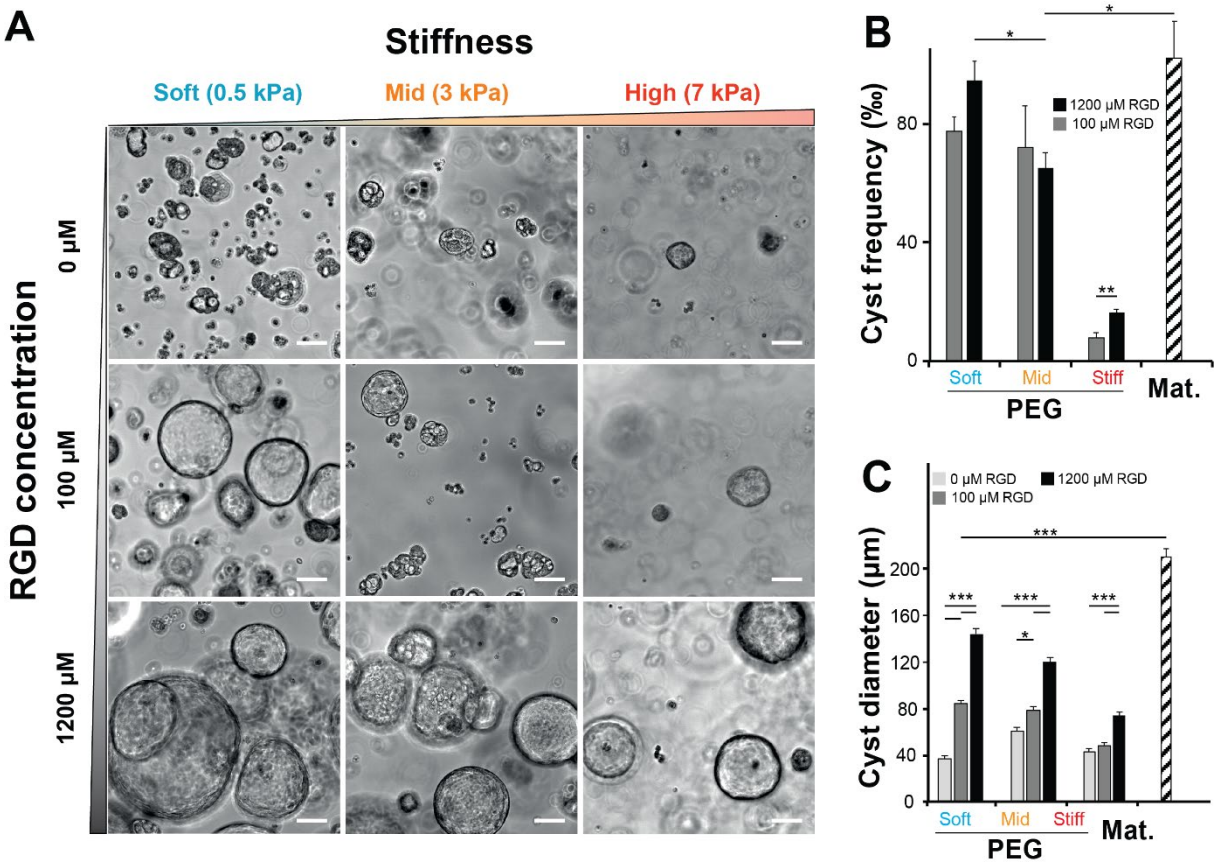

Figure 43: Impact of matrix composition on cyst formation.

(A) Bright field images of NRC cysts cultured for 10 days in hydrogels of various compositions. (B, C) Quantification of cyst size and cyst frequency, respectively, at day 10 across soft, intermediate, and stiff polyethylene glycol gels and in Matrigel. Scale bar = 100µm.

When we quantified the cyst formation frequency across conditions, we found that both 2.5% and 4.5% hydrogels (with storage moduli in the range of 0.5-0.6 and 2.5-3.0 kPa, respectively) led to frequencies close to that of encapsulation in Matrigel. Only 4.5% hydrogel +1200 µM RGD was found significantly lower than Matrigel condition ($p < 0.05$). On the other hand, 6.5% hydrogels (with storage moduli >5 kPa) led to a more than 6-fold decrease in cysts formation frequency (Figure 43B). Overall, the capacity of cholangiocytes to form cysts seems mostly driven by a permissive stiffness than it seems impacted by RGD ligand density.

When we quantified the average cyst size, we found that softer gels favored the formation of larger cysts with the largest cysts being systematically produced in Matrigel (approximatively 20% larger than in the best PEG condition). In addition, this experiment also showed that the presence of RGD was critical for the formation of large cysts (Figure 43C). Interestingly, the measurement of cyst sizes across the nine RGD/Stiffness conditions showed that while increasing RGD concentration in soft gels dramatically increased cyst size, inducing a 3.9-fold increase in cyst diameter when comparing 0 and 1200 µM RGD, it only had a much lower (though still significant $p < 0.001$) effect in stiff gels (1.7-fold increase).

Taken together these data clearly show that both cholangiocytes cyst formation frequency and size are determined to a large extent by variation in the elastic modulus of the substrate. The presence of RGD ligand in high concentration further improved this trend.

b) Accessibility of encapsulated cells for assays

Immunostaining encapsulated structures

Immunostaining of encapsulated cysts was pursued, and was found to be only feasible by adapting the incubation times in presence of each staining. Since naked hydrogels already present low permeability to large molecules (such as antibodies, *cf.* Figure 38), incubation times had to be extended according to the size of each molecule. Permeabilization (with 0.5% Triton X-100) was extended for up to 2 h, Antigen blocking (2% BSA, 0.1% Tween-20) up to 3 h, primary and secondary staining for up to 4 days, and nuclei and f-actin staining for 2 days.

This modified protocol allowed us to visualize the expression and location of actin and E-Cadherin in cholangiocytes encapsulated in PEG hydrogels. We found that large NRC cysts stain positive for basolateral E-Cadherin and apical F-actin (Figure 44A). This canonical epithelial polarity was observed in cysts of different dimensions across the tested 3D culture conditions.

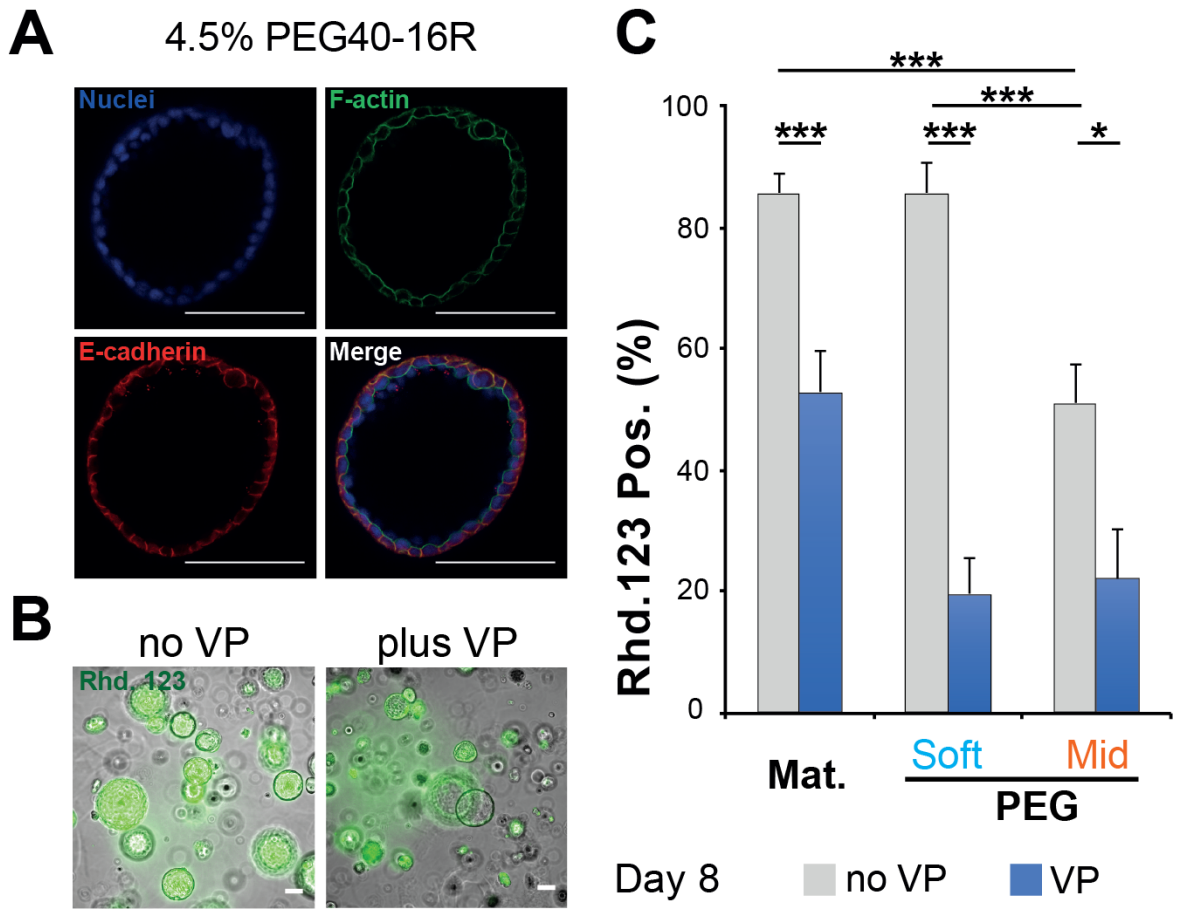

Figure 44: Encapsulated cells remain accessible for biological assays.

Phenotypic and functional assessment of Normal Rat Cholangiocytes (NRC) cysts produced in both polyethylene glycol and Matrigel hydrogels. ***(A)*** *Scanning confocal microphotographs of immunostained NRC cysts after 10 days of culture. Both structures stain positive for actin (apically) and E-cadherin (basolateraly).* ***(B, C)*** *Wide field microphotographs and subsequent quantification showing the accumulation of rhodamine 123 (Rhd. 123) in the lumen of NRC cysts. Adding the channel blocking agent verapamil (VP) reduced this accumulation. Scale bar = 100µm.*

Rhodamine intake

We also pursued a functional assay relying on smaller molecules: Rhodamine 123 (0.38 kDa) intake and Multi-Drug Resistance transporter 1 (MDR1) reversal by verapamil (0.45 kDa). Here, we found that 1 h incubation in 50 µM Rhodamine 123 was more than sufficient to perform this assay. After several washes and a 2h incubation prior to imaging, we could observe that formed cysts (Matrigel and PEG hydrogels) could accumulate rhodamine in their lumen (Figure 44B, C). If this protocol was done after a 30 min exposure of the hydrogel to 50 µM verapamil, this accumulation was blocked.

On the functional level, this clearly indicates that the accumulation of rhodamine is resulting from MDR1 activity and not passive diffusion. Furthermore, we could show that the frequency of rhodamine accumulating cysts was reduced when matrix stiffness was increased (Figure 44 C).

On the engineering level, we note that PEG40-16R hydrogels revealed themselves promising for cell encapsulation, considering (a) their biocompatibility, (b) their ease of tuning to investigate the impact of several chemical and physical factors independently, and (c) their compatibility with biological assays, even when relying on large molecules such as antibodies.

c) Discussion

In 2003, the team of Matthias Lutolf described the properties of a PEG hydrogel crosslinked by cysteine-bearing peptides[183, 187]. Interestingly, said peptides were MMP sensitive and allowed encapsulated cells to degrade their local microenvironment. Indeed, being limited in size by their surrounding matrix has been a shortcoming of many synthetic hydrogels.

We benefited from this side project to investigate the impact of addition of terminator peptides on hydrogel stiffness. Indeed, we had found in the literature examples of experiments in which this impact was overlooked[350]. This sadly weakens the conclusion we can draw, since addition of terminator molecule is expected to have the same effect as stoichiometric imbalance: increased swelling ratio, decreased stiffness. Since this could also be perceived favorably by the encapsulated cells, drawing conclusion is hazardous.

For that reason, it is preferable to investigate the mechanical properties of all chemical conditions. In this case, addition of 1200 µM RGD to 6.5% was roughly equivalent to a loss of 20% of its PE content. Investigating upfront the two (physical and chemical) properties allowed us to decouple their respective role in cyst formation and growth.

In later experiments, we witnessed the possibility to access structures encapsulated in this PEG hydrogel, even with large molecules such as antibodies, though the incubation times had to be largely revised, as reported above.

SECTION IV
CONCLUSION, PERSPECTIVES

This doctoral project has allowed us to develop a novel microfluidic organ-on-chip system that uses hydrogels as force transducers. The Idea was to provide a plateform capable of reconstituting the full breadth of physical cues (matrix stiffness, sheer stress and strain) that exist at several “mobile” tissue locations.

Developing such a chip presented a certain number of challenges, among which:

- Characterizing hydrogel and identify recipes with relevant mechanical properties.
- Design of a microfluidic setup allowing the independent control of flow and actuation.
- Characterizing its deformation upon submission to pressure.
- Re-design of the proof-of-concept chip.
- Producing a structured intestinal epithelium.
- Characterization of polarity and barrier function of the epithelium.

A large data base has been constituted on PEG hydrogels. Several hundreds of samples have been characterized and can serve as a starting point for the future projects of the team. Biocompatible hydrogels, allowing encapsulation or not, covering a large range of storage modulus (from 0.5 to 25 kPa) are now available.

The conception of a practical microfluidic setup was paved with difficulties essentially linked to the obtention of fabrication yields compatible with downstream biological experiments. Today, a robust setup is available at the platform to control flow and pressure within a microfluidic chip. However, the use of syringe pumps and pressure controller through distinct software still hinders our ability to synchronize two complex flow and pressure patterns. This did not pose problem, technically speaking, since we mostly investigated constant flows, but it is a shortcoming to acknowledge. In addition, gathering all commands through a single software could also go with efforts to multiplex the hardware, in order to increase the throughput.

The deformation of the hydrogel layer in three dimensions necessitated that we addressed it with a novel tool. Here, the usual landmark tracking in 2D from which stretch measurement is easy could not be used. Moreover, the hydrogel layer was too thick (compared to its width) to be assimilated to a flat sheet. This led to the development of an analysis tool that could hopefully be useful elsewhere in the future.

While preliminary results seemed to indicate stretching of the cells cultivated on the surface of the high-pressure channel, we had to go back to the drawing board after detailed mapping of the hydrogel deformation was achieved. This led to the development of a second version of the HAHL chip. At the same time, the PDMS-hydrogel assembly step has been greatly improved, necessitating less dexterity and allowing for softer gels to be included in the chip.

Production of a simple intestinal epithelium was achieved relying on Caco-2/TC7 cells. Screening of various flow and actuation condition was made possible by the microfluidic setup conceived, and led, in the best flow conditions, to visible structuration of the epithelium. Said structuration has been shown to be correctly polarized, and to ensure a proper barrier function towards 4 kDa molecules.

Lastly, prospective work has been done towards the identification of hydrogel recipes suitable for encapsulation.

Overall, we have demonstrated that the HAHL chip can be used to derive a gut on chip model sitting on soft matter. Proper benchmarking against existing solutions is still needed to better define strength and weaknesses. However, we can clearly see that unlike other systems “Gut on HAHL” can be used to quantify the impact of elastic modulus of the substrate on the gut epithelium. It is also reasonable to think the HAHL devices could be developed further to encompass a 3rd and a 4th type of cells namely mesenchymal and immune cells in order to add extra layers of emulation.

On the short term, addressing the following questions will be key to judge the potential reach of the HAHL concept.

(1) How thin should the hydrogel layer be to avoid the apparition of a compression region on the high-pressure side? Can it be achieved while maintaining good resistance to fatigue?
(2) In thick HAHL systems, can we capitalize on that heterogeneous mechanical response and link it to epithelial cell / pathogen behavior? The idea there will be to demonstrate that the combination of compression and strain area further improve biomimicry.

(3) How to couple 3D cell culture in PEG Hydrogels with the HAHL technology? While the chemistry is perfectly compatible, a mechanical conundrum will have to be resolved: How to lower the elasticity of the synthetic gel in order to ease cell culture while maintaining good level of handling?
(4) Can we capitalize on the MMP sensitivity of hydrogel to permit immune cell invasion?
(5) Would it be possible to structure the actuated PEG substrate in order to add pre-imposed topographic features?

All together this original HAHL body of work shows encouraging results that indicated that we are now one step closer to the development of next generation OoC devices moving away from the standard recapitulation of wound healing response in order to reach true tissue homeostasis on chip.

REFERENCES

1. Sato, T. et al. Single Lgr5 stem cells build crypt-villus structures in vitro without a mesenchymal niche. *Nature* **459**, 262-265 (2009).
2. Wufuer, M. et al. Skin-on-a-chip model simulating inflammation, edema and drug-based treatment. *Scientific Reports* **6**, 37471 (2016).
3. Franco, C. & Gerhardt, H. Blood vessels on a chip. *Nature* **488**, 465-466 (2012).
4. Ahn, S.I. et al. Microengineered human blood–brain barrier platform for understanding nanoparticle transport mechanisms. *Nature Communications* **11**, 175 (2020).
5. Huh, D. et al. Reconstituting organ-level lung functions on a chip. *Science* **328**, 1662-1668 (2010).
6. Grassart, A. et al. Bioengineered Human Organ-on-Chip Reveals Intestinal Microenvironment and Mechanical Forces Impacting Shigella Infection. *Cell Host & Microbe* **26**, 435-444.e434 (2019).
7. Kim, H.J., Huh, D., Hamilton, G. & Ingber, D.E. Human gut-on-a-chip inhabited by microbial flora that experiences intestinal peristalsis-like motions and flow. *Lab Chip* **12**, 2165-2174 (2012).
8. Kim, S., Lee, H., Chung, M. & Jeon, N.L. Engineering of functional, perfusable 3D microvascular networks on a chip. *Lab Chip* **13**, 1489-1500 (2013).
9. Beaurivage, C. et al. Development of a human primary gut-on-a-chip to model inflammatory processes. *Scientific Reports* **10**, 21475 (2020).
10. Zamprogno, P. et al. Second-generation lung-on-a-chip with an array of stretchable alveoli made with a biological membrane. *Communications Biology* **4**, 168 (2021).
11. Kyle, R.A., Steensma, D.P. & Shampo, M.A. Otto Wichterle—Inventor of the First Soft Contact Lenses. *Mayo Clinic Proceedings* **91**, e45-e46 (2016).
12. Petersen, O.W., Ronnov-Jessen, L., Howlett, A.R. & Bissell, M.J. Interaction with basement membrane serves to rapidly distinguish growth and differentiation pattern of normal and malignant human breast epithelial cells. *Proc Natl Acad Sci U S A* **89**, 9064-9068 (1992).
13. Convery, N. & Gadegaard, N. 30 years of microfluidics. *Micro and Nano Engineering* **2**, 76-91 (2019).

14. Engler, A.J., Sen, S., Sweeney, H.L. & Discher, D.E. Matrix elasticity directs stem cell lineage specification. *Cell* **126**, 677-689 (2006).
15. Gyles, D.A., Castro, L.D., Silva, J.O.C. & Ribeiro-Costa, R.M. A review of the designs and prominent biomedical advances of natural and synthetic hydrogel formulations. *European Polymer Journal* **88**, 373-392 (2017).
16. Gjorevski, N. et al. Designer matrices for intestinal stem cell and organoid culture. *Nature* **539**, 560-564 (2016).
17. Mueller, S.N. & Germain, R.N. Stromal cell contributions to the homeostasis and functionality of the immune system. *Nature Reviews Immunology* **9**, 618-629 (2009).
18. Hooke, R. Micrographia. (BoD–Books on Demand, 2020).
19. Schwann, T., Smith, H. & Schleiden, M.J. Microscopical researches into the accordance in the structure and growth of animals and plants. (Sydenham Society, London; 1847).
20. The Micro-Organisms of the Soil1. *Nature* **46**, 576-579 (1892).
21. Tyndall, J. Fragments of Science. (P. F. Collier, 1905).
22. Virchow, R. Die Cellularpathologie in ihrer Begründung auf physiologische und pathologische Gewebelehre: zwanzig Vorlesungen, gehalten während der Monate Februar, März und April 1858 im pathologischen Institute zu Berlin. (Hirschwald, 1859).
23. Mazzarello, P. A unifying concept: the history of cell theory. *Nat Cell Biol* **1**, E13-15 (1999).
24. Rodríguez-Hernández, C. et al. Cell culture: history, development and prospects. *Int J Curr Res Aca Rev* **2**, 188-200 (2014).
25. Carrel, A. & Burrows, M.T. CULTIVATION OF TISSUES IN VITRO AND ITS TECHNIQUE. *J Exp Med* **13**, 387-396 (1911).
26. Harrison, R.G. Observations on the living developing nerve fiber. *Proceedings of the Society for Experimental Biology and Medicine* **4**, 140-143 (1906).
27. Millet, L.J. & Gillette, M.U. Over a century of neuron culture: from the hanging drop to microfluidic devices. *Yale J Biol Med* **85**, 501-521 (2012).
28. Ringer, S. Concerning the Influence exerted by each of the Constituents of the Blood on the Contraction of the Ventricle. *J Physiol* **3**, 380-393 (1882).
29. Ringer, S. A further Contribution regarding the influence of the different Constituents of the Blood on the Contraction of the Heart. *J Physiol* **4**, 29-42.23 (1883).

30. Carrel, A. & Burrows, M.T. AN ADDITION TO THE TECHNIQUE OF THE CULTIVATION OF TISSUES IN VITRO. *J Exp Med* **14**, 244-247 (1911).
31. Carrel, A. ON THE PERMANENT LIFE OF TISSUES OUTSIDE OF THE ORGANISM. *J Exp Med* **15**, 516-528 (1912).
32. Rous, P. & Jones, F.S. A METHOD FOR OBTAINING SUSPENSIONS OF LIVING CELLS FROM THE FIXED TISSUES, AND FOR THE PLATING OUT OF INDIVIDUAL CELLS. *J Exp Med* **23**, 549-555 (1916).
33. Carrel, A. ARTIFICIAL ACTIVATION OF THE GROWTH IN VITRO OF CONNECTIVE TISSUE. *J Exp Med* **17**, 14-19 (1913).
34. Ebeling, A.H. A TEN YEAR OLD STRAIN OF FIBROBLASTS. *J Exp Med* **35**, 755-759 (1922).
35. Witkowski, J.A. Dr. Carrel's immortal cells. *Med Hist* **24**, 129-142 (1980).
36. Corner, G.W. Warren Harmon Lewis, June 17, 1870-July 3, 1964. *Biograph Memoirs Natl Acad Sci* **39**, 323-358 (1967).
37. Lewis, M.R. & Lewis, W.H. The cultivation of tissues from chick embryos in solutions of NaCl, CaCl2, KC1 and NaHCO3. *The Anatomical Record* **5**, 277-293 (1911).
38. Lewis, W.H. & Lewis, M.R. The cultivation of chick tissues in media of known chemical constitution. *The Anatomical Record* **6**, 207-211 (1912).
39. Lewis, M.R. THE IMPORTANCE OF DEXTROSE IN THE MEDIUM OF TISSUE CULTURES. *J Exp Med* **35**, 317-322 (1922).
40. Baker, L.E. & Carrel, A. ACTION ON FIBROBLASTS OF THE PROTEIN FRACTION OF EMBRYONIC TISSUE EXTRACT. *J Exp Med* **44**, 387-395 (1926).
41. Carrel, A. & Baker, L.E. THE CHEMICAL NATURE OF SUBSTANCES REQUIRED FOR CELL MULTIPLICATION. *J Exp Med* **44**, 503-521 (1926).
42. Baker, L.E. & Carrel, A. EFFECT OF THE AMINO ACIDS AND DIALYZABLE CONSTITUENTS OF EMBRYONIC TISSUE JUICE ON THE GROWTH OF FIBROBLASTS. *J Exp Med* **44**, 397-407 (1926).
43. Vogelaar, J.P. & Erlichman, E. A feeding solution for cultures of human fibroblasts. *The American Journal of Cancer* **18**, 28-38 (1933).
44. Baker, L.E. ARTIFICIAL MEDIA FOR THE CULTIVATION OF FIBROBLASTS, EPITHELIAL CELLS AND MONOCYTES. *Science* **83**, 605 (1936).
45. Yao, T. & Asayama, Y. Animal-cell culture media: History, characteristics, and current issues. *Reprod Med Biol* **16**, 99-117 (2017).

46. Foster, P.R. in Transfusion Medicine: Quo Vadis? What Has Been Achieved, What Is to Be Expected: Proceedings of the jubilee Twenty-Fifth International Symposium on Blood Transfusion, Groningen, 2000, Organized by the Sanquin Division Blood Bank Noord Nederland. (eds. C.T.S. Sibinga & J.D. Cash) 87-101 (Springer US, Boston, MA; 2001).

47. Stretton, A.O.W. The first sequence. Fred Sanger and insulin. *Genetics* **162**, 527-532 (2002).

48. Watson, J.D. & Crick, F.H. Molecular structure of nucleic acids; a structure for deoxyribose nucleic acid. *Nature* **171**, 737-738 (1953).

49. Wilkins, M.H.F., Stokes, A.R. & Wilson, H.R. Molecular Structure of Nucleic Acids: Molecular Structure of Deoxypentose Nucleic Acids. *Nature* **171**, 738-740 (1953).

50. Franklin, R.E. & Gosling, R.G. Molecular configuration in sodium thymonucleate. *Nature* **171**, 740-741 (1953).

51. Gey, G. Tissue culture studies of the proliferative capacity of cervical carcinoma and normal epithelium. *Cancer Res.* **12**, 264-265 (1952).

52. Skloot, R. (Unabridged. New York : Random House Audio, [2010] ℗2010, 2010).

53. LEWIS, W.H. NORMAL AND MALIGNANT CELLS. *Science* **81**, 545-553 (1935).

54. Fischer, A. & Davidsohn, F. Present Condition of a Twelve-Year Old Pure Strain of Carcinoma Cells in vitro. *Nature* **143**, 436-437 (1939).

55. Earle, W.R. & Chief, C.V. The Mode of Action of Methylcholanthrene on Cultures of Normal Tissues. *The American Journal of Cancer* **34**, 373-390 (1938).

56. Earle, W.R. & Voegtlin, C. A Further Study of the Mode of Action of Methylcholanthrene on Normal Tissue Cultures. *Public Health Reports (1896-1970)* **55**, 303-322 (1940).

57. Earle, W.R. & CRISP, L.R. Production of malignancy in vitro. *Journal* **4**, 147 (1943).

58. Sanford, K.K., Earle, W.R. & Likely, G.D. The growth in vitro of single isolated tissue cells. *J Natl Cancer Inst* **9**, 229-246 (1948).

59. Sanford, K.K., Hobbs, G.L. & Earle, W.R. The tumor-producing capacity of strain L mouse cells after 10 years in vitro. *Cancer Res* **16**, 162-166 (1956).

60. Tjio, J.H. & Puck, T.T. Genetics of somatic mammalian cells. II. Chromosomal constitution of cells in tissue culture. *J Exp Med* **108**, 259-268 (1958).

61. Green, I.J. Serial Propagation of Influenza B (Lee) Virus in a Transmissible Line of Canine Kidney Cells. *Science* **138**, 42-43 (1962).
62. Leighton, J., Estes, L.W., Mansukhani, S. & Brada, Z. A cell line derived from normal dog kidney (MDCK) exhibiting qualities of papillary adenocarcinoma and of renal tubular epithelium. *Cancer* **26**, 1022-1028 (1970).
63. Hayflick, L. & Moorhead, P.S. The serial cultivation of human diploid cell strains. *Experimental Cell Research* **25**, 585-621 (1961).
64. Eagle, H. The specific amino acid requirements of a mammalian cell (strain L) in tissue culture. *J Biol Chem* **214**, 839-852 (1955).
65. Eagle, H. The specific amino acid requirements of a human carcinoma cell (Stain HeLa) in tissue culture. *J Exp Med* **102**, 37-48 (1955).
66. Fischer, A., Astrup, T. & et al. Growth of animal tissue cells in artificial media. *Proc Soc Exp Biol Med* **67**, 40-46 (1948).
67. Fischer, A. Amino-acid metabolism of tissue cells in vitro. *Biochem J* **43**, 491-497 (1948).
68. Eagle, H. Nutrition needs of mammalian cells in tissue culture. *Science* **122**, 501-514 (1955).
69. Eagle, H. Amino acid metabolism in mammalian cell cultures. *Science* **130**, 432-437 (1959).
70. Mc, C.T., Maxwell, M. & Kruse, P.F., Jr. The amino acid requirements of the Jensen sarcoma in vitro. *Cancer Res* **19**, 591-595 (1959).
71. Dulbecco, R. & Freeman, G. Plaque production by the polyoma virus. *Virology* **8**, 396-397 (1959).
72. Moore, G.E., Ito, E., Ulrich, K. & Sandberg, A.A. Culture of human leukemia cells. *Cancer* **19**, 713-723 (1966).
73. Moore, G.E., Gerner, R.E. & Franklin, H.A. Culture of normal human leukocytes. *Jama* **199**, 519-524 (1967).
74. White, P.R. Cultivation of animal tissues in vitro in nutrients of precisely known constitution. *Growth* **10**, 231-289 (1946).
75. Jacoby, F. & Darke, S.J. Animal Tissue Culture with a Synthetic Medium. *Nature* **161**, 768-769 (1948).
76. Parker, R.C. Methods of tissue culture. *Methods of tissue culture.* (1950).

77. Evans, V.J. et al. Studies of nutrient media for tissue cells in vitro. II. An improved protein-free chemically defined medium for long-term cultivation of strain L-929 cells. *Cancer Res* **16**, 87-94 (1956).

78. Waymouth, C. Rapid proliferation of sublines of NCTC clone 929 (strain L) mouse cells in a simple chemically defined medium (MB 752/1). *J Natl Cancer Inst* **22**, 1003-1017 (1959).

79. McKeehan, W.L., Hamilton, W.G. & Ham, R.G. Selenium is an essential trace nutrient for growth of WI-38 diploid human fibroblasts. *Proc Natl Acad Sci U S A* **73**, 2023-2027 (1976).

80. Guilbert, L.J. & Iscove, N.N. Partial replacement of serum by selenite, transferrin, albumin and lecithin in haemopoietic cell cultures. *Nature* **263**, 594-595 (1976).

81. Hayashi, I. & Sato, G.H. Replacement of serum by hormones permits growth of cells in a defined medium. *Nature* **259**, 132-134 (1976).

82. Harrison, R.G. The outgrowth of the nerve fiber as a mode of protoplasmic movement. *Journal of Experimental Zoology* **9**, 787-846 (1910).

83. Ambrose, C.T. The Tissue Culture Laboratory of Dr. George Otto Gey 60 yrs ago as recalled by a former student. *In Vitro Cellular & Developmental Biology - Animal* **53**, 467-473 (2017).

84. Huzella, T. & Lengyel, J. Orientation de la croissance des cultures de tissus sur la trame fibrillaire artificielle coagulée de la solution de "collagène A" (Nageotte) par les forces de la cristallisation. *Compt. Rend. Soc. Biol.* **109**, 515-518 (1932).

85. Ehrmann, R.L. & Gey, G.O. The growth of cells on a transparent gel of reconstituted rat-tail collagen. *J Natl Cancer Inst* **16**, 1375-1403 (1956).

86. Amstein, C.F. & Hartman, P.A. Adaptation of plastic surfaces for tissue culture by glow discharge. *J Clin Microbiol* **2**, 46-54 (1975).

87. Hudis, M. in Techniques and Applications of Plasma Chemistry, Edn. John Wiley & Sons Inc. (ed. J.R.H.A.T. Bell) (1974).

88. Ramsey, W.S., Hertl, W., Nowlan, E.D. & Binkowski, N.J. Surface treatments and cell attachment. *In Vitro* **20**, 802-808 (1984).

89. Ryan, J.A. (2021).

90. Piez, K.A. History of extracellular matrix: a personal view. *Matrix Biol* **16**, 85-92 (1997).

91. Horwitz, A.R. The origins of the molecular era of adhesion research. *Nature reviews. Molecular cell biology* **13**, 805-811 (2012).

92. Hynes, R.O. Integrins: a family of cell surface receptors. *Cell* **48**, 549-554 (1987).

93. Hynes, R.O. The emergence of integrins: a personal and historical perspective. *Matrix biology : journal of the International Society for Matrix Biology* **23**, 333-340 (2004).

94. Hauschka, S.D. & Konigsberg, I.R. The influence of collagen on the development of muscle clones. *Proc Natl Acad Sci U S A* **55**, 119-126 (1966).

95. Michalopoulos, G. & Pitot, H.C. Primary culture of parenchymal liver cells on collagen membranes. Morphological and biochemical observations. *Exp Cell Res* **94**, 70-78 (1975).

96. Emerman, J.T., Enami, J., Pitelka, D.R. & Nandi, S. Hormonal effects on intracellular and secreted casein in cultures of mouse mammary epithelial cells on floating collagen membranes. *Proc Natl Acad Sci U S A* **74**, 4466-4470 (1977).

97. Lee, E.Y., Parry, G. & Bissell, M.J. Modulation of secreted proteins of mouse mammary epithelial cells by the collagenous substrata. *J Cell Biol* **98**, 146-155 (1984).

98. Sabin, A.B. & Olitsky, P.K. Cultivation of Poliomyelitis Virus in vitro in Human Embryonic Nervous Tissue. *Proceedings of the Society for Experimental Biology and Medicine* **34**, 357-359 (1936).

99. Enders, J.F., Weller, T.H. & Robbins, F.C. Cultivation of the Lansing Strain of Poliomyelitis Virus in Cultures of Various Human Embryonic Tissues. *Science* **109**, 85-87 (1949).

100. Weller, T.H., Robbins, F.C. & Enders, J.F. Cultivation of poliomyelitis virus in cultures of human foreskin and embryonic tissues. *Proc Soc Exp Biol Med* **72**, 153-155 (1949).

101. Enders, J.F. SOME RECENT ADVANCES IN THE STUDY OF POLIOMYELITIS. *Medicine* **33** (1954).

102. NobelPrize.org, Vol. 2021 (1954).

103. Dulbecco, R. & Vogt, M. Plaque formation and isolation of pure lines with poliomyelitis viruses. *J Exp Med* **99**, 167-182 (1954).

104. SALK, J.E. A Plastic Plate for Use in Tests Involving Virus Hemagglutination and Other Similar Reactions. *Science* **108**, 749-749 (1948).

105. Diþu, L.M. et al. In vitro assessment of the antimicrobial activity of new N-acyl-thiourea derivatives. *ROMANIAN ARCHIVES* **26**, 41 (1962).

106. Catt, K. & Tregear, G.W. Solid-Phase Radioimmunoassay in Antibody-Coated Tubes. *Science* **158**, 1570-1572 (1967).

107. Engvall, E. & Perlmann, P. Enzyme-linked immunosorbent assay (ELISA). Quantitative assay of immunoglobulin G. *Immunochemistry* **8**, 871-874 (1971).

108. Blay, V., Tolani, B., Ho, S.P. & Arkin, M.R. High-Throughput Screening: today's biochemical and cell-based approaches. *Drug Discovery Today* **25**, 1807-1821 (2020).

109. Mullis, K. et al. Specific enzymatic amplification of DNA in vitro: the polymerase chain reaction. *Cold Spring Harb Symp Quant Biol* **51 Pt 1**, 263-273 (1986).

110. Quainoo, S. et al. Whole-Genome Sequencing of Bacterial Pathogens: the Future of Nosocomial Outbreak Analysis. *Clinical Microbiology Reviews* **30**, 1015-1063 (2017).

111. Bertelli, C. & Greub, G. Rapid bacterial genome sequencing: methods and applications in clinical microbiology. *Clinical Microbiology and Infection* **19**, 803-813 (2013).

112. Fleischmann, R.D. et al. Whole-Genome Random Sequencing and Assembly of Haemophilus influenzae Rd. *Science* **269**, 496-512 (1995).

113. Smith, H.O. & Welcox, K.W. A Restriction enzyme from Hemophilus influenzae: I. Purification and general properties. *Journal of Molecular Biology* **51**, 379-391 (1970).

114. Cohen, S.N., Chang, A.C., Boyer, H.W. & Helling, R.B. Construction of biologically functional bacterial plasmids in vitro. *Proc Natl Acad Sci U S A* **70**, 3240-3244 (1973).

115. Wirth, R., Friesenegger, A. & Fiedler, S. Transformation of various species of gram-negative bacteria belonging to 11 different genera by electroporation. *Molecular and General Genetics MGG* **216**, 175-177 (1989).

116. Palmiter, R.D. et al. Dramatic growth of mice that develop from eggs microinjected with metallothionein–growth hormone fusion genes. *Nature* **300**, 611-615 (1982).

117. Adli, M. The CRISPR tool kit for genome editing and beyond. *Nature Communications* **9**, 1911 (2018).

118. Hsu, Patrick D., Lander, Eric S. & Zhang, F. Development and Applications of CRISPR-Cas9 for Genome Engineering. *Cell* **157**, 1262-1278 (2014).

119. Ideker, T., Galitski, T. & Hood, L. A NEW APPROACH TO DECODING LIFE: Systems Biology. *Annual Review of Genomics and Human Genetics* **2**, 343-372 (2001).

120. Krewski, D. et al. Toxicity testing in the 21st century: a vision and a strategy. *J Toxicol Environ Health B Crit Rev* **13**, 51-138 (2010).

121. Guillouzo, A. & Guguen-Guillouzo, C. Evolving concepts in liver tissue modeling and implications for in vitro toxicology. *Expert Opin Drug Metab Toxicol* **4**, 1279-1294 (2008).

122. Demetrius, L. Aging in mouse and human systems: a comparative study. *Ann N Y Acad Sci* **1067**, 66-82 (2006).

123. Barber, E.D., Teetsel, N.M., Kolberg, K.F. & Guest, D. A comparative study of the rates of in vitro percutaneous absorption of eight chemicals using rat and human skin. *Fundamental and Applied Toxicology* **19**, 493-497 (1992).

124. Ross, J.H., Driver, J.H., Harris, S.A. & Maibach, H.I. Dermal absorption of 2,4-D: a review of species differences. *Regul Toxicol Pharmacol* **41**, 82-91 (2005).

125. Zhao, Y.H. et al. Evaluation of rat intestinal absorption data and correlation with human intestinal absorption. *Eur J Med Chem* **38**, 233-243 (2003).

126. Cao, X. et al. Why is it challenging to predict intestinal drug absorption and oral bioavailability in human using rat model. *Pharm Res* **23**, 1675-1686 (2006).

127. Russell, W.M.S. & Burch, R.L., Vol. 2021 (Johns Hopkins Bloomberg School of Public Health, 1959).

128. Olesen, S.P., Clapham, D.E. & Davies, P.F. Haemodynamic shear stress activates a K+ current in vascular endothelial cells. *Nature* **331**, 168-170 (1988).

129. Lansman, J.B., Hallam, T.J. & Rink, T.J. Single stretch-activated ion channels in vascular endothelial cells as mechanotransducers? *Nature* **325**, 811-813 (1987).

130. de Groot, R.P. et al. Microgravity decreases c-fos induction and serum response element activity. *J Cell Sci* **97 (Pt 1)**, 33-38 (1990).

131. Von Der Mark, K., Gauss, V., Von Der Mark, H. & MÜLler, P. Relationship between cell shape and type of collagen synthesised as chondrocytes lose their cartilage phenotype in culture. *Nature* **267**, 531-532 (1977).

132. Chen, C.S., Mrksich, M., Huang, S., Whitesides, G.M. & Ingber, D.E. Geometric control of cell life and death. *Science* **276**, 1425-1428 (1997).

133. Pelham, R.J., Jr. & Wang, Y.l. High resolution detection of mechanical forces exerted by locomoting fibroblasts on the substrate. *Mol Biol Cell* **10**, 935-945 (1999).

134. Parker, K.K. et al. Directional control of lamellipodia extension by constraining cell shape and orienting cell tractional forces. *Faseb J* **16**, 1195-1204 (2002).

135. Unadkat, H.V. et al. An algorithm-based topographical biomaterials library to instruct cell fate. *Proceedings of the National Academy of Sciences* **108**, 16565-16570 (2011).

136. Ullah, I., Subbarao, R.B. & Rho, G.J. Human mesenchymal stem cells - current trends and future prospective. *Biosci Rep* **35** (2015).

137. Bharti, D. et al. Differentiation potential of different regions-derived same donor human Wharton's jelly mesenchymal stem cells into functional smooth muscle-like cells. *Cell Tissue Res* **377**, 229-243 (2019).

138. Gilbert, P.M. et al. Substrate elasticity regulates skeletal muscle stem cell self-renewal in culture. *Science* **329**, 1078-1081 (2010).

139. Wang, N., Butler, J.P. & Ingber, D.E. Mechanotransduction across the cell surface and through the cytoskeleton. *Science* **260**, 1124-1127 (1993).

140. Ingber, D.E. & Ingber, D.E. Tensegrity: the architectural basis of cellular mechanotransduction. *Annu Rev Physiol* **59**, 575-599 (1997).

141. Mooney, D.J., Langer, R., Ingber, D.E. & Ingber, D.E. Cytoskeletal filament assembly and the control of cell spreading and function by extracellular matrix. *J Cell Sci* **108 (Pt 6)**, 2311-2320 (1995).

142. Wang, Y. & Riechmann, V. The role of the actomyosin cytoskeleton in coordination of tissue growth during Drosophila oogenesis. *Curr Biol* **17**, 1349-1355 (2007).

143. Peyton, S.R., Raub, C.B., Keschrumrus, V.P. & Putnam, A.J. The use of poly(ethylene glycol) hydrogels to investigate the impact of ECM chemistry and mechanics on smooth muscle cells. *Biomaterials* **27**, 4881-4893 (2006).

144. Iwamoto, H. et al. A p160ROCK-specific inhibitor, Y-27632, attenuates rat hepatic stellate cell growth. *J Hepatol* **32**, 762-770 (2000).

145. Zhao, Z. & Rivkees, S.A. Rho-associated kinases play an essential role in cardiac morphogenesis and cardiomyocyte proliferation. *Dev Dyn* **226**, 24-32 (2003).

146. Numaguchi, K., Eguchi, S., Yamakawa, T., Motley, E.D. & Inagami, T. Mechanotransduction of rat aortic vascular smooth muscle cells requires RhoA and intact actin filaments. *Circ Res* **85**, 5-11 (1999).

147. Liu, W.F., Nelson, C.M., Tan, J.L. & Chen, C.S. Cadherins, RhoA, and Rac1 are differentially required for stretch-mediated proliferation in endothelial versus smooth muscle cells. *Circ Res* **101**, e44-52 (2007).

148. Altman, G.H. et al. Cell differentiation by mechanical stress. *Faseb J* **16**, 270-272 (2002).

149. Wozniak, M.A. & Chen, C.S. Mechanotransduction in development: a growing role for contractility. *Nat Rev Mol Cell Biol* **10**, 34-43 (2009).

150. Terry, S., Jerman, J. & Angell, J. A gas chromatographic air analyzer fabricated on a silicon wafer. *IEEE Transactions on electronic devices.* **26**, 1880-1886 (1979).

151. Reyes, D.R., Iossifidis, D., Auroux, P.-A. & Manz, A. Micro Total Analysis Systems. 1. Introduction, Theory, and Technology. *Analytical Chemistry* **74**, 2623-2636 (2002).

152. Manz, A., Graber, N. & Widmer, H.M. Miniaturized total chemical analysis systems: A novel concept for chemical sensing. *Sensors and Actuators B: Chemical* **1**, 244-248 (1990).

153. Zhang, C. & Xing, D. Miniaturized PCR chips for nucleic acid amplification and analysis: latest advances and future trends. *Nucleic acids research* **35**, 4223-4237 (2007).

154. Wang, J. On-chip enzymatic assays. *ELECTROPHORESIS* **23**, 713-718 (2002).

155. Gérard, A. et al. High-throughput single-cell activity-based screening and sequencing of antibodies using droplet microfluidics. *Nature Biotechnology* **38**, 715-721 (2020).

156. Tan, J.L. et al. Cells lying on a bed of microneedles: An approach to isolate mechanical force. *Proceedings of the National Academy of Sciences* **100**, 1484-1489 (2003).

157. Liu, Y.J. et al. Confinement and low adhesion induce fast amoeboid migration of slow mesenchymal cells. *Cell* **160**, 659-672 (2015).

158. Orkin, R.W. et al. A murine tumor producing a matrix of basement membrane. *J Exp Med* **145**, 204-220 (1977).

159. Futaki, S. et al. Molecular basis of constitutive production of basement membrane components. Gene expression profiles of Engelbreth-Holm-Swarm tumor and F9 embryonal carcinoma cells. *J Biol Chem* **278**, 50691-50701 (2003).

160. Kleinman, H.K. et al. Basement membrane complexes with biological activity. *Biochemistry* **25**, 312-318 (1986).

161. Kubota, Y., Kleinman, H.K., Martin, G.R. & Lawley, T.J. Role of laminin and basement membrane in the morphological differentiation of human endothelial cells into capillary-like structures. *J Cell Biol* **107**, 1589-1598 (1988).

162. Kleinman, H.K. & Martin, G.R. Matrigel: basement membrane matrix with biological activity. *Semin Cancer Biol* **15**, 378-386 (2005).

163. Hughes, C.S., Postovit, L.M. & Lajoie, G.A. Matrigel: a complex protein mixture required for optimal growth of cell culture. *Proteomics* **10**, 1886-1890 (2010).

164. Soofi, S.S., Last, J.A., Liliensiek, S.J., Nealey, P.F. & Murphy, C.J. The elastic modulus of Matrigel™ as determined by atomic force microscopy. *Journal of Structural Biology* **167**, 216-219 (2009).

165. Aisenbrey, E.A. & Murphy, W.L. Synthetic alternatives to Matrigel. *Nature Reviews Materials* **5**, 539-551 (2020).

166. Benya, P.D. & Shaffer, J.D. Dedifferentiated chondrocytes reexpress the differentiated collagen phenotype when cultured in agarose gels. *Cell* **30**, 215-224 (1982).

167. Wang, F. et al. Reciprocal interactions between beta1-integrin and epidermal growth factor receptor in three-dimensional basement membrane breast cultures: a different perspective in epithelial biology. *Proc Natl Acad Sci U S A* **95**, 14821-14826 (1998).

168. Weaver, V.M. et al. Reversion of the malignant phenotype of human breast cells in three-dimensional culture and in vivo by integrin blocking antibodies. *J Cell Biol* **137**, 231-245 (1997).

169. Talbot, N.C. & Caperna, T.J. Proteome array identification of bioactive soluble proteins/peptides in Matrigel: relevance to stem cell responses. *Cytotechnology* **67**, 873-883 (2015).

170. Vukicevic, S. et al. Identification of multiple active growth factors in basement membrane matrigel suggests caution in interpretation of cellular activity related to extracellular matrix components. *Experimental Cell Research* **202**, 1-8 (1992).

171. Ravi, M., Paramesh, V., Kaviya, S.R., Anuradha, E. & Solomon, F.D.P. 3D Cell Culture Systems: Advantages and Applications. *Journal of Cellular Physiology* **230**, 16-26 (2015).

172. Baker, E.L., Bonnecaze, R.T. & Zaman, M.H. Extracellular matrix stiffness and architecture govern intracellular rheology in cancer. *Biophysical journal* **97**, 1013-1021 (2009).

173. Baker, E.L., Srivastava, J., Yu, D., Bonnecaze, R.T. & Zaman, M.H. Cancer cell migration: integrated roles of matrix mechanics and transforming potential. *PLoS One* **6**, e20355 (2011).

174. Sung, K.E. et al. Control of 3-dimensional collagen matrix polymerization for reproducible human mammary fibroblast cell culture in microfluidic devices. *Biomaterials* **30**, 4833-4841 (2009).

175. Lee, K.Y. & Mooney, D.J. Hydrogels for Tissue Engineering. *Chemical Reviews* **101**, 1869-1880 (2001).

176. DeForest, C.A. & Anseth, K.S. Advances in bioactive hydrogels to probe and direct cell fate. *Annu Rev Chem Biomol Eng* **3**, 421-444 (2012).

177. Zhu, J. Bioactive modification of poly(ethylene glycol) hydrogels for tissue engineering. *Biomaterials* **31**, 4639-4656 (2010).

178. Chatani, S., Nair, D.P. & Bowman, C.N. Relative reactivity and selectivity of vinyl sulfones and acrylates towards the thiol–Michael addition reaction and polymerization. *Polymer Chemistry* **4**, 1048-1055 (2013).

179. Nair, D.P. et al. The Thiol-Michael Addition Click Reaction: A Powerful and Widely Used Tool in Materials Chemistry. *Chemistry of Materials* **26**, 724-744 (2014).

180. Nguyen, Q.T., Hwang, Y., Chen, A.C., Varghese, S. & Sah, R.L. Cartilage-like mechanical properties of poly (ethylene glycol)-diacrylate hydrogels. *Biomaterials* **33**, 6682-6690 (2012).

181. Temenoff, J.S., Athanasiou, K.A., Lebaron, R.G. & Mikos, A.G. Effect of poly (ethylene glycol) molecular weight on tensile and swelling properties of oligo (poly (ethylene glycol) fumarate) hydrogels for cartilage tissue engineering. *Journal of Biomedical Materials Research: An Official Journal of The Society for Biomaterials, The Japanese Society for Biomaterials, and The Australian Society for Biomaterials and the Korean Society for Biomaterials* **59**, 429-437 (2002).

182. Bryant, S.J., Chowdhury, T.T., Lee, D.A., Bader, D.L. & Anseth, K.S. Crosslinking density influences chondrocyte metabolism in dynamically loaded photocrosslinked poly (ethylene glycol) hydrogels. *Ann Biomed Eng* **32**, 407-417 (2004).

183. Lutolf, M.P. et al. Synthetic matrix metalloproteinase-sensitive hydrogels for the conduction of tissue regeneration: Engineering cell-invasion characteristics. *Proceedings of the National Academy of Sciences* **100**, 5413-5418 (2003).

184. Phelps, E.A. et al. Maleimide Cross-Linked Bioactive PEG Hydrogel Exhibits Improved Reaction Kinetics and Cross-Linking for Cell Encapsulation and In Situ Delivery. *Advanced Materials* **24**, 64-70 (2012).

185. Phelps, E.A., Templeman, K.L., Thulé, P.M. & García, A.J. Engineered VEGF-releasing PEG–MAL hydrogel for pancreatic islet vascularization. *Drug Delivery and Translational Research* **5**, 125-136 (2015).

186. Kharkar, P.M., Rehmann, M.S., Skeens, K.M., Maverakis, E. & Kloxin, A.M. Thiol-ene click hydrogels for therapeutic delivery. *ACS Biomater Sci Eng* **2**, 165-179 (2016).

187. Lutolf, M.P., Raeber, G.P., Zisch, A.H., Tirelli, N. & Hubbell, J.A. Cell-Responsive Synthetic Hydrogels. *Advanced Materials* **15**, 888-892 (2003).

188. Raeber, G.P., Lutolf, M.P. & Hubbell, J.A. Molecularly engineered PEG hydrogels: a novel model system for proteolytically mediated cell migration. *Biophys J* **89**, 1374-1388 (2005).

189. Patterson, J. & Hubbell, J.A. Enhanced proteolytic degradation of molecularly engineered PEG hydrogels in response to MMP-1 and MMP-2. *Biomaterials* **31**, 7836-7845 (2010).

190. Chai, C. & Leong, K.W. Biomaterials approach to expand and direct differentiation of stem cells. *Mol Ther* **15**, 467-480 (2007).

191. Saha, K., Pollock, J.F., Schaffer, D.V. & Healy, K.E. Designing synthetic materials to control stem cell phenotype. *Curr Opin Chem Biol* **11**, 381-387 (2007).

192. Lutolf, M.P., Gilbert, P.M. & Blau, H.M. Designing materials to direct stem-cell fate. *Nature* **462**, 433-441 (2009).

193. Roorda, W.E., Boddé, H.E., De Boer, A.G., Bouwstra, J.A. & Junginer, H.E. Synthetic hydrogels as drug delivery systems. *Pharm Weekbl Sci* **8**, 165-189 (1986).

194. Pritchard, C.D. et al. An injectable thiol-acrylate poly(ethylene glycol) hydrogel for sustained release of methylprednisolone sodium succinate. *Biomaterials* **32**, 587-597 (2011).

195. Onaciu, A., Munteanu, R.A., Moldovan, A.I., Moldovan, C.S. & Berindan-Neagoe, I. Hydrogels Based Drug Delivery Synthesis, Characterization and Administration. *Pharmaceutics* **11**, 432 (2019).

196. Anderson, D.G., Levenberg, S. & Langer, R. Nanoliter-scale synthesis of arrayed biomaterials and application to human embryonic stem cells. *Nat Biotechnol* **22**, 863-866 (2004).

197. Rheinwald, J.G. & Green, H. Serial cultivation of strains of human epidermal keratinocytes: the formation of keratinizing colonies from single cells. *Cell* **6**, 331-343 (1975).

198. Nahmias, Y., Schwartz, R.E., Hu, W.-S., Verfaillie, C.M. & Odde, D.J. Endothelium-Mediated Hepatocyte Recruitment in the Establishment of Liver-like Tissue In Vitro. *Tissue Engineering* **12**, 1627-1638 (2006).

199. Eiraku, M. et al. Self-Organized Formation of Polarized Cortical Tissues from ESCs and Its Active Manipulation by Extrinsic Signals. *Cell Stem Cell* **3**, 519-532 (2008).

200. Barker, N. et al. Identification of stem cells in small intestine and colon by marker gene Lgr5. *Nature* **449**, 1003-1007 (2007).

201. Spence, J.R. et al. Directed differentiation of human pluripotent stem cells into intestinal tissue in vitro. *Nature* **470**, 105-109 (2011).

202. Workman, M.J. et al. Engineered human pluripotent-stem-cell-derived intestinal tissues with a functional enteric nervous system. *Nature medicine* **23**, 49-59 (2017).

203. Barker, N. et al. Lgr5+ve Stem Cells Drive Self-Renewal in the Stomach and Build Long-Lived Gastric Units In Vitro. *Cell Stem Cell* **6**, 25-36 (2010).

204. Stange, Daniel E. et al. Differentiated Troy+ Chief Cells Act as Reserve Stem Cells to Generate All Lineages of the Stomach Epithelium. *Cell* **155**, 357-368 (2013).

205. Taka-aki, K.N. et al. Generation of stomach tissue from mouse embryonic stem cells. *Nat Cell Biol* **17**, 984-993 (2015).

206. Takasato, M. et al. Directing human embryonic stem cell differentiation towards a renal lineage generates a self-organizing kidney. *Nat Cell Biol* **16**, 118-126 (2014).

207. Takasato, M. et al. Kidney organoids from human iPS cells contain multiple lineages and model human nephrogenesis. *Nature* **526**, 564-568 (2015).

208. Huch, M. et al. In vitro expansion of single Lgr5+ liver stem cells induced by Wnt-driven regeneration. *Nature* **494**, 247-250 (2013).

209. Takebe, T. et al. Vascularized and functional human liver from an iPSC-derived organ bud transplant. *Nature* **499**, 481-484 (2013).

210. Hu, H. et al. Long-term expansion of functional mouse and human hepatocytes as 3D organoids. *Cell* **175**, 1591-1606. e1519 (2018).

211. Zhang, L. et al. Establishing estrogen-responsive mouse mammary organoids from single Lgr5+ cells. *Cellular signalling* **29**, 41-51 (2017).

212. Jamieson, P.R. et al. Derivation of a robust mouse mammary organoid system for studying tissue dynamics. *Development* **144**, 1065-1071 (2017).

213. Nikolić, M.Z. et al. Human embryonic lung epithelial tips are multipotent progenitors that can be expanded in vitro as long-term self-renewing organoids. *Elife* **6**, e26575 (2017).

214. Dye, B.R. et al. In vitro generation of human pluripotent stem cell derived lung organoids. *elife* **4**, e05098 (2015).

215. Lancaster, M.A. et al. Cerebral organoids model human brain development and microcephaly. *Nature* **501**, 373-379 (2013).

216. Bagley, J.A., Reumann, D., Bian, S., Lévi-Strauss, J. & Knoblich, J.A. Fused cerebral organoids model interactions between brain regions. *Nature methods* **14**, 743-751 (2017).

217. Jo, J. et al. Midbrain-like organoids from human pluripotent stem cells contain functional dopaminergic and neuromelanin-producing neurons. *Cell Stem Cell* **19**, 248-257 (2016).

218. Hofer, M. & Lutolf, M.P. Engineering organoids. *Nat Rev Mater*, 1-19 (2021).

219. Clevers, H. Modeling development and disease with organoids. *Cell* **165**, 1586-1597 (2016).

220. Karthaus, W.R. et al. Identification of multipotent luminal progenitor cells in human prostate organoid cultures. *Cell* **159**, 163-175 (2014).

221. Tadokoro, T. et al. IL-6/STAT3 promotes regeneration of airway ciliated cells from basal stem cells. *Proceedings of the National Academy of Sciences* **111**, E3641-E3649 (2014).

222. Tsai, Y.-H. et al. In vitro patterning of pluripotent stem cell-derived intestine recapitulates in vivo human development. *Development* **144**, 1045-1055 (2017).

223. Völkner, M. et al. Retinal organoids from pluripotent stem cells efficiently recapitulate retinogenesis. *Stem cell reports* **6**, 525-538 (2016).

224. Chen, Y.-W. et al. A three-dimensional model of human lung development and disease from pluripotent stem cells. *Nat Cell Biol* **19**, 542-549 (2017).

225. Freedman, B.S. et al. Modelling kidney disease with CRISPR-mutant kidney organoids derived from human pluripotent epiblast spheroids. *Nature communications* **6**, 1-13 (2015).

226. Cugola, F.R. et al. The Brazilian Zika virus strain causes birth defects in experimental models. *Nature* **534**, 267-271 (2016).

227. Garcez, P.P. et al. Zika virus impairs growth in human neurospheres and brain organoids. *Science* **352**, 816-818 (2016).

228. Dang, J. et al. Zika virus depletes neural progenitors in human cerebral organoids through activation of the innate immune receptor TLR3. *Cell Stem Cell* **19**, 258-265 (2016).

229. Monteil, V. et al. Inhibition of SARS-CoV-2 Infections in Engineered Human Tissues Using Clinical-Grade Soluble Human ACE2. *Cell* **181**, 905-913.e907 (2020).

230. Broutier, L. et al. Human primary liver cancer–derived organoid cultures for disease modeling and drug screening. *Nature medicine* **23**, 1424-1435 (2017).

231. Zhou, T. et al. High-content screening in hPSC-neural progenitors identifies drug candidates that inhibit Zika virus infection in fetal-like organoids and adult brain. *Cell Stem Cell* **21**, 274-283. e275 (2017).

232. Fisher, R., Pusztai, L. & Swanton, C. Cancer heterogeneity: implications for targeted therapeutics. *British Journal of Cancer* **108**, 479-485 (2013).

233. Chin, L., Andersen, J.N. & Futreal, P.A. Cancer genomics: from discovery science to personalized medicine. *Nature Medicine* **17**, 297-303 (2011).

234. Vlachogiannis, G. et al. Patient-derived organoids model treatment response of metastatic gastrointestinal cancers. *Science* **359**, 920-926 (2018).

235. Driehuis, E. et al. Pancreatic cancer organoids recapitulate disease and allow personalized drug screening. *Proceedings of the National Academy of Sciences* **116**, 26580-26590 (2019).

236. Yan, H.H. et al. A comprehensive human gastric cancer organoid biobank captures tumor subtype heterogeneity and enables therapeutic screening. *Cell Stem Cell* **23**, 882-897. e811 (2018).

237. Baker, B.M. & Chen, C.S. Deconstructing the third dimension: how 3D culture microenvironments alter cellular cues. *J Cell Sci* **125**, 3015-3024 (2012).

238. Jensen, C. & Teng, Y. Is It Time to Start Transitioning From 2D to 3D Cell Culture? *Frontiers in Molecular Biosciences* **7** (2020).

239. Bertaux-Skeirik, N. et al. CD44 Plays a Functional Role in Helicobacter pylori-induced Epithelial Cell Proliferation. *PLOS Pathogens* **11**, e1004663 (2015).

240. Bartfeld, S. et al. In vitro expansion of human gastric epithelial stem cells and their responses to bacterial infection. *Gastroenterology* **148**, 126-136. e126 (2015).

241. Nash, T.J., Morris, K.M., Mabbott, N.A. & Vervelde, L. Inside-out chicken enteroids with leukocyte component as a model to study host–pathogen interactions. *Communications Biology* **4**, 377 (2021).

242. Lu, D. & Kassab, G.S. Role of shear stress and stretch in vascular mechanobiology. *Journal of the royal society interface* **8**, 1379-1385 (2011).

243. Abraham, G. et al. Growth and differentiation of primary and passaged equine bronchial epithelial cells under conventional and air-liquid-interface culture conditions. *BMC veterinary research* **7**, 1-13 (2011).

244. Kim, J., Koo, B.-K. & Knoblich, J.A. Human organoids: model systems for human biology and medicine. *Nat Rev Mol Cell Biol* **21**, 571-584 (2020).

245. Yin, X. et al. Engineering Stem Cell Organoids. *Cell Stem Cell* **18**, 25-38 (2016).

246. Brassard, J.A. & Lutolf, M.P. Engineering Stem Cell Self-organization to Build Better Organoids. *Cell Stem Cell* **24**, 860-876 (2019).

247. Viravaidya, K., Sin, A. & Shuler, M.L. Development of a microscale cell culture analog to probe naphthalene toxicity. *Biotechnology progress* **20**, 316-323 (2004).

248. Park, T.H. & Shuler, M.L. Integration of cell culture and microfabrication technology. *Biotechnol Prog* **19**, 243-253 (2003).

249. Sin, A. et al. The design and fabrication of three‐chamber microscale cell culture analog devices with integrated dissolved oxygen sensors. *Biotechnology progress* **20**, 338-345 (2004).

250. Khetani, S.R. & Bhatia, S.N. Microscale culture of human liver cells for drug development. *Nature Biotechnology* **26**, 120-126 (2008).

251. Beaurivage, C. et al. Development of a Gut-on-a-Chip Model for High Throughput Disease Modeling and Drug Discovery. *International Journal of Molecular Sciences* **20**, 5661 (2019).

252. Booth, R. & Kim, H. Characterization of a microfluidic in vitro model of the blood-brain barrier (μBBB). *Lab on a Chip* **12**, 1784-1792 (2012).

253. Brown, J.A. et al. Metabolic consequences of inflammatory disruption of the blood-brain barrier in an organ-on-chip model of the human neurovascular unit. *Journal of neuroinflammation* **13**, 1-17 (2016).

254. Vriend, J. et al. Flow stimulates drug transport in a human kidney proximal tubule-on-a-chip independent of primary cilia. *Biochimica et Biophysica Acta (BBA) - General Subjects* **1864**, 129433 (2020).

255. Nunes, S.S. et al. Biowire: a platform for maturation of human pluripotent stem cell–derived cardiomyocytes. *Nature Methods* **10**, 781-787 (2013).

256. van Duinen, V. et al. Robust and Scalable Angiogenesis Assay of Perfused 3D Human iPSC-Derived Endothelium for Anti-Angiogenic Drug Screening. *International Journal of Molecular Sciences* **21**, 4804 (2020).

257. Onakpoya, I.J., Heneghan, C.J. & Aronson, J.K. Post-marketing withdrawal of 462 medicinal products because of adverse drug reactions: a systematic review of the world literature. *BMC medicine* **14**, 1-11 (2016).

258. McAleer, C.W. et al. On the potential of in vitro organ-chip models to define temporal pharmacokinetic-pharmacodynamic relationships. *Scientific Reports* **9**, 9619 (2019).

259. Dame, K. & Ribeiro, A.J. Microengineered systems with iPSC-derived cardiac and hepatic cells to evaluate drug adverse effects. *Exp Biol Med (Maywood)* **246**, 317-331 (2021).

260. Oleaga, C. et al. Multi-Organ toxicity demonstration in a functional human in vitro system composed of four organs. *Scientific Reports* **6**, 20030 (2016).

261. Tanumihardja, E. et al. Measuring Both pH and O2 with a Single On-Chip Sensor in Cultures of Human Pluripotent Stem Cell-Derived Cardiomyocytes to Track Induced Changes in Cellular Metabolism. *ACS Sensors* **6**, 267-274 (2021).

262. Sung, J.H., Choi, J.-r., Kim, D. & Shuler, M.L. Fluorescence optical detection in situ for real-time monitoring of cytochrome P450 enzymatic activity of liver cells in multiple microfluidic devices. *Biotechnol Bioeng* **104**, 516-525 (2009).

263. Wang, Y.I., Abaci, H.E. & Shuler, M.L. Microfluidic blood-brain barrier model provides in vivo-like barrier properties for drug permeability screening. *Biotechnol Bioeng* **114**, 184-194 (2017).

264. Kimura, H., Yamamoto, T., Sakai, H., Sakai, Y. & Fujii, T. An integrated microfluidic system for long-term perfusion culture and on-line monitoring of intestinal tissue models. *Lab on a Chip* **8**, 741-746 (2008).

265. Park, S.E., Georgescu, A. & Huh, D. Organoids-on-a-chip. *Science* **364**, 960-965 (2019).

266. Nikolaev, M. et al. Homeostatic mini-intestines through scaffold-guided organoid morphogenesis. *Nature* **585**, 574-578 (2020).

267. Sanchez-Esteban, J. et al. Mechanical stretch promotes alveolar epithelial type II cell differentiation. *Journal of Applied Physiology* **91**, 589-595 (2001).

268. Shyer, A.E. et al. Villification: how the gut gets its villi. *Science* **342**, 212-218 (2013).

269. Campbell, J., Berry, J. & Liang, Y. in Shackelford's Surgery of the Alimentary Tract, 2 Volume Set (Eighth Edition). (ed. C.J. Yeo) 817-841 (Elsevier, Philadelphia; 2019).

270. Chelakkot, C., Ghim, J. & Ryu, S.H. Mechanisms regulating intestinal barrier integrity and its pathological implications. *Experimental & Molecular Medicine* **50**, 1-9 (2018).

271. Fleming, M.A., Ehsan, L., Moore, S.R. & Levin, D.E. The Enteric Nervous System and Its Emerging Role as a Therapeutic Target. *Gastroenterology Research and Practice* **2020**, 8024171 (2020).

272. Costa, M., Brookes, S.J. & Hennig, G.W. Anatomy and physiology of the enteric nervous system. *Gut* **47 Suppl 4**, iv15-iv26 (2000).

273. Guiu, J. & Jensen, K.B. From Definitive Endoderm to Gut-a Process of Growth and Maturation. *Stem Cells Dev* **24**, 1972-1983 (2015).

274. Krause, W.J. Brunner's glands: a structural, histochemical and pathological profile. *Prog Histochem Cytochem* **35**, 259-367 (2000).

275. Jung, C., Hugot, J.-P. & Barreau, F. Peyer's Patches: The Immune Sensors of the Intestine. *Int J Inflam* **2010**, 823710-823710 (2010).

276. Barker, N. Adult intestinal stem cells: critical drivers of epithelial homeostasis and regeneration. *Nat Rev Mol Cell Biol* **15**, 19-33 (2014).

277. Bevins, C.L. & Salzman, N.H. Paneth cells, antimicrobial peptides and maintenance of intestinal homeostasis. *Nat Rev Microbiol* **9**, 356-368 (2011).

278. Yousefi, M., Li, L. & Lengner, C.J. Hierarchy and Plasticity in the Intestinal Stem Cell Compartment. *Trends in cell biology* **27**, 753-764 (2017).

279. Crawley, S.W., Mooseker, M.S. & Tyska, M.J. Shaping the intestinal brush border. *J Cell Biol* **207**, 441-451 (2014).

280. Helander, H.F. & Fändriks, L. Surface area of the digestive tract - revisited. *Scand J Gastroenterol* **49**, 681-689 (2014).

281. Mabbott, N.A., Donaldson, D.S., Ohno, H., Williams, I.R. & Mahajan, A. Microfold (M) cells: important immunosurveillance posts in the intestinal epithelium. *Mucosal Immunol* **6**, 666-677 (2013).

282. Keita, Å.V. et al. Characterization of antigen and bacterial transport in the follicle-associated epithelium of human ileum. *Laboratory Investigation* **86**, 504-516 (2006).

283. Powell, D.W., Pinchuk, I.V., Saada, J.I., Chen, X. & Mifflin, R.C. Mesenchymal cells of the intestinal lamina propria. *Annu Rev Physiol* **73**, 213-237 (2011).

284. van den Brink, G.R. Hedgehog signaling in development and homeostasis of the gastrointestinal tract. *Physiol Rev* **87**, 1343-1375 (2007).

285. Walker, M.R., Patel, K.K. & Stappenbeck, T.S. The stem cell niche. *J Pathol* **217**, 169-180 (2009).

286. Yen, T.H. & Wright, N.A. The gastrointestinal tract stem cell niche. *Stem Cell Rev* **2**, 203-212 (2006).

287. Roulis, M. & Flavell, R.A. Fibroblasts and myofibroblasts of the intestinal lamina propria in physiology and disease. *Differentiation* **92**, 116-131 (2016).

288. Owens, B.M.J. & Simmons, A. Intestinal stromal cells in mucosal immunity and homeostasis. *Mucosal Immunol* **6**, 224-234 (2013).

289. van der Flier, L.G. & Clevers, H. Stem cells, self-renewal, and differentiation in the intestinal epithelium. *Annu Rev Physiol* **71**, 241-260 (2009).

290. Li, X. et al. Deconvoluting the intestine: molecular evidence for a major role of the mesenchyme in the modulation of signaling cross talk. *Physiol Genomics* **29**, 290-301 (2007).

291. Gregorieff, A. et al. Expression pattern of Wnt signaling components in the adult intestine. *Gastroenterology* **129**, 626-638 (2005).

292. Sukegawa, A. et al. The concentric structure of the developing gut is regulated by Sonic hedgehog derived from endodermal epithelium. *Development* **127**, 1971-1980 (2000).

293. Sommer, F. & Bäckhed, F. The gut microbiota — masters of host development and physiology. *Nature Reviews Microbiology* **11**, 227-238 (2013).

294. Smith, K., McCoy, K.D. & Macpherson, A.J. Use of axenic animals in studying the adaptation of mammals to their commensal intestinal microbiota. *Seminars in Immunology* **19**, 59-69 (2007).

295. Sjögren, K. et al. The gut microbiota regulates bone mass in mice. *Journal of Bone and Mineral Research* **27**, 1357-1367 (2012).

296. Mostafa, R.-M., Moustafa, Y.M. & Hamdy, H. Interstitial cells of Cajal, the Maestro in health and disease. *World J Gastroenterol* **16**, 3239-3248 (2010).

297. Deloose, E., Janssen, P., Depoortere, I. & Tack, J. The migrating motor complex: control mechanisms and its role in health and disease. *Nat Rev Gastroenterol Hepatol* **9**, 271-285 (2012).

298. Lennernäs, H. Intestinal permeability and its relevance for absorption and elimination. *Xenobiotica* **37**, 1015-1051 (2007).

299. Estudante, M., Morais, J.G., Soveral, G. & Benet, L.Z. Intestinal drug transporters: an overview. *Adv Drug Deliv Rev* **65**, 1340-1356 (2013).

300. Fernandez, M.I. et al. A newborn mouse model for the study of intestinal pathogenesis of shigellosis. *Cellular Microbiology* **5**, 481-491 (2003).

301. Rey, C. et al. Transcytosis subversion by M cell-to-enterocyte spread promotes Shigella flexneri and Listeria monocytogenes intracellular bacterial dissemination. *PLOS Pathogens* **16**, e1008446 (2020).

302. Williams, P.C.M. & Berkley, J.A. Guidelines for the treatment of dysentery (shigellosis): a systematic review of the evidence. *Paediatr Int Child Health* **38**, S50-S65 (2018).

303. Andoh, A., Bamba, S., Brittan, M., Fujiyama, Y. & Wright, N.A. Role of intestinal subepithelial myofibroblasts in inflammation and regenerative response in the gut. *Pharmacology & Therapeutics* **114**, 94-106 (2007).

304. Baumgart, D.C. & Sandborn, W.J. Crohn's disease. *The Lancet* **380**, 1590-1605 (2012).

305. Atreya, R. & Neurath, M.F. Molecular pathways controlling barrier function in IBD. *Nature Reviews Gastroenterology & Hepatology* **12**, 67-68 (2015).

306. Moyer, M.P. Culture of human gastrointestinal epithelial cells. *Proc Soc Exp Biol Med* **174**, 12-15 (1983).

307. Fogh, J., Orfeo, T., Tiso, J. & Sharkey, F.E. Establishment of human colon carcinoma lines in nude mice. *Exp Cell Biol* **47**, 136-144 (1979).

308. Le Ferrec, E. et al. In vitro models of the intestinal barrier. The report and recommendations of ECVAM Workshop 46. European Centre for the Validation of Alternative methods. *Altern Lab Anim* **29**, 649-668 (2001).

309. Antunes, F., Andrade, F., Ferreira, D., Nielsen, H.M. & Sarmento, B. Models to predict intestinal absorption of therapeutic peptides and proteins. *Curr Drug Metab* **14**, 4-20 (2013).

310. Lesuffleur, T., Barbat, A., Dussaulx, E. & Zweibaum, A. Growth adaptation to methotrexate of HT-29 human colon carcinoma cells is associated with their ability to differentiate into columnar absorptive and mucus-secreting cells. *Cancer Res* **50**, 6334-6343 (1990).

311. Hilgendorf, C. et al. Caco-2 versus Caco-2/HT29-MTX co-cultured cell lines: permeabilities via diffusion, inside- and outside-directed carrier-mediated transport. *J Pharm Sci* **89**, 63-75 (2000).

312. Kernéis, S., Bogdanova, A., Kraehenbuhl, J.P. & Pringault, E. Conversion by Peyer's patch lymphocytes of human enterocytes into M cells that transport bacteria. *Science* **277**, 949-952 (1997).

313. des Rieux, A. et al. An improved in vitro model of human intestinal follicle-associated epithelium to study nanoparticle transport by M cells. *Eur J Pharm Sci* **30**, 380-391 (2007).

314. van der Lubben, I.M. et al. Transport of chitosan microparticles for mucosal vaccine delivery in a human intestinal M-cell model. *J Drug Target* **10**, 449-456 (2002).

315. Lai, Y.H. & D'Souza, M.J. Microparticle transport in the human intestinal M cell model. *J Drug Target* **16**, 36-42 (2008).

316. Kadiyala, I., Loo, Y., Roy, K., Rice, J. & Leong, K.W. Transport of chitosan-DNA nanoparticles in human intestinal M-cell model versus normal intestinal enterocytes. *Eur J Pharm Sci* **39**, 103-109 (2010).

317. Pocock, K. et al. Intestine-on-a-Chip Microfluidic Model for Efficient in Vitro Screening of Oral Chemotherapeutic Uptake. *ACS Biomater Sci Eng* **3**, 951-959 (2017).

318. Imura, Y., Asano, Y., Sato, K. & Yoshimura, E. A Microfluidic System to Evaluate Intestinal Absorption. *Analytical Sciences* **25**, 1403-1407 (2009).

319. Kim, H.J. & Ingber, D.E. Gut-on-a-Chip microenvironment induces human intestinal cells to undergo villus differentiation. *Integr Biol (Camb)* **5**, 1130-1140 (2013).

320. Vila, A. et al. Hydrogel co-networks of gelatine methacrylate and poly(ethylene glycol) diacrylate sustain 3D functional in vitro models of intestinal mucosa. *Biofabrication* **12**, 025008 (2020).

321. Yu, J., Peng, S., Luo, D. & March, J.C. In vitro 3D human small intestinal villous model for drug permeability determination. *Biotechnol Bioeng* **109**, 2173-2178 (2012).

322. Hidalgo, I.J., Raub, T.J. & Borchardt, R.T. Characterization of the Human Colon Carcinoma Cell Line (Caco-2) as a Model System for Intestinal Epithelial Permeability. *Gastroenterology* **96**, 736-749 (1989).

323. Ma, C., Peng, Y., Li, H. & Chen, W. Organ-on-a-Chip: A New Paradigm for Drug Development. *Trends Pharmacol Sci* **42**, 119-133 (2021).

324. Esch, E.W., Bahinski, A. & Huh, D. Organs-on-chips at the frontiers of drug discovery. *Nat Rev Drug Discov* **14**, 248-260 (2015).

325. Ronaldson-Bouchard, K. & Vunjak-Novakovic, G. Organs-on-a-Chip: A Fast Track for Engineered Human Tissues in Drug Development. *Cell Stem Cell* **22**, 310-324 (2018).

326. Even-Ram, S., Artym, V. & Yamada, K.M. Matrix control of stem cell fate. *Cell* **126**, 645-647 (2006).

327. Mammoto, T., Mammoto, A. & Ingber, D.E. Mechanobiology and Developmental Control. *Annual Review of Cell and Developmental Biology* **29**, 27-61 (2013).

328. Lee, D.A., Knight, M.M., Campbell, J.J. & Bader, D.L. Stem cell mechanobiology. *Journal of Cellular Biochemistry* **112**, 1-9 (2011).

329. Martino Mikaël, M. et al. Engineering the Growth Factor Microenvironment with Fibronectin Domains to Promote Wound and Bone Tissue Healing. *Science Translational Medicine* **3**, 100ra189-100ra189 (2011).

330. Martino, M.M. et al. Controlling integrin specificity and stem cell differentiation in 2D and 3D environments through regulation of fibronectin domain stability. *Biomaterials* **30**, 1089-1097 (2009).

331. Zhu, J. & Marchant, R.E. Design properties of hydrogel tissue-engineering scaffolds. *Expert Rev Med Devices* **8**, 607-626 (2011).

332. Vroman, B. & LaRusso, N.F. Development and characterization of polarized primary cultures of rat intrahepatic bile duct epithelial cells. *Lab Invest* **74**, 303-313 (1996).

333. de Groen, P.C., Vroman, B., Laakso, K. & LaRusso, N.F. Characterization and growth regulation of a rat intrahepatic bile duct epithelial cell line under hormonally defined, serum-free conditions. *In Vitro Cell Dev Biol Anim* **34**, 704-710 (1998).

334. EmulateBio., Vol. 2021 (Emulate Bio, 2019).

335. Altay, G. in Faculty of Pharmacy and Food Sciences, Vol. Doctoral Thesis 342 (University of Barcelona, 2018).

336. Zheng, W. et al. A microfluidic flow-stretch chip for investigating blood vessel biomechanics. *Lab on a Chip* **12**, 3441-3450 (2012).

337. Varone, A. et al. "A novel Organ-Chip system emulates three-dimensional architecture of the human epithelia and allows fine control of mechanical forces acting on it.". *bioRxiv*, 2020.2008.2002.233338 (2020).

338. Campillo, N. et al. A Novel Chip for Cyclic Stretch and Intermittent Hypoxia Cell Exposures Mimicking Obstructive Sleep Apnea. *Frontiers in Physiology* **7** (2016).

339. Yoshimoto, K. et al. Recapitulation of Human Embryonic Heartbeat to Promote Differentiation of Hepatic Endoderm to Hepatoblasts. *Front Bioeng Biotechnol* **8**, 568092 (2020).

340. Ingber, D. Mechanobiology and diseases of mechanotransduction. *Annals of medicine* **35**, 564-577 (2003).

341. Rutkowski, J.M. & Swartz, M.A. A driving force for change: interstitial flow as a morphoregulator. *Trends in Cell Biology* **17**, 44-50 (2007).

342. Steinway, S.N., Saleh, J., Koo, B.K., Delacour, D. & Kim, D.H. Human Microphysiological Models of Intestinal Tissue and Gut Microbiome. *Front Bioeng Biotechnol* **8**, 725 (2020).

343. Kamble, H. et al. An Electromagnetically Actuated Double-Sided Cell-Stretching Device for Mechanobiology Research. *Micromachines (Basel)* **8**, 256 (2017).

344. Shin, W. & Kim, H.J. Intestinal barrier dysfunction orchestrates the onset of inflammatory host–microbiome cross-talk in a human gut inflammation-on-a-chip. *Proceedings of the National Academy of Sciences* **115**, E10539-E10547 (2018).

345. Henry, O.Y.F. et al. Organs-on-chips with integrated electrodes for trans-epithelial electrical resistance (TEER) measurements of human epithelial barrier function. *Lab on a Chip* **17**, 2264-2271 (2017).

346. Lea, T. in The Impact of Food Bioactives on Health: in vitro and ex vivo models. (eds. K. Verhoeckx et al.) 103-111 (Springer International Publishing, Cham; 2015).

347. Sun, H., Chow, E.C., Liu, S., Du, Y. & Pang, K.S. The Caco-2 cell monolayer: usefulness and limitations. *Expert Opin Drug Metab Toxicol* **4**, 395-411 (2008).

348. Sambuy, Y. et al. The Caco-2 cell line as a model of the intestinal barrier: influence of cell and culture-related factors on Caco-2 cell functional characteristics. *Cell Biol Toxicol* **21**, 1-26 (2005).

349. Funfak, A. et al. Biophysical Control of Bile Duct Epithelial Morphogenesis in Natural and Synthetic Scaffolds. *Frontiers in Bioengineering and Biotechnology* **7** (2019).

350. Enemchukwu, N.O. et al. Synthetic matrices reveal contributions of ECM biophysical and biochemical properties to epithelial morphogenesis. *Journal of Cell Biology* **212**, 113-124 (2015).

APPENDIX A
PUBLISHED ARTICLE

frontiers in Bioengineering and Biotechnology

ORIGINAL RESEARCH
published: 13 December 2019
doi: 10.3389/fbioe.2019.00417

Biophysical Control of Bile Duct Epithelial Morphogenesis in Natural and Synthetic Scaffolds

Anette Funfak[1], *Latifa Bouzhir*[2], *Emilie Gontran*[2], *Nicolas Minier*[1,3], *Pascale Dupuis-Williams*[2,4*†] *and Samy Gobaa*[1*†]

[1] Institut Pasteur, Biomaterials and Microfluidics Core Facility, Paris, France, [2] Université Paris-Saclay, UMR-S1174 INSERM, Orsay, France, [3] Université de Technologie de Compiègne, Alliance Sorbonne Université, Compiègne, France, [4] ESPCI, PSL University, Paris, France

OPEN ACCESS

Edited by:
Elena Martinez,
Institute for Bioengineering of Catalonia (IBEC), Spain

Reviewed by:
Sharon DeMorrow,
University of Texas at Austin, United States
Romina Mancinelli,
Sapienza University of Rome, Italy

***Correspondence:**
Pascale Dupuis-Williams
pascale.dupuis-williams@u-psud.fr
Samy Gobaa
samy.gobaa@pasteur.fr

†These authors have contributed equally to this work

Specialty section:
This article was submitted to Tissue Engineering and Regenerative Medicine, a section of the journal Frontiers in Bioengineering and Biotechnology

Received: 02 October 2019
Accepted: 29 November 2019
Published: 13 December 2019

Citation:
Funfak A, Bouzhir L, Gontran E, Minier N, Dupuis-Williams P and Gobaa S (2019) Biophysical Control of Bile Duct Epithelial Morphogenesis in Natural and Synthetic Scaffolds. Front. Bioeng. Biotechnol. 7:417. doi: 10.3389/fbioe.2019.00417

The integration of bile duct epithelial cells (cholangiocytes) in artificial liver culture systems is important in order to generate more physiologically relevant liver models. Understanding the role of the cellular microenvironment on differentiation, physiology, and organogenesis of cholangiocytes into functional biliary tubes is essential for the development of new liver therapies, notably in the field of cholangiophaties. In this study, we investigated the role of natural or synthetic scaffolds on cholangiocytes cyst growth, lumen formation and polarization. We demonstrated that cholangiocyte cyst formation efficiency can be similar between natural and synthetic matrices provided that the mechanical properties of the hydrogels are matched. When using synthetic matrices, we also tried to understand the impact of elasticity, matrix metalloprotease-mediated degradation and integrin ligand density on cyst morphogenesis. We demonstrated that hydrogel stiffness regulates cyst formation. We found that controlling integrin ligand density was key in the establishment of large polarized cysts of cholangiocytes. The mechanism of lumen formation was found to rely on cell self-organization and proliferation. The formed cholangiocyte organoids showed a good MDR1 (multi drug resistance protein) transport activity. Our study highlights the advantages of fully synthetic scaffold as a tool to develop bile duct models.

Keywords: bile duct, microenvironment, organoids, hydrogels, 3D cell culture

INTRODUCTION

Cellular microenvironment cues, including surface topography, substrate rigidity and biochemical signals determine to a large extent the outcome of many biological processes (Tan et al., 2003; Gobaa et al., 2011; Unadkat et al., 2011). Strikingly, the exposure of stem cells to mechanical cues allows steering the differentiation process (Engler et al., 2006). Gaining control over the mechanical stress landscape of the cell was cornerstone in the development of successful organ-on-chip and strategies (Huh et al., 2013; Benam et al., 2016) and of advanced 3D culture systems (Gjorevski et al., 2016).

Recapitulating a physiological hepatic function *in vitro* is currently a very active line of research. Approaches, based on the use of primary adult hepatic cells (Broutier et al., 2016) or on the controlled differentiation of induced Pluripotent Stem Cells (iPSC) (Takebe et al., 2014) have led to the derivation of new organotypic models. These advanced cell culture systems were developed in order to improve on the physiological relevance of standard 2D culture hepatic cell lines.

Despite great successes (Broutier et al., 2016) in recapitulating the hepatic function *in vitro*, the inclusion of a biliary tree capable of removing the toxic metabolite is yet to be developed. The biliary tree is composed of intra and extra hepatic ducts organized in a complex network of interconnected tubes with luminal diameters ranging from $<15\,\mu m$ to a few mm capable of carrying the bile from the liver to the intestine (Roskams et al., 2004; Boyer, 2013). The bile ducts are lined with the epithelial cholangiocytes which regulate, through secretion and adsorption, the composition and flow of the bile (Bogert and LaRusso, 2007).

The biliary system is itself the target of a vast array of liver pathologies called cholangiopathies (Cheung et al., 2018) that account for a large proportion of liver transplants (Murray et al., 2005). Today's treatments of cholangiopathies consist mostly in either largely ineffective pharmacotherapies or in surgeries that are restricted to the extrahepatic large duct. Living donors of liver grafts often suffer from biliary complications like stricture formation, bile leaks and infection (De Assuncao et al., 2017).

The field of bile duct engineering, previously hindered by the lack of available cells, has recently benefited from progress in the understanding of biliary physiopathology and the availability of cholangiocytes cell lines or methods recapitulating differentiation of hepatic precursor cells, stem cells or iPSCs, using various mixtures of growth factors known to direct bile duct embryogenesis (Dianat et al., 2014; De Assuncao et al., 2015; Ogawa et al., 2015; Sampaziotis et al., 2015; Takayama et al., 2016). What remains to be explored when considering developing innovative liver therapies is to understand how the microenvironment guides the self-organization of cholangiocytes into functional biliary tubes (Shiojiri and Sugiyama, 2004; Raynaud et al., 2011).

Cell culture in 3D has shown that cholangiocytes possess *in vitro* morphogenetic capabilities in natural hydrogels like collagen or Matrigel (Ishida et al., 2001; Tanimizu et al., 2007; Hashimoto et al., 2008; Kido et al., 2015). The scaffolding properties of Matrigel help supporting the 3D reorganization of adult cells. The production of "cholangioids" in Matrigel from healthy cholangiocytes versus issued from patients with primary sclerosing cholangitis (PSC) (Soroka et al., 2019) has recently exemplified their interest for the study of pathogenicity of biliary diseases and their putative use in the identification of therapeutic targets (Loarca et al., 2017). Matrigel embedding is also used as a final step in most cholangiocytes differentiation protocols, to assess their capacity to organize in biliary cysts (Dianat et al., 2014; De Assuncao et al., 2015; Ogawa et al., 2015; Sampaziotis et al., 2015; Takayama et al., 2016). However, relaying on hydrogels based on natural extracellular matrix (ECM) clearly hinders the mechanistic understanding of organogenesis or cysts formation as these scaffolds prohibits the decoupling of the biophysical and biochemical signaling. Similarly, liver stiffness is a key marker of liver pathology (Wells, 2008; Mueller and Sandrin, 2010) and marks the development of chronic fibrotic diseases (Saneyasu et al., 2016). In this context using liver organoids to study disease progression begs for the development of hydrogel systems with tunable mechanical properties. Interestingly, the stiffness-dependent differentiation of cholangiocytes seems to be modulated by the biochemical nature of the used matrix (Kourouklis et al., 2016). This indicates the high level of intricacy of both the biochemical and biophysical cues for these finely regulated biological processes.

This complex, and sometime undefined, nature of ECM-based hydrogels including Matrigel (MT) hinders the mechanistic understanding of organogenesis in a dish. On the other hand, synthetic hydrogels technology, such as systems based on the polymerization of polyethylene glycol (PEG), underwent many developments in the last decades placing them at the top of the list of the most physiologically relevant yet fully defined substrates for cell culture (Gjorevski et al., 2016). Today, synthetic hydrogel systems gained key functionalities including physiological elastic moduli (Ranga et al., 2014), easy tethering of biochemical ligands (Mosiewicz et al., 2013) and matrix metalloprotease (MMP) mediated proteolytic degradation allowing cell migration (Lutolf and Hubbell, 2003). These engineered functionalities opened the door for the establishment of advanced and physiologically relevant assays in fully synthetic scaffolds including the production of intestinal organoids (Gjorevski et al., 2016), the differentiation of embryoid bodies into neural tubes (Ranga et al., 2016) and the production of epithelial cysts (Enemchukwu et al., 2016). Therefore, the side-by-side comparison of organotypic development in both synthetic (PEG) and natural (MT) hydrogels could help with defining the set of microenvironment features that are essential to the proper self-organization of the seeded cells.

Cholangiocytes, like most other epithelial cells are able, when embedded in natural ECM like Matrigel or collagen, to self-organize into polarized monolayers enclosing a central lumen termed cyst. These structures are good models for studying duct morphogenesis since they share with the tubes the same topology and the same organization of the epithelium, where the polarized cells are connected by adherens and tight junctions, thus ensuring secretion, cohesiveness, and coordinated growth of the monolayer. Here we report on the quantitative impacts of biochemical and biophysical cues on the development of cholangiocyte cysts *in vitro*. We demonstrate that cholangiocytes can organize and produce polarized cysts in both natural and synthetic scaffolds. We also show that the biophysical and biochemical parameters of the extracellular milieu are key for cyst morphogenesis. We also report on the dynamics of lumen formation and how this process is influenced by the extracellular milieu.

MATERIALS AND METHODS

Cell Culture

Normal Rat Cholangiocytes (NRC) cell line was obtained from N. LaRusso's laboratory (Vroman and LaRusso, 1996). The cells were cultured on collagen coated T25 flasks and maintained in DMEM F12 medium supplemented with 5% fetal bovine serum (Life Technologies), 1× Antibiotic-Antimycotic (Life Technologies) and growth active factors including Insulin (Life Technologies), Dexomethosane (Sigma), 3,3,5-Triiodo-L-thyroninen sodium salt (Sigma), Bovine Pituitary Extract (BPE, Life Technologies) were added as described in de Groen et al. (1998).

Hydrogel Formation

Synthetic hydrogels were formed by Michael-type addition of bicystein-bearing peptides onto star-shaped, vinylsulfone-functionalized, polyethylene glycol macromeres. Lyophilized peptides were ordered from Pepmic (China). Peptide sequences 16A (Ac-GCRD-GPQG↓I**A**GQ-DRCG-NH2) and 16R (Ac-GCRD-VPMS↓M**R**GG-DRCG-NH2) were chosen in order to ensure varying MMP sensitivity as established elsewhere (Lutolf and Hubbell, 2003; Patterson and Hubbell, 2010). An RGD peptide (Ac-GCGYG**RGD**SPG-NH2) was used at various concentrations in order to promote the integrin mediated adhesion of encapsulated cells. Briefly, peptides were resuspended in Milli-Q water to obtain a 12% (w/v) working solution. Before using these peptides to form hydrogel, we controlled their integrity and purity on a Bruker UltrafeXtreme MALDI-TOF/TOF instrumentation (Bruker-Daltonics, Germany). One microliter of peptide at 0.1 mg/ml was deposited on a MTP 384 ground steel target plate with 1 μl of 2,5-Dihydroxybenzoic acid (2,5-DHB) in 50% acetonitrile, 0.1% trifluoroacetic acid as matrix solution. Data were acquired using Flexcontrol software (Bruker-Daltonics, Germany) and shots were recorded in positive ion reflectron mode. Mass spectra were externally calibrated in the m/z range of 700–3,500 Da with a peptide calibration standard (Bruker-Daltonics, Germany) and analyzed with the Flexanalysis software (Bruker). Next, we performed an Ellman assay as per the manufacturer instructions in order to quantify free thiol concentration in each peptide working solution. The difference between theoretical and measured thiol concentration was taken in consideration in order to produce hydrogels with the desired Thiol (Th)/Vinyl Sulfone (VS) stoichiometry. Finally, we measured the peptide net content by hydrolyzing the samples in 1% phenol 6 N HCL for 20 and 48 h at 110°C in presence of known amount of NorLeucine as internal standard. After HCL evaporation the samples are analyzed on a L-8800 Hitachi amino acids analyzer (post-column derivatization with ninhydrin after ion-exchange chromatography separation).

Eight-arm polyethylene glycol-vinyl sulfone or PEG-VS 40 kDa macromeres were ordered as a custom synthesis from NOF (Japan). Lyophilized powder was dissolved in a 0.3 M, pH 7.5, HEPES buffer (Dominique Dutscher, France) at 12% (w/v). Hydrogel sterility was ensured by filtering both peptide and PEG-VS working solutions on a 0.22 μm syringe filter (Millex-GS, Merck). Polyethylene glycol (PEG) hydrogels were produced as described in Lutolf and Hubbell (2003). Rapidly, 4.5% (w/v) containing 100 μM RGD gels were formed by mixing 63 μl PEG-VS macromere (12% w/v) with 103 μl HEPES buffer, 2 μl RGD peptide (10 mM) and 40 μl NRC cells resuspended in HEPES buffer with a cell concentration of 1.5×10^6 cells/ml. In a second step we added 12 μl of 16R or 16A peptide working solutions (12% w/v). Before gelation, the mixture was pipetted up and down gently. Fifty microliters drops of gel mixture were sandwiched between two mirror-polished PTFE pieces separated with a 1 mm spacer in order to produce 50 μl hydrogel disks. The assemblage was then placed in a Heracell 150i incubator (ThermoFisher Scientific, Waltham, MA USA) at 37°C, 100% relative humidity for 30 min. Upon crosslinking, gel disks were demolded and transferred to a 12 well plate (Falcon® multiwell plate, Corning) loaded with the adequate cell culture medium.

For Matrigel experiments, NRC cells were first mixed with a 7 mg/ml growth factor reduced Matrigel (Corning) solution and then diluted to 3.5 mg/ml with pre-cooled NRC complete medium on ice with a cell concentration of 3×10^5 cells/ml. Before the filling of 8-well μ-slides with the Matrigel-cell mixture, the pre-cooled slides were coated with 50 μl 3.5 mg/ml Matrigel solution and polymerized for 15 min at 37°C and 5% CO_2. Subsequently 300 μl of Matrigel-cell mixture was pipetted in each well and polymerized for 15 min at 37°C and 5% CO_2 before adding cell culture medium.

For both hydrogel systems NRC cells were pre-dissociated by up and down pipetting of the cell suspension followed by a post-dissociation step using a 40 μm cell strainer (Merck). The dissociated cell suspension was then diluted to the aimed cell concentration and mixed with the hydrogel solutions. It is to mention, that the natural and synthetic hydrogel system required a different state of cell dissociation (low for PEG hydrogel and high for Matrigel) due to the system requirements and the inhibition of NRC cell migration in PEG hydrogels. This was achieved by the adjustment of the pre-dissociation step.

Rheology

The hydrogel shear modulus was obtained by rheometric measurement with a Kinexus Ultra Plus Rheometer (Malvern Panalytical, UK). Briefly, gels of different concentration were casted as cylinders of 4 mm in diameter after swelling in water overnight. The rheometer was fitted with a 4 mm geometry. Each gel disk was compressed to 80% of its nominal height in order to avoid slippage during the measurements. An amplitude sweep was performed to determine the linear viscoelasticity region (LVER) of the measured material. Shear moduli were extracted from a frequency sweep analysis performed with a constant 1% strain. The reported G' values were obtained at 0.5 Hz.

The hydrogel shear modulus for Matrigel was obtained by a direct polymerization of the polymer solution on the working stage of the rheometer. Therefore, samples of 314 μl were added to the center of the pre-cooled (4°C) lower working plate. The geometry of 20 mm was then immediately lowered before the gel started to form, to a working gap of 1 mm. For the polymerization of the polymer suspension, the temperature was increased stepwise with a rate of 5°C/min from 4 to 37°C and kept at 37°C during measurement. A solvent trap cover was used to prevent evaporation effects around the working stage. Rheometric measurements were performed at 0.5 Hz and a constant 0.1% strain.

Viability/Cytotoxicity Assay

PEG and Matrigel hydrogels were washed with PBS and then incubated for 30 min at 37°C, 5% CO_2 with 4 μM Ethidium homodimer-1 and 2 μM Calcein, AM (ThermoFisher scientific) in growth medium. After a second washing step, the gels were imaged as described below. In average 12 images were acquired per condition. Fluorescence intensity was measured after background correction and normalized for the variations in

cyst surface using ImageJ, an image analysis software available on the NCBI website (https://imagej.nih.gov/ij/).

Functionality Assays

To demonstrate the multidrug resistance protein 1 (MDR1) transporter activity of single or multi-lumen cysts, polyethylene glycol (PEG) and Matrigel hydrogels were treated with 50 μM rhodamine 123 (Rh123, Sigma) in serum free medium for 1 h at 37°C. After a washing step (3× in serum free medium) the hydrogels were incubated for 2 h at 37°C, 5% CO_2 in fresh complete medium. To inhibit the MDR1 transporter activity the cysts containing hydrogels were incubated with 50 μM verapamil (Sigma-Aldrich) at 37°C for 30 min before adding Rh123. The rhodamine assay was then repeated as described above. For the quantification of the Rh123 assay the number of cysts containing Rh 123 in the luminal space and the number of cysts showing Rh 123 signal only at the level of the epithelium (blocked cysts) were counted with ImageJ.

Immunostaining of the Cysts

Immunostaining were performed without extracting the NRC cysts from PEG hydrogel or Matrigel. The PEG hydrogels were washed with PBS and then fixed with 4% paraformaldehyde (PFA) overnight at 4°C. Cysts were permeabilized with 0.5% Triton X-100 in PBS for 1–2 h at 4°C and then blocked with 2% BSA, 0.1% Tween-20 in PBS for 3 h. The primary polyclonal anti-E-cadherin antibody (Thermo Fisher Scientific PA5-32178, 1: 400) was diluted in blocking solution and incubated for 2–4 days at 4°C. Unbound primary antibodies were washed by incubating the gels in blocking buffer (3 times, 10 min each). The secondary antibody Goat anti-Rabbit IgG (H+L), Alexa Fluor Plus 647 (Thermo Fisher Scientific A32733, 1:400) was diluted in blocking solution and incubated for 2–4 days at 4°C. Nuclei and f-actin filaments were stained by adding 10 μM Hoechst and 16.5 nM Phalloidin 488 (Thermo Fisher Scientific) in PBS containing 1% BSA. Gels were incubated for 2 days at 4°C. Stained gels were then washed intensively in PBS.

Matrigel hydrogels were washed with PBS and fixed with 4% paraformaldehyde and 5% sucrose in PBS. Cyst were permeabilized with 0.5% Triton X-100 in PBS for 30 min and then blocked with 0.1% BSA and 1% goat serum for 30 min at RT. The primary polyclonal anti-E-cadherin antibody (Thermo Fisher Scientific PA5-32178, 1: 400) and 16.5 nM Phalloidin 488 (Thermo Fisher Scientific) were diluted in blocking solution and incubated overnight at 4°C. The Matrigel gels were washed by incubation in PBS containing 0.05% Tween (3 times, 10 min each). The secondary antibody Goat anti-Rabbit IgG (H+L), Alexa Fluor Plus 647 (Thermo Fisher Scientific A32733, 1:400) was diluted in blocking solution and incubated for 1 h at RT. After washing, the gels were mounted with Prolong Gold antifade reagent (Invitrogen Molecular probes) containing DAPI for nuclei staining.

Imaging

Wide field microscopy was performed on an inverted axio Observer Z1 inverted microscope from Zeiss (Carl Zeiss Microscopy GmbH, Jena, Germany) equipped with an OrcaFlash 4 V2.0 camera (Hamamatsu, Hamamatsu city, Japan) and Plan-Apochromat phase 1 10× (NA, 0.45) or Plan-Apochromat phase 2 20× (NA, 0.5) objectives. In case of live imaging (cyst growth in PEG hydrogel) temperature and CO_2 were ensured with a PeCon incubator equipped with the corresponding CO_2 and temperature modules.

Confocal imaging was performed on an SP8 inverted microscope (Leica Microsystems, Germany) equipped with HC FLUOTAR L 25×/0.95 W 0.17 VISIR objective and a white laser system. Confocal imaging of cyst polarization in Matrigel was acquired with a confocal microscope Nikon Eclipse TE-2000-E equipped with a X20/0.45 Plan Fluor ELWD Ph1 DM objective (∞/0–2 WD 7.4).

Quantification of Cysts Growth and Morphology

For the quantification of cyst growth, cyst and lumen formation in PEG and Matrigel hydrogels up to 15 z-stacks per condition and time point were acquired. Between 2 and 3 z-stacks were taken from non-overlapping regions within a hydrogel. Z-stacks were performed from the bottom to the top of the hydrogel with fixed height and image sampling number for all condition. Cyst size, number of cysts and number of single- or multi-lumen formed per imaged z-stack was then analyzed using Matlab Image processing toolbox. The cyst formation frequency was determined by relating the cyst number per z-stack to the corresponding initial cell number per z-stack. Lumen formation was also characterized by staining for actin, E-cadherin, and DNA as described above.

Statistical Analysis

All values are expressed as mean±SEM except for the rheological and viability measurements (mean±SD). Statistical significance was determined using Kruskal-Wallis *t*-test. The dynamics of cyst formation and single lumen production were analyzed in R (3.6.0) or the R project for statistical computing downloadable from https://www.r-project.org/. The fitted curves were generated with the GLM function fed with the models: Cyst frequency ∼ scaffold * log(Day) and single lumen ∼ scaffold * exp(Day). The obtained *p*-values were corrected for multiple comparisons with the Benjamini and Yekutieli method (BY) (Benjamini and Yekutieli, 2001).

RESULTS

Normal Rat Cholangiocytes Form Cysts Upon Culture in 3D Scaffolds

Triggering morphogenetic processes and achieving high levels cell-self organization is best recapitulated when initiated in the presence of a three-dimensional support or scaffold. The initial objective of this study was to identify 3D microenvironments supportive of cholangiocytes self-organization. Based on observations made with other epithelial cell lines we first seeded Normal Rat Cholangiocytes (NRC) in both synthetic, fully defined polyethylene glycol (PEG) hydrogels and in natural extracellular matrix-based Matrigel (MT) (**Figure 1A**). We quickly confirmed that NRCs can survive and proliferate in both

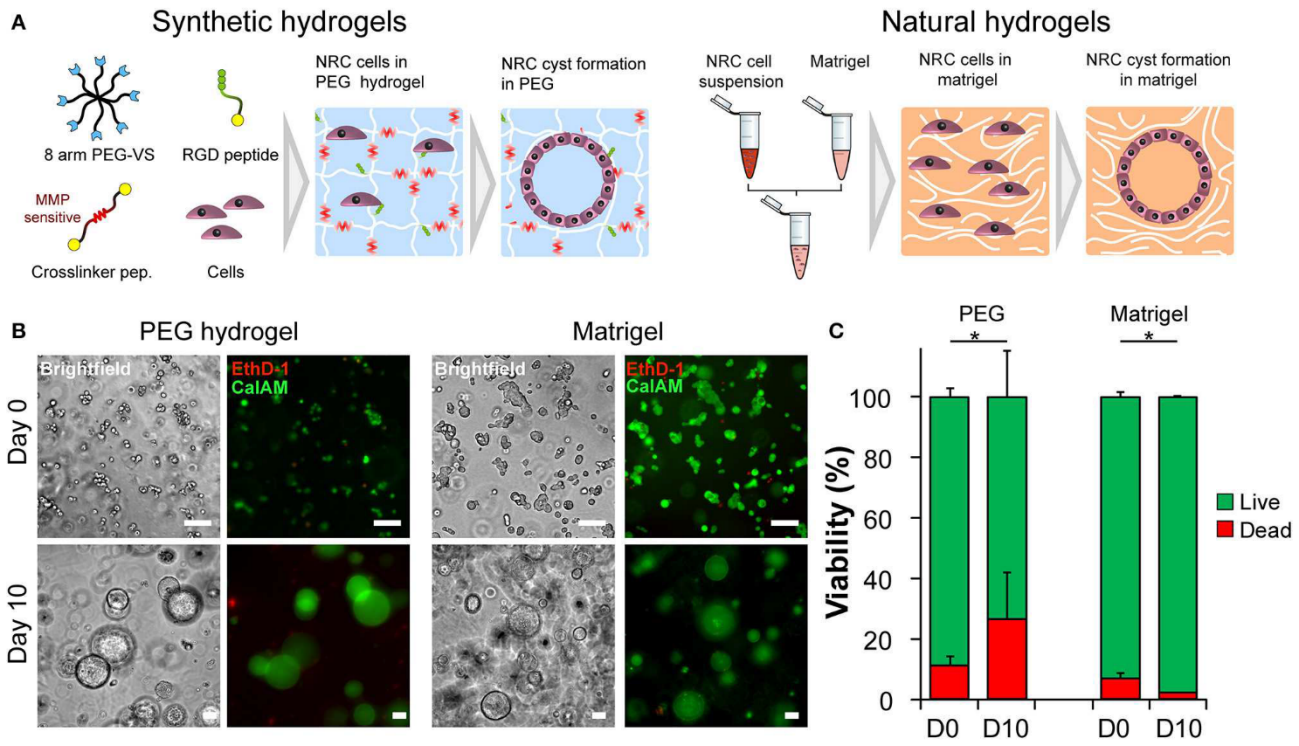

FIGURE 1 | Normal Rat Cholangiocyte (NRC) encapsulation and viability assessment. **(A)** Schematic representation of the used encapsulation procedure showing the differences between PEG (synthetic) and Matrigel (natural) hydrogels in terms of composition. In order to assess the self-organization capabilities of NRCs in synthetic and natural matrices, harvested cells were seeded into PEG hydrogels and Matrigel. Eight-arm PEG macromers bearing a vinyl sulfone function at the end of each arm were crosslinked with different peptides sensitive to matrix metalloprotease degradation in order to produce synthetic hydrogels. These synthetic PEG scaffolds were further functionalized with integrin ligands and proteolytic degradation capabilities in order to ensure NRC survival whereas in Matrigel encapsulated NRCs naturally formed cysts. **(B)** Brightfield and fluorescent images of live/dead staining of NRCs cultured in PEG and MT for 3 h or 10 days. The NRC cells when maintained for 10 days in culture formed hollow 3D structures, termed cysts. **(C)** When viability was assessed we found that the obtained structures were viable with PEG hydrogel causing slightly higher cell mortality. Represented PEG hydrogels condition corresponds to 4.5% (w/v) functionalized with 1,200 μM RGD ligand. $n = 3$. *Significant at $p < 0.05$ in a Kruskal-Wallis test. Error bars represent SD. Scale bar equal 100 μm.

conditions. Over a culture period of 10 days, cultured NRCs self-organized into hollow spheres or cysts where a very thin layer of epithelial cells marked the boundary between an inner lumen and the extracellular milieu (**Video S1**). We also observed that unlike in MT, NRCs cannot migrate in PEG and that cyst formation was mostly due to the seeding of small cell aggregates rather than single cells. When assessing cell viability, we found that encapsulated NRC showed globally a good viability in PEG and in MT. At day 10 a modest decrease in viability was observed in PEG, most probably due to the death of the cells that could not form cysts (**Figures 1B,C**). Overall, the growth kinetics (**Video S2**) in both materials allowed for the formation of cysts with sizes ranging from 40 to 800 μm. At this stage, we could not observe obvious differences between cysts cultured in either synthetic or natural scaffolds.

Matrix Stiffness and Integrin Ligand Density Modulate Cyst Formation

After confirming that NRC could self-organize into 3D structures reminiscent of polarized cysts. Unlike unpolarized cell aggregates, the obtained structure clearly showed a large lumen, cells organized as a monolayer that are staining positive for actin on the apical side and for E-cadherin on the basolateral side. First, we sought to investigate the determinants of cyst formation dynamics across gel composition (natural vs. synthetic matrices), matrix stiffness (or elastic modulus noted G') regime and integrin ligand density. Initially, we varied both the PEG concentration and the integrin ligand density (**Figure 2A**) of the synthetic hydrogel system while documenting the impact of PEG concentration of the elastic modulus (**Figure 2B**). Unlike ECM-based scaffolds, PEG hydrogels can be produced at varying elastic moduli while maintaining a constant molarity of integrin ligand (Gobaa et al., 2011). In this scenario the impact of increased RGD concentration on elastic modulus remains important and often overlooked (Enemchukwu et al., 2016). In order to quantify the impact of RGD peptides on the mechanical properties of the gel we measured the shear modulus of gels of different concentration while also varying RGD molarity. This showed that the incorporation of 100 μM RGD peptides to the hydrogel network had a very limited impact on the gel stiffness. Increasing the RGD dose up to 1,200 μM led to a 32% decrease of elastic modulus in the stiffest gels (**Figure 2B**). This RGD-mediated

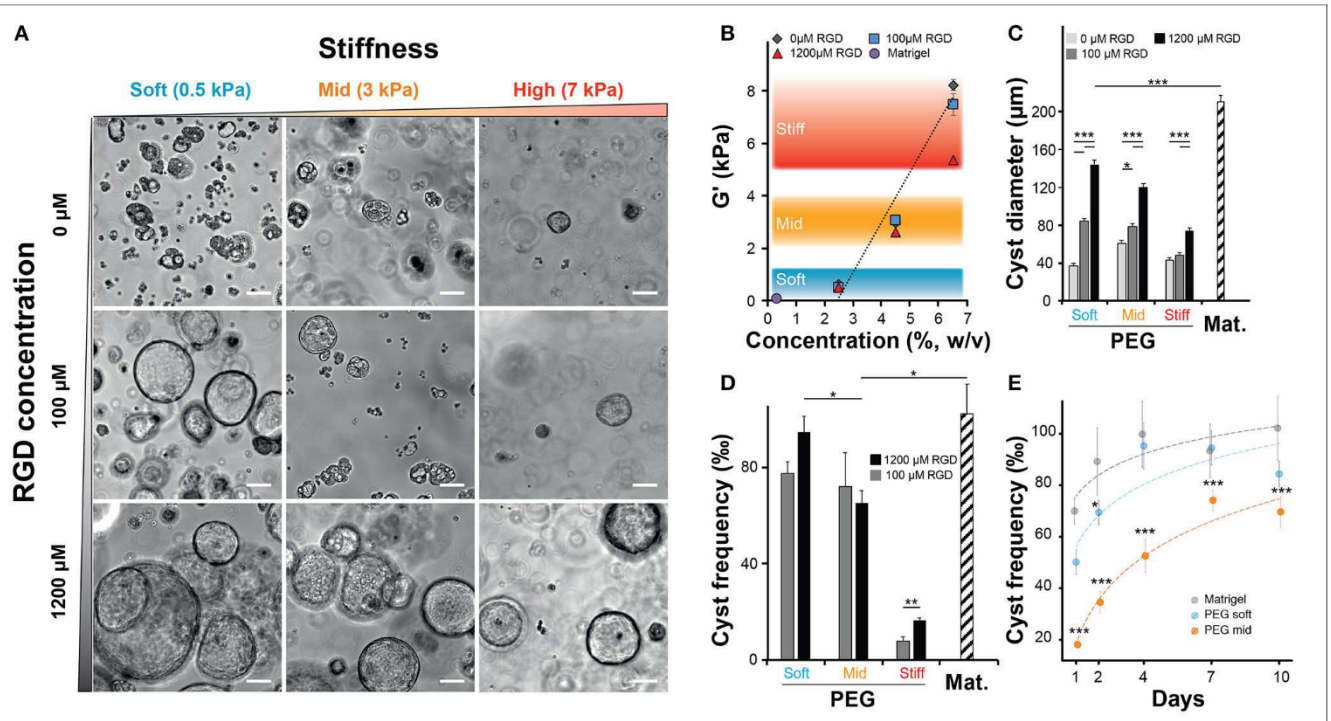

FIGURE 2 | Impact of matrix stiffness and integrin ligand density on Normal Rat Cholangiocytes (NRC) cyst formation. **(A)** Brightfield images of NRC cysts cultured for 10 days. NRCs were encapsulated in PEG hydrogels crosslinked with an MMP sensitive peptide (16R) and varying for concentration (w/v) and integrin ligand density. **(B)** Quantification of the impact of varying PEG and RGD concentration on the elastic modulus or G′ indicating the stiffness of produced PEG hydrogels. There we defined three stiffness domains including soft (2.5% PEG w/v, around 0.5 kPa), intermediate (4.5% PEG w/v, around 3 kPa) and stiff gels (6.5% PEG w/v, >5.5 kPa). The addition of up to 1,200 µM RGD had an overall moderate impact on the elasticity regime. **(C,D)** Quantification of cyst size and cyst frequency, respectively, at day 10 across soft, intermediate, and stiff polyethylene glycol gels and in Matrigel. **(E)** Dynamic study showing the evolution of the frequency of cyst production across the studied conditions. *, **, and *** Significant at $p < 0.05$, $p < 0.01$, and $p < 0.001$, respectively. $n = 4$. Error bars represent SEM. Scale bar equal 100 µm.

decrease in stiffness is relatively modest when compared to the impact of varying PEG concentration. Altogether, the measured rheological data showed that varying PEG concentration allowed the production of soft (around 0.5 kPa), intermediate (2–4 kPa) and stiff (around 7 kPa) gels while the measured stiffness of the Matrigel scaffolds was several orders of magnitude lower. Furthermore, we also investigated the impact of gel proteolytic degradation by tuning the matrix metalloproteases sensitivity of PEG hydrogels according to Patterson and Hubbell (2010). There we found that cell survival was independent of the proteolytic degradation of the substrate (**Figure S3**). We also demonstrated that the most sensitive gels crosslinked with the 16R peptide allowed systematically for a higher efficiency of cyst formation across the entire range of gel stiffness and RGD concentrations (**Figure S4**).

When we quantified the average cyst size, we found that softer gels favored the formation of larger cysts with the largest cysts being systematically produced in Matrigel (approximatively 20% larger than in the best PEG condition). In addition, this experiment also showed that the presence of RGD, in a dose dependent manner, was critical for the formation of large cysts (**Figure 2C**). Interestingly, the measurement of cyst sizes across the nine RGD/Stiffness conditions showed that while increasing RGD concentration in soft gels dramatically increased cyst size, it only had a much lower (but still significant $p < 0.001$) effect in stiff gels. This indicates that stiffness seems to be the parameter that determines the possible maximum cyst size while the addition of RGD allows for the realization of that potential. Conversely, high stiffness clearly overrides the effect of integrin engagement and prohibits the formation of larger NRC cysts. This trend was further confirmed when we looked at the frequency of cyst formation (**Figures 2D,E**). There we found that increasing the elastic modulus of the hydrogels significantly reduced the frequency of cyst formation. When looking at maximal cyst formation efficiency we found that Matrigel and soft synthetic gels (1,200 µM RGD) had reached comparable levels. We also found that removing RGD from soft PEG drastically limited cyst formation (**Figure S5**). Finally, when quantifying cyst formation efficiency over 10 days we confirmed that both soft PEG and Matrigel imposed a similar logarithmic increase. Increasing the matrix stiffness was sufficient to significantly ($p < 0.001$) reduce this efficiency while the logarithmic trend was maintained (**Figure 2E**). Taken together these data clearly show that both, cholangiocytes cyst formation frequency and size are determined to a large extent by variation in the elastic modulus of the substrate. The presence of RGD ligand in high concentration further improved this trend.

Establishment of Cyst Polarity

When cultured in 3D, epithelial cells such as the kidney cell line (MDCK) self-assemble in hollow spheres and recapitulate the morphogenetic program leading to the production of rudimentary epithelial organoids (McAteer et al., 1986). Detailed analysis showed that interactions between key integrins and the extracellular matrix (ECM) regulate the establishment of cell polarity and morphogenesis (Manninen, 2015). In both cases whether NRC cysts can become polarized upon cultured in a synthetic 3D scaffold was investigated first by immunochemistry and rhodamine transport assay. There we found that large NRC cysts stain positive for basolateral E-Cadherin and apical F-actin (**Figure 3A**; **Figure S6**). Canonical epithelial polarity was observed in cysts of different dimensions across the tested 3D culture conditions. NRC cysts with inverted polarity could also be observed as described elsewhere (Enemchukwu et al., 2016). However, these observations were very seldom and did appear to correlate with either stiffness or RGD concentration. When looking at the shape of the nuclei of the cholangiocytes lining the cyst wall, we found that in Matrigel these structures seemed to be more elongated and placed tangentially to the formed circle whereas in PEG the nuclei seemed rounder, organized into a mixed mono- and/or double-layer structure (**Figure 3A**). *In vivo*, the morphology of the nuclei in the lining of the bile duct seems to vary from round to oval with preferentially a basal localization in the cell. On the functional level we found that, in MT or in PEG hydrogels, formed cysts could accumulate rhodamine 123 in their lumen and that this accumulation was blocked by the addition of verapamil in the culture medium. This clearly indicates that the accumulation of rhodamine is resulting from transmembrane channel protein-multidrug resistance protein-1 (MDR1) activity and not passive diffusion (**Figure 3B**). Furthermore, we could show that the frequency of rhodamine accumulating cysts was reduced when matrix stiffness was increased (**Figure 3C**). These data suggest that NRC cysts cultured in either PEG or MT are showing apicobasal polarity and functioning as mature epithelial cysts.

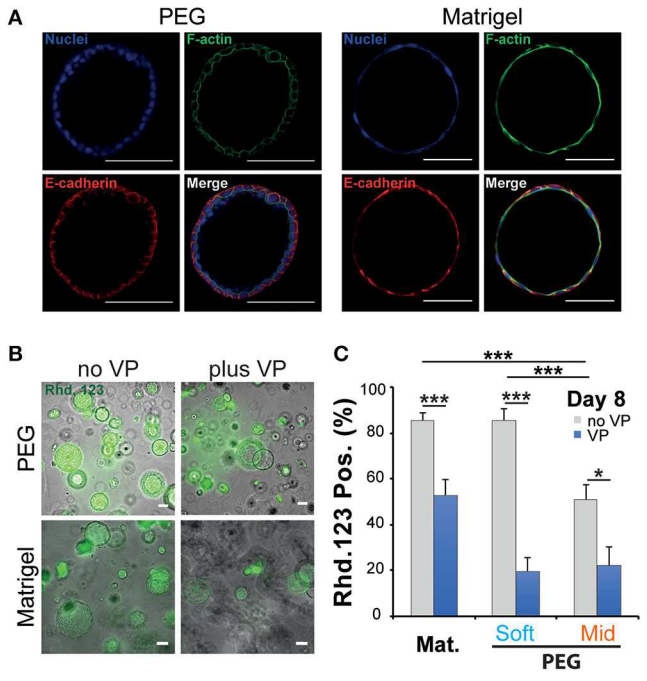

FIGURE 3 | Phenotypic and functional assessment of Normal Rat Cholangiocytes (NRC) cysts produced in both polyethylene glycol and Matrigel hydrogels. **(A)** Scanning confocal microphotographs of immunostained NRC cysts after 10 days of culture. Both structures stain positive for actin (apically) and E-cadherin (basolaterally). **(B,C)** Widefield microphotographs and subsequent quantification showing the accumulation of rhodamine 123 (Rhd. 123) in the lumen of NRC cysts. Adding the channel blocking agent verapamil (VP) reduced this accumulation. * and *** Significant at $p < 0.05$ and $p < 0.001$ respectively. $n = 4$. Error bars represent SEM. Scale bar equal 100 μm.

Morphogenesis and Lumen Formation

When imaging the different structures obtained after culturing NRC in PEG and MT hydrogels, we have identified different cell organizations including large cysts including a unique lumen bordered by a thin layer of cells (SL) (**Figure 3A**; **Video S1**), spherical cell structures containing multiple gaps (ML) (**Figure 4A**; **Figure S7**) and small and compact cell aggregates. We found that the hydrogel recipe was determining to a certain extent the frequency of each structure. Quantifications preformed on different scaffolding conditions showed that decreasing the hydrogel stiffness and increasing the RGD concentration increased the frequency of SL structures (**Figures 4B–D**). More interestingly the effect of stiffness seemed to plateau for gels between 2.5 and 4.5% (w/v) PEG. We observed that NRCs cultured in 2.5% PEG hydrogel ($G' \approx$ 0.5 kPa) showed a SL frequency of 73 and 56% for high and low RGD concentrations respectively. The formation of SL was decreased by 20% when using stiffer gels. An even further decrease was observed when using low RGD in the stiffest gels. This indicates that above a certain elasticity threshold (between 0.5 and 2.5 kPa) the luminal organization seems to be rather independent of the hydrogel stiffness whereas RGD density remains an important determinant for the formation of single lumen with normal polarity. Although comparable at day 10, the frequency of SL cyst formation did not appear to follow identical trajectories in PEG vs. MT. Observing the dynamics of SL cyst formation over the course of 10 days revealed that the formation of SL cysts seemed to follow an exponential law in PEG whereas cyst formation dynamics was found more linear in MT. These dynamics reveal that the gap in percent of SL cyst formation is strongly decreasing over time when comparing MT and PEG (**Figure 4C**). When investigating cyst organization in relation to size we found that ML cysts are significantly smaller than SL cysts. This observation remained true for longer observations (2 weeks plus) (**Figure S7**). We also found that limiting the dose of RGD clearly restricted the growth of the produced ML cysts (**Figure 4D**). This experiment also showed that cyst size and organization are not fully correlated and that the two parameters could respond to different microenvironment cues.

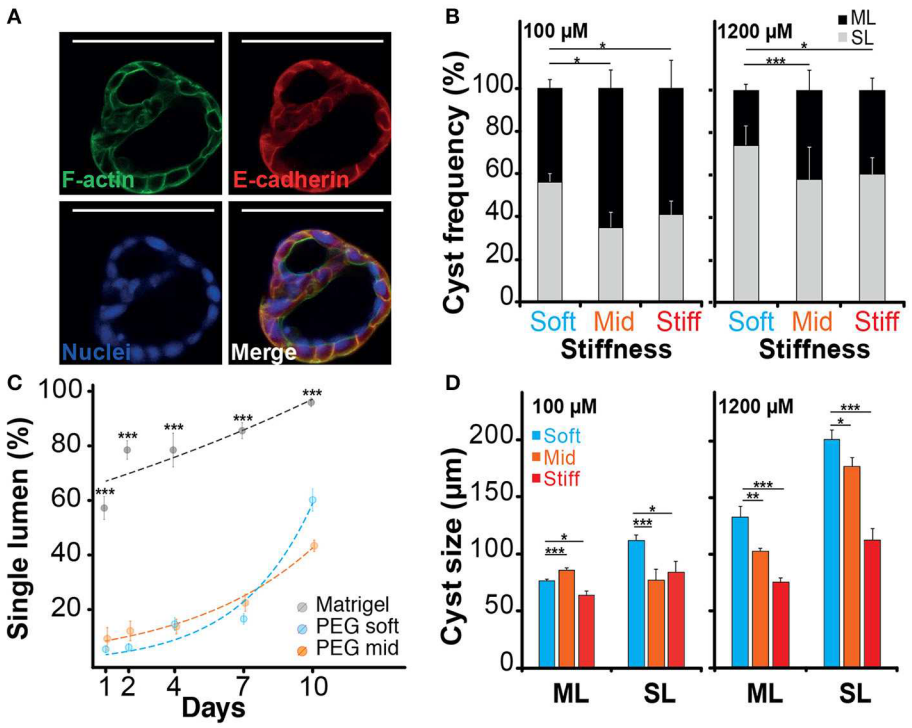

FIGURE 4 | Impact of the microenvironment on lumen formation. **(A)** Immunostaining of f-actin and E-cadherin localization in normal rat cholangiocyte (NRC) cyst with multi-lumen phenotype. The observation of Normal Rat Cholangiocytes (NRC) cysts formation in different matrices showed that some NRC cysts could comprise multiple lumens. **(B)** Quantification of single lumen formation of NRC cysts during 10 day. The quantifications showed that this phenomenon was prevalent in PEG hydrogel and marginal in Matrigel. We also found that the fraction of single lumen cysts in PEG tended to exponentially increase over time. **(C)** The analysis of the "multi-lumen" and "single-lumen" phenotype frequency indicated that a soft microenvironment containing 1,200 µM RGD caused the lowest rates of multi-lumen formation. **(D)** Finally, cyst size analysis showed that variation in RGD concentration seemed to alter the multi-lumen/single-lumen ratio. SL and ML is for single-lumen and multi-lumen, respectively. *, **, and *** Significant at $p < 0.05$, $p < 0.01$, and $p < 0.001$, respectively. $n = 4$. Error bars represent SEM. Scale bar equal 100 µm.

DISCUSSION

The ECM-cholangiocyte interaction is essential for the formation of the biliary tree. *In vitro,* the ECM is classically mimicked by natural hydrogels known to promote well-cholangiocyte differentiation and morphogenesis (Tanimizu et al., 2007). Understanding the role of the microenvironment cues on bile duct formation is clearly limited by the type of assays that can recapitulate this process *in vitro*. On one hand, hydrogels based on naturel ECM allow to faithfully recapitulate key morphogenetic processes (Tanimizu et al., 2007). However, mechanistic studies in these systems are difficult because of the intertwined biochemical and biophysical signaling. On the other hand, synthetic hydrogels are more amenable to experiment design and systematic variation (Ranga et al., 2014) but less efficient in the support of biological processes. In this work we clearly benefitted from these developments in order to produce synthetic, and fully defined scaffolds capable of efficiently supporting cholangiocyte cyst formation.

Structure wise, epithelial organoids are organized as a monolayer of polarized epithelial cells surrounding a central lumen. Two typical structures can emerge from this basic concept: cysts or tubes. Nevertheless, the precise underlying morphogenetic mechanism remains elusive and the contribution of the microenvironment is yet to be quantified (Yu et al., 2007; Martin-Belmonte et al., 2008). Other studies have shown that primary biliary mouse epithelial cells (BECs) do form cysts from a single cell when cultured in Matrigel and that the resulting cyst formation efficiency is determined by the initial cell number in the aggregates (Rizki-Safitri et al., 2018). Similarly, the encapsulation of single MDCK cells was found sufficient to trigger cyst formation in synthetic and natural hydrogels (Martin-Belmonte et al., 2008; Enemchukwu et al., 2016). Interestingly, the cell aggregation route for the formation of MDCK cysts was also shown pertinent when these cells were encapsulated at high density. Unlike NRCs or MDCKs, other cell types showing very limited proliferation capabilities such as epithelial lung cells (AT II) still produce cysts with sizes directly linked to initial cell density (Yu et al., 2007). Our experiments showed that the encapsulation of aggregates of multiple NRC resulted in cyst formation by cellular rearrangement whereas single cells systematically failed to proliferate and organize. Similar findings were made for NRC cyst formation in MT with the difference that single cells could migrate and aggregate before proliferating and forming cysts.

When stiffness was considered, we demonstrated that matrix elasticity variation modulates cyst formation (**Figure 2D**). Strikingly, cyst formation was found to be very comparable in soft PEG gels and in MT despite the order of magnitude difference in elastic moduli. This is probably due to the fact that both MT and soft PEG conditions are still below the elastic modulus of a healthy liver (~1 kPa) (Yeh et al., 2002). Globally, the cyst formation process was found to tolerate departure from the healthy liver condition. Even recapitulating fibrotic liver conditions (~5 kPa, Stiff PEG) did not fully block the process. Very interestingly this observation is consistent with the fact that an abnormal increase in intrahepatic biliary mass is taking place during the earliest stages of liver fibrogenesis (Schuppan et al., 2018). In comparison, when encapsulating MDCK cells cyst formation is completely blocked at 7 kPa (Enemchukwu et al., 2016). Matrix elasticity was found to play a key role in other systems including intestinal organoids and lung adenocarcinoma spheres (Gill et al., 2012; Raza et al., 2013; Gjorevski et al., 2016; Broguiere et al., 2018). In these systems, relatively high initial stiffness was needed to drive cell compaction. A quick softening over time was also important in order to help with the 3D rearrangement of cells.

When considering the biochemical cues, we first tried to recapitulate physiologically relevant integrin ligand densities by adjusting the RGD peptide concentration in the PEG hydrogels. However, as the *in vivo* density of RGD motifs accessible to intrahepatic cholangiocytes is hard to assess we employed 100 μM as the best approximation based on the fibrin structure (Raeber et al., 2005) and 1,200 μM as the most efficient concentration for cysts derivation in an equivalent MDCK model (Enemchukwu et al., 2016). In these conditions NRC cyst formation frequency was found independent of the level of integrin engagement. This is in good agreement with the work performed on MDCK cells in synthetic hydrogels (Enemchukwu et al., 2016). This way we found that cyst size (growth of cysts) and thus lumen formation relied on integrin engagement (**Figures 2C, 4B**). The growth in diameter of NRC cysts is known to be fueled by fluid secretion into the cyst lumen and cell proliferation (Neufeld et al., 1992; Doctor et al., 2007). Our results suggest that hydrogel elasticity and cell adhesion can synergistically determine the growth of NRC cysts. When comparing Matrigel and PEG-based systems, Matrigel systematically produced larger cysts. This might be due to the different mechanisms of lumen formation, where NRC cysts cultured in MT achieved cyst polarization at an early time point of cyst formation followed by rapid cyst expansion. The formation of a central lumen is a key feature of epithelial morphogenesis. The mechanism of lumen formation in MDCK cysts grown in natural hydrogels depends on the used ECM composition. MDCK cells cultured in collagen I showed later cell polarization during cyst formation and formed lumen by center cell apoptosis passing through a multi lumen state, whereas MDCK cysts grown in laminin rich Matrigel induced early cell polarization and formed lumen through cell proliferation with almost negligible center cell apoptosis (Martin-Belmonte et al., 2008). This was further confirmed when MDCK cysts were found to form luminal space even when apoptosis was suppressed, hinting to the involvement of multiple lumen forming mechanisms (O'Brien et al., 2002). In comparison, cysts derived from lung epithelial cells cultured in natural hydrogels formed lumen through cell rearrangement without cell proliferation and cell apoptosis (Yu et al., 2007).

In general, epithelial cysts grown in natural hydrogels clearly show single lumen phenotype predominantly. In synthetic hydrogels different phenotypes were observed for NRC and MDCK cells (Enemchukwu et al., 2016). We demonstrated that NRC cyst grown in PEG hydrogels or in MT both formed lumen with a typical apical-basolateral polarity (**Figure 3A**). The accumulation of Rhodamine 123 in the produced cysts hints to a proper and functional organization of the cells. Staining for primary cilia and quantifying the response to farnesoid X receptor could help further confirm this aspect. The mechanisms of lumen formation for cysts cultured in PEG hydrogels was found to be based on cell rearrangement, rather than on early cell polarization as shown in MT. Hydrogel stiffness and RGD concentrations were found to be linked to polarization and to the frequency of single lumen formation. A high integrin engagement was shown to enhance the single lumen phenotype over multi-lumen phenotype in NRC cysts for Soft and Stiff PEG hydrogels, respectively. A positive correlation between lumen formation and adhesive ligand density of a synthetic scaffold was also demonstrated in lung adenocarcinoma models (Gill et al., 2012). Not providing polarization cues in synthetic 3D culture systems systematically delays the acquisition of the cyst polarity (Martin-Belmonte et al., 2008; deLeon et al., 2012). For MDCKs a delayed polarization led to the production of multiple lumens that could fuse at later stages. The size of multi-lumen MDCK cysts cultured in natural and synthetic hydrogels was reported to be similar to cysts containing a single lumen (Martin-Belmonte et al., 2008; Enemchukwu et al., 2016). In our hands a majority of NRC cysts with a single lumen derive from multi-lumen structures. In some cases, these multi-lumen cysts persist. In the MDCK system, the multi-lumen cysts phenotype was found associated with the mislocalization of basal components leading to the accumulation of ECM in the luminal space (Torkko et al., 2008). Unlike MDCKs, the NRC multi-lumen cysts were found to be systematically smaller when compared to single-lumen cysts. The suppression of outer layer coat complex II in human intestinal epithelial cells (Caco-2) cultured in 3D resulted in cysts with defective lumen expansion attributed to a faulty ECM signaling when spatially directing cell division. Similar to multi-lumen NRCs, these cysts show a reduced cell number, multi-lumen formation, and smaller sizes (Townley et al., 2012). We speculate that providing NRCs cultured in PEG with a stronger polarization cues by replacing RGD with laminin or laminin derived peptides could significantly stimulate single-lumen formation and expansion of NRC cysts.

In summary, we have established a tunable PEG-based hydrogel system that can be used for cholangiocyte cyst formation and morphogenesis studies. We demonstrated that making these gel cell responsive by adding MMP sensitivity and integrin ligand contributed to meet the cyst

production capacity of NRCs encapsulated in MT. We expect that in the future, this system will be employed to study pathogenicity of biliary diseases and to identify therapeutic targets.

DATA AVAILABILITY STATEMENT

The datasets generated for this study are available on request to the corresponding author.

AUTHOR CONTRIBUTIONS

AF carried out the experiments performed in PEG hydrogel including cell culture, hydrogel casting, and cell encapsulation, helped with the main figures, and arranged the supplementary figures. NM Performed the rheology tests on PEG gels. LB and EG carried out the experiments in natural hydrogels, including cell culture, cell encapsulation, microscopy, and rheology tests on Matrigel. SG, PD-W, and AF produced together a first outline of the manuscript. PD-W wrote part of the introduction. SG arranged the four main figures, wrote the abstract, part of the introduction, the results, and the discussion. All the authors reviewed the manuscript.

FUNDING

This work received the financial support of both the iLite RHU program (grant ANR ANR-16-RHUS-0005) and the Institut Carnot Pasteur. France-BioImaging infrastructure was supported by the French National Research Agency (ANR 10-INSB-04, Investments for the Future).

ACKNOWLEDGMENTS

The authors would like thank Sébastien Brûlé from the protein quality control service of the molecular biophysics facility in Institut Pasteur for technical assistance with MALDI experiments. We also would like to extend our thanks to Françoise Baleux for her help with measuring the net peptide. Finally, we acknowledged the support of UTechS PBI (Imagopole) a France-BioImaging infrastructure.

SUPPLEMENTARY MATERIAL

The Supplementary Material for this article can be found online at: https://www.frontiersin.org/articles/10.3389/fbioe.2019.00417/full#supplementary-material

REFERENCES

Benam, K. H., Villenave, R., Lucchesi, C., Varone, A., Hubeau, C., Lee, H. H., et al. (2016). Small airway-on-a-chip enables analysis of human lung inflammation and drug responses *in vitro*. *Nat. Methods* 13, 151–157. doi: 10.1038/nmeth.3697

Benjamini, Y., and Yekutieli, D. (2001). The control of the false discovery rate in multiple testing under dependency. *Ann. Stat.* 29, 1165–1188. doi: 10.1214/aos/1013699998

Bogert, P. T., and LaRusso, N. F. (2007). Cholangiocyte biology. *Curr. Opin. Gastroenterol.* 23, 299–305. doi: 10.1097/MOG.0b013e3280b079fb

Boyer, J. L. (2013). Bile formation and secretion. *Compr. Physiol.* 3, 1035–1078. doi: 10.1002/cphy.c120027

Broguiere, N., Isenmann, L., Hirt, C., Ringel, T., Placzek, S., Cavalli, E., et al. (2018). Growth of epithelial organoids in a defined hydrogel. *Adv. Mater.* 30:e1801621. doi: 10.1002/adma.201801621

Broutier, L., Andersson-Rolf, A., Hindley, C. J., Boj, S. F., Clevers, H., Koo, B. K., et al. (2016). Culture and establishment of self-renewing human and mouse adult liver and pancreas 3D organoids and their genetic manipulation. *Nat. Protoc.* 11, 1724–1743. doi: 10.1038/nprot.2016.097

Cheung, A. C., Lorenzo Pisarello, M. J., and LaRusso, N., F. (2018). Pathobiology of biliary epithelia. *Biochim. Biophys. Acta Mol. Basis Dis.* 1864(4 Pt B), 1220–1231. doi: 10.1016/j.bbadis.2017.06.024

De Assuncao, T. M., Jalan-Sakrikar, N., and Huebert, R. C. (2017). Regenerative medicine and the biliary tree. *Semin. Liver Dis.* 37, 17–27. doi: 10.1055/s-0036-1597818

De Assuncao, T. M., Sun, Y., Jalan-Sakrikar, N., Drinane, M. C., Huang, B. Q., Li, Y., et al. (2015). Development and characterization of human-induced pluripotent stem cell-derived cholangiocytes. *Lab. Invest.* 95, 684–696. doi: 10.1038/labinvest.2015.51

de Groen, P. C., Vroman, B., Laakso, K., and LaRusso, N. F. (1998). Characterization and growth regulation of a rat intrahepatic bile duct epithelial cell line under hormonally defined, serum-free conditions. *In Vitro Cell Dev. Biol. Anim.* 34, 704–710. doi: 10.1007/s11626-998-0066-1

deLeon, O., Puglise, J. M., Liu, F., Smits, J., ter Beest, M. B., and Zegers, M. M. (2012). Pak1 regulates the orientation of apical polarization and lumen formation by distinct pathways. *PLoS ONE* 7:e41039. doi: 10.1371/journal.pone.0041039

Dianat, N. H., Dubois-Pot-Schneider, Steichen, C., Desterke, C., Leclerc, P., Raveux, A., et al. (2014). Generation of functional cholangiocyte-like cells from human pluripotent stem cells and HepaRG cells. *Hepatology* 60, 700–714. doi: 10.1002/hep.27165

Doctor, R. B., Johnson, S., Brodsky, K. S., Amura, C. R., Gattone, V., Fitz, J., et al. (2007). Regulated ion transport in mouse liver cyst epithelial cells. *Biochim. Biophys. Acta* 1772, 345–354. doi: 10.1016/j.bbadis.2006.11.006

Enemchukwu, N. O., Cruz-Acuna, R., Bongiorno, T., Johnson, C. T., Garcia, J. R., Sulchek, T., et al. (2016). Synthetic matrices reveal contributions of ECM biophysical and biochemical properties to epithelial morphogenesis. *J. Cell Biol.* 212, 113–124. doi: 10.1083/jcb.201506055

Engler, A. J., Sen, S., Sweeney, H. L., and Discher, D., E. (2006). Matrix elasticity directs stem cell lineage specification. *Cell* 126, 677–689. doi: 10.1016/j.cell.2006.06.044

Gill, B. J., Gibbons, D. L., Roudsari, L. C., Saik, J. E., Rizvi, Z. H., Roybal, J. D., et al. (2012). A synthetic matrix with independently tunable biochemistry and mechanical properties to study epithelial morphogenesis and EMT in a lung adenocarcinoma model. *Cancer Res.* 72, 6013–6023. doi: 10.1158/0008-5472.CAN-12-0895

Gjorevski, N., Sachs, N., Manfrin, A., Giger, S., Bragina, M. E., Ordonez-Moran, P., et al. (2016). Designer matrices for intestinal stem cell and organoid culture. *Nature* 539, 560–564. doi: 10.1038/nature20168

Gobaa, S., Hoehnel, S., Roccio, M., Negro, A., Kobel, S., Lutolf, M., et al. (2011). Artificial niche microarrays for probing single stem cell fate in high throughput. *Nat. Methods* 8, 949–955. doi: 10.1038/nmeth.1732

Hashimoto, W., Sudo, R., Fukasawa, K., Ikeda, M., Mitaka, T., and Tanishita, K. (2008). Ductular network formation by rat biliary epithelial cells in the dynamical culture with collagen gel and dimethylsulfoxide stimulation. *Am. J. Pathol.* 173, 494–506. doi: 10.2353/ajpath.2008.071024

Huh, D., Kim, H. J., Fraser, J. P., Shea, D. E., Khan, M., Bahinski, A., et al. (2013). Microfabrication of human organs-on-chips. *Nat. Protoc.* 8, 2135–2157. doi: 10.1038/nprot.2013.137

Ishida, Y., Smith, S., Wallace, L., Sadamoto, T., Okamoto, M., Auth, M., et al. (2001). Ductular morphogenesis and functional polarization of normal human